

# THE FATIGUE BEHAVIOR OF SMALL CRACKS IN AIRCRAFT TURBINE DISK ALLOYS

by  
Glenn R. Romanoski, Jr.  
B.S. University of Cincinnati, 1979  
M.S. University of Cincinnati, 1981

SUBMITTED IN PARTIAL FULFILLMENT  
OF THE REQUIREMENTS FOR THE  
DEGREE OF

DOCTOR OF PHILOSOPHY

at the

MASSACHUSETTS INSTITUTE OF TECHNOLOGY  
February 1990

© Massachusetts Institute of Technology 1990  
All rights reserved

Signature of Author .....

Department of Materials Science  
and Engineering  
January 12, 1990

Certified by .....

Prof. Regis M. Pelloux  
Thesis Supervisor

Accepted by .....

Prof. Lynn W. Hobbs  
Chairman  
Department Graduate Committee

MASSACHUSETTS INSTITUTE  
OF TECHNOLOGY

MAR 08 1990

LIBRARIES

ARCHIVES

# The Fatigue Behavior of Small Cracks in Aircraft Turbine Disk Alloys

by

Glenn R. Romanoski, Jr.

Submitted to the Department of Materials Science and Engineering  
on January 12, 1990 in partial fulfillment of the  
requirements for the Degree of Doctor of Philosophy in Metallurgy

## ABSTRACT

The fatigue behavior of small cracks was investigated in three aircraft turbine disk alloys at elevated temperatures. The alloys and test temperatures were: Waspaloy (427C), Inconel 718 (427C) and powder metallurgy Gatorized® IN100 (649C). Cracks were initiated at laser defects or at intrinsic micropores. Fatigue crack growth rates were measured by the plastic replication technique over the crack length regime from 100  $\mu\text{m}$  to 1 mm. Tests were performed in load control for Waspaloy and Inconel 718 under high stress ( $\sigma_{\text{max}} \leq 0.9\sigma_{\text{ys}}$ ) elastic fatigue conditions with  $-1 \leq R_{\sigma} \leq 0.5$  and frequency = 20 cpm. Tests were performed for Gatorized® IN100 in load control under high stress ( $\sigma_{\text{max}} \leq 0.9\sigma_{\text{ys}}$ ) elastic fatigue conditions with  $-1 \leq R_{\sigma} \leq 0.1$  and frequency = 10 cpm. Strain control tests were performed under elastic-plastic fatigue conditions with  $\Delta\epsilon_1 = 0.6\%$  to 1.2%,  $R_{\epsilon} = 0$ , and frequency = 10 cpm.

Under elastic fatigue conditions, the LEFM stress intensity factor range correlated small crack ( $100 \mu\text{m} < a < 1 \text{ mm}$ ) with long crack growth rates and consolidated small crack growth rates at different stress levels. Small crack growth rates at different  $R_{\sigma}$ -ratios were consolidated using the Walker-modified stress intensity factor range. The results for the elastic tests are discussed in terms of the validity of employing LEFM at high stress levels and small crack sizes.

Small crack growth rates under elastic-plastic fatigue conditions in powder metallurgy Gatorized® IN100 were consolidated using EPFM parameters including: the pseudostress intensity factor ( $\Delta\text{PK}$ ), the equivalent stress intensity factor ( $\Delta\text{K}_{\text{eq}}$ ) and the cyclic J-integral ( $\Delta\text{J}$ ). Consolidation of small crack growth rates was achieved only when the total stress range or total strain range was used in calculating  $\Delta\text{PK}$ ,  $\Delta\text{K}_{\text{eq}}$  and  $\Delta\text{J}$ . The relationship between these parameters was established. A linear relationship between  $\Delta\sigma_1$  and  $\Delta\sigma_{\text{eff}}$  was found using Newman's crack closure model. The role of the compressive stress-strain excursion in promoting higher crack growth rates is discussed. Anomalous crack growth behavior was not observed for small Mode I cracks under the conditions considered here.

Thesis Supervisor: Professor Regis M. Pelloux  
Department of Materials Science and Engineering

# Table of Contents

	<u>Page</u>
ABSTRACT .....	2
TABLE OF CONTENTS .....	3
LIST OF FIGURES .....	6
LIST OF TABLES .....	14
ACKNOWLEDGEMENTS .....	15
DEDICATION .....	16
1. INTRODUCTION .....	17
1.1 The Aircraft Turbine Disk .....	19
1.2 Turbine Disk Operating Conditions .....	19
2. LITERATURE REVIEW .....	25
2.1 Defect Tolerant Design and Life Management .....	25
• Safe-Life Approach	
• Defect Tolerant Approach	
2.2 The Small Crack Problem in Fatigue .....	30
• Historical Perspective	
• Threshold Stress and Stress Intensity	
• Crack Growth Rates	
• Definition of Short and Small Fatigue Cracks	
2.3 Linear Elastic Fracture Mechanics .....	39
• Basic Concepts	
• Crack Closure and $\Delta K_{eff}$	
• Applicability of LEFM to Small Cracks	
• Similitude Requirements	
2.4 Elastic-Plastic Fracture Mechanics .....	53
• Empirical Approach	
• Strain Intensity and Equivalent Stress Intensity	
• The J-integral	
• The Cyclic J-integral Range	
2.5 Modeling of Small Crack Behavior .....	67
• Intrinsic Crack Length	
• Constant Plastic Zone Size Criterion	
• Shear Displacement Criterion	
• Blocked Slip Band (BSB) Model	

• Fracture Surface Roughness and Crack Closure Model	
2.6 Fatigue Behavior of Small Cracks in Aircraft Turbine Disk Alloys	79
• Turbine Disk Alloys at Room Temperature	
• Turbine Disk Alloys at Elevated Temperature	
3. EXPERIMENTAL PROCEDURES	88
3.1 Materials	88
• Waspaloy	
• Inconel 718	
• Powder Metallurgy Gatorized® IN100	
3.2 Test Specimen	98
• Specimen Geometry	
• Specimen Preparation	
• Initiation of Small Cracks	
• Precracking	
3.3 Crack Length Measurement by Plastic Replication	100
3.4 Crack Length Measurement by A.C. Potential Drop	101
3.5 Small Crack Growth Testing at Elevated Temperature	102
• Load Controlled Testing	
• Strain Controlled Testing	
3.6 Data Analysis	108
• Computation of Crack Growth Rates	
• Stress Intensity Factor Calculations	
4. RESULTS AND DISCUSSION	114
4.1 The Fatigue Behavior of Small Cracks in Waspaloy at 427C	114
• Effect of Maximum Stress	
• Applicability of LEFM	
• Similitude Requirements	
• Crack Growth Rate versus Plastic Zone Size	
• Effect of R-ratio	
• Empirical Approaches to Consolidating R-ratio Data	
• Crack Closure Concepts Applied to Consolidating R-ratio Data	
• Effect of Temperature	
4.2 The Fatigue Behavior of Small Cracks in Inconel 718 at 427C	136
• Small versus Long Crack Growth Behavior	
• Effect of Maximum Stress	
• Effect of R-ratio	
• Applicability of LEFM	
4.3 The Fatigue Behavior of Small Cracks in Powder Metallurgy Gatorized® IN100 at 649C; Elastic Tests	144
• Effect of Maximum Stress	

• Effect of R-ratio	
• Empirical Consolidation of R-ratio Data	
4.4 Stress-Strain Response of Powder Metallurgy	
Gatorized® IN100 at 649C .....	155
• Monotonic Stress-Strain Response	
• Cyclic Stress-Strain Response	
4.5 The Fatigue Behavior of Small Cracks in Powder Metallurgy	
Gatorized® IN100 at 649C; Elastic-Plastic Tests .....	162
• Stress Intensity Factor Range	
• Comparison of Elastic-Plastic Tests in Terms of the Stress Intensity Factor Range	
• Pseudostress Intensity Factor Range	
• Equivalent Stress Intensity Factor Range	
• The Cyclic J-integral Range	
4.6 Appendant Studies for Gatorized® IN100 at 649C .....	185
• Continuous Cycling	
• Strain Hold Test	
• Crack Growth from Intrinsic Microporosity	
4.7 Fractography .....	190
• Waspaloy, 427C; Elastic Fatigue Conditions	
• Inconel 718, 427C; Elastic Fatigue Conditions	
• IN100 (PM), 649C; Elastic-Fatigue Conditions	
• IN100 (PM), 649C; Elastic-Plastic Fatigue Conditions	
5. GENERAL DISCUSSION .....	210
5.1 The Effect of Negative R-ratio on Fatigue Crack Growth Rates .....	213
5.2 Crack Opening and Closure Measurements .....	217
• Crack Opening-Closure under Elastic Fatigue Conditions	
• Crack Opening-Closure under Elastic-Plastic Fatigue Conditions	
5.3 Models for Predicting Crack Opening and Closure .....	224
5.4 Newman's Model Applied to Gatorized® IN100 at 649C .....	228
• Elastic Tests	
• Elastic-Plastic Tests	
• Reconciliation; $\Delta\sigma_{tot}$ with $\Delta\sigma_{eff}$	
5.5 Fatigue Crack Growth and Crack Tip Strain Reversals .....	237
6. CONCLUSIONS .....	242
7. RECOMMENDATIONS FOR FUTURE RESEARCH.....	244
REFERENCES .....	245

## List of Figures

		<u>Page</u>
Figure 1.1	Aircraft turbine disk: (a) overview, (b) cross-section [Ref. 1.9].	..... 21
Figure 1.2	Turbine disk fir-tree attachment with corner crack.	..... 22
Figure 1.3	Typical transport flight cycle.	..... 23
Figure 1.4	Hypothetical notch/net section response in a turbine disk fir-tree for a transport flight cycle.	..... 24
Figure 2.1	Total fatigue life segmented into stages of crack growth. The variation in equivalent initial flaw size (EIFS) and small crack behavior dominates total fatigue life.	..... 28
Figure 2.2	Distribution of fatigue life in a population of turbine disks [Ref. 2.3].	..... 29
Figure 2.3	Defect tolerant life extension involves inspection and return-to-service until a quantifiable defect is found, resulting in disk retirement [Ref. 2.3].	..... 29
Figure 2.4	Schematic showing the two stages of subcritical fatigue crack growth first proposed by Forsyth [Refs. 2.4, 2.5].	..... 35
Figure 2.5	Log stress versus log crack length illustrating the threshold stress between propagating and nonpropagating cracks.	..... 36
Figure 2.6	Apparent threshold stress intensity factor range versus crack length illustrating the two regimes of propagating and nonpropagating cracks.	..... 36
Figure 2.7	Crack growth rates versus $\Delta K$ or $a$ ; comparison of long crack behavior with anomalous small crack behavior.	..... 37
Figure 2.8	Crack in an infinite plate subjected to a remotely applied stress [Ref. 2.12'].	..... 47
Figure 2.9	Elastic crack tip stress field [Ref. 2.12'].	..... 47
Figure 2.10	Crack tip plastic zones: (a) Assumed elastic stress distribution, (b) Approximate stress distribution after yielding is accounted for [Ref. 2.12'].	..... 48
Figure 2.11	Fatigue crack growth rate versus stress intensity factor range for a typical long crack exhibiting three distinct regimes of behavior.	..... 49

Figure 2.12	(a) Schematic of crack opening and closure in a single fatigue cycle. (b) Identification of crack opening and closure level from the load versus displacement plot.	..... 50
Figure 2.13	Schematic comparison of the various crack closure mechanisms [Ref. 2.15].	..... 51
Figure 2.14	Schematic of (a) global and (b) local application of fracture mechanics [Ref. 2.25].	..... 52
Figure 2.15	Definition of the pseudostress range according to Solomon [Ref. 2.52].	..... 62
Figure 2.16	Definition of the equivalent stress range according to Starkey and Skelton [Ref. 2.54].	..... 63
Figure 2.17	The J-integral of Rice [Ref. 2.55].	..... 64
Figure 2.18	Stress-strain hysteresis loops plotted on shifted axes [Ref. 2.61].	..... 65
Figure 2.19	Estimation of small crack $\Delta J_t$ from stress-strain hysteresis loops [Ref. 2.61].	..... 66
Figure 2.20	Effect of crack length on the threshold stress range for fatigue crack growth in G40.11 steel [Ref. 2.71].	..... 74
Figure 2.21	Effect of R-ratio and environment on the threshold stress amplitude and endurance limit ( $5 \times 10^7$ cycles) for 13 Cr cast steel with micro-shrinkage cavities [Ref. 2.74].	..... 74
Figure 2.22	Small crack embedded in the elastic-plastic field of a notch [Ref. 2.75].	..... 75
Figure 2.23	Schematic illustration of the elastic-plastic and linear elastic characterization of crack growth rate for a small crack propagating from a notch [Ref. 2.75].	..... 76
Figure 2.24	Schematic illustration of the BSB model [Ref. 2.78]. (a) Crack-tip slip band blocked by a grain boundary and (b) Coplanar slip band emanating from the tip of an isolated crack.	..... 77
Figure 2.25	Illustration of roughness induced crack closure at an average distance $X_0$ behind the crack tip. [Ref. 2.83]	..... 78
Figure 2.26	Crack mouth opening displacement (at zero load) versus surface crack length for a 6Al-2Sn-4Zn-6Mo titanium alloy [Ref. 2.83].	..... 78

Figure 2.27	Crack growth rates versus $\Delta K$ for small cracks in fine-grained (5 $\mu\text{m}$ ) and coarse-grained (50 $\mu\text{m}$ ) Astroloy and equivalent single crystal material [Ref. 2.96].	.....87
Figure 3.1	Typical microstructure of Waspaloy used in this investigation; (a) duplex grain structure with average grain sizes of 7 $\mu\text{m}$ and 200 $\mu\text{m}$ , (b) matrix $\gamma'$ exhibiting a spheroidal morphology.	.....91
Figure 3.2	Typical microstructure of Inconel 718 used in this investigation; average grain size is 32 $\mu\text{m}$ .	.....94
Figure 3.3	Typical microstructure of powder metallurgy Gatorized <sup>®</sup> IN100 with an average grain size of 3-5 $\mu\text{m}$ . (a) Optical micrograph, (b) SEM micrograph exhibiting a duplex $\gamma'$ structure.	.....97
Figure 3.4	Specimen geometry used in this investigation; cylindrical gage section.	....104
Figure 3.5	Modification to cylindrical gage section of specimen shown in Figure 3.4.	....105
Figure 3.6	Typical laser defects.	....106
Figure 3.7	High temperature testing system.	....107
Figure 3.8	Semi-elliptical surface crack in a finite elastic body.	....113
Figure 4.1	Crack depth versus cycle number for Waspaloy tested at 427C under nominally elastic fatigue conditions; stress range was varied at R=-1, Freq.=20 cpm.	....128
Figure 4.2	Summary of crack growth rates versus stress intensity factor range for Waspaloy tested at 427C under nominally elastic fatigue conditions; stress range was varied at R=-1, Freq.=20 cpm.	....129
Figure 4.3	Crack depth versus cycle number for Waspaloy tested at 427C under nominally elastic fatigue conditions; R-ratio was varied, Freq.=20 cpm.	....130
Figure 4.4	Summary of crack growth rates versus stress intensity factor range for Waspaloy tested at 427C under nominally elastic fatigue conditions; R-ratio was varied, Freq.=20 cpm.	....131
Figure 4.5	Effect of R-ratio on relative crack growth rates for Waspaloy tested at 427C under nominally elastic fatigue conditions. Crack growth rates are compared at $\Delta K=20 \text{ MPa}\sqrt{\text{m}}$ and normalized with respect to $da/dN(R=0)$ .	....132

Figure 4.6	Summary of crack growth rates versus the Walker modified stress intensity factor range ( $\alpha=0.5$ ) for Waspaloy tested at 427C under nominally elastic fatigue conditions, R-ratio varied, Freq.=20 cpm.	....133
Figure 4.7	Comparison of crack growth rates versus stress intensity factor range for Waspaloy tested at 25C and 427C, R=-1.	....134
Figure 4.8	Comparison of crack growth rates versus stress intensity factor range for Waspaloy tested at 25C and 427C, R=0.	....135
Figure 4.9	Crack depth versus cycle number for Inconel 718 tested at 427C under nominally elastic fatigue conditions; Freq = 20 cpm.	....140
Figure 4.10	Crack growth rates versus stress intensity factor range for Inconel 718 tested at 427C under nominally elastic fatigue conditions; small crack versus long crack, R=0.05 and Freq = 20 cpm.	....141
Figure 4.11	Summary of crack growth rates versus stress intensity factor range for Inconel 718 tested at 427C under nominally elastic fatigue conditions. Stress range was varied at R=-1, Freq. = 20 cpm.	....142
Figure 4.12	Summary of crack growth rates versus stress intensity factor range for Inconel 718 tested at 427C under nominally elastic fatigue conditions; R-ratio varied at Max. Stress = 758 MPa, Freq. = 20 cpm.	....143
Figure 4.13	Crack depth versus cycle number for IN100(PM) tested at 649C under nominally elastic fatigue conditions; stress range was varied at R=0.1, Freq. = 10 cpm.	....150
Figure 4.14	Summary of crack growth rates versus stress intensity factor range for IN100(PM) tested at 649C under nominally elastic fatigue conditions; stress range was varied at R=0.1, Freq.=10 cpm. Two cracks are shown arrested at A' and B'.	....151
Figure 4.15	Crack depth versus cycle number for IN100(PM) tested at 649C under nominally elastic fatigue conditions; R-ratio was varied at a maximum stress of 965 MPa, Freq.=10 cpm.	....152
Figure 4.16	Summary of crack growth rates versus stress intensity factor range for IN100(PM) tested at 649C under nominally elastic fatigue conditions; R-ratio was varied at a maximum stress of 965 MPa, Freq.=10 cpm.	....153

Figure 4.17	Summary of crack growth rates versus the Walker-modified stress intensity factor range ( $\alpha=0.5$ ) for IN100(PM) tested at 649C under nominally elastic fatigue conditions; R-ratio was varied at a maximum stress of 965 MPa, Freq.=10 cpm.	....154
Figure 4.18	Monotonic and cyclic stress-strain response for IN100(PM) at 649C. Strain rate was $\sim 0.3\%/sec$ in the monotonic test and Freq.=10 cpm in the cyclic tests.	....159
Figure 4.19	Total stress range versus plastic strain range for IN100(PM) at 649C. Test Freq.=10 cpm.	....160
Figure 4.20a	Monotonic stress versus plastic strain for IN100(PM) at 649C. Strain rate was $\sim 0.3\%/sec$ .	....161
Figure 4.20b	Cyclic total stress range versus plastic strain range for IN100(PM) at 649C. Freq. = 10 cpm.	....161
Figure 4.21	Total strain range versus cycles to a 5% stress range drop for IN100(PM) tested at 649C under continuous cycling and tensile strain dwell conditions, Ref [4.23].	....171
Figure 4.22	Crack growth rates versus stress intensity factor range for IN100(PM) tested at 649C under elastic-plastic fatigue conditions; total strain range was varied, Freq. = 10 cpm.	....172
Figure 4.23	Crack growth rates versus stress intensity factor range for IN100(PM) tested at 649C under elastic and elastic-plastic fatigue conditions; $R_{\sigma} = -0.5$ in both cases, Freq. = 10 cpm.	....173
Figure 4.24	Crack growth rates versus stress intensity factor range for IN100(PM) tested at 649C under elastic and elastic-plastic fatigue conditions; $R_{\sigma} = -0.75$ in both cases, Freq. = 10 cpm.	....174
Figure 4.25	Crack growth rates versus stress intensity factor range for IN100(PM) tested at 649C under elastic and elastic-plastic fatigue conditions; $R_{\sigma} = -1.0$ in both cases, Freq. = 10 cpm.	....175
Figure 4.26	Crack growth rates versus the pseudostress intensity factor range for IN100(PM) tested at 649C under elastic-plastic fatigue conditions; total strain range was varied, Freq. = 10 cpm.	....176
Figure 4.27	Crack growth rates versus the pseudostress intensity factor range for IN100(PM) tested at 649C under elastic fatigue conditions; total stress range was varied, Freq. = 10 cpm.	....177

Figure 4.28	Summary of crack growth rates versus the pseudostress intensity factor range for IN100(PM) tested at 649C under elastic and elastic-plastic fatigue conditions; Freq. = 10 cpm.	....178
Figure 4.29	Crack growth rates versus the equivalent stress intensity factor range for IN100(PM) tested at 649C under elastic-plastic fatigue conditions; total strain range was varied, Freq. = 10 cpm.	....179
Figure 4.30	Crack growth rates versus the cyclic J-integral range for IN100(PM) tested at 649C under elastic-plastic fatigue conditions; total strain range was varied, Freq. = 10 cpm.	....180
Figure 4.31	Crack growth rates versus the cyclic J-integral range for IN100(PM) tested at 649C under elastic fatigue conditions; total stress range was varied, Freq. = 10 cpm.	....181
Figure 4.32	Summary of crack growth rates versus the cyclic J-integral range for IN100(PM) tested at 649C under elastic and elastic-plastic fatigue conditions; Freq. = 10 cpm.	....182
Figure 4.33	Crack growth rates versus the positive J-integral range for IN100(PM) tested at 649C under elastic-plastic fatigue conditions; only $\Delta\sigma_{pos}$ was used to calculate $\Delta J$ , Freq. = 10 cpm.	....183
Figure 4.34	Crack growth rates versus $\Delta K$ for two elastic-plastic tests at $\Delta\epsilon_t = 0$ to 0.8%. Crack growth rates were determined by both the secant and 7-point polynomial technique.	....187
Figure 4.35	Crack growth rates versus $\Delta K$ for elastic-plastic tests at $\Delta\epsilon_t = 0$ to 0.8%. Comparison of continuous cycling data (10 cpm) with 60 sec hold at maximum strain data.	....188
Figure 4.36	Crack growth rates versus $\Delta K$ for elastic-plastic tests at $\Delta\epsilon_t = 0$ to 0.8%. Comparison of crack growth behavior from pores to that from laser defects.	....189
Figure 4.37	Crack front profiles as evidenced by the presence of oxidation on the fracture surfaces of Waspaloy specimens tested at 427C under elastic fatigue conditions.	....192
Figure 4.38	Fractographs of Waspaloy tested at 427C under nominally elastic fatigue conditions; (a) laser defect surrounded by the precrack region, (b) typical transgranular fracture surface features.	....193
Figure 4.39	Typical crack front profiles as evidenced by the presence of oxidation on the fracture surfaces of Inconel 718 specimens tested at 427C under elastic fatigue conditions.	....195

Figure 4.40	Optical micrographs of a typical surface crack trace in Inconel 718 tested at 427C under elastic fatigue conditions; (a) small crack propagating from laser defect, (b) crack tip extending parallel and perpendicular to persistent slip bands.	....196
Figure 4.41	Typical transgranular fracture surface features for Inconel 718 tested at 427C under elastic fatigue conditions.	....197
Figure 4.42	Typical crack front profiles as evidenced by the presence of oxidation on the fracture surfaces of IN100(PM) specimens tested at 649C under elastic fatigue conditions.	....200
Figure 4.43	Typical fracture surface features for IN100(PM) tested at 649C under elastic fatigue conditions; (a) room temperature precracked region exhibiting a transgranular fracture path, (b) high temperature fatigue crack region exhibiting an intergranular fracture path.	....201
Figure 4.44	Metallographic section through a fatigue crack in IN100(PM) tested at 649C under elastic fatigue conditions; Max stress = 965 MPa and R = 0.1. Fracture path is predominantly intergranular.	....202
Figure 4.45	Crack initiation at slightly subsurface pores in IN100(PM) tested at 649C under elastic fatigue conditions; Max. stress = 965 MPa and R = 0.1; (a) dominant crack, (b) noncritical crack.	....203
Figure 4.46	Typical fracture surface features for IN100(PM) tested at 649C under elastic-plastic fatigue conditions, (a) intergranular fracture path for $\Delta\epsilon_t = 0$ to 0.82% ( $\Delta\epsilon_p = 0.015\%$ ), (b) intergranular fracture path for $\Delta\epsilon_t = 0$ to 1.23% ( $\Delta\epsilon_p = 0.13\%$ ).	....206
Figure 4.47	Crack initiation at pores in IN100(PM) tested at 649C under elastic-plastic fatigue conditions; (a) surface intersected pore and (b) slightly subsurface pore.	....207
Figure 4.48	Transition from transgranular to intergranular fracture path with increasing crack length for IN100(PM) tested at 649C under elastic-plastic fatigue conditions.	....208
Figure 4.49	Schematic representing crack initiation at surface and subsurface pores.	....209
Figure 5.1	General variation in crack growth rate versus R-ratio for a variety of engineering alloys.	....216
Figure 5.2	Surface crack trace open at zero load in an IN100(PM) specimen after testing at 649C in strain control ( $\Delta\epsilon_t = 0$ to 0.8%).	....222

Figure 5.3	Comparison of experimental results with Newman's analysis for normalized crack opening stress versus maximum stress for a 1026 steel, $R = -1$ . From Ref. [5.22].	....223
Figure 5.4	Crack surface displacement and stress distribution along the crack line for Newman's modification to the Dugdale strip yield model. From Ref. [5.31].	....227
Figure 5.5	Normalized crack opening stress level (calculated from Newman's model) versus R-ratio for IN100(PM) tested at 649C under elastic fatigue conditions; max. stress = 965 MPa.	....232
Figure 5.6	Crack growth rates versus the effective stress intensity factor range (calculated using $\Delta\sigma_{eff}$ from Newman's model) for IN100(PM) tested at 649C under elastic fatigue conditions; R-ratio was varied at max. stress = 965 MPa, Freq. = 10 cpm.	....233
Figure 5.7	Crack growth rates versus the effective J-integral range, (calculated using $\Delta\sigma_{eff}$ from Newman's model) for IN100(PM) tested at 649C and under elastic-plastic fatigue conditions; total strain range was varied, Freq. = 10 cpm.	....234
Figure 5.8	Summary of crack growth rates versus the effective J-integral range, (calculated using $\Delta\sigma_{eff}$ from Newman's model) for IN100(PM) tested under elastic and elastic-plastic fatigue conditions; Freq = 10 cpm.	....235
Figure 5.9	Effective stress range (calculated from Newman's model) versus total stress range for IN100(PM) tested under elastic and elastic-plastic fatigue conditions, Freq. = 10 cpm.	....236
Figure 5.10a	Crack tip stress fields and crack wake residual stresses for $R = 0$ loading; max. stress = $0.72\sigma_{ys}$ , crack length = $0.6 \cdot (\text{notch radius})$ . From Ref. [5.36].	....240
Figure 5.10b	Crack tip stress fields and crack wake residual stresses for $R = -1$ loading; max. stress = $0.72\sigma_{ys}$ , crack length = $0.6 \cdot (\text{notch radius})$ . From Ref. [5.36].	....240
Figure 5.11a	Crack tip monotonic and reversed plastic zones for $R = 0$ loading; max. stress = $0.72\sigma_{ys}$ , crack length = $0.6 \cdot (\text{notch radius})$ . From Ref. [5.36].	....241
Figure 5.11b	Crack tip monotonic and reversed plastic zones for $R = -1$ loading; max. stress = $0.72\sigma_{ys}$ , crack length = $0.6 \cdot (\text{notch radius})$ . From Ref. [5.36].	....241

## List of Tables

		<u>Page</u>
Table 2.1	Classes of Small Fatigue Cracks	..... 38
Table 3.1	Alloy and Test Temperature	..... 88
Table 3.2	Waspaloy • Chemical Composition • Heat Treatment • Mechanical Properties	..... 90
Table 3.3	Inconel 718 • Chemical Composition • Heat Treatment • Mechanical Properties	..... 93
Table 3.4	Powder Metallurgy Gatorized® IN100 • Chemical Composition • Heat Treatment • Mechanical Properties	..... 96
Table 4.1	Test Conditions for Waspaloy	....127
Table 4.2	Test Conditions for Inconel 718 at 427C	....139
Table 4.3	Tests Conditions for Powder Metallurgy Gatorized® IN100 at 649C	....149
Table 4.4	Components of Strain Range and J-integral Range for IN100(PM) at 649C	....184

## Acknowledgements

This investigation was performed under sponsorship of the Air Force Office of Scientific Research under Grant # AFOSR-84-0075. Dr. A. Rosenstein was grant monitor.

I would like to thank: M. Blackburn, J. Hill and V. Moreno of Pratt and Whitney Aircraft; D. Backman, R. H. Van Stone, M. Henry and D. Krueger of General Electric; and K. Bain of Allison Gas Turbine Division of General Motors for material support and valuable discussions.

Special thanks go to my thesis advisor, Professor Regis Pelloux, for his patience and guidance throughout the course of my studies and research at MIT. I also wish to thank my other thesis committee members: Professor Owen, Professor Ballinger and Professor Russell.

I would like to express my deep appreciation to a special group of friends: my close colleagues, the staff of our fatigue and fracture research group, and the staff of the Department of Material Science and Engineering for their technical assistance and encouragement.

I would like to thank the members of my family, especially my parents for their financial and emotional support throughout my lengthy graduate career. And finally, and most prominently, I would like to thank Libby Reyes for her <sup>\*</sup>dedication to my personal well being, as well as her time and skill in transforming my hieroglyphics into the document you see before you. Her assistance was invaluable.

*To my family*

# 1. Introduction

Turbine disks are regarded as the most critical flight safety components of high performance jet engines. Traditionally, turbine disks have been designed on the basis of a low-cycle-fatigue (LCF) life limitation criterion. This "safe life" design philosophy considers the useful life to be exhausted after a crack initiation phase results in the development of a small fatigue crack of 0.79 mm (1/32 in) in length in 0.1% of the disks. Due to the conservative nature of the "safe life" approach, there is considerable economic incentive to extend service lives by combining crack initiation and crack propagation criteria in life prediction.

The United States Air Force (USAF) has developed a Retirement for Cause (RFC) program [1.1-1.3] in which service lives for components may be extended until crack initiation is detected during inspection. Implementation of RFC requires a "damage tolerant" approach which employs fracture mechanics to assure adequate fatigue crack propagation lives between inspections. The initial crack size is taken to be the maximum size which may just escape detection.

Some materials are subject to premature fatigue crack initiation due to handling, machining damage, fretting or intrinsic defects such as porosity and inclusions usually found in powder metallurgy (PM) alloys. Assuming that premature cracking is present, it is necessary to employ a "damage tolerant" design approach to assure adequate crack propagation lives from small initial defects and/or cracks. The USAF has initiated the Engine Structural Integrity Program (ENSIP) [1.4-1.6] which establishes guidelines for damage tolerant design of engine components.

To achieve either of the two goals described above, extending lives of LCF damaged disks (RFC) or assuring safe lives for defect-containing disks (ENSIP), requires the

application of linear elastic fracture mechanics (LEFM) to very small cracks ( $< 1$  mm) and high stress ranges approaching the yield strength of the material. The fracture mechanics database employed in damage tolerant analysis was generated using conventional LEFM test specimens with long cracks ( $> 1$  mm). In recent years it has been demonstrated that the fatigue behavior of small cracks in many alloys exhibit anomalous behavior when compared to data obtained on long cracks [1.7-1.8]. Small cracks were observed to propagate below the threshold stress intensity factor range,  $\Delta K_{TH}$ , and grow at rates exceeding long crack growth rates at the same nominal value of  $\Delta K$ . This behavior has been termed the "short crack" effect and it poses a serious concern that damage tolerant analysis using long crack LEFM could potentially be nonconservative.

The objective of this research is to determine the fatigue crack growth behavior of small cracks ( $10\mu\text{m} < a < 1\text{mm}$ ) in aircraft turbine disk alloys at elevated temperature under conditions of high cyclic stress and to determine the suitability of LEFM for correlating crack growth rates under these conditions. Since most fatigue crack initiation in turbine disks is associated with notch configurations, such as bolt holes and blade attachments, the fatigue behavior of small cracks subjected to elastic-plastic cyclic conditions was also investigated. A number of elastic-plastic fracture mechanics (EPFM) parameters was considered to consolidate crack growth rates. The materials and test temperatures were: Waspaloy (427C), Inconel 718 (427C) and powder metallurgy Gatorized<sup>®</sup> IN100 (649C). Stress ratios ( $\sigma_{\min}/\sigma_{\max}$ ) ranged from -1 to 0.5 in elastic tests. In elastic-plastic tests,  $\epsilon_{\min}/\epsilon_{\max} = 0$ . Test frequencies were 20 cpm for Waspaloy and Inconel 718, and 10 cpm for powder metallurgy Gatorized<sup>®</sup> IN100.

## 1.1 The Aircraft Turbine Disk

A modern aircraft turbine disk is shown in Figure 1.1. The alloy property requirements vary with location and specific structural detail and reflect the temperature and stress levels present under service conditions [1.9]. The bore of the disk experiences the highest net section stresses and requires high yield and ultimate tensile strengths. The bore may be life limited by the growth of fatigue cracks from small intrinsic or processing defects.

The rim operates under lower stresses but at higher temperatures and requires adequate creep resistance. The rim is slotted to hold turbine blades in a unique serrated geometry often called a "fir-tree" attachment. A typical blade attachment geometry is shown in Figure 1.2. Here, the disk material requires adequate notch stress rupture and creep-fatigue resistance. A variety of geometrical discontinuities such as rim-slot cooling holes and bolt holes are susceptible to low-cycle fatigue failure.

## 1.2 Turbine Disk Operating Conditions

Under normal operation, aircraft turbine disks are nominally elastic bodies with the exception of notch configurations where the disk material experiences cyclic stresses and strains greater than the elastic limit. The definition of a single cycle can be put in its simplest terms for a transport type of application as the stress and temperature history from take-off to landing as shown in Figure 1.3. Net section stresses may approach a significant fraction of the materials' yield strength. Temperatures shown are for the rim of the disk. Military flight cycles include significant subcycles per flight making turbine disk life assessment more complex.

Consider the turbine blade attachment slot shown in Figure 1.2. At the root of notches, the local stresses and strains exceed the elastic limit while the net section stress in the disk fir-tree remains nominally elastic. Figure 1.4 shows the hypothetical notch/net section

response for the root of a typical fir tree operating at a maximum temperature around 650C. Note that  $R_\epsilon = 0$  (where  $R_\epsilon = \epsilon_{\min}/\epsilon_{\max}$ ) and that stress relaxation occurs after take-off and throughout cruise. The stress relaxation is a result of creep strain accumulating in the notch as well as in the net section. The magnitude of the inelastic strain is exaggerated in Figure 1.4. The maximum total strain range experienced at the notch root is estimated to be on the order of 0.8%.

It is not the objective of this thesis to assess the fatigue endurance of any specific turbine disk structural feature but to assess the suitability of LEFM and EPFM parameters to correlate crack growth rates for small cracks under elastic and elastic-plastic fatigue conditions. Alloys, test temperatures and stress-strain ranges were chosen to approach relevant turbine disk conditions. Stress-strain-time cycles were simplified with respect to actual turbine disk operation (Figure 1.4) to facilitate testing. A detailed discussion of turbine disk cyclic life prediction may be found in the literature [1.10-1.14].

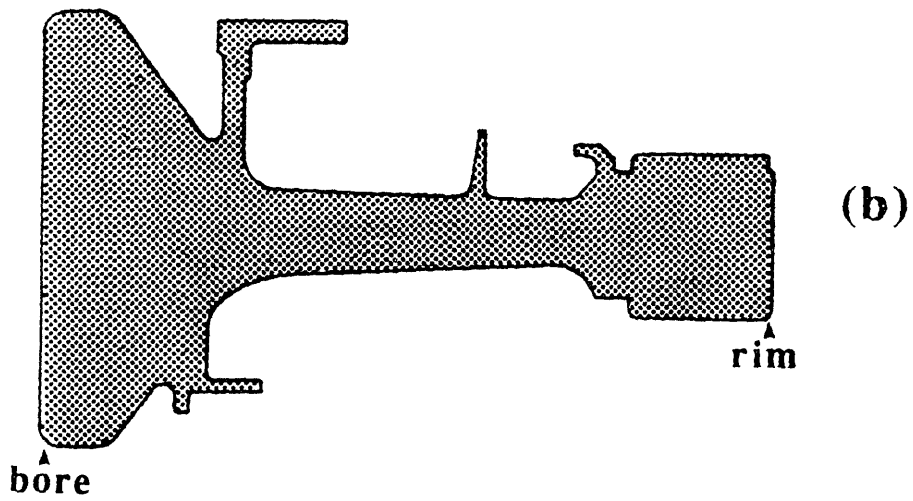
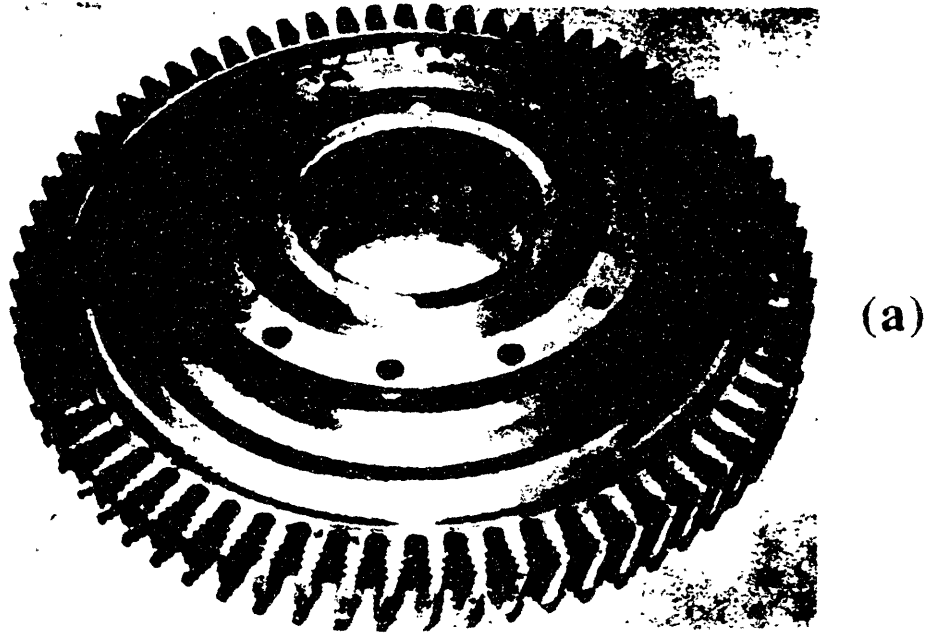


Figure 1.1 Aircraft turbine disk: (a) overview, (b) cross-section [Ref. 1.9].

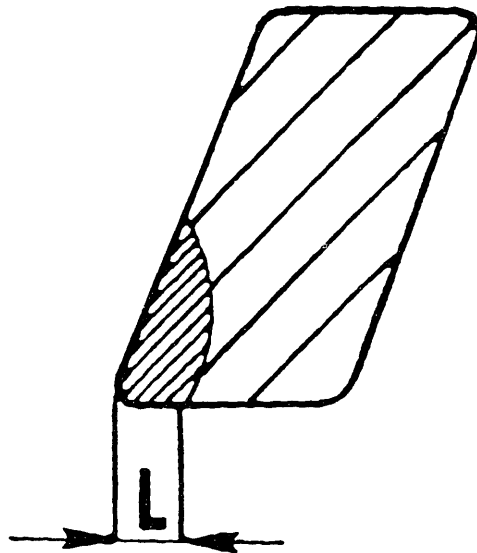
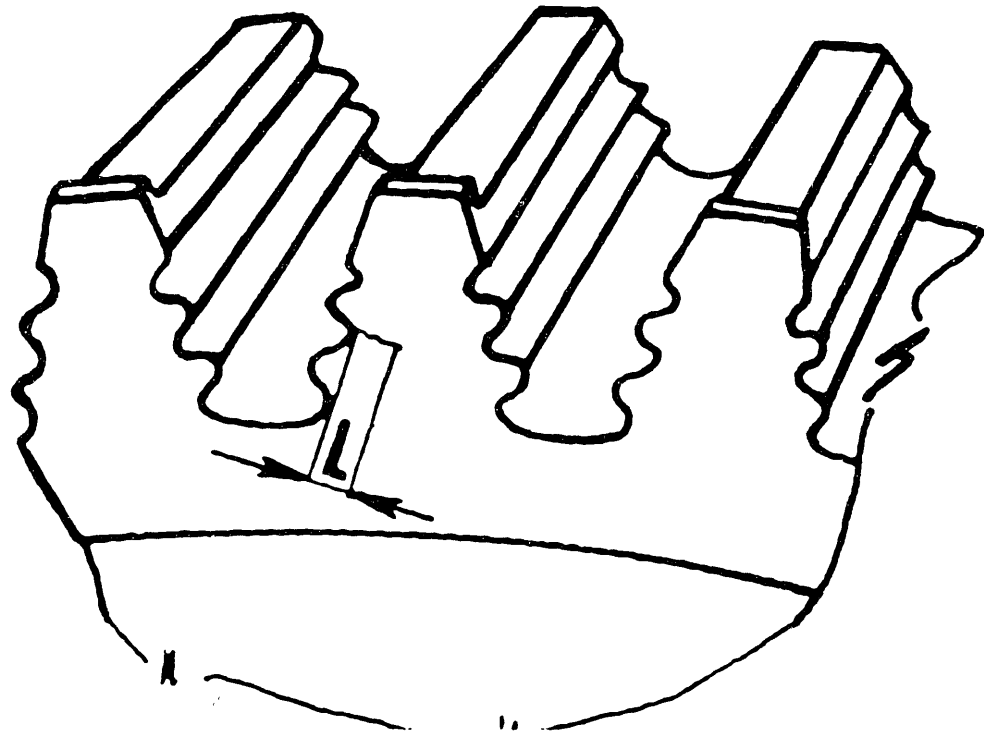


Figure 1.2 Turbine disk fir-tree attachment with corner crack.

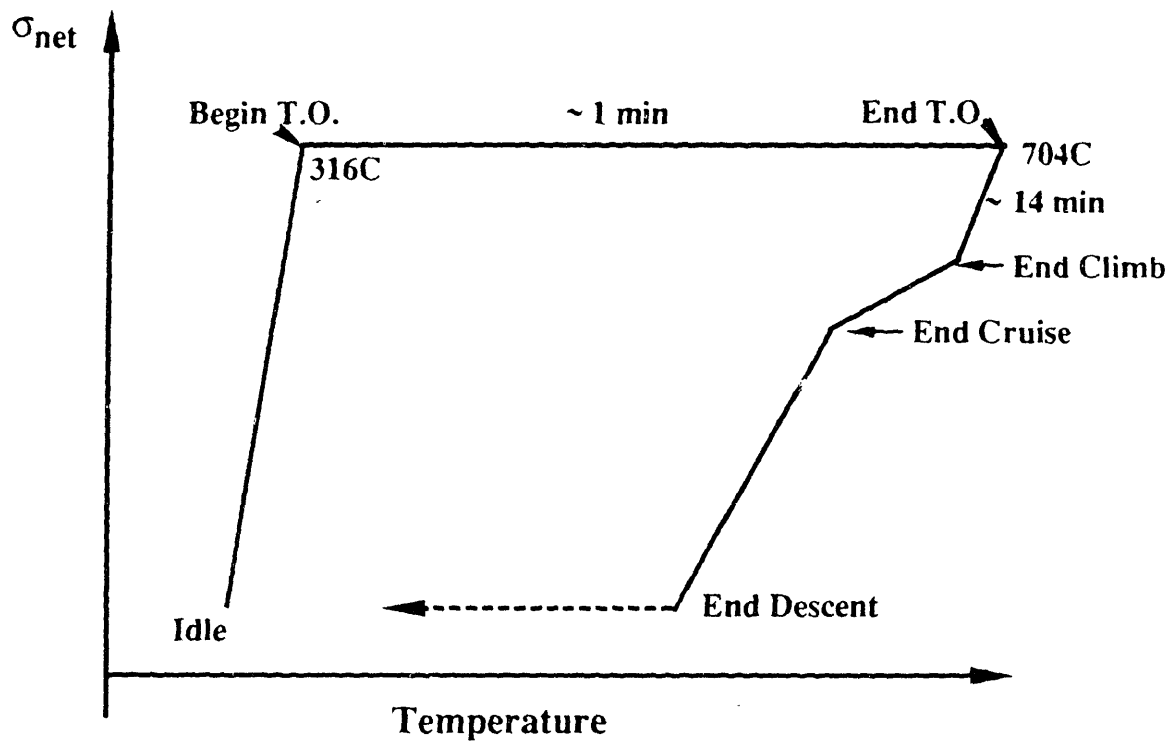


Figure 1.3 Typical transport flight cycle.

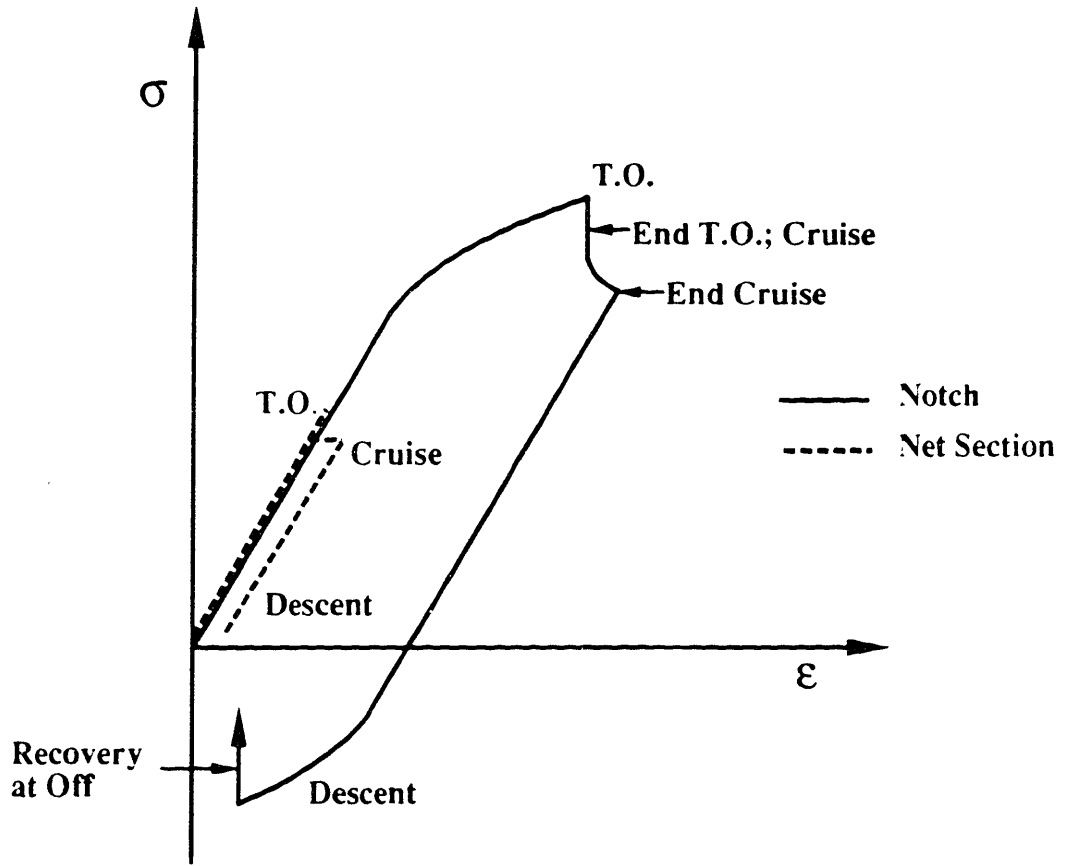


Figure 1.4 Hypothetical notch/net section response in a turbine disk fir-tree for a transport flight cycle.

## **2. Literature Review**

The subject of the fatigue behavior of small cracks in commercial alloys has recently been reviewed by a number of authors [1.7-1.8]. The objectives of this literature review are threefold:

- 1) To establish the engineering relevance of this investigation to the design and life management of aircraft turbine disks.
- 2) To give a general overview of fracture mechanics theory and fatigue methodologies which have been applied to the fatigue crack growth of small cracks. Here the depth of treatment often yields to a desire to discuss the many factors which have been shown to influence this problem. A more detailed review will be made of approaches later used to evaluate the results of this investigation.
- 3) To make a comprehensive review of published results on small crack behavior in turbine disk alloys. Specific references to other commercial alloy systems will be made only when it illustrates some relevant behavior. Some pertinent references may have been regretfully overlooked due to time constraints.

### **2.1 Defect Tolerant Design and Life Management**

The development of fatigue cracks in gas turbine disk alloys can be viewed as progressing in four stages:

Crack initiation may occur at physical discontinuities or at susceptible microstructural features. The duration of the crack initiation period exhibits considerable scatter and is the principal source of variability in total fatigue life. The number of cycles or time required for crack initiation varies with the nature, size, shape orientation and location of defects. The effect of defect size distribution on crack initiation and total fatigue life is illustrated in Figure

2.1. The values and distribution of equivalent initial flaw sizes (EIFS) are shown [2.1]. The EIFS is a fictitious crack length which can be substituted for intrinsic defects of equivalent size to integrate total fatigue life. Also depicted is the nondestructive evaluation (NDE) limit which is the minimum size which can be detected by nondestructive inspection.

The second stage of crack development is microcrack growth. Cracks in this size regime are termed "short cracks" if crack growth rates exceed the predictions of LEFM. The third stage is subcritical small crack growth where crack growth rates can be described by LEFM and correlated with much longer cracks. The final stage is rapid unstable crack extension as the fracture toughness of the alloy is approached and exceeded.

#### Safe-Life Approach

Historically turbine disks have been designed and retired on the basis of a safe life philosophy. A low-cycle fatigue life limitation criterion was employed. The useful life is considered to be exhausted after a crack initiation phase results in the development of a small fatigue crack of 0.79 mm (1/32 inch) in length. Due to variability in material quality and inherent scatter in fatigue properties, the LCF life is taken to be the lower bound performance where 1 in 1000 disks would be expected to have initiated a small crack. This corresponds to a -3 sigma lower bound. At the lower bound life, all 1000 disks would be retired from service. Figure 2.2 illustrates the distribution of available life in a population of disks. As can be seen, a large fraction of the retired disks have considerable residual life.

#### Defect Tolerant Approach

The defect tolerant design approach assumes that defects are present at fabrication and that useful life represents crack propagation from these defects to a subcritical size. This concept is the basis for the USAF Airframe Structural Integrity Program (ASIP) [2.2] and Engine Structural Integrity Program (ENSIP) [1.4-1.5].

A defect tolerant approach may also be used as a means for extending lives of disks until a crack of quantifiable size is detected upon inspection and the disk is "retired for cause" (RFC). The retirement for cause approach to life management may be employed regardless of the philosophy used in disk design.

Figure 2.3 illustrates the defect tolerant approach. After nondestructive inspection of the disk, cracks must be assumed to exist at the most failure critical locations and of a size equivalent to the maximum crack size which will just escape detection. The eddy current technology presently used for nondestructive inspection of disks has the sensitivity to detect semicircular surface cracks of 125  $\mu\text{m}$  depth (250  $\mu\text{m}$  surface length). In practice, surface cracks of 250  $\mu\text{m}$  depth can be reliably detected. The disk may be returned to service provided that fracture mechanics analysis guarantees crack growth will not exceed some subcritical size before the next inspection interval. Figure 2.3 illustrates several inspection and return to service intervals before the disk is finally retired.

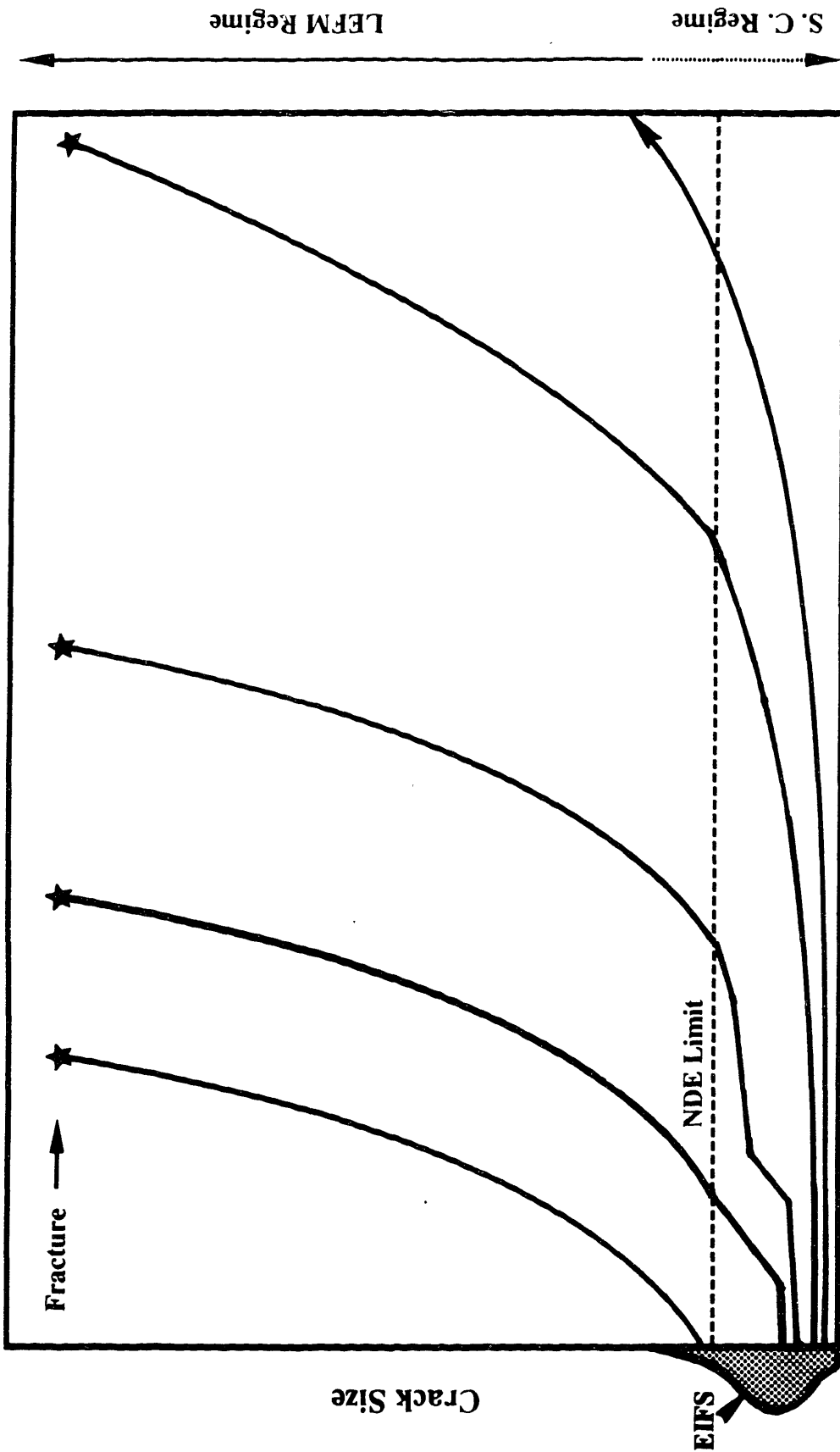


Figure 2.1 Total fatigue life segmented into stages of crack growth. The variation in equivalent initial flaw size (EIFS) and small crack behavior dominates total fatigue life.

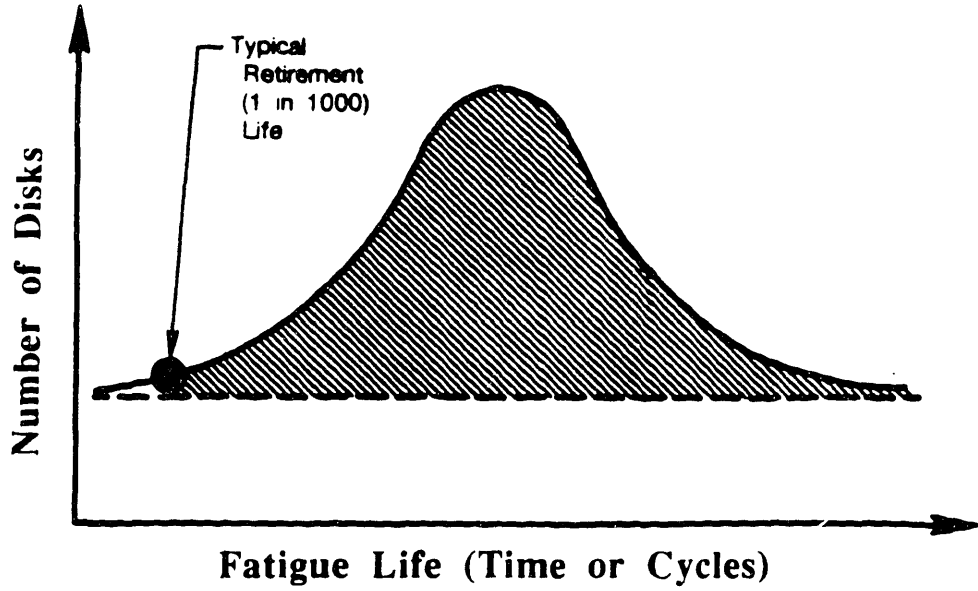


Figure 2.2 Distribution of fatigue life in a population of turbine disks [Ref. 2.3].

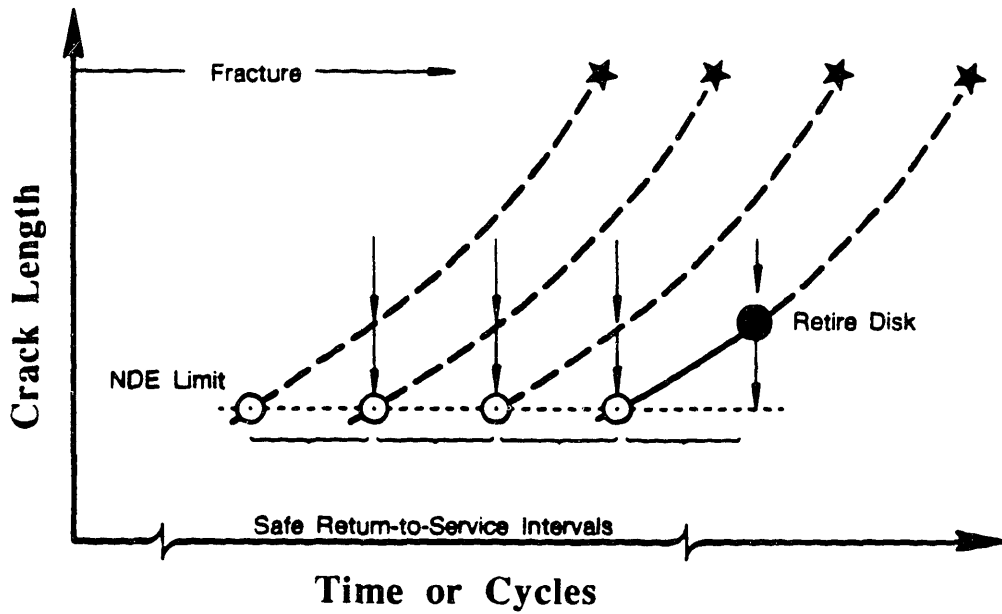


Figure 2.3 Defect tolerant life extension involves inspection and return-to-service until a quantifiable defect is found, resulting in disk retirement [Ref. 2.3].

## 2.2 The Small Crack Problem in Fatigue

### Historical Perspective

It would be remiss to suggest that the earliest investigators of the fatigue phenomenon did not recognize that the initiation and propagation of microscopic cracks dominated the fatigue life of highly stressed components and laboratory specimens. Hence, the "short crack" problem is not a new issue in fatigue.

It has long been recognized that fatigue crack initiation in many alloys resulted from the formation of intrusions, extrusions and persistent slip bands followed by crack extension in a shear mode at the free surface (Stage I growth) [2.4-2.5] as illustrated in Figure 2.4. Stage I is followed by a transition of the crack plane to an orientation perpendicular to the maximum applied stress where cracks extend by an opening mode (Stage II growth). Although early investigators did not report crack growth rates for Stage I cracks, these cracks were not expected to exhibit behavior similar to Stage II cracks since they were recognized as being physically different.

De Lange [2.6] employed a plastic replica method to investigate the nucleation and growth of fatigue cracks in a steel and an aluminum alloy and he noted that the behavior was dependent on crack length. He observed three stages of fatigue crack growth: 1) *Incipient Crack*; After nucleation, which occurred in the first few percent of life, fatigue cracks exhibited high growth rates. This stage was very sensitive to local crystallographic conditions such as the orientation of neighboring grains and grain boundary structure. 2) *Hesitating Crack*; After the first period of rapid growth, the fatigue crack entered a long stage of slow growth for approximately 10 to 70 percent of total life. 3) *Running Crack*; The crack growth rate suddenly increased again. This final stage was insensitive to local crystal orientation. Note that this reference (1964) predates the more recent "discovery" of

anomalous "short crack" behavior by more than ten years, yet describes the observation of high fatigue crack growth rates for small cracks (the *Incipient Crack*) in a manner quite familiar in the more recent literature.

### Threshold Stress and Stress Intensity

The unique behavior of small cracks with respect to the threshold stress for nonpropagation was first recognized by Frost [2.7] who reported a minimum crack length, on the order of the grain size, where the propagation stress no longer varied with crack length but converged to the fatigue limit.

Kitagawa and Takahashi [2.8] reported similar results for small surface cracks in a mild steel and presented their results in terms of a log stress versus log initial crack length plot similar to that shown in Figure 2.5. This presentation establishes quite clearly a deviation from LEFM behavior at small crack sizes.

The LEFM threshold stress intensity factor range,  $\Delta K_{TH}$ , defines a regime of crack sizes and applied stress ranges for which fatigue crack growth does not occur. For the case of a semicircular surface crack of depth  $a$ , this regime is defined by

$$Y \Delta \sigma_{pos} \sqrt{\pi a} \leq \Delta K_{TH} \quad (2.1)$$

where  $\Delta \sigma_{pos}$  is the remote applied tensile stress range and  $Y$  is a geometric correction factor. For a given mean stress, environment and frequency,  $\Delta K_{TH}$  is assumed to be a constant for long cracks. As the crack size to which Equation 2.1 is applied becomes smaller, a larger applied stress is required to maintain a constant  $\Delta K_{TH}$ . If, however, this stress exceeds the smooth bar endurance limit,  $\Delta \sigma_e$ , crack growth may occur. These two limiting conditions are illustrated in Figure 2.5 by the Kitagawa-Takahashi plot. The fatigue threshold stress for very small cracks is controlled by the endurance limit causing an apparent decrease in the

threshold stress intensity factor (Figure 2.6) if calculated in the usual manner. These trends have been observed for numerous alloys.

The minimum crack length,  $a_0$ , for which LEFM applies (upper limit of the short crack) varies with different materials and specimen geometries. For an edge crack  $a_0 = (1/\pi)(\Delta K_{TH}/\Delta\sigma_e)^2$ , which for a mild steel gives  $a_0 \approx 260 \mu\text{m}$ , while for a high strength steel  $a_0 \approx 50 \mu\text{m}$ . This example demonstrates a basic difference between low strength and higher strength materials in defining the short crack regime. In general, LEFM is applicable to much smaller crack sizes in high strength alloys than in low strength alloys due to generally low values of  $\Delta K_{TH}$  and high values of  $\Delta\sigma_e$ . This fact will later be explained through considerations of continuum mechanics restrictions.

### Crack Growth Rates

The fatigue crack growth behavior of small cracks has been characterized as anomalous when compared to longer cracks in the context of LEFM where

$$\Delta K = Y \Delta\sigma_{\text{pos}} \sqrt{\pi a} \quad (2.2)$$

is taken as the parameter which uniquely defines the mechanical driving force for crack growth. The anomalous behavior of so called "short cracks" is illustrated in Figure 2.7. Short cracks have been observed to propagate below the long crack  $\Delta K_{TH}$  and grow at rates exceeding long cracks at the same nominal value of  $\Delta K$ . It is characteristic for short cracks to exhibit a temporary or permanent arrest usually as a result of interactions with grain boundaries. There are numerous examples in the literature of small fatigue cracks exhibiting anomalous behavior under nominally elastic cycling for a variety of commercial alloys. Specific references will be made in subsequent sections to illustrate factors affecting small crack behavior in turbine disk alloys.

Some of the earliest investigations in which small crack growth rates were measured and reported in terms of LEFM are notable. Pearson [2.9] examined the initiation and subsequent growth of small cracks ( $6 \mu\text{m} < a < 250 \mu\text{m}$ ) in two aluminum alloys. He found microcrack growth rates to exceed rates for long ( $a > 250 \mu\text{m}$ ) through-section cracks when compared at nominally similar values of  $\Delta K$ .

Similar results were found by El Haddad et al. [2.10] on a CSA G40.11 steel at  $R = -1$  using sheet specimens containing small edge cracks. These results were compared with long crack data on the same material, and again the data show small crack growth rates to be faster.

Other investigators have measured crack growth rates for small cracks in specimens which were plastically strained, and therefore elastic-plastic fracture mechanics analysis was required to interpret the results. Apart from providing a means of correlating small crack data, elastic-plastic methods are significant in that they are relevant to the important problem of the behavior of small cracks in notches. EPFM will be considered in much more detail in a subsequent section.

### Definition of Short and Small Fatigue Cracks

Throughout much of the literature it is obvious that the term "short crack" is operationally defined. By definition a short crack is a physical discontinuity in a material which exhibits anomalous crack growth behavior compared to long cracks when both are analyzed using LEFM. The upper limit of the short crack is naturally that minimum length for which long crack LEFM parameters adequately describe behavior. The lower limit of the short crack will be that length for which the initiation event (or process) is considered complete. The actual range of lengths which characterize the short crack regime will likely be a function of material (grain size, mechanical properties, precipitate spacing, etc.),

temperature, environment and loading conditions. Short crack behavior is typically observed for crack lengths  $\leq 1$  mm.

In this investigation, the term "small crack" will be used to describe all cracks which are small in size, i.e., less than 2 mm. This awkward issue of semantics concerning the use of the terms "short crack" or "small crack" has been spread throughout the literature and the possibility of adopting a standard is likely too late. The term "small crack" as defined here is more general and preferred. "Small cracks" may or may not exhibit anomalous fatigue behavior. The term "short crack" will be used only when citing the work of others where it is used to describe anomalous fatigue behavior at small crack sizes.

Ritchie and Lankford [2.11] have taken an alternative approach by classifying small cracks according to the factors responsible for the deviation from long crack behavior as shown in Table 2.1. They have defined a small crack under the following categories: 1) Mechanically small cracks have lengths comparable to the scale of local plasticity, e.g., a small crack embedded in the plastic zone of a notch or a crack with length comparable with its own crack tip plastic zone. This definition implies an LEFM limitation. 2) Microstructurally small cracks have lengths comparable to the scale of the microstructure, i.e.,  $a_0 < \text{grain size}$ . This definition implies a continuum mechanics limitation. 3) Physically small cracks are simply small,  $a_0 < 1$  mm. This may result in less crack flank closure than occurs for long cracks. 4) Chemically small cracks are small with respect to the local crack tip environment. The bulk environment dominates the crack tip environment. In long cracks, the crack tip environment may differ dramatically from the bulk chemical solution due to restricted fluid transport to the crack tip between the crack flanks.

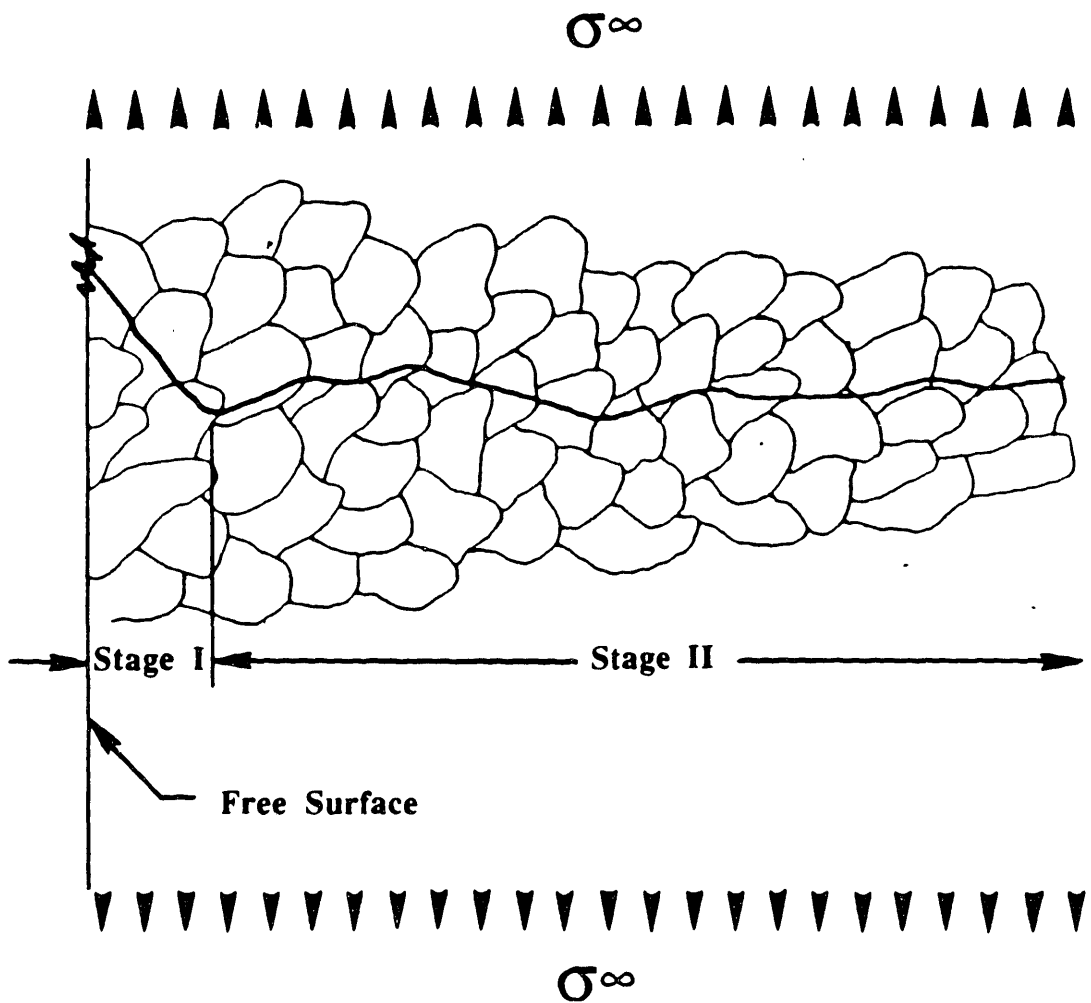


Figure 2.4 Schematic showing the two stages of subcritical fatigue crack growth first proposed by Forsyth [Refs. 2.4, 2.5].

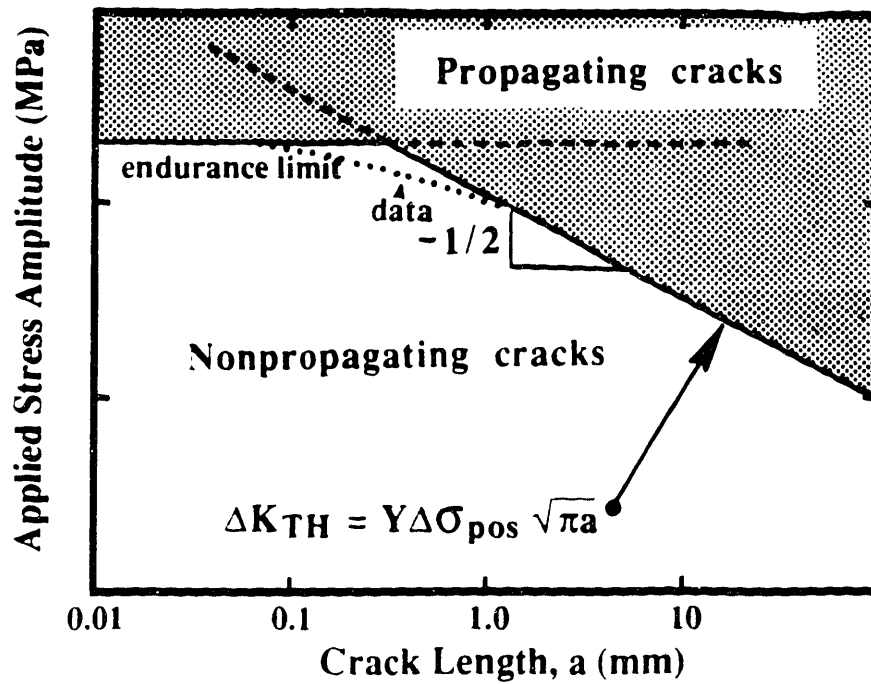


Figure 2.5 Log stress versus log crack length illustrating the threshold stress between propagating and nonpropagating cracks.

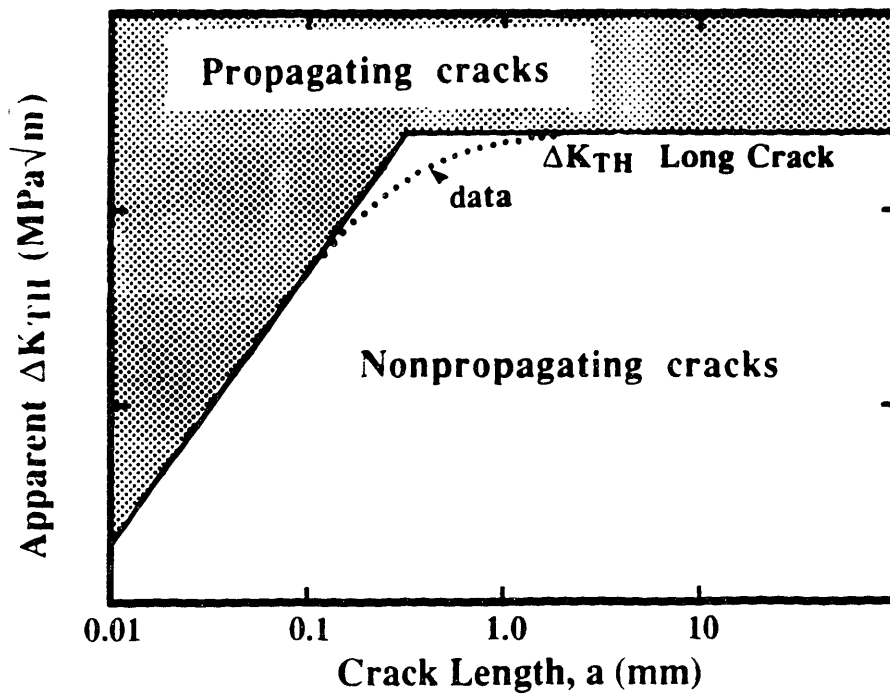


Figure 2.6 Apparent threshold stress intensity factor range versus crack length illustrating the two regimes of propagating and nonpropagating cracks.

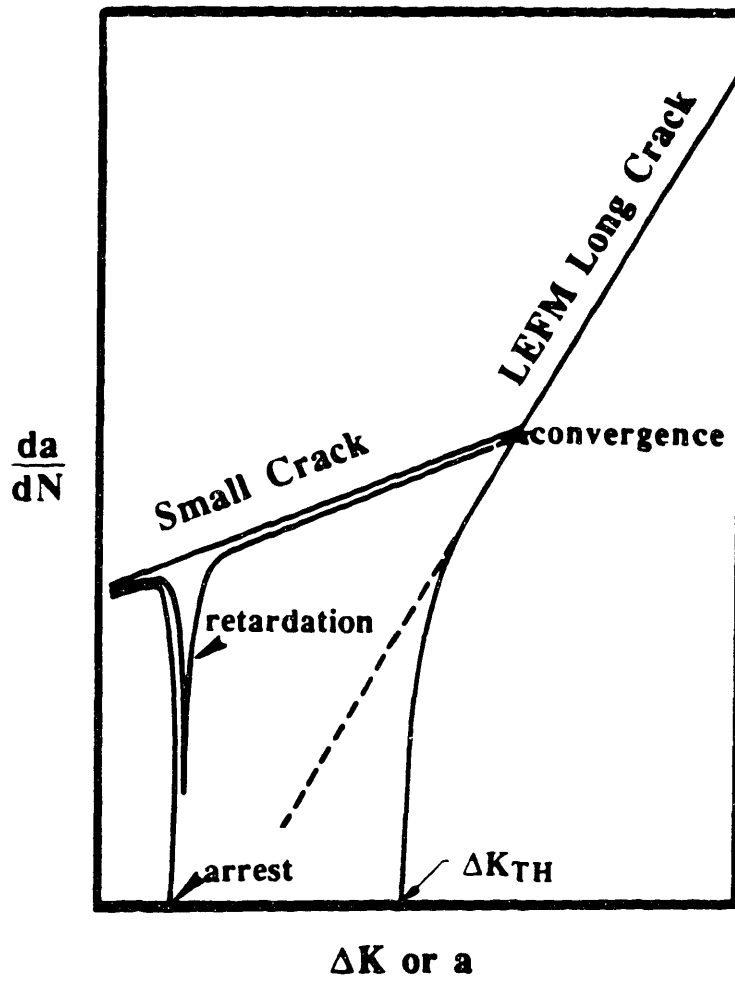


Figure 2.7 Crack growth rates versus  $\Delta K$  or  $a$ ; comparison of long crack behavior with anomalous small crack behavior.

**Table 2.1**  
**Classes of Small Fatigue Cracks**

Type of Small Crack	Dimension	Responsible Mechanism	Potential Solution
Mechanically small	$a \leq r_p$	excessive (active) plasticity	use of $\Delta J$ , $\Delta S$ , CTOD
Microstructurally small	$a \leq d_g$ $2c \leq 5-10 d_g$	crack tip shielding*, enhanced $\Delta \epsilon_p$ , crack shape	probabilistic approach
Physically small	$a \leq 1 \text{ mm}$	crack tip shielding* (crack closure)	use of $\Delta K_{eff}$
Chemically small †	up to 10 mm	local crack tip environment	?

$r_p$  is the plastic zone size or plastic field of notch

$d_g$  is critical microstructural dimension, e.g., grain size,  $a$  is the crack depth and  $2c$  the surface length

†critical size is a function of frequency and reaction kinetics

\*Crack tip shielding refers to the mechanical closure of the crack above zero load which prevents the crack tip from experiencing the full range of stress and strain as defined by  $\Delta K_{applied}$ .

## 2.3 Linear Elastic Fracture Mechanics

### Basic Concepts

Linear Elastic Fracture Mechanics is based on a mathematical description of the near crack tip stress field developed by Irwin [2.12]. Consider a crack in an infinite plate shown in Figure 2.8 with crack length  $2a$  and a remotely applied tensile stress acting perpendicular to the crack plane (Mode I). Irwin expressed the near crack tip stress field as a series solution:

$$\sigma_{ij}(r, \theta) = \frac{K_I}{\sqrt{2\pi r}} f_{ij}(\theta) + O\left(\frac{1}{r^2}\right) + \dots \quad (2.3)$$

where  $K_I = \sigma^\infty \sqrt{\pi a}$  and  $r, \theta$  are the cylindrical polar coordinates of a point with respect to the crack tip. In the near crack tip region ( $r \rightarrow 0$ ) the first term of the series solution serves as an adequate approximation to the elastic stress field

$$\sigma_{ij}(r, \theta) = \frac{K_I}{\sqrt{2\pi r}} f_{ij}(\theta) = \frac{\sigma^\infty \sqrt{\pi a}}{\sqrt{2\pi r}} f_{ij}(\theta) \quad (2.4)$$

$K_I$  is the Mode I stress intensity factor which serves as a scalar multiplier of the crack tip stress field.

The variation of the stress  $\sigma_y$  as a function of  $r$  at  $\theta = 0$  is illustrated in Figure 2.9. For large values of  $r$ ,  $\sigma_y$  approaches zero, while it should go to  $\sigma^\infty$ . As  $r$  approaches zero at the crack tip,  $\sigma_y$  approaches infinity, while it should not exceed  $\sigma_{UTS}$ . Hence, it is clear that Eq. 2.4 is valid only for a limited region around the crack tip and is more accurate for low values of  $\sigma^\infty$ .

Rather than bearing an infinite stress at the crack tip, yielding occurs resulting in a volume of plastically deformed material along the crack front called the plastic zone as shown

in Figure 2.10a. The size of the plastic zone under a monotonic tensile stress can be approximated by substituting  $\sigma = \sigma_{ys}$  into Eq. 2.4 for the horizontal plane,  $\theta = 0$

$$r_{pm}^* = \frac{1}{2\pi} \left( \frac{K_I}{\sigma_{ys}} \right)^2 \quad (2.5)$$

In reality, the stress above the plastic zone exceeding  $\sigma_{ys}$  is redistributed giving a somewhat larger monotonic plastic zone as shown in Figure 2.10b. Hence, for monotonic loading, under conditions of small scale yielding, the crack driving force may be expressed in terms of  $K_{max} = Y\sigma_{max} \sqrt{\pi a}$ .

Paris and Erdogan [2.13] extended the use of LEFM and  $K$  to correlating fatigue crack growth rates under conditions of cyclic loading. The tensile range of the stress intensity factor is used to express the crack driving force according to:

$$\Delta K = K_{max} - K_{min} \quad (2.6)$$

for all  $K_{min} \geq 0$ . The principal variables are  $K_{max}$  and R-ratio ( $K_{min}/K_{max}$  or  $\sigma_{min}/\sigma_{max}$ ).

Crack growth rate data for long cracks is usually considered in terms of a plot of  $\log da/dN$  versus  $\log \Delta K$  as shown in Figure 2.11. Three regimes of behavior are generally observed:

- I) a threshold regime in which crack growth rates tend to zero and are asymptotic to the threshold value,  $\Delta K_{TH}$ . This regime is sensitive to microstructure, load ratio and environment.
- II) a linear regime in which subcritical crack growth rates obey the Paris-Erdogan relation:

$$\frac{da}{dN} = C\Delta K^m \quad (2.7)$$

where C and m are constants.

III) a regime of accelerating crack growth rates which becomes asymptotic to the fracture toughness,  $K_{IC}$ .

The extent of the cyclic plastic zone size  $r_{pc}$  is approximately a quarter of the size of the monotonic zone and is given by:

$$r_{pc} = \frac{1}{2\pi} \left( \frac{\Delta K}{2\sigma_{yc}} \right)^2 \quad (2.8)$$

where  $\sigma_{yc}$  is the cyclic yield stress.

#### Crack Closure and $\Delta K_{eff}$

Crack growth rates are often observed to vary significantly at the same nominal value of  $\Delta K$  ( $= Y \Delta\sigma_{pos} \sqrt{\pi a}$ ) for different values of R-ratio. Elber [2.14] was the first to explain this observation in terms of the crack closure phenomenon. He determined, by measuring specimen compliance, that fatigue cracks open and close at the crack tip at positive values of stress due to contact between crack surfaces behind the crack tip. Figure 2.12a illustrates a typical elastic fatigue cycle for which  $R_\sigma > 0$ . The crack opens and closes at positive values of load, P, and  $\Delta K$  on loading and unloading. For elastic fatigue conditions it is generally found that  $P_{op} = P_{cl}$  and  $K_{op} = K_{cl}$ .

Experimentally, the closure level is determined by measuring the crack mouth opening displacement,  $\delta$ , during a fatigue cycle and plotting P versus  $\delta$  as shown in Figure 2.12b. A distinct deviation from a linear relationship on loading and unloading indicates the point of crack opening and closure. The linear region at higher loads has a slope  $C = \partial\delta/\partial P$  which defines the compliance of the cracked body.

The effective stress range was defined by Elber as:

$$\Delta\sigma_{\text{eff}} = \sigma_{\text{max}} - \sigma_{\text{op}} \quad (2.9)$$

Correspondingly, the effective stress intensity factor range,  $\Delta K_{\text{eff}}$ , may be expressed as

$$\Delta K_{\text{eff}} = Y(\sigma_{\text{max}} - \sigma_{\text{op}})\sqrt{\pi a} \quad (2.10)$$

According to Elber, crack closure occurs as a consequence of crack tip plasticity. The growing fatigue crack generates monotonic plastic zones ahead of the crack tip. As the crack advances, there is residual plastic deformation consisting of monotonically stretched material behind the crack tip due to prior plastic zones. This stretched material does not fit in the surrounding elastic body, therefore, the crack flanks make physical contact at a high positive value of load on unloading. A high positive load is also required to open the crack. Under elastic fatigue conditions crack opening and closure occur at approximately the same value of load. This mechanism of crack closure is generally referred to as plasticity induced closure and is shown schematically in Figure 2.13. Also illustrated are the physical mechanisms of roughness induced closure and oxide induced closure.

Roughness (or asperity) induced crack closure [2.15 - 2.19] is caused by fracture surface asperities making contact at positive loads on unloading. The crack opening load is also positive. This mechanism of closure depends on fracture surface morphology (therefore microstructure) and results in fracture surface mismatch.

Oxide induced crack closure [2.20 - 2.21] is a result of oxides or corrosion products forming behind the crack tip causing mechanical contact at positive values of load. This closure mechanism is sometimes referred to as "nonclosure" because the fracture surfaces are prevented from making direct physical contact.

In addition to the R-ratio effect, crack closure has been used to explain: anomalous small crack behavior, load interactions under spectrum loading, and the influence of residual stresses, microstructure and environment on fatigue crack growth rate. Closure is more important in plane stress than plane strain regardless of the closure mechanism. Banerjee[2.22] has recently reviewed the subject of fatigue crack closure.

### Applicability of LEFM to Small Cracks

The failure of LEFM to correlate crack growth behavior of small cracks with that of long cracks under nominally elastic conditions may be attributed to a breakdown of the underlying continuum mechanics assumptions. The basic assumptions of fracture mechanics are: 1) that the material behaves as a linear elastic isotropic continuum and 2) the crack tip plastic zone size is small with respect to all other dimensions (small scale yielding). Here we consider the limitations of using the term  $\Delta K = Y\Delta\sigma_{\text{pos}}\sqrt{\pi a}$  to describe the mechanical driving force for fatigue crack extension of small cracks at high values of cyclic stress.

The stress intensity factor is a first term approximation to a series solution for the near crack tip elastic stress field. The accuracy of this approximation decreases with distance from the crack tip. Evans and Luxmoore [2.23] compared the approximation given by  $K/\sqrt{2\pi r}$  to the full equations of the Westergaard stress function for a central crack in an infinite plate and found errors on the order of 10% in the local stress components when the near crack tip field was limited to  $a/10$ . Wilson [2.24] found errors in local stress components to exceed 10% at the  $a/10$  boundary when typical fracture mechanics specimens were considered. Consequently,  $K$  serves as a good parameter to estimate the near crack tip elastic field when its extent is limited to  $a/10$ .

Smith [2.25] reasoned that for a global application of fracture mechanics (Figure 2.14a) where  $\sigma_1$  represents the stress applied to a structure or laboratory specimen, the near

crack tip field ( $a/10$ ) should be at least the size of the largest structural feature, that is, the grain size. Therefore, the crack length must be ten times the grain size if  $K_I$  is to accurately represent stresses in the crack tip field.

On the other hand, if  $\sigma_2$  represents the boundary stress applied to a single grain (Figure 2.14b), the crack length would be half a grain size and the near crack tip field would extend over a distance of  $0.1 \times (\text{grain size}/2)$ , which is many orders of magnitude greater than the lattice spacing. However, for this localized application of fracture mechanics, the local material behavior is no longer an isotropic continuum.

In metals, plastic deformation occurs at the crack tip, yielding a plastic zone. Smith [2.25] has argued that the elastic stress intensity factor is adequate to describe the crack tip field condition if the plastic zone is limited in size compared with the near crack tip field, which is then assumed to dominate the crack tip plastic response. He suggested that the plastic zone be  $1/5$  of the size of the near crack tip elastic field ( $a/10$ ). This limitation is in accordance with the generally accepted limitation on the maximum size of the plastic zone allowed in a valid fracture toughness test [2.26,2.27]. For the case of fatigue crack propagation, the minimum crack size for which continuum considerations hold should be at least  $50 \times (r_{pc})$ .

Smith [2.25] and Lankford [2.28] have also suggested that the minimum fatigue crack size for which continuum considerations hold should be at least 50 times that of the minimum fatigue microstructural element, i.e. a subgrain slip band. A value of  $0.5 \mu\text{m}$  was suggested as a representative minimum crack tip subcell size based on TEM measurements [2.29-2.31], resulting in a minimum crack size of  $\approx 25 \mu\text{m}$ .

### Similitude Requirements

The utility of  $\Delta K$  or any EPFM parameter to describe the mechanical driving force for fatigue crack growth is based on the ability of that parameter to characterize the stress-strain conditions at the crack tip in a manner which accounts for a variety of crack lengths, component geometries and loading conditions. Equal values of  $\Delta K$  should correspond to equal crack tip stress-strain conditions and, consequently, to identical fatigue crack growth rates. In such a case we have mechanical similitude. Mechanical similitude implies equivalent crack tip plastic zones and equivalent elastic stress fields. Fracture mechanics is based on the formulation of parameters which express crack tip similitude.

Leis et al. [2.32] have recently reviewed similitude requirements for the application of LEFM to fatigue crack growth. Mechanical similitude as discussed above requires: 1) a small plastic zone size with respect to all length dimensions, including crack front length, 2) a small plastic zone size with respect to the distance over which the first term of the stress field solution is dominant, 3) equivalent  $K_{\max}$  and  $\Delta K$ , 4) equivalent constraint, i.e., plane stress or plane strain, and 5) equivalent crack closure fields.

In addition, metallurgical similitude requires that the crack tip be embedded in a metallurgically similar material. The material should be equivalent in terms of phase, crystal orientation, precipitate size and distribution, dislocation density, etc. This condition is satisfied when the crack front is long with respect to metallurgical features, particularly the grain size, and therefore encounters an average metallurgical condition.

It is obvious that sufficiently small cracks will violate one or more similitude requirements listed above. Therefore, it is not surprising that LEFM fails to consolidate small crack data with long crack data in some cases. The various factors which influence small crack behavior (i.e. which influence similitude) will be discussed further and illustrated with

examples from the literature in a later section. In spite of the potential which small cracks have for violating similitude conditions, the need to describe small crack growth rates in terms of fracture mechanics remains a requirement of defect tolerant design and life management.

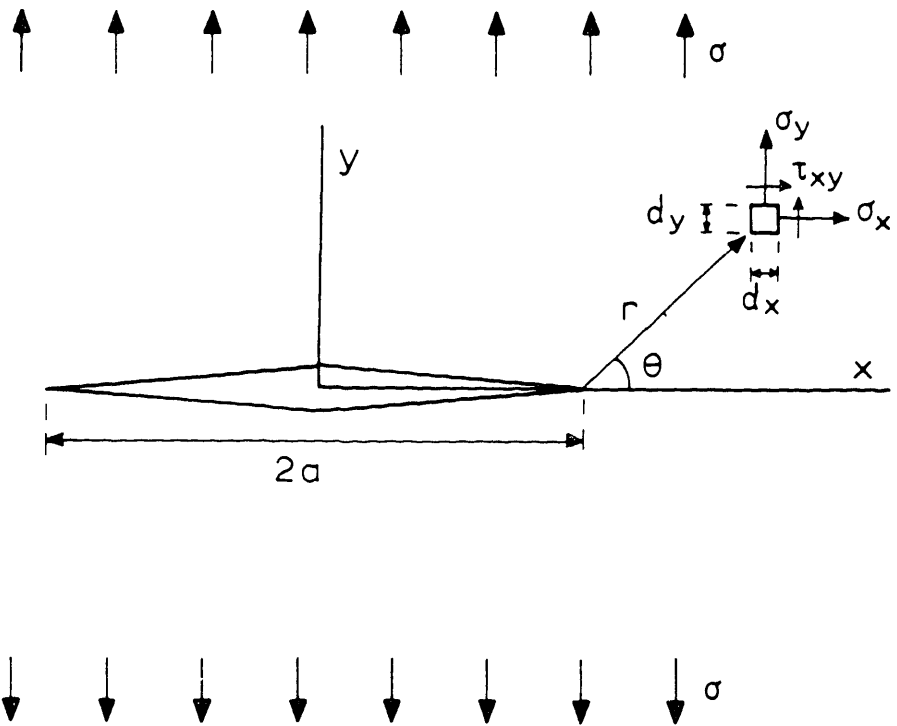


Figure 2.8 Crack in an infinite plate subjected to a remotely applied stress [Ref. 2.12'].

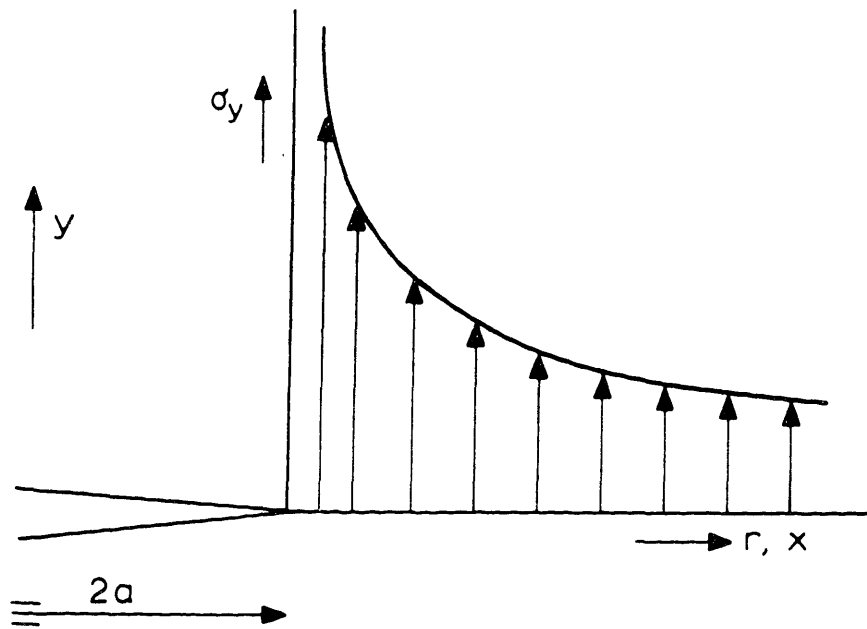


Figure 2.9 Elastic crack tip stress field [Ref. 2.12'].

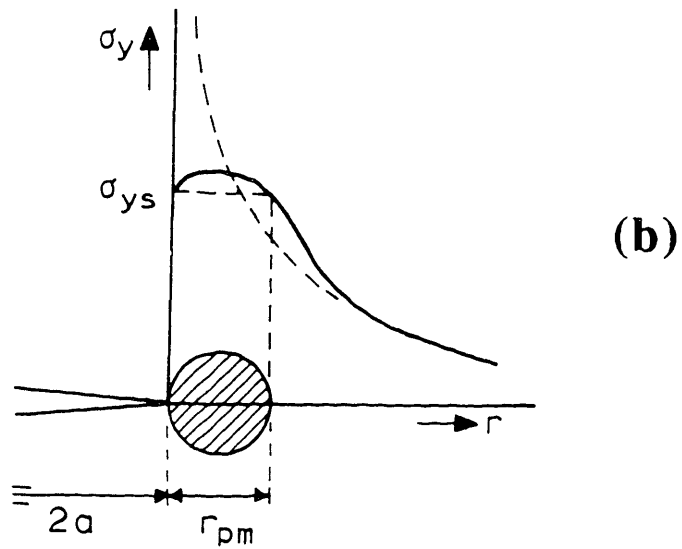
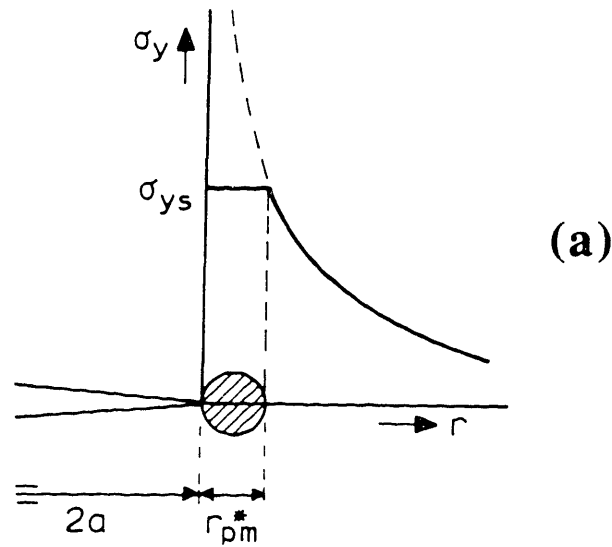


Figure 2.10 Crack tip plastic zones: (a) Assumed elastic stress distribution, (b) Approximate stress distribution after yielding is accounted for [Ref. 2.12'].

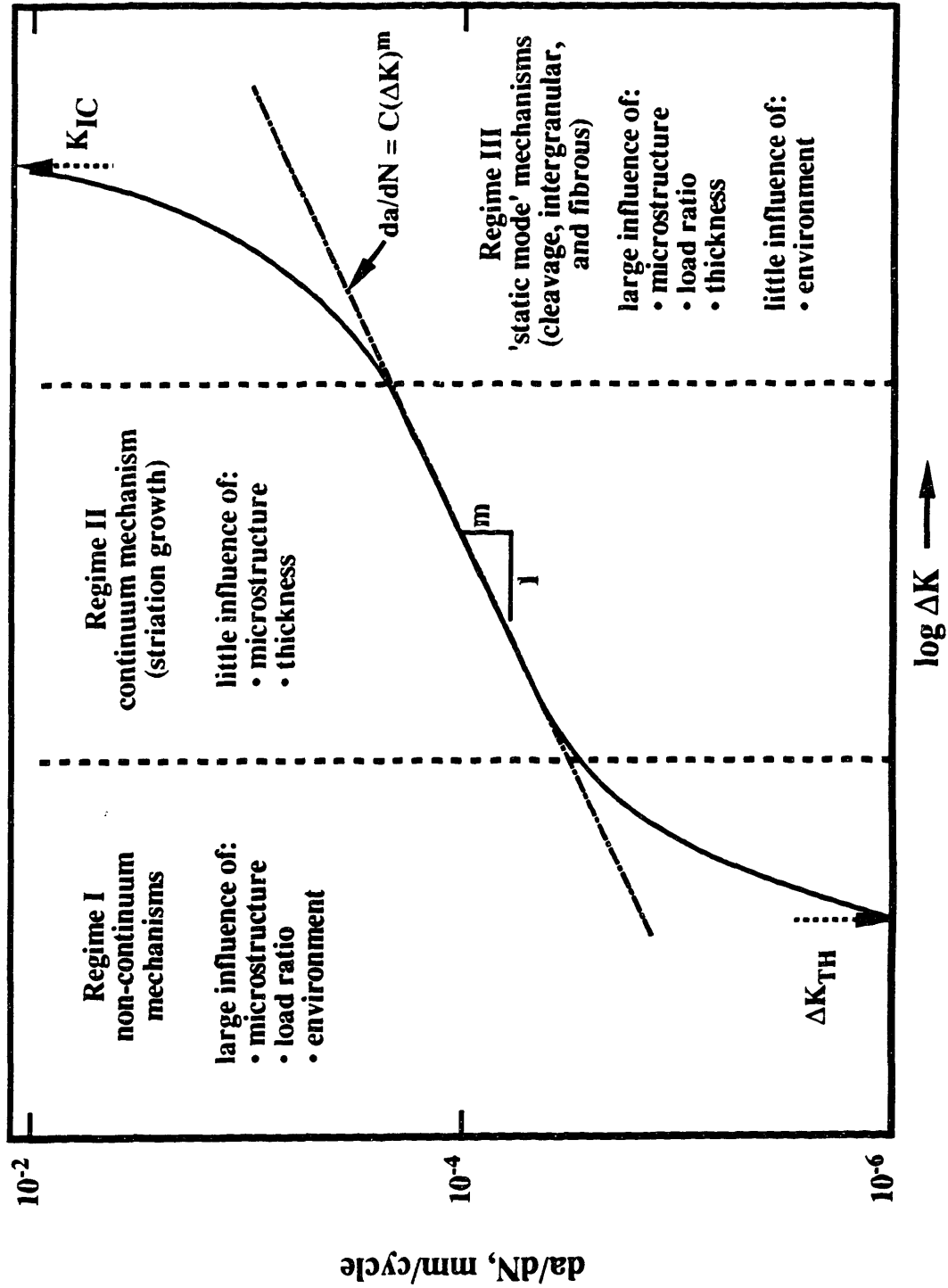


Figure 2.11 Fatigue crack growth rate versus stress intensity factor range for a typical long crack exhibiting three distinct regimes of behavior.

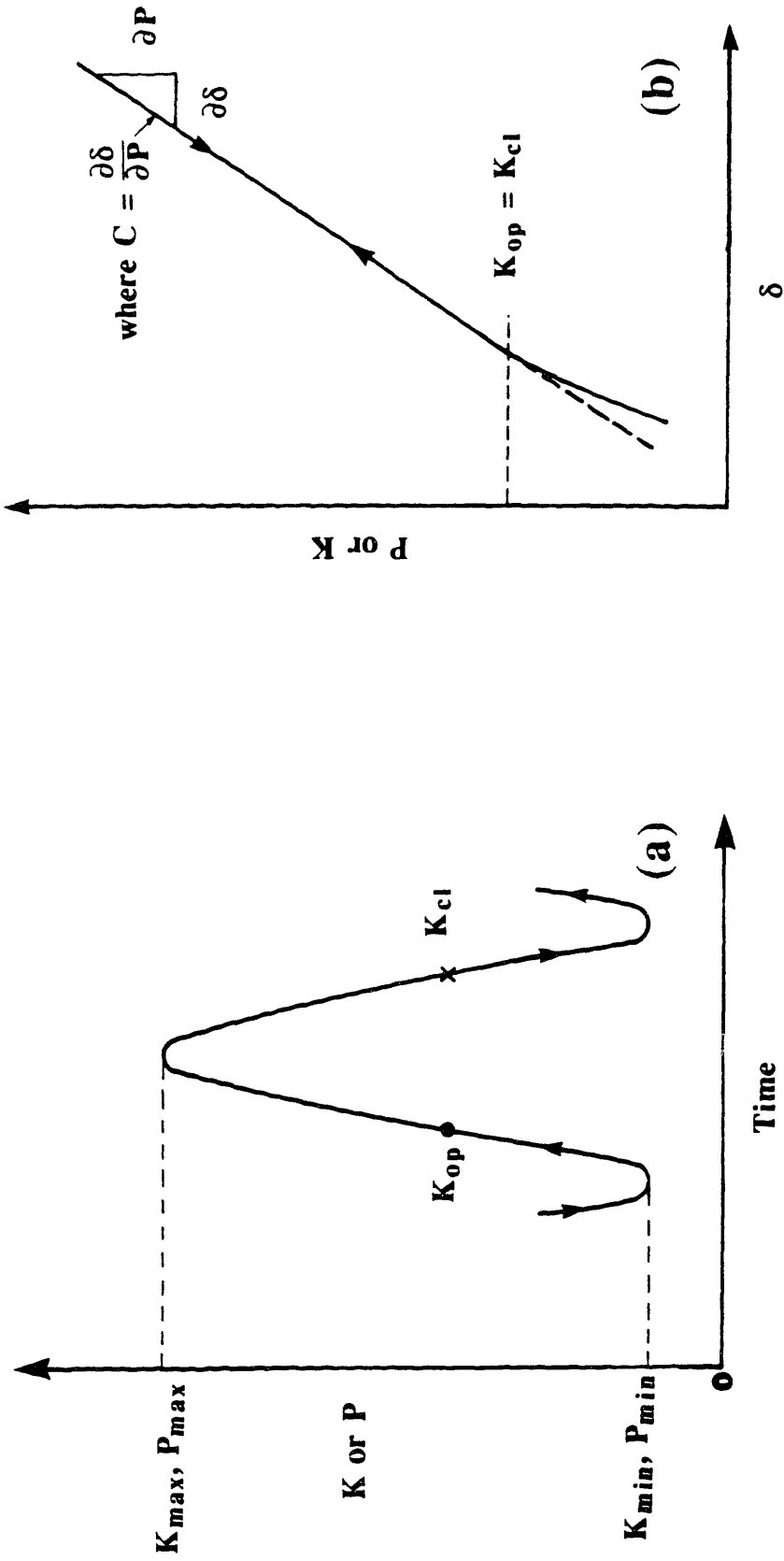


Figure 2.12 (a) Schematic of crack opening and closure in a single fatigue cycle. (b) Identification of crack opening and closure level from the load versus displacement plot.

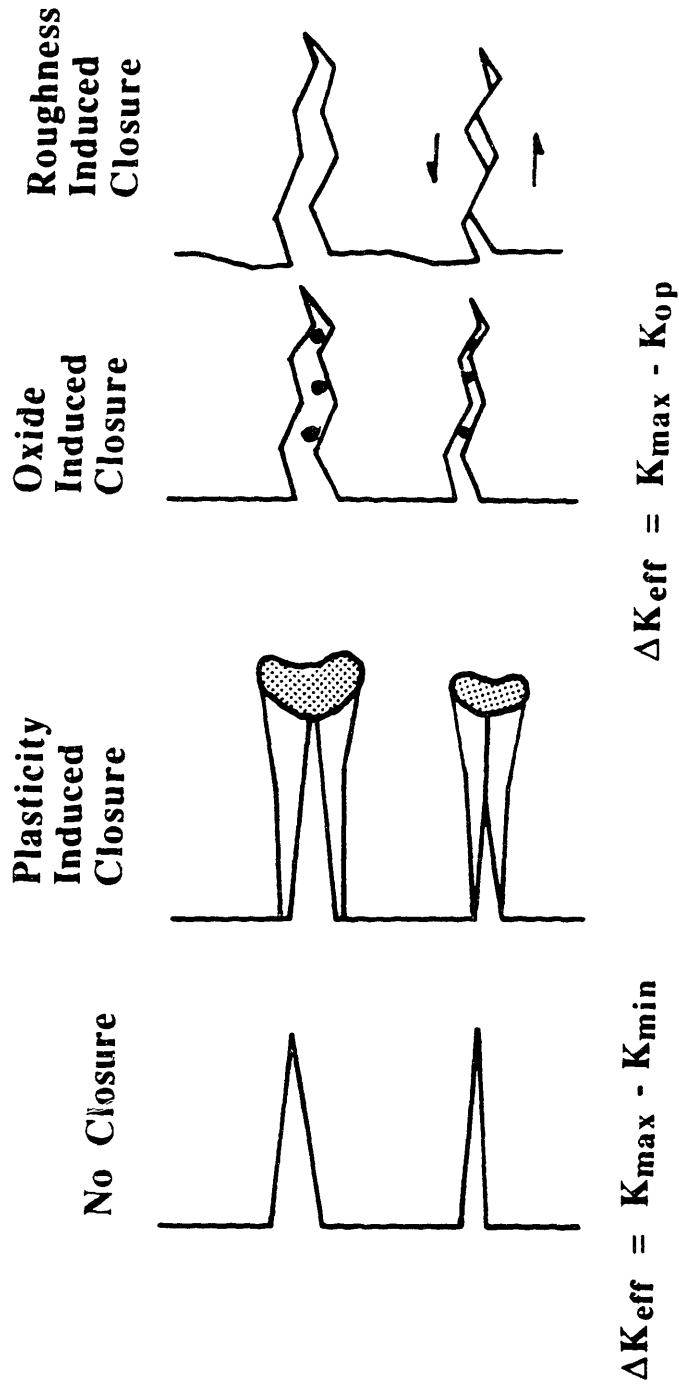


Figure 2.13 Schematic comparison of the various crack closure mechanisms [Ref. 2.15].

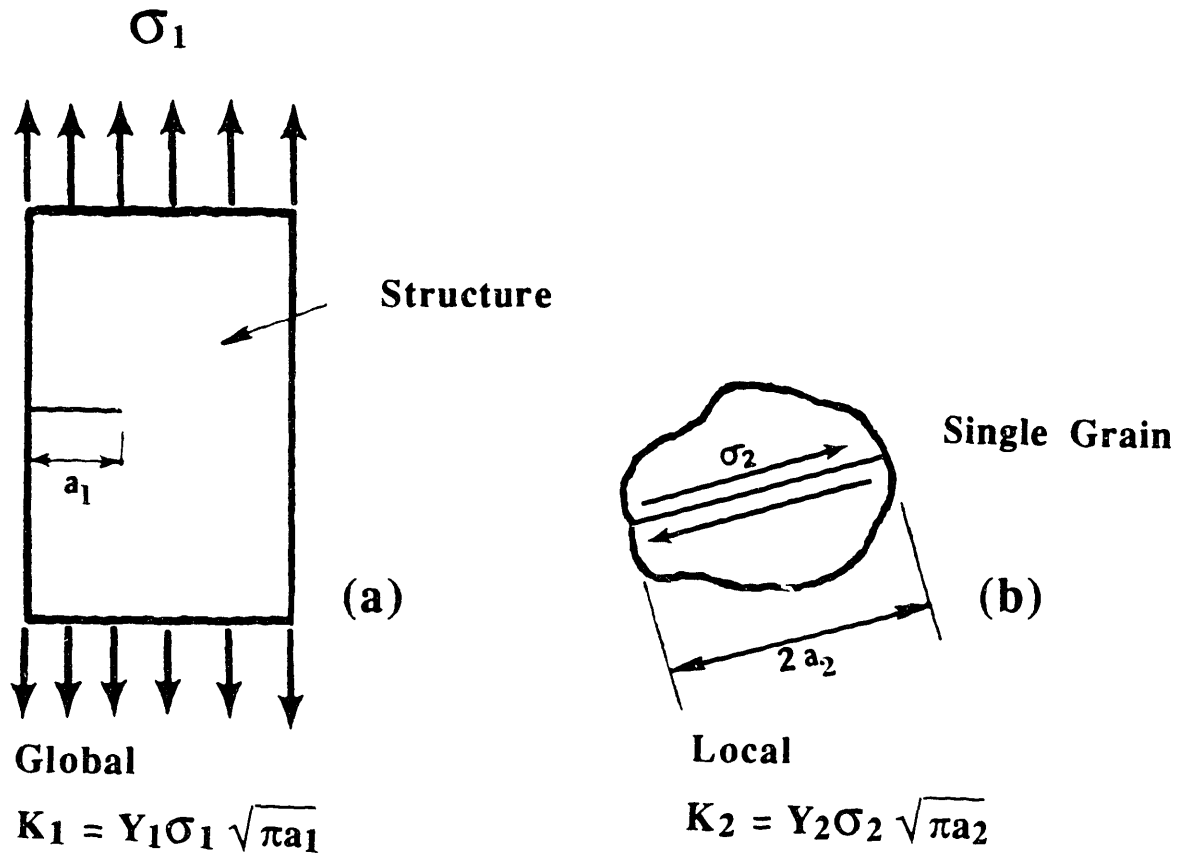


Figure 2.14 Schematic of (a) global and (b) local application of fracture mechanics [Ref. 2.25].

## 2.4 Elastic-Plastic Fracture Mechanics

Elastic-plastic fracture mechanics was developed in response to the small scale yielding (confined plastic flow) limitations imposed on the validity of LEFM testing and applications. The standards of the American Society of Testing and Materials (ASTM) for a valid  $K_{IC}$  test [2.27] requires, for a compact tension specimen, that all characteristic dimensions, i.e., the crack length, the uncracked ligament and the specimen thickness be greater than  $25 r_{pm}$ . These conditions are easily met for high strength alloys.

The validity of LEFM is questionable for applications and testing involving low and intermediate strength metals. For an intermediate strength steel used in pressure vessels,  $r_{pm}$  at fracture initiation under monotonic loads can be as large as 1 cm. A valid  $K_{IC}$  test would therefore require a test specimen of considerable size. Fracture toughness testing provided ample motivation for the development of nonlinear fracture mechanics.

### Empirical Approach

Skelton [2.33] has recently reviewed the subject of high strain fatigue crack growth. Many studies have led to the characterization of fatigue crack growth rates with empirical relationships [2.34-2.35]. A frequently used form that appears to have broad application is

$$\frac{da}{dN} = C(\Delta\epsilon_p)^\alpha a^Q \quad (2.11)$$

where  $a$  is the crack length,  $\Delta\epsilon_p$  is the bulk plastic strain range and  $C$ ,  $\alpha$ , and  $Q$  are constants that depend on the material and test geometry. The value of  $Q$  is  $\geq 1$  and generally thought to be related to the mechanism of crack extension. Tomkins [2.49] proposed that  $Q = 1$  when crack advance per cycle occurs by irreversible shear decohesion at the crack tip. This microplasticity mechanism leads to ductile fatigue striation formation [2.34,2.46,2.50]. Most of the published data which show good correlation using Eq. 2.11 is limited to crack lengths

greater than 250  $\mu\text{m}$ . One conclusion to be drawn from a review of the published work is that there is not a universally applicable empirical relationship which adequately describes high strain fatigue crack growth.

### Strain Intensity and Equivalent Stress Intensity

Numerous parameters which employ cyclic strain values ( $\Delta\epsilon_p$ ,  $\Delta\epsilon_e$  and  $\Delta\epsilon_t$ ) have been proposed to correlate crack growth rates under elastic-plastic fatigue conditions. One of these parameters is identified as the strain intensity factor range,  $\Delta K_\epsilon$ , which combines strain and crack length in a manner analogous to the more familiar elastic stress intensity factor. The strain intensity factor can be transformed into an equivalent stress intensity factor range,  $\Delta K_{eq}$ , simply by multiplication by the elastic modulus.

Boettner et al. [2.51] combined the plastic strain range and crack length to correlate high strain ( $\Delta\epsilon_p = 2\%$  to  $5\%$ ) fatigue crack growth rates for copper at room temperature. Crack growth rates were described by

$$\frac{da}{dN} \propto \Delta\epsilon_p^2 a \propto \{ \Delta\epsilon_p \sqrt{a} \}^2 \quad (2.12)$$

where  $a$  is the crack length.

This expression can be seen as a particular case of Eq. 2.11 which was considered to be purely empirical. In either case, the basic implication is that crack tip conditions are dominated by the bulk plastic strain range. This is likely a good assumption since most of the conditions considered involve high values of  $\Delta\epsilon_p$ .

The shortcomings of ignoring elastic strains in Equations 2.11 and 2.12 are: (i) service relevant fatigue conditions (resulting in adequate fatigue lives) are associated with much lower values of  $\Delta\epsilon_p$  where  $\Delta\epsilon_p \ll \Delta\epsilon_e$ , (ii) since small cracks usually propagate out of high strain elastic-plastic fields into elastic fields, approaches which combine both elastic and

plastic parameters are required to correlate relevant data and define crack propagation behavior through this transition.

Solomon [2.52] employed a pseudostress intensity factor to correlate crack growth rates in 1018 steel at room temperature under elastic-plastic fatigue conditions ( $\Delta\epsilon_p = 0.1\%$  to  $5\%$ ). He calculated the pseudostress range as  $E \cdot \Delta\epsilon_t$  (see Figure 2.15). The pseudostress intensity factor range was defined as

$$\Delta PK = E \Delta\epsilon_t \sqrt{a} \quad (2.13)$$

and the corresponding crack growth rate given as

$$\frac{da}{dN} \propto [E\Delta\epsilon_t\sqrt{a}]^h \propto [E(\Delta\epsilon_e + \Delta\epsilon_p)\sqrt{a}]^h \quad (2.14)$$

The correlation of  $da/dN$  with  $\Delta PK$ , for all values of  $\Delta\epsilon_p$ , was far superior to that achieved with  $\Delta K$  calculated using the positive elastic stress range. Divergence in the data was greatest at low values of  $\Delta\epsilon_p$ . It should be noted that  $\Delta PK$  makes use of the full range of elastic and plastic strains, i.e., the tensile and compressive parts of hysteresis loops. This approach ignores the role of crack closure.

Haigh and Skelton [2.53] employed an electrical potential technique to determine the stress-strain point of opening and closure of a small crack in 316 stainless steel at 625C under elastic-plastic fatigue conditions ( $\Delta\epsilon_p = 0.1\%$ ). They observed crack opening and closure to occur near zero load. In this case, the crack was open for all of the plastic strain range and half of the elastic strain range,  $\Delta\epsilon_p + 0.5\Delta\epsilon_e$ , which was denoted the "equivalent elastic strain range". This was used to express the strain intensity factor range as

$$\Delta K_\epsilon = (\Delta\epsilon_p + 0.5\Delta\epsilon_e) \sqrt{\pi a} \quad (2.15)$$

The above approach was made more general by Starkey and Skelton [2.54] by expressing the damaging strain range as  $\Delta\epsilon_p + q_0\Delta\epsilon_e$ , where  $q_0$  is the fraction of the stress

range over which the crack was open (usually  $0.5 < q_0 < 1$ ). Multiplying this strain range by  $E$  yields an equivalent stress range,  $\Delta\sigma_{eq}$ , as shown in Figure 2.16. The equivalent stress range can be used to calculate the "equivalent stress intensity factor range" as

$$\Delta K_{eq} = Y E (\Delta\varepsilon_p + q_0 \Delta\varepsilon_e) \sqrt{\pi a} \quad (2.16)$$

where  $Y$  is the geometric correction factor.

Under purely elastic fatigue conditions,  $\Delta\varepsilon_p = 0$ , Equation 2.16 becomes the more familiar "effective stress intensity factor range" over which the crack is considered open

$$\Delta K_{eff} = Y q_0 \Delta\sigma \sqrt{\pi a} = Y (\sigma_{max} - \sigma_{op}) \sqrt{\pi a} \quad (2.17)$$

Hence,  $\Delta K_{eq}$  expresses the crack driving force in a manner which is applicable under both elastic and elastic-plastic fatigue conditions and exhibits a smooth transition between the two regimes, i.e., at low values of  $\Delta\varepsilon_p$ . Solomon's data on 1018 steel [2.53] at room temperature was analyzed in terms of  $\Delta K_{eq}$  and exhibited less divergence in correlating crack growth rates, especially at low values of  $\Delta\varepsilon_p$ . They further employed  $\Delta K_{eq}$  to correlate crack growth rates in Cr-Mo-V steels under elastic and elastic-plastic ( $\Delta\varepsilon_p = 0.02\%$  to  $0.4\%$ ) fatigue conditions at 550 C. The elastic-plastic (small crack) data fell between the upper bound LEFM (long crack) data at  $R = -1$  and lower bound LEFM (long crack) data at  $R \geq 0$ .

### The J-integral

Rice [2.55] introduced the J-integral to address the problem of concentrated strain fields near notches and cracks in nonlinear materials. The primary interest in nonlinear materials lies with the elastic-plastic fracture of metals. In his original development, Rice assumed a small strain deformation theory of plasticity (i.e. a small strain, nonlinearly elastic) material model. The strain energy density of the material,  $W(\epsilon)$ , with stress given by

$$\sigma_{ij} = \frac{\partial W}{\partial \epsilon_{ij}} \quad (2.18)$$

Physically, this means that the stress must be a function of the current strain only and not of the deformation history. Consider the cracked body shown in Figure 2.17a (in plane stress or plane strain) with the crack lying along the x axis. The two dimensional path independent line integral expression for J is

$$J = \int_{\Gamma} \left( W \, dy - \mathbf{T} \cdot \frac{\partial \mathbf{u}}{\partial \mathbf{x}} \, ds \right) \quad (2.19)$$

where  $W$  is the loading work per unit volume (or the strain energy density for elastic bodies),  $\Gamma$  is any contour encircling the tip of the crack in a counterclockwise direction,  $ds$  is an increment of the contour path,  $\mathbf{T}$  is the outward traction vector on  $ds$  defined according to the outward normal along  $\Gamma$ ,  $T_i = \sigma_{ij}n_j$ , and  $\mathbf{u}$  is the displacement vector at  $ds$ .

The physical interpretation of J for nonlinear elastic materials is that a measure of the potential energy change  $dU$ , caused by a small increase in crack length,  $da$ , is related to the J-integral as

$$J = - \frac{1}{B} \frac{\partial U}{\partial a} \quad (2.20)$$

where  $B$  is the specimen thickness (see Figure 2.17b).

For linear elastic conditions, J reduces to the strain energy release rate, G. In Mode I the rate of decrease of the potential energy of the system per unit crack extension per unit thickness is

$$J_e = G = (1 - \nu^2) \frac{K^2}{E} \quad (\text{plane strain}) \quad (2.21)$$

$$J_e = G = \frac{K^2}{E} \quad (\text{plane stress}) \quad (2.22)$$

where E is Young's modulus and  $\nu$  is Poissons ratio.

For elastic-plastic materials, the quantity U in Eq. 2.20 cannot be interpreted as the potential energy. More appropriately, it is the elastic-plastic work required to deform the specimen. J retains its physical significance as a measure of the intensity of crack-tip strain field [2.56]. This interpretation of J is similar to the stress intensity concept which gives the intensity of the stress field surrounding the cracks tip. J has been extensively employed as a criterion for monotonic fracture of ductile metals [2.57 - 2.59].

### The Cyclic J-integral Range

Dowling and Begley [2.60] first proposed the use of the cyclic J-integral range as a parameter to correlate crack growth rates in 25 mm thick compact tension specimens of A533B steel subjected to bulk cyclic plastic deformations. These tests were conducted under displacement control. Values of  $\Delta J$  were estimated from areas under load versus deflection curves during rising load. Since macroscopic crack closure occurred, the point at which the crack opened was estimated and  $\Delta J$  was calculated from the area above this point. Excellent correlation was obtained between  $\Delta J$  and fatigue crack growth rates for these tests. The results were also found to be in agreement with LEFM data on the same material.

Dowling [2.61] expanded the use of the cyclic J-integral range as a parameter to correlate the crack growth rates of small surface cracks in smooth axial specimens subjected to fully plastic cycling in A533B steel. In making the estimation of  $\Delta J$  for small semi-circular surface cracks, cycled under elastic-plastic conditions, Dowling developed expressions for the linear elastic and power law hardening cases separately and then combined the two for the more generalized elastic-plastic type of stress-strain behavior. The following general approach was employed with specific reference to Dowling's computations for A533B steel.

For the elastic case, the stress intensity may be expressed as follows:

$$\Delta K = Y \Delta \sigma \sqrt{\pi a} \quad (2.23)$$

where  $Y$  is the combined flaw shape and boundary correction factor. Using Eq. 2.22 for the elastic component of the J-integral

$$\Delta J_e = Y^2 \frac{\Delta \sigma^2 \pi a}{E} = Y^2 2\pi \Delta W_e a \quad (2.24)$$

For semicircular surface cracks Dowling computed  $\Delta J_e$  as

$$\Delta J_e = \left( \frac{2}{\pi} \times 1.12 \right)^2 \frac{\Delta \sigma^2 \pi a}{E} = 3.2 \Delta W_e a \quad (2.25)$$

For the plastic case, the material model for the cyclic stress-strain curve may be expressed as:

$$\Delta \sigma_t = k (\Delta \epsilon_p)^n \quad (2.26)$$

where  $n$  is the cyclic strain hardening exponent. Here, the stabilized stress-strain hysteresis loops were shifted so that the compressive tips coincided at a new origin as shown in Figure 2.18. To a close approximation, the stress range depends only on the strain range and is nearly independent of the deformation path. Following an estimate made by Shih and Hutchinson [2.56], the plastic component of the J-integral range is

$$\Delta J_p = Y^2 2\pi f(n) \Delta W_p a \quad (2.27)$$

where  $f(n)$  is a function of the cyclic strain hardening exponent and is given by:

$$f(n) = \frac{(n+1)}{2\pi} \left( 3.85 \frac{(1-n)}{\sqrt{n}} + \pi n \right) \quad (2.28)$$

It is assumed that the same boundary and flaw shape correction factor used for the linear elastic case is applicable here also. This is reasonable since Okazaki and Koizumi [2.62] have shown that LCF crack fronts at high temperatures adopt shapes expected from purely elastic considerations. Substituting  $f(n)$  given above into Eq. 2.27,

$$\Delta J_p = Y^2 2\pi \frac{(n+1)}{2\pi} \left( 3.85 \frac{(1-n)}{\sqrt{n}} + \pi n \right) \left( \frac{\Delta\sigma\Delta\epsilon_p}{n+1} \right) a \quad (2.29)$$

For A533B steel ( $n=0.165$ ) and  $f(n)=1.56$ , hence

$$\Delta J_p = 5.0 \Delta W_p a \quad (2.30)$$

The resulting estimate of the cyclic J-integral range for semicircular cracks in A533B steel as computed by Dowling is

$$\Delta J_t = 3.2 \Delta W_e a + 5.0 \Delta W_p a \quad (2.31)$$

The physical interpretation of  $\Delta J_t$  as the range of elastic and plastic work experienced in a single fatigue cycle is shown schematically in Figure 2.19. The general formulation for the J-integral range under elastic-plastic cyclic conditions is

$$\Delta J_t = \Delta J_e + \Delta J_p = Y^2 2\pi a (\Delta W_e + f(n) \Delta W_p) \quad (2.32)$$

or

$$\Delta J_t = Y^2 \frac{\Delta\sigma^2 \pi a}{E} + Y^2 (\Delta\sigma\Delta\epsilon_p a) \left( 3.85 \frac{(1-n)}{\sqrt{n}} + \pi n \right) \quad (2.33)$$

The mathematical developments leading to the J-integral concept imply, for elastic-plastic materials, that the J-integral is valid where the deformation theory of plasticity is valid. Since the deformation theory of plasticity cannot directly account for plasticity effects observed on unloading, there is some question concerning the applicability of the J-integral concept to cyclic loading. Starkey and Skelton [2.63] suggest that theoretical objections may be countered by noting that in high strain fatigue that  $\Delta J$  is always calculated from the same point (the common origin of Figure 2.18) in the tension-going direction during the steady cyclic state by ignoring the details of the arrival path.

Dowling [2.61] used the entire stress range in estimating  $\Delta J_t$  from hysteresis loops. Using the above procedures, Dowling found excellent correlation between crack growth rates and  $\Delta J_t$  for fully plastic cycling at crack depths greater than 180  $\mu\text{m}$ . It was concluded that the lack of correlation for smaller cracks was due to a physical size effect.

There is general disagreement over using the full stress range or some fraction of the stress range over which cracks are assumed to be open in calculating  $\Delta J_t$ . Réger et al. [2.64 - 2.65] assume that the positive stress range is operative. Following Dowling's lead many investigators have employed the full stress range [2.62,2.66,2.67].

Huang and Pelloux [2.67] investigated the crack propagation behavior of Hastelloy-X, at 25C and 760C in the fully plastic low cycle fatigue regime,  $R_e = -1$ . They employed the entire range of stress and strain to calculate  $\Delta J_t$ . The crack growth rate data for different strain levels correlated with  $\Delta J_t$ . There was also general agreement with linear elastic tests.

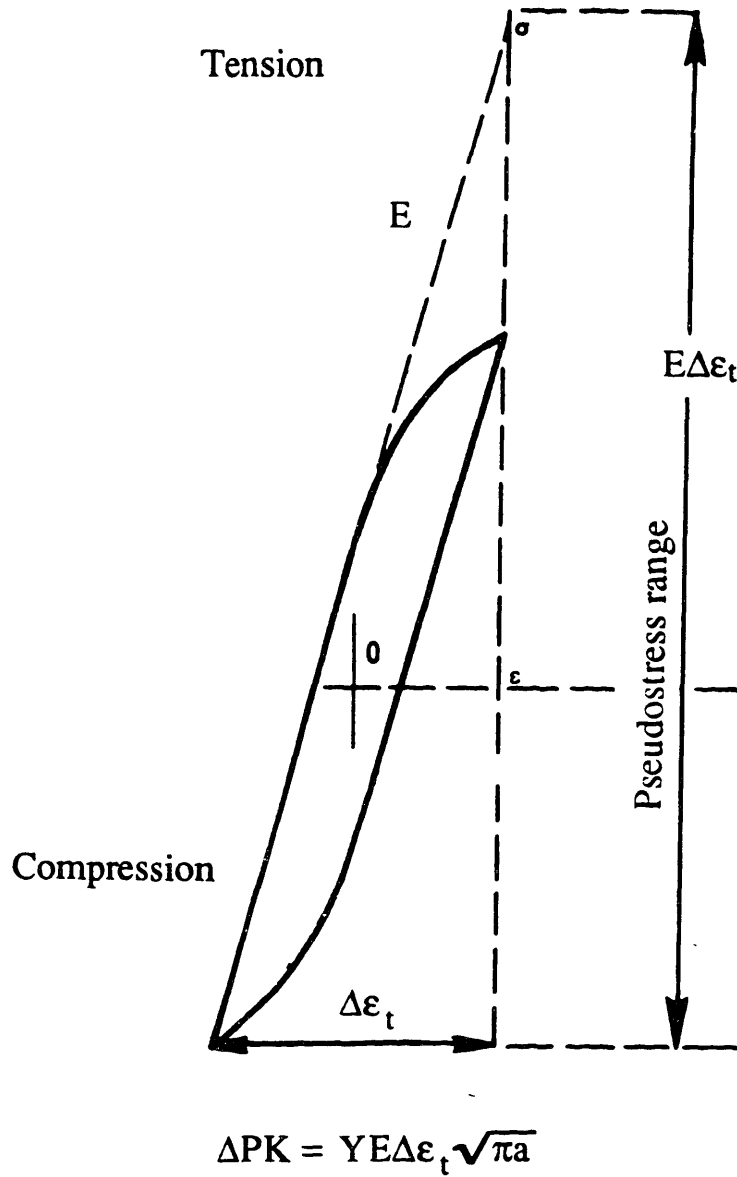


Figure 2.15 Definition of the pseudostress range according to Solomon [Ref. 2.52].

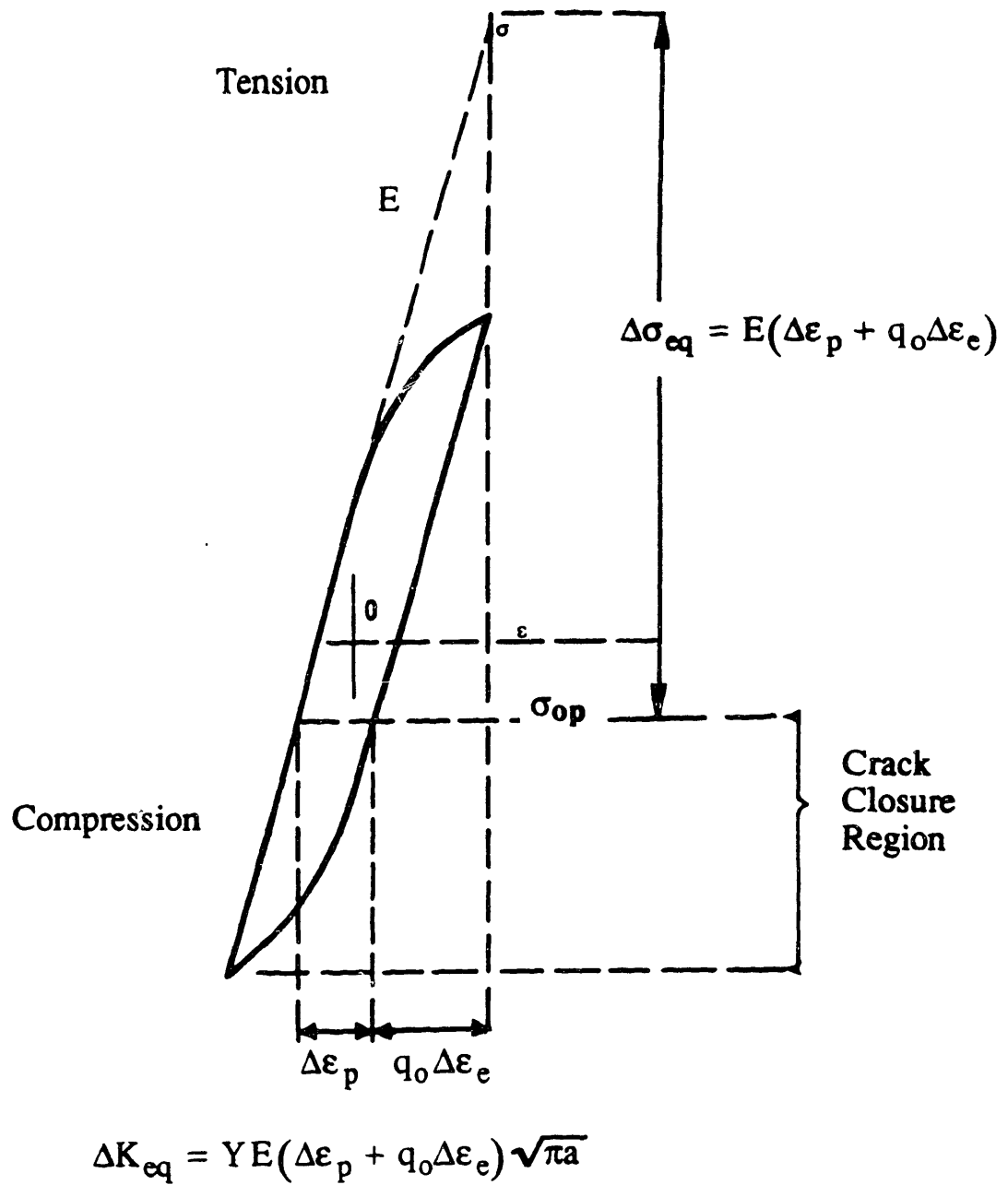
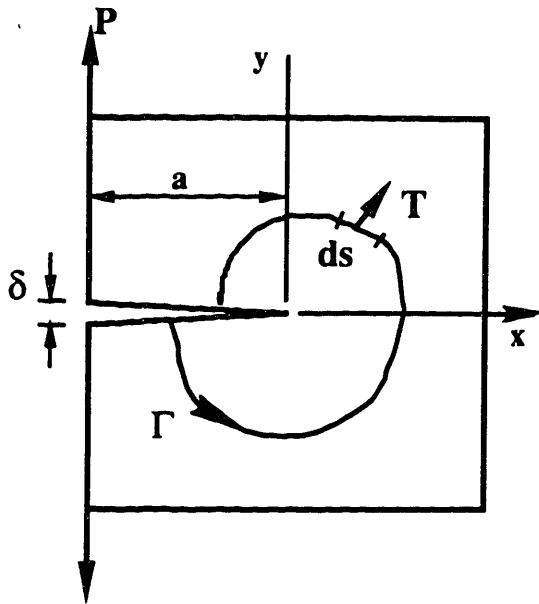


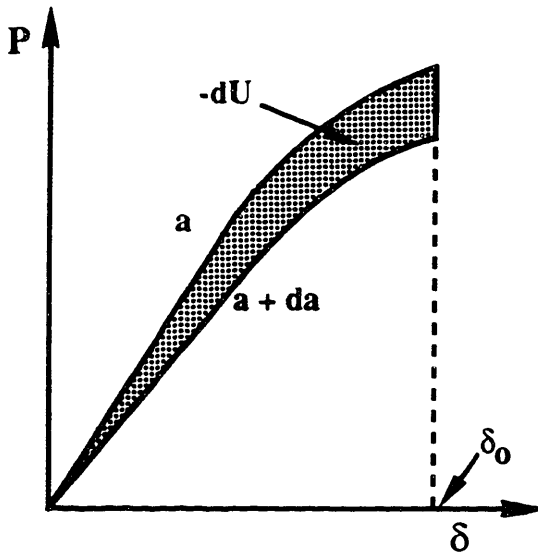
Figure 2.16 Definition of the equivalent stress range according to Starkey and Skelton [Ref. 2.54].



a) Energy Line Integral

$$J = \int_{\Gamma} \left( W dy - \mathbf{T} \cdot \frac{\partial \mathbf{u}}{\partial \mathbf{x}} ds \right)$$

$$W = \int_0^{\epsilon_p} \sigma_{ij} d\epsilon_{ij}$$



b) Potential Energy Difference

$$J = -\frac{1}{B} \frac{\partial U}{\partial a}$$

B = Thickness

Figure 2.17 The J-integral of Rice [Ref. 2.55].

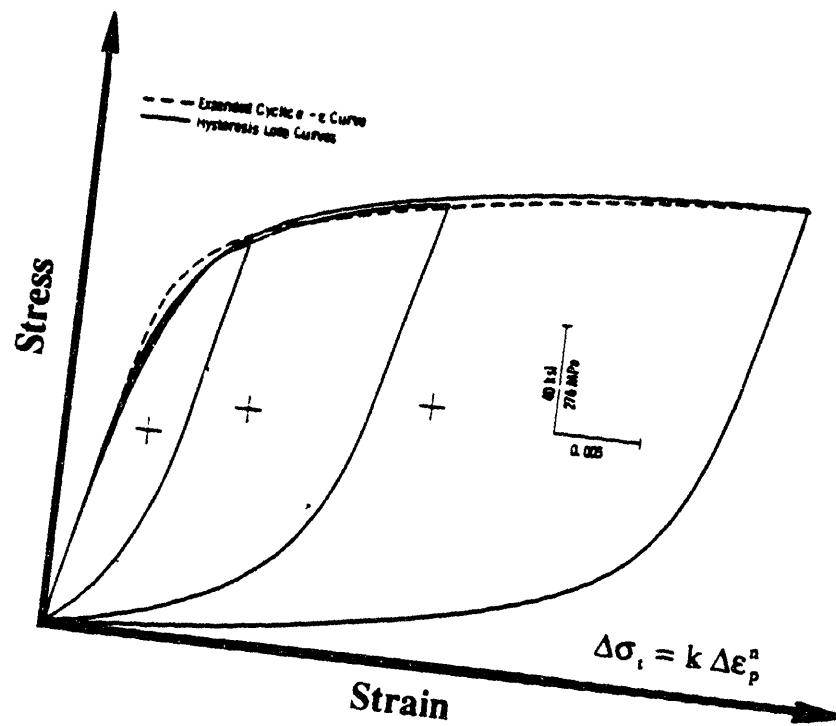
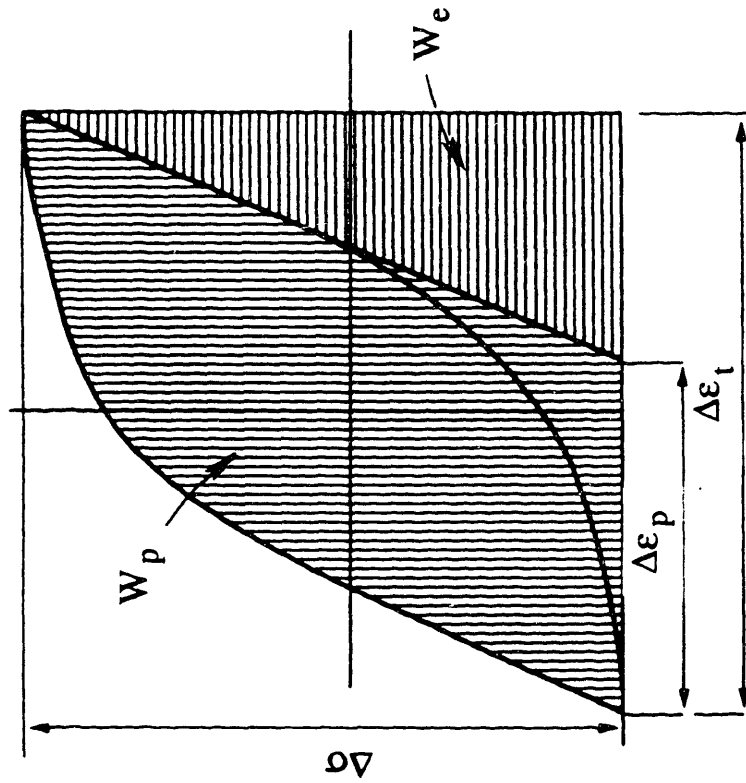


Figure 2.18 Stress-strain hysteresis loops plotted on shifted axes [Ref. 2.61].



$$\Delta\sigma = k\Delta\varepsilon_p^n$$

$$\Delta W_e = \frac{\Delta\sigma^2}{2E}; \quad \Delta W_p = \left( \frac{\Delta\sigma\Delta\varepsilon_p}{n+1} \right).$$

$$\Delta J_t = \Delta J_e + \Delta J_p = Y^2 2\pi a (\Delta W_e + f(n)\Delta W_p)$$

$$\Delta J_t = \frac{Y^2 \Delta\sigma^2 \pi a}{E} + Y^2 (\Delta\sigma \Delta\varepsilon_p a) \left( 3.85 \frac{(1-n)}{\sqrt{n}} + \pi n \right)$$

Figure 2.19 Estimation of small crack  $\Delta J_t$  from stress-strain hysteresis loops [Ref. 2.61].

## 2.5 Modeling of Small Crack Behavior

### Intrinsic Crack Length

El Haddad, Smith and Topper [2.68,2.69] proposed an empirical approach to predict the effect of crack length on threshold stress amplitude for fatigue crack growth in smooth specimens. They have suggested that the following expression for the elastic stress intensity factor be used:

$$\Delta K = \Delta \sigma \sqrt{\pi(a + l_0)} \quad (2.34)$$

where  $l_0$  is the intrinsic crack length which is a constant for a given material and material condition.

The threshold stress range at very small crack lengths has been shown [2.68,2.70] to approach the endurance limit of the material,  $\Delta \sigma_e$ ; hence,  $l_0$  may be obtained from Equation 2.34 as:

$$l_0 = \frac{1}{\pi} \left( \frac{\Delta K_{TH}}{\Delta \sigma_e} \right)^2 \quad (2.35)$$

where  $\Delta K_{TH}$  is the LEFM threshold stress intensity factor range for a long crack. At any crack length, the threshold stress range is then obtained through equation 2.34 as:

$$\Delta \sigma_{TH} = \frac{\Delta K_{TH}}{\sqrt{\pi(a + l_0)}} \quad (2.36)$$

As the crack length decreases, the intrinsic length  $l_0$  constitutes an increasing fraction of the effective crack length ( $a + l_0$ ), until at very short lengths it represents a fictitious crack length which, above the endurance limit stress, can propagate into the interior of the specimen.

A series of experiments were performed on CSA G40-11 steel to examine the accuracy of Eq. 2.36 in correlating experimental threshold and small crack results [2.71]. Figure 2.20 presents these experimental results and the prediction of Eq. 2.36. Agreement between the predictions of Eq. 2.36 and the test data is excellent, indicating that the equation adequately describes the crack size effect on the threshold stress intensity. Figure 2.20 also indicates that, for crack lengths less than 1 mm, the term  $l_0$  constitutes an important fraction of the effective crack length, resulting in the threshold stress range deviating from the more usual prediction of Eq. 2.36 with  $l_0 = 0$ .

The principal criticism of this model is that no physical justification has been given for the term  $l_0$  and it appears to act as a mathematical operator forcing the truncation of the threshold stress at the endurance limit.

### Constant Plastic Zone Size Criterion

Ohuchida, Usami and Nishioka [2.72,2.73] introduced a criterion for threshold stress and stress intensity. They assume that, at the threshold, the cyclic plastic zone size at the crack tip is a material constant. Using the Dugdale model for cyclic plastic zone size, the criterion for the endurance limit of a cracked material may be expressed as follows:

$$r_{pc(w)} = a_e \left[ \sec \left( \frac{\pi \Delta \sigma_w}{4 \sigma_y} \right) - 1 \right] = \text{const.}; R \geq 0 \quad (2.37)$$

$$r_{pc(w)} = a_e \left[ \sec \left( \frac{\pi}{2(2\sigma_{yc}/\sigma_{\max,w} + R)} \right) - 1 \right] = \text{const.}; R \leq 0 \quad (2.38)$$

where  $r_{pc(w)}$  is the cyclic plastic zone size at threshold,  $\Delta \sigma_w$  is the stress range at the endurance limit,  $\sigma_{\max,w}$  is the maximum stress at the endurance limit,  $\sigma_{yc}$  is the cyclic yield stress,  $a_e$  is the effective crack length, i.e.,

$$a_e = \frac{1}{\pi} \left( \frac{\Delta K}{\Delta \sigma} \right)^2 \quad (2.39)$$

By knowing the cyclic plastic zone size at threshold for long cracks, estimates can be made of the threshold stress  $\Delta\sigma_w$  and the corresponding threshold stress intensity for very small crack lengths in the same material.

This criterion has been shown to predict the effects of crack length and stress ratio [2.74]. Agreement between calculated and experimental values is reasonably good, as can be seen in Figure 2.21.

### Shear Displacement Criterion

Hammouda and Miller [2.75,2.76], in modeling the behavior of small cracks growing in the elastic-plastic strain fields of notches, have suggested that the driving force for crack extension is the total shear displacement at a crack tip.

$$\phi_t = \phi_p + \phi_e \quad (2.40)$$

where  $\phi_t$  is the total,  $\phi_p$  the plastic and  $\phi_e$  the elastic displacement at the crack tip. Cracks were considered small relative to the extent of the plastic field of the notch as illustrated in Figure 2.22. When the crack is very long  $\phi_t \approx \phi_e$  and LEFM controls crack growth. When the crack is very small,  $\Delta K$  is small,  $\phi_e$  is negligible, and  $\phi_t \approx \phi_p$ . Calculations of  $\phi_t$  for a range of crack lengths predicts behavior such as that depicted in Figure 2.23.

Lankford extended this treatment to small crack behavior in smooth specimens [2.77]. He argued that, for smooth specimens cycled near the fatigue limit, bulk plasticity is provided by preferential microplasticity in certain grains. Microcracks may initiate and propagate in such grains, but as they approach the first subsurface grain boundary, a decrease in  $da/dN$  is observed due to a lower contribution of  $\phi_p$  to  $\phi_t$ .

After the crack encounters the first grain boundary, two things may happen. If the second grain does not contribute significant microplasticity to  $\phi_t$ , and if this value of  $\phi_t$

corresponds to a  $\Delta K$  below the LEFM threshold stress intensity, the crack will become nonpropagating. On the other hand, if the next grain penetrated by the crack is sufficiently microplastic,  $da/dN$  will increase rapidly, and the crack will continue to grow faster than would be expected on the basis of LEFM. Once the crack becomes long enough for its intrinsic LEFM crack tip plastic zone to supersede the maximum grain size,  $\phi_t$  will be approximately  $\phi_e$ , resulting in the small crack and the long crack data merging.

There is excellent agreement between the predictions based on the above arguments (depicted in Figure 2.23) and anomalous small crack behavior.

### Blocked Slip Band (BSB) Model

Another criterion for threshold stress or stress intensity for small cracks has been proposed by Tanaka and co-workers [2.78 - 2.81]. They suggested that the condition for no crack growth occurs when the slip band emanating from the tip of an isolated crack is blocked by a grain boundary. This situation is illustrated in Figure 2.24a. The density of pile-up dislocations at the tip of the slip band is infinite, and the elastic stress field near its tip is similar to the singular stress field near a Mode II elastic crack tip. The intensity of this field is characterized by a microscopic stress intensity factor. The analysis of this criterion was carried out for the case of the slip band coplanar to the crack plane in a two-dimensional field, as shown in Figure 2.24b. The threshold stress is given by:

$$\sigma_{TH} = \frac{K_c^m}{\sqrt{\pi b}} + \frac{2}{\pi} \sigma_{fr}^* \cos^{-1}\left(\frac{a}{b}\right) \quad (2.41)$$

where  $K_c^m$  is the critical value of microscopic stress intensity factor,  $\omega_0$  is the slip band process zone,  $b = a + \omega_0$  and  $\sigma_{fr}$  is a uniform frictional stress which acts against climbing motion of dislocations in the slip bands. If the threshold condition is expressed in terms of the stress intensity factor:

$$K_{TH} = \sigma_{TH} \sqrt{\pi a} = K_c^m \sqrt{\frac{a}{b}} + 2 \sqrt{\frac{a}{b}} \sigma_{fr}^* \cos^{-1}\left(\frac{a}{b}\right) \quad (2.42)$$

For long cracks, the threshold stress intensity factor,  $\Delta K_o$ , is obtained by taking the limit of  $\Delta K_{TH}$  as  $\omega_o$  becomes smaller than  $a$ ,

$$\Delta K_o = \Delta K_c^m + 2 \sqrt{\frac{2}{\pi}} \sigma_{fr}^* \sqrt{\omega_o} \quad (2.43)$$

and the fatigue limit of smooth specimens,  $\sigma_o$ , can be derived by substituting  $a = 0$  in Eq. 2.41:

$$\sigma_o = \sigma_{fr}^* + \frac{K_c^m}{\sqrt{\pi \omega_o}} \quad (2.44)$$

The application of the BSB model to fatigue crack growth thresholds is based on the assumption that some process zone with a certain crack length,  $\omega_o$ , is required ahead of the crack tip for the crack to grow. For purposes of determining the threshold values of stress or stress intensity for small cracks under cyclic stress, the experimental values needed are two of three parameters:  $\sigma_o$ ,  $\Delta K_o$  and  $a_o$ .

Morris, James and Buck [2.82] have proposed a modification to the BSB model. They have shown that the closure stress developed at the surface tips of microcracks is a function of the distance of the crack tip from a grain boundary. They suggested that closure stress, resulting from unreversed tensile strain at a crack tip, has to be exceeded before a crack tip experiences any effective opening which might result in crack advance. Therefore, the stress intensity factor becomes:

$$\Delta K_{eff} = (\sigma_{max} - \sigma_c) \sqrt{\pi a} \quad (2.45)$$

where  $\Delta K_{eff}$  is the effective stress intensity range,  $\sigma_{max}$  is the maximum cyclic stress and  $\sigma_c$  is the crack closure stress.

The model proposed by Morris et al. combines the BSB model and crack closure phenomenon. The underlying assumptions are that slip responsible for early propagation does not extend in significant amounts beyond the next grain boundary in the direction of crack propagation (BSB model) and that retardation of crack growth by a crack closure stress can be calculated from the location of a crack tip relative to the grain boundary. In theory, this model explains the anomalous behavior of small cracks as observed in many alloys where the crack size is less than the grain size.

### Fracture Surface Roughness and Crack Closure Model

Morris et al. [2.83] have proposed a model which relates the threshold stress intensity to the crack closure stress arising from fracture surface roughness. Their model successfully predicts the variation in  $\Delta K_{TH}$  with crack length for small surface cracks in Ti-6Al-2Sn-4Zn-6Mo alloy, based on measured values of crack opening displacement arising from roughness.

The basic physical mechanism is shown in Figure 2.25. Fracture surface asperities make contact a short distance behind the crack tip and prop open the crack, resulting in a measurable crack opening displacement [2.84]. Based on an expression derived by Green and Sneddon [2.85], the opening displacement can be related to the distance from the crack tip and the applied stress. For small displacements

$$U(X) \approx \frac{\sigma}{E} \sqrt{2cX} \quad (2.46)$$

where  $U(X)$  is the crack opening displacement,  $\sigma$  is the applied stress,  $c$  is the half length of a surface crack, and  $X$  is the distance from crack tip to point of contact of opposing fracture surfaces. It is surmised that the average distance  $X_0$  and the effective height  $U_0$  of the discontinuities are constant if the crack tip is of sufficient length resulting in  $\Delta K_{TH}$  approaching  $\Delta K_0$  (asymptotic value of  $\Delta K_{TH}$  for long cracks).

Alternatively,  $\Delta K_{TH}$  will be a function of crack length if the effectiveness of roughness in propping open a crack varies with crack length. Crack opening displacement data,  $U_{min} = f(2c)$ , for a Ti 6Al-2Sn-4Zr-6Mo alloy is shown in Figure 2.26. For this alloy, the opening increases with crack length approaching an asymptotic value  $U_o$  at  $2c \approx 150 \mu\text{m}$ . A model to predict the contribution to  $\Delta K_{TH}$  arising from fracture surface roughness ( $\Delta K_{TH}$ ) was derived. The resulting expression for the threshold stress intensity is:

$$\Delta K_{TH} = \Delta K_{oR} \frac{U_{\min(2c)}}{U_o} + \beta \quad (2.47)$$

where  $\Delta K_{oR}$  is the contribution to  $\Delta K_o$  arising from fracture surface roughness,  $U_{\min(2c)}$  is the value of  $U(2c)$  at minimum load,  $U_o$  is the asymptotic value of  $U_{\min}$  for long cracks,  $c$  is the half length of surface cracks and  $\beta$  is the parameter which includes the contribution to  $\Delta K_{TH}$  from all mechanisms in addition to roughness.

Included in the parameter  $\beta$  are possible contributions to threshold from residual plasticity, surface oxide, residual stress in the plastic zone, a criterion for the onset of microplasticity, and mechanisms particularly important to small crack growth such as an elastic-plastic correction to the cyclic stress intensity [2.86,2.87], grain boundary blocking of crack growth [2.88] and a plastic zone size determined by non-continuum constraints [2.89]. Several of these mechanisms may also be dependent on crack length. Although this model attempts to be general, the inclusion of the term  $\beta$  can be viewed as a very nonspecific "fudge factor".

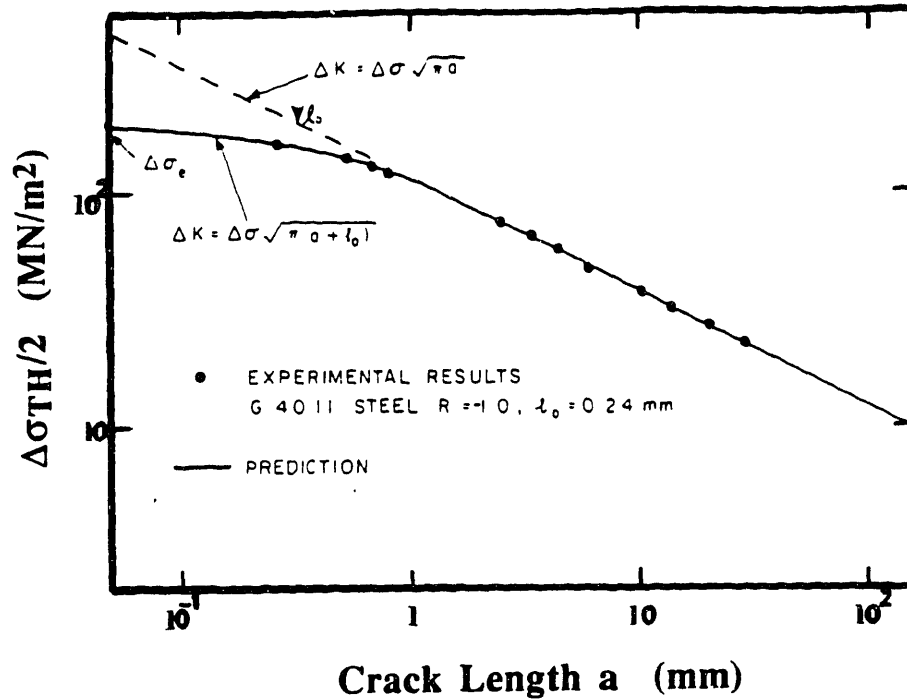


Figure 2.20 Effect of crack length on the threshold stress range for fatigue crack growth in G40.11 steel [Ref. 2.71].

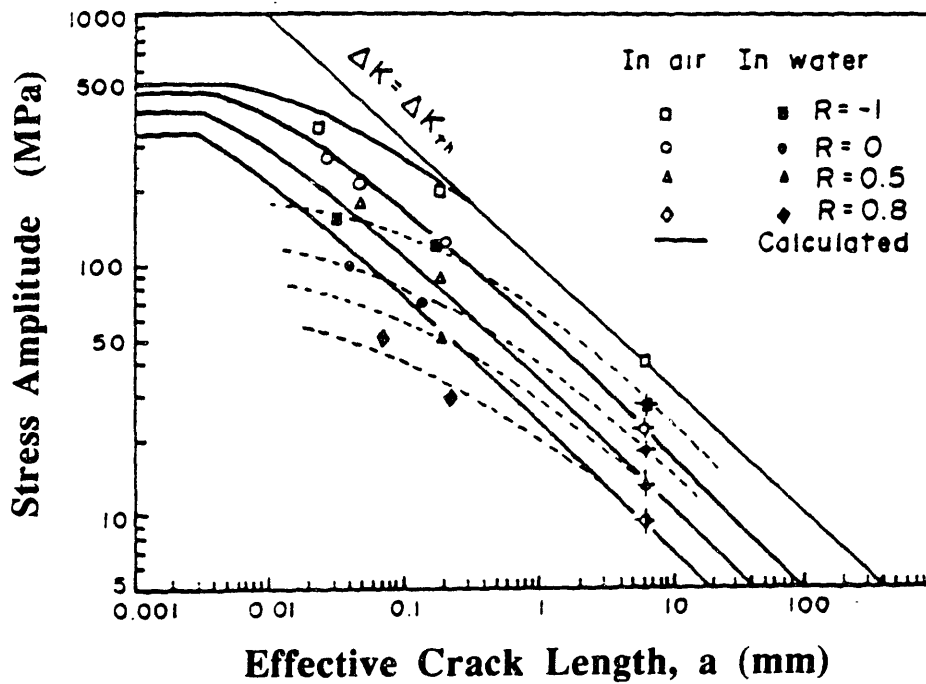


Figure 2.21 Effect of R-ratio and environment on the threshold stress amplitude and endurance limit ( $5 \times 10^7$  cycles) for 13 Cr cast steel with micro-shrinkage cavities [Ref. 2.74].

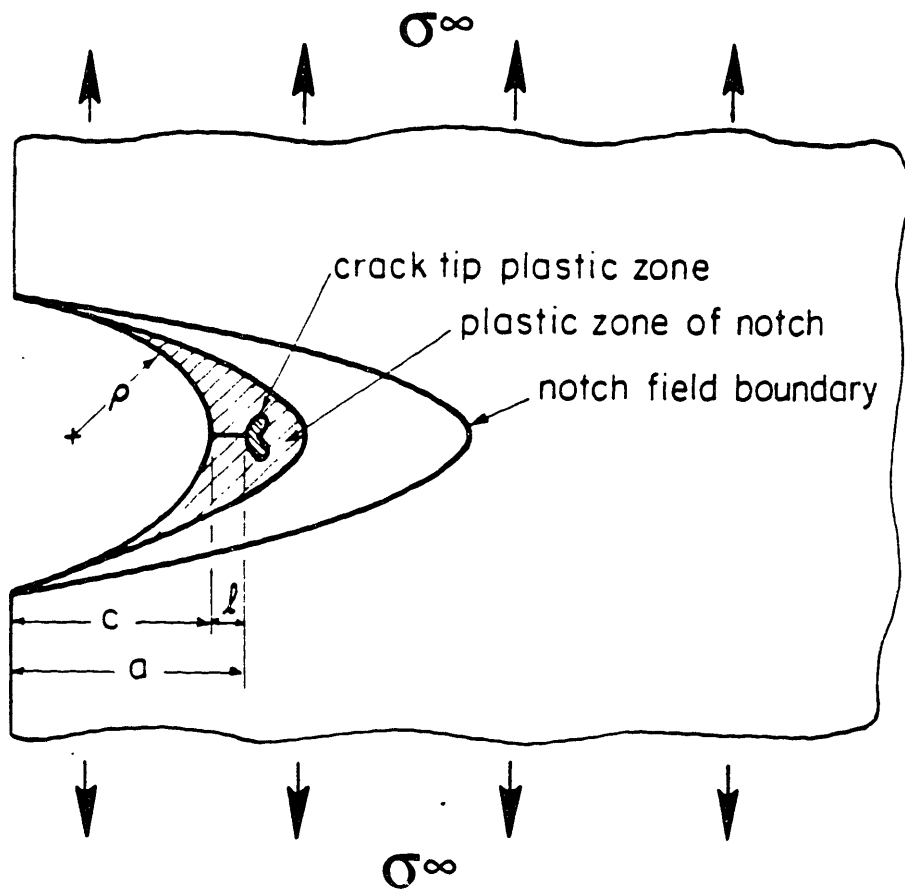


Figure 2.22 Small crack embedded in the elastic-plastic field of a notch [Ref. 2.75].

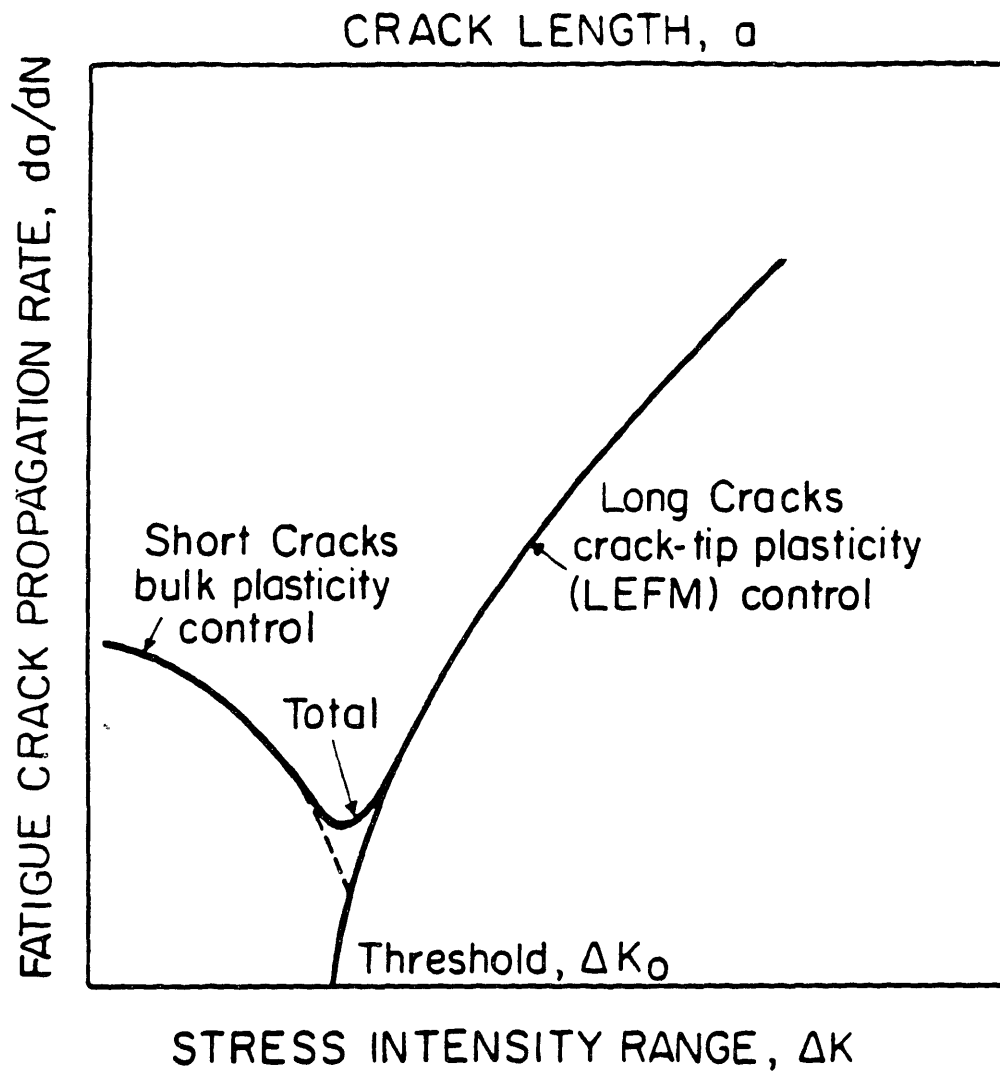


Figure 2.23 Schematic illustration of the elastic-plastic and linear elastic characterization of crack growth rate for a small crack propagating from a notch [Ref. 2.75].



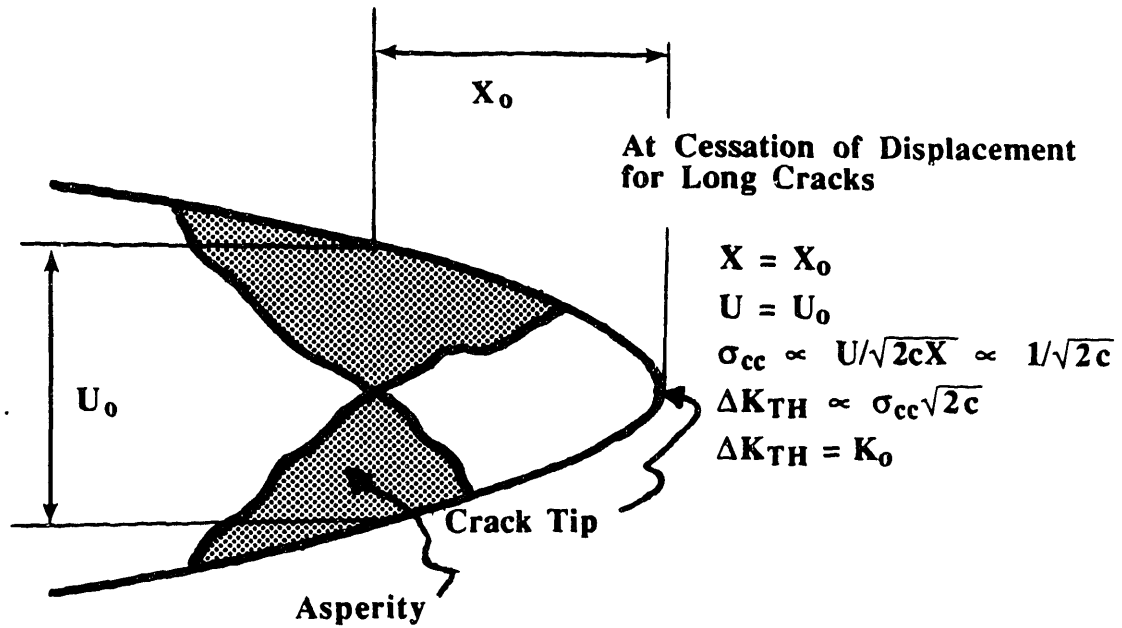


Figure 2.25 Illustration of roughness induced crack closure at an average distance  $X_0$  behind the crack tip. [Ref. 2.83]

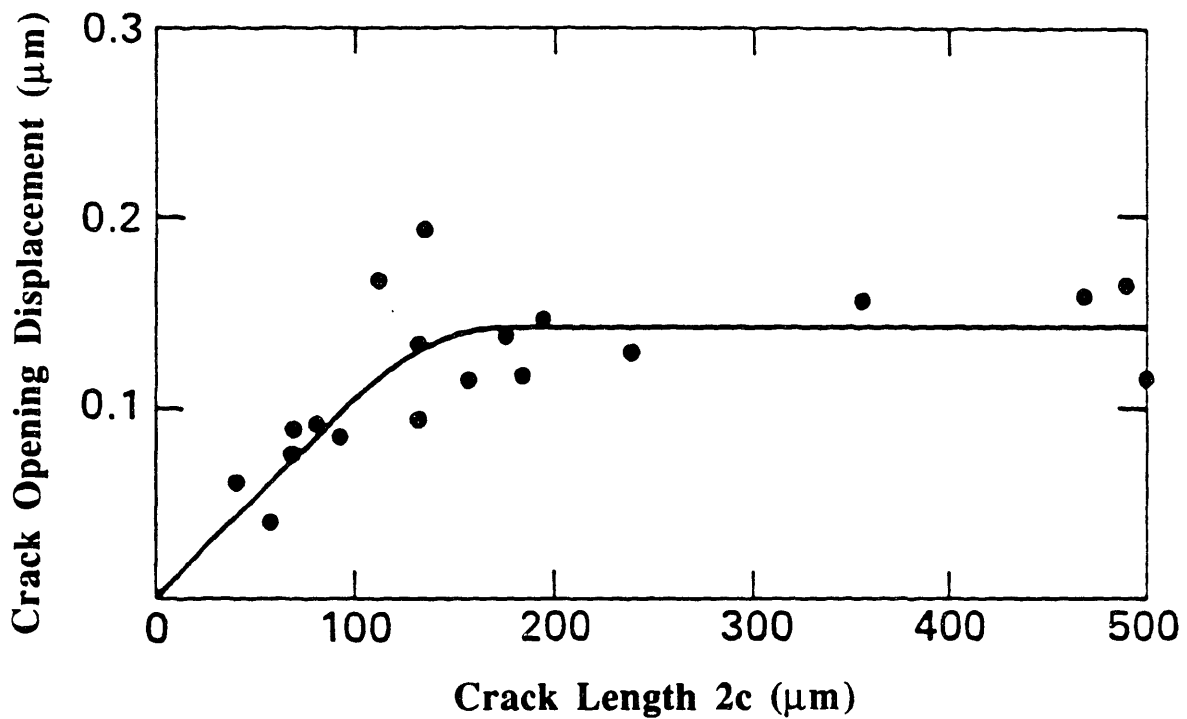


Figure 2.26 Crack mouth opening displacement (at zero load) versus surface crack length for a 6Al-2Sn-4Zn-6Mo titanium alloy [Ref. 2.83].

## 2.6 Fatigue Behavior of Small Cracks in Aircraft Turbine Disk Alloys

A review of the fatigue behavior of small cracks in commercial alloys will be limited to aircraft turbine disk alloys. Fatigue crack growth behavior for long cracks in turbine disk alloys have been reported extensively in the open literature. Several excellent reviews can be found in References 2.90 - 2.94. Reporting of small crack growth behavior is scarce in the open literature and elevated temperature data even more so due to the difficulty associated with experimentation and the proprietary nature of the results.

### Turbine Disk Alloys at Room Temperature

Hicks, Brown and King [2.95 - 2.97] investigated the effect of microstructure on the long and small fatigue crack growth behavior in Astroloy. Tests were performed at room temperature on specimens loaded in three point bending. Crack lengths were measured by d. c. potential drop. Their results are shown in Figure 2.27 for fine-grained (5  $\mu\text{m}$ ), coarse grained (50  $\mu\text{m}$ ) and single crystal microstructures. Crack growth rates for small cracks (within a single grain) exceeded that for long cracks in the polycrystalline microstructures at low values of  $\Delta K$  with small cracks propagating below the long crack  $\Delta K_{\text{TH}}$ . Small crack growth rates merged with long crack growth rates as  $r_{\text{pc}}$  approached the grain size. There was little difference between small crack and long crack behavior in single crystal Astroloy. In contrast to long crack behavior, fine grained Astroloy exhibited better short crack propagation resistance than the coarse grained form. Changes in the  $\gamma'$  morphology in the coarse grained microstructure did not affect small crack growth rates. Waspaloy with a 50  $\mu\text{m}$  grain size tested under the same conditions exhibited identical small crack growth rate behavior as the 50  $\mu\text{m}$  grain size Astroloy. It was concluded that defect tolerant life predictions based on long crack behavior would be nonconservative for this alloy at room temperature.

Newman and Beevers [2.98, 2.99] investigated crack initiation and propagation from pores in powder metallurgy Astroloy at room temperature under nominally elastic fatigue conditions. A two stage replica technique was employed which permitted crack growth rates and crack opening behavior to be determined. The specimens were loaded in three-point bending under nominally elastic conditions;  $\sigma_{\max} = 0.6\sigma_{ys}$  and  $R = 0.1$ . Surface intersected pores dominated as crack initiation sites with initial crack extension occurring along  $\{111\}$  planes as determined by an electron channelling technique. Crack growth rates were measured over the range:  $10 \mu\text{m} < 2c < 250 \mu\text{m}$ . Small crack growth rates within a single grain exceeded that for long cracks and exhibited considerably lower values of  $\Delta K_{TH}$ . Cracks existing within a single grain grew at initially high rates until encountering the first grain boundary where retardation or arrest occurred.

Small cracks encountering many grains in powder metallurgy Astroloy exhibited crack growth rates similar to that for long crack  $\Delta K_{eff}$  data. Threshold stress intensities were also similar to that for long cracks. The crack opening mode at all small crack lengths ( $2c < 250 \mu\text{m}$ ) was predominantly Mode I with no evidence of crack closure.

Newman and Beevers [2.98,2.99] also investigated small crack (12  $\mu\text{m}$  to 200  $\mu\text{m}$ ) growth behavior in cast and wrought Nimonic 901 with grain sizes in the 160  $\mu\text{m}$  to 300  $\mu\text{m}$  range. Crack growth rates for small cracks within individual grains exceeded long crack  $\Delta K_{eff}$  behavior and exhibited a lack of threshold behavior. Individual cracks showed no significant arrest or retardation when the first grain boundary was encountered. These results are similar to that observed by Feng [2.100]. It was concluded that small cracks within a single grain exhibit a lower intrinsic resistance to growth than multigrained small cracks.

Soniak and Rémy [2.101] measured crack growth rates in H.I.P. plus forged, powder metallurgy Astroloy for long and small through cracks ( $a > 200 \mu\text{m}$ ). The microstructure consisted of a necklace structure of coarse 50  $\mu\text{m}$  grains surrounded by fine

grains of  $\sim 2 \mu\text{m}$  diameter. Long crack tests were performed at R-ratios of: 0.1, 0.5, 0.7 and 0.9. Crack growth rates for these long crack tests were consolidated using  $\Delta K_{\text{eff}}$  calculated from crack closure measurements. Fatigue crack growth rates were measured for small cracks at  $R = 0.1$ . Small cracks were able to propagate below the long crack  $\Delta K_{\text{TH}}$  and grow at rates thirty times that of long cracks. However, when considered in terms of  $\Delta K_{\text{eff}}$ , long and small crack data were consolidated. This behavior was attributed to less closure for small cracks. The values of  $K_{\text{Op}}$  for small cracks increased from zero for  $200 \mu\text{m} < a < 500 \mu\text{m}$  and merged with long crack  $K_{\text{Op}}$  values for  $a \approx 2 \text{ mm}$ . Using  $\Delta K_{\text{eff}}$  resulted in conservative predictions of crack propagation life. Note that in this investigation, the minimum crack size was  $200 \mu\text{m}$  (4 x g.s.); significantly greater than that considered by Hicks et al.

Vecchio and Hertzberg [2.102] investigated fatigue crack growth rates for long and small cracks at room temperature in powder metallurgy Astroloy with grain sizes of  $5 \mu\text{m}$  and  $26 \mu\text{m}$ . Long crack tests were performed on compact tension specimens at R-ratios of 0.1 and 0.5. Small crack ( $a \geq 300 \mu\text{m}$ ) tests were performed on four point bending specimens with through thickness cracks at the same R-ratios. It was concluded that small crack data only "appeared" anomalous when plotted in terms of  $\Delta K$ . When the strain energy density,  $\Delta S$ , was employed as the mechanical driving force parameter, long and small crack growth rates were consolidated.

McCarver and Ritchie [2.103] measured fatigue thresholds for long and small ( $10 \mu\text{m}$  -  $200 \mu\text{m}$ ) cracks in cast and wrought René 95. The microstructure consisted of a necklace structure of warm-worked  $\gamma$  grains (g.s.  $\sim 90 \mu\text{m}$ ) surrounded by recrystallized  $\gamma$  grains (g.s.  $10 - 20 \mu\text{m}$ ). Tests were performed at room temperature at R-ratios of 0.1 and 0.8. The long crack  $\Delta K_{\text{TH}}$  for  $R = 0.1$  loading was 60% greater than the short crack  $\Delta K_{\text{TH}}$  at the same R-ratio. The long crack  $\Delta K_{\text{TH}}$  for  $R = 0.8$  loading was approximately the same as the small crack  $\Delta K_{\text{TH}}$  for  $R = 0.1$  loading. The results were rationalized in terms of roughness

induced crack closure. It was concluded that defect-tolerant fatigue lifetime predictions based on long crack data at low R-ratios would be nonconservative for this alloy.

Lankford, Cook, Sheldon and Jones [2.104, 2.105] investigated small crack behavior in powder metallurgy Gatorized<sup>®</sup> IN100 at room temperature under nominally elastic conditions. Small cracks were produced artificially by machining away a large crack to yield a remnant small crack ( $a \approx 75 \mu\text{m}$ ) at one acute corner of a specimen with a parallelogram cross section. Crack growth rates for small cracks were initially greater than that for long cracks but dropped through a minimum below the long crack rates before merging at higher values of  $\Delta K$ . The initially high crack growth rates for small cracks was attributed to a specimen geometry artifact. The subsequent region of crack growth, in which the small crack data lie below that for long cracks was caused by the greater influence of grain boundaries on small cracks. Grain boundary retardation was fully overcome only when the cyclic plastic zone size exceeded the average grain diameter, consequently, short and long crack data merged. Small and large cracks exhibited identical fracture paths at the same stress intensities with a transition from crystallographic transgranular to striated growth with increasing  $\Delta K$ . As will be seen later, the fatigue fracture path at disk rim temperatures ( $\sim 650\text{C}$ ) is intergranular for powder metallurgy Gatorized<sup>®</sup> IN100.

It should be noted that, in this study, the crack length regime over which small crack growth rates exceeded long cracks was not extensive and would not result in a significantly nonconservative prediction of a small crack propagation life using the long crack data. The crack length regime over which small crack growth rates were less than that for long cracks was more significant.

A study of crack tip deformation fields [2.105] showed that the reversed plastic zone sizes were the same at equivalent values of  $\Delta K$  for both large and small crack tested under the

conditions described above. Hence, mechanical similitude requirements were met at all crack sizes. Metallurgical similitude requirements were met as crack lengths became longer.

### Turbine Disk Alloys at Elevated Temperatures

Hudak et al. [2.106] investigated small crack growth rates in fine grained (12  $\mu\text{m}$ ) and coarse grained (30  $\mu\text{m}$ ) powder metallurgy Astroloy and in coarse grained (42  $\mu\text{m}$ ) cast and wrought Waspaloy at temperatures of 25C, 200C and 600C. Small cracks initiated in persistent slip bands and propagated on {111} planes or at pores in fine grained Astroloy.

Crack growth rates for small cracks exceeded that for long cracks when compared on the basis of  $\Delta K$  in all cases except that of fine grained Astroloy at 600C. Small crack growth rates were found to be similar for coarse grain Astroloy and Waspaloy at room temperature and 600C. However, at 600C small cracks in fine grained Astroloy did not exhibit anomalously high growth rates and were found to grow significantly slower than small cracks in coarse grained Astroloy.

The fracture surface morphology of small and long cracks exhibited the same dependence on temperature and stress level indicating that the crack propagation mechanism was the same in both cases. Consequently, differences in crack growth rates were attributed to differences in mechanical driving force. An SEM stereoimaging technique was employed to quantify local crack tip displacements, strain fields and closure levels. Crack tip strain fields and the nature and magnitude of crack closure varied significantly for small and long cracks. Local crack tip measurements were used to define an elastic-plastic crack driving force based on the relationship between  $\Delta CTOD$  and  $\Delta J$ . Crack growth rates for small and long cracks were consolidated using  $\Delta K_{eq}$  derived from  $\Delta J$ .

Using data from long cracks resulted in overprediction of fatigue crack propagation lives. The overprediction was associated with the occurrence of  $\Delta K_{TH}$  for long cracks. It

was concluded that  $\Delta K_{TH}$  (long crack) and near-threshold growth rate data are not applicable to material selection, design and damage tolerant analysis of turbine disks.

Leis et al. [2.107] investigated small crack growth behavior in Inconel 718 (g.s. = 10  $\mu\text{m}$ ) at room temperature and at 643C (4 tests out of 33 were performed at elevated temperature). Specimens were machined from 2.3 mm thick sheet. Small fatigue cracks were propagated from center-hole-notch specimens (dia. = 1.27 cm) and EDM surface flaw specimens (dia. = 350  $\mu\text{m}$ ). Crack lengths were recorded by an automated photographic system.

At room temperature and under elastic fatigue conditions, long and small crack growth rates could be consolidated using LEFM. In the elastic-plastic field of notches and at elevated temperatures higher crack growth rates were observed. Fracture surfaces for 643C testing were smooth compared to the 20C counterparts. Consequently, the decrease in surface roughness (and therefore closure level) at higher temperatures accounts for higher values of  $\Delta K_{eff}$  at the same  $\Delta K_{app}$  and R-ratio. Anomalous crack growth behavior was not observed in these experiments.

Cook et al. [2.108] investigated the fatigue behavior of powder metallurgy Gatorized<sup>®</sup> IN100 at room temperature and at 650C. Fatigue crack initiation was often associated with pores. At 650C under continuous cycling elastic fatigue conditions, small and long crack growth rates were consolidated using LEFM. The fatigue fracture path was intergranular. At 650C, one minute dwell small crack growth rates were five times slower than long crack growth rates. This behavior was attributed to increased time dependent plastic deformation at the surface slowing the fatigue crack growth rates.

Van Stone and Henry [2.109] investigated fatigue crack initiation and early growth in numerous processing and microstructural variants of powder metallurgy René 95 at 538C to establish a correlation with defect tolerance. The five processing conditions of René 95

included: two hot isostatic press (HIP) conditions of -400 mesh ( $< 37 \mu\text{m}$ ) PM René 95, thermally mechanically processed (TMP) HIP-compacted PM René 95, large grained cast and wrought René 95, and shot peened PM René 95. In addition, fatigue failure mode and deformation mode characteristics were studied for eight selected conditions of HIP-compacted René 95.

HIP compacted René 95 was intentionally doped with  $250 \mu\text{m}$  diameter alumina contaminants. Crack initiation and growth from these defects were studied by replication of surfaces of polished fatigue specimens. Fatigue crack initiation occurred in less than 1% of total fatigue life. Since EDM defects were shown to result in the same fatigue lives as naturally occurring surface defects of similar dimension; a d.c. potential drop technique was used to monitor fatigue crack initiation and growth from EDM defects providing a quantitative measure of cyclic defect tolerance and fatigue crack growth rates. Using the above two approaches, the microstructural conditions which resulted in improved defect tolerance and higher fatigue capability were identified.

Of all the conditions evaluated, large grained cast and wrought René 95 exhibited the lowest crack growth rates, presumably due to the grain size which was four times greater than the largest powder metallurgy condition (the strength was 25% lower). For the eight processing variants of HIP-compacted PM René 95, increasing defect tolerance correlated with increased amounts of secondary deformation band cracking. A reduction in small crack growth rates also correlated with a transition from fine-wavy to coarse-planar slip. In this study of René 95, it is obvious that microstructure can strongly influence defect tolerance. Differences in small crack growth rates can be attributed to a lack of metallurgical similitude.

To summarize this review of the fatigue behavior of small crack in aircraft turbine disk alloys, the following issues dominate:

### *Metallurgical Similitude*

- Anomalous crack growth behavior was generally attributed to a lack of metallurgical similitude (usually related to grain size) due to the anisotropic nature of the material structure at this size level. Anomalous behavior was generally observed when crack sizes were less than the grain size.
- Convergence of small and long crack growth rates generally occurred when  $r_{pc} \approx$  grain size.

### *Mechanical Similitude*

- Differences in crack closure levels for small and long cracks is responsible for the higher range of mechanical driving force experienced by small cracks in some cases.
- The lack of three dimensional constraint (plane stress) at specimen and component surfaces exerts a greater influence at small crack sizes. Defect tolerance calculations indicate that, under high cyclic stresses, a large portion of usable fatigue life is limited to the small crack regime.

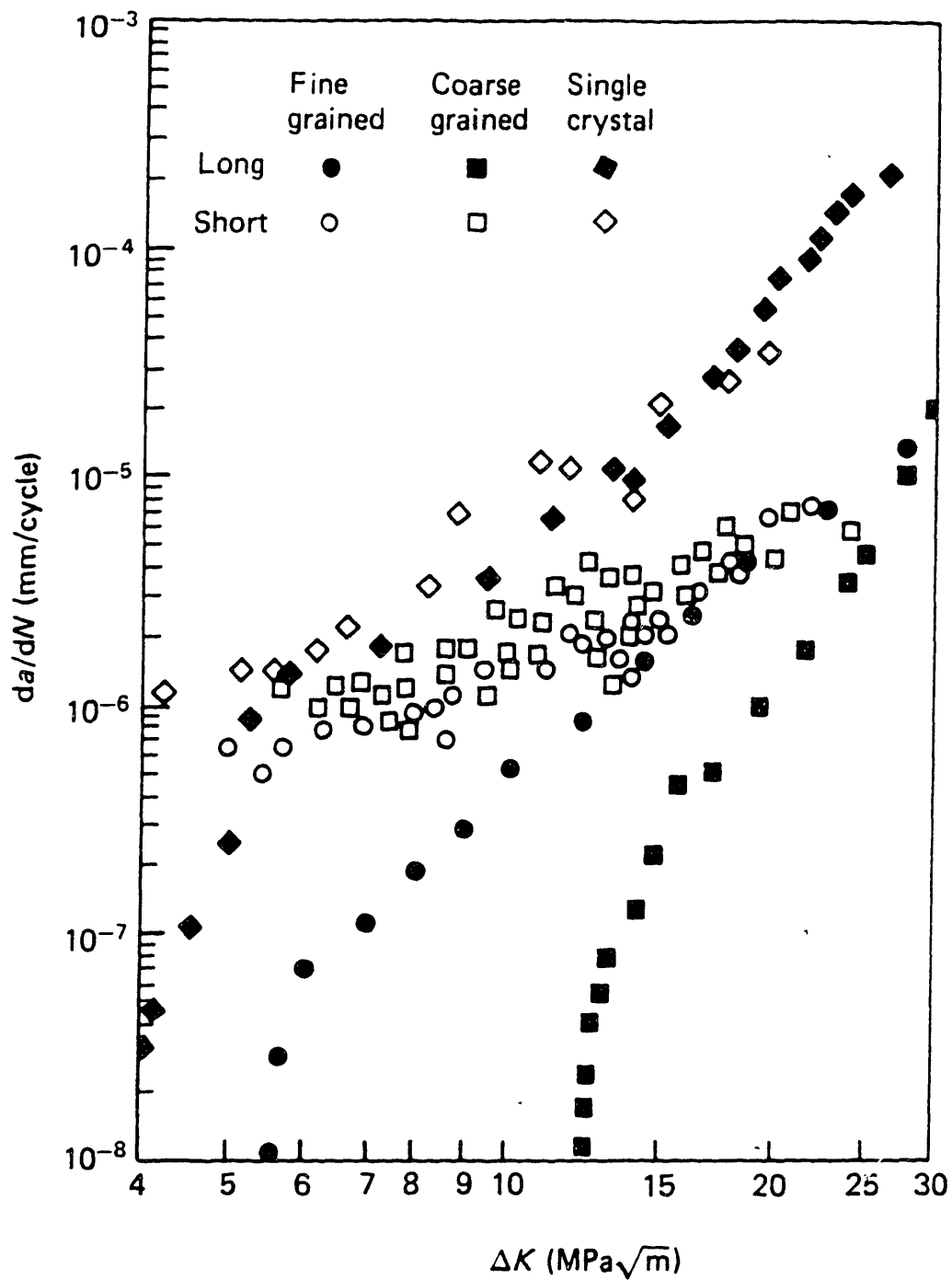


Figure 2.27 Crack growth rates versus  $\Delta K$  for small cracks in fine-grained ( $5\ \mu\text{m}$ ) and coarse-grained ( $50\ \mu\text{m}$ ) Astroloy and equivalent single crystal material [Ref. 2.96].

### 3. Experimental Procedures

#### 3.1 Materials

The alloys selected for this investigation are three nickel-base superalloys currently being used for aircraft turbine disks. They include conventional cast and wrought alloys and a powder metallurgy processed alloy. The alloys are listed in Table 3.1 with the test temperatures.

**Table 3.1**

<u>Alloy</u>	<u>Test Temperature</u>
Waspaloy	25C and 427C
Inconel 718	427C
Gatorized® IN100(PM)	649C

The chemical composition, heat treatments and mechanical properties are given for each alloy in Tables 3.2, 3.3 and 3.4.

#### Waspaloy

Waspaloy is a conventionally processed nickel-base superalloy currently used for aircraft turbine disks. The microstructure consists of a nickel-rich austenite matrix,  $\gamma$ , strengthened by Al, Cr, Mo and Co in solid solution and by coherent  $\gamma'$  precipitates. Cr provides oxidation resistance at elevated temperatures. The precipitation of  $\gamma'$  is based on the ordered  $\text{Ni}_3(\text{Al,Ti})$  intermetallic phase having an  $\text{L1}_2$  structure. The compatibility of the  $\gamma'$  and  $\gamma$  crystal structures (~0 to 1% mismatch) allows for homogeneous nucleation of  $\gamma'$

throughout the matrix with low surface energy and long time stability. Fully heat treated Waspaloy consists of ~30 volume percent  $\gamma'$  having a spheroidal morphology [3.1].

Extensive reviews of the microstructural aspects of superalloys can be found in the literature [3.2-3.4].

The Waspaloy used in this investigation was received as hot rolled plate and given the heat treatment described in Table 3.2. The typical microstructure of the heat treated alloy is shown in Figure 3.1. The microstructure is comprised of a duplex grain structure with average grain sizes of 7  $\mu\text{m}$  and 200  $\mu\text{m}$ . The large grains give good creep properties to the detriment of low temperature tensile strength. The matrix  $\gamma'$  exhibits a spheroidal morphology. The same lot of Waspaloy was used for small crack growth testing at room temperature and at 427C.

**Table 3.2**

Chemical Composition of Waspaloy

Element	Wt. %	
	min	max
Carbon	0.02	0.10
Manganese	---	0.10
Silicon	---	0.15
Phosphorus	---	0.015
Sulfur	---	0.015
Chromium	18.00	21.00
Cobalt	12.00	15.00
Molybdenum	3.50	5.00
Titanium	2.75	3.25
Aluminum	1.20	1.60
Zirconium	0.02	0.08
Boron	0.003	0.010
Iron	---	2.00
Copper	---	0.10
Nickel	balance	

Heat Treatment of Waspaloy

Solution: 1018C / 4 hrs. / OQ or WQ

Stabilization: 845C / 4 hrs. / AC

Age: 760C / 16 hrs. / AC

OQ Oil Quench  
 WQ Water Quench  
 AC Air Cool

Mechanical Properties of Waspaloy

	25C	427C
E (GPa)	206	---
$\sigma_{0.2\%}$ (MPa)	903	841
$\sigma_{UTS}$ (MPa)	1324	1276
Elongation (%)	24	24

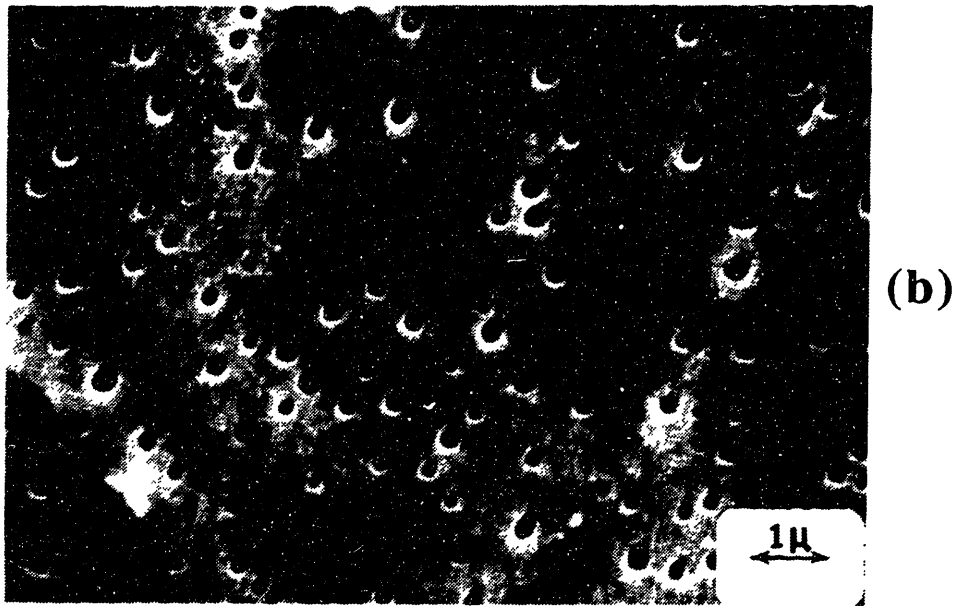
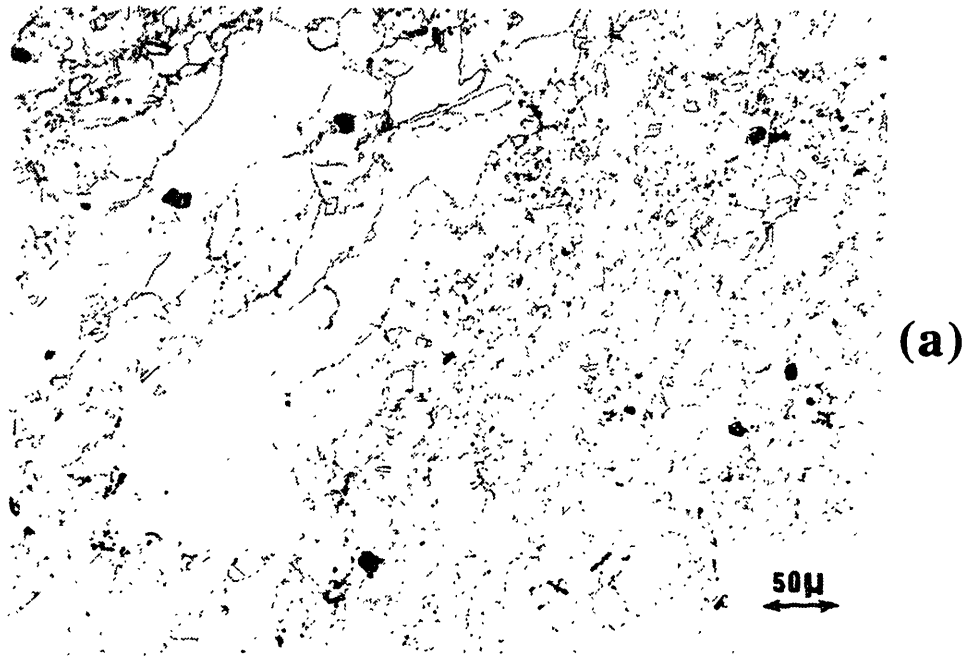


Figure 3.1 Typical microstructure of Waspaloy used in this investigation; (a) duplex grain structure with average grain sizes of 7  $\mu\text{m}$  and 200  $\mu\text{m}$ , (b) matrix  $\gamma'$  exhibiting a spheroidal morphology.

## Inconel 718

Inconel 718 is a conventionally processed nickel-iron based superalloy currently used for aircraft turbine disks. The microstructure consists of a nickel rich austenite matrix,  $\gamma$ , strengthened by elements in solid solution and by coherent  $\gamma'$  and  $\gamma''$  precipitates. Solid solution strengthening is provided by Cr and Mo. Cr also provides oxidation resistance at elevated temperatures.

The  $\gamma'$  precipitates in Inconel 718 generally have a spheroidal morphology and contribute little to the precipitate strengthening. The major strengthening is attributed to the  $\gamma''$  precipitates.  $\gamma''$  is a metastable, coherent precipitate having a body centered tetragonal crystal structure with a  $\text{Ni}_3(\text{Nb, Al, Ti})$  stoichiometry. The  $c/a$  ratio of 2.04 causes significant distortion and large coherency strains. The  $\gamma''$  precipitates have a disk shaped morphology. Oblak et al. [3.5] proposed that the strengthening mechanism in Alloy 718 is due to coherency strains arising from the  $\gamma''$  lattice distortion and not antiphase boundary or order strengthening normally associated with the  $\gamma'$  phase. In the fully aged condition,  $\gamma''$  constitutes approximately 25% of the total  $\gamma' + \gamma''$  precipitate formed. The total amount of  $\gamma' + \gamma''$  precipitate in Alloy 718 is ~19 volume percent [3.5].

The material used in this investigation was received in the form of hot rolled bars of 22.2 mm diameter from Huntington Alloys. The material was given the conventional solution plus 2-step ageing heat treatment as described in Table 3.3. The typical microstructure of the heat treated Inconel 718 is shown in Figure 3.2. The microstructure is uniform with an average grain diameter of 32  $\mu\text{m}$ .

**Table 3.3**

Chemical Composition of Inconel 718

Element	Wt. %
Carbon	0.04
Manganese	0.13
Iron	17.61
Sulfur	0.002
Silicon	0.18
Copper	0.16
Nickel	53.80
Chromium	18.00
Aluminum	0.62
Titanium	0.94
Cobalt	0.28
Molybdenum	3.01
Niobium and Tantalum	5.23
Phosphorus	0.012
Boron	0.003

Heat Treatment of Inconel 718

Solution: 955C / 1 hr. / AC

Age: 720C / 8 hrs. / FC to 620C @ 56C/hr.  
620C / 8 hrs. / AC

FC Furnace Cool  
AC Air Cool

Mechanical Properties of Inconel 718

	25C	427C
E (GPa)	204	183
$\sigma_{0.2\%}$ (MPa)	1131	1100
$\sigma_{UTS}$ (MPa)	1340	1250
Elongation (%)	23	47

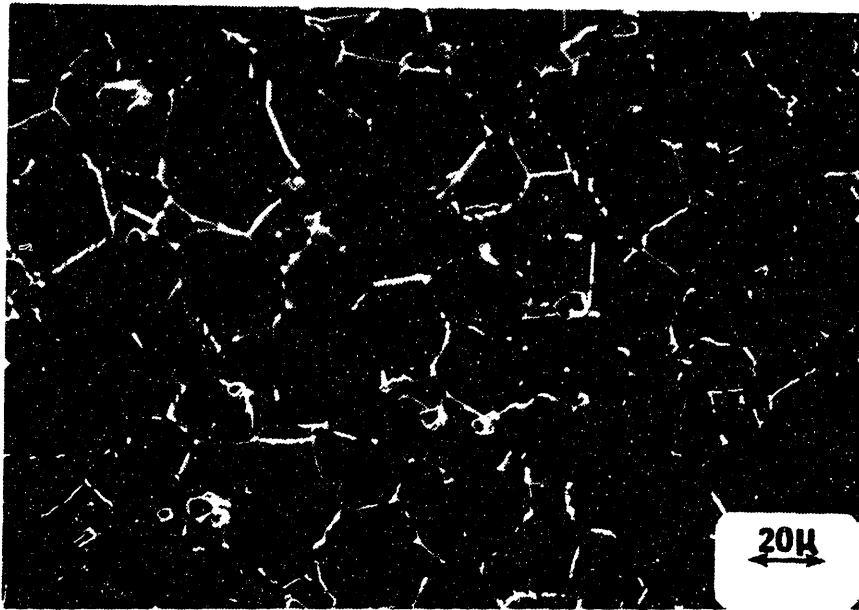


Figure 3.2 Typical microstructure of Inconel 718 used in this investigation; average grain size is 32  $\mu\text{m}$ .

### Powder Metallurgy Gatorized® IN100

IN100(PM) is a high strength nickel-base superalloy which is processed by the powder metallurgy route and is currently used for advanced aircraft turbine disks. Strengthening is based on a high volume fraction of  $\gamma'$  precipitates (~60 volume percent) which are coherent with the matrix. Solid solution strengthening elements play the same role in this alloy as in those described above. The high solute content is required to achieve the high volume fraction of  $\gamma'$  present in this alloy. The rapid solidification rates provided by inert gas atomization of the powders prevents gross elemental segregation which would otherwise occur during conventional processing. After initial powder consolidation, the extruded billet is superplastically forged by Pratt and Whitney's Gatorizing® process [3.6].

The material used in this investigation was supplied by Pratt and Whitney Aircraft as specimens machined from a Gatorized® disk. The heat treatment employed is described in Table 3.4. The typical microstructure of IN100(PM) is shown in Figure 3.3. The average grain diameter is 3-5  $\mu\text{m}$ . Large blocky  $\gamma'$  precipitates reside at grain boundaries and much finer cuboidal  $\gamma'$  reside within the  $\gamma$  matrix. Pores resulting from gas entrapped during atomization are uniformly present throughout the microstructure with sizes ranging from 10 to 30  $\mu\text{m}$  in diameter.

**Table 3.4**

Chemical Composition of Gatorized® IN100(PM)

Element	Wt. %	
	min	max
Carbon	0.05	0.09
Manganese	---	0.020
Sulfur	---	0.010
Phosphorus	---	0.010
Silicon	---	0.010
Chromium	11.90	12.90
Cobalt	18.00	19.00
Molybdenum	2.80	3.60
Titanium	4.15	4.50
Aluminum	4.80	5.15
Vanadium	0.58	0.98
Boron	0.016	0.024
Zirconium	0.04	0.08
Tungsten	---	0.05
Iron	---	0.30
Copper	---	0.07
Niobium and Tantalum	---	0.04
Lead	---	0.0002
Bismuth	---	0.00005
Oxygen	---	0.010
Nickel	balance	

Heat Treatment of Gatorized® IN100(PM)

Solution: 1121C / 2 hrs. / OQ  
 Stabilization: 871C / 40 mins. / AC < 371C  
 982C / 45 mins. / AC  
 Age: 649C / 24 hrs. / AC  
 760C / 4 hrs. / AC

OQ Oil Quench  
 AC Air Cool

Mechanical Properties of Gatorized® IN100(PM) at 649C

E (GPa)	210
$\sigma_{0.2\%}$ (MPa)	1100
$\sigma_{UTS}$ (MPa)	1380
Elongation (%)	22
Elastic Limit	
$\epsilon_0$ (%)	0.5
$\sigma_0$ (MPa)	1050

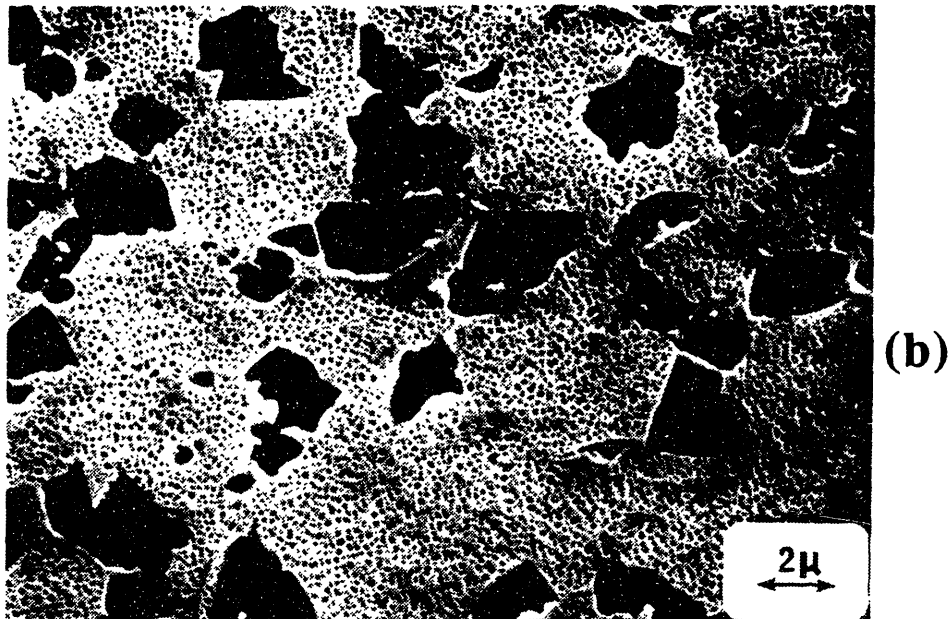
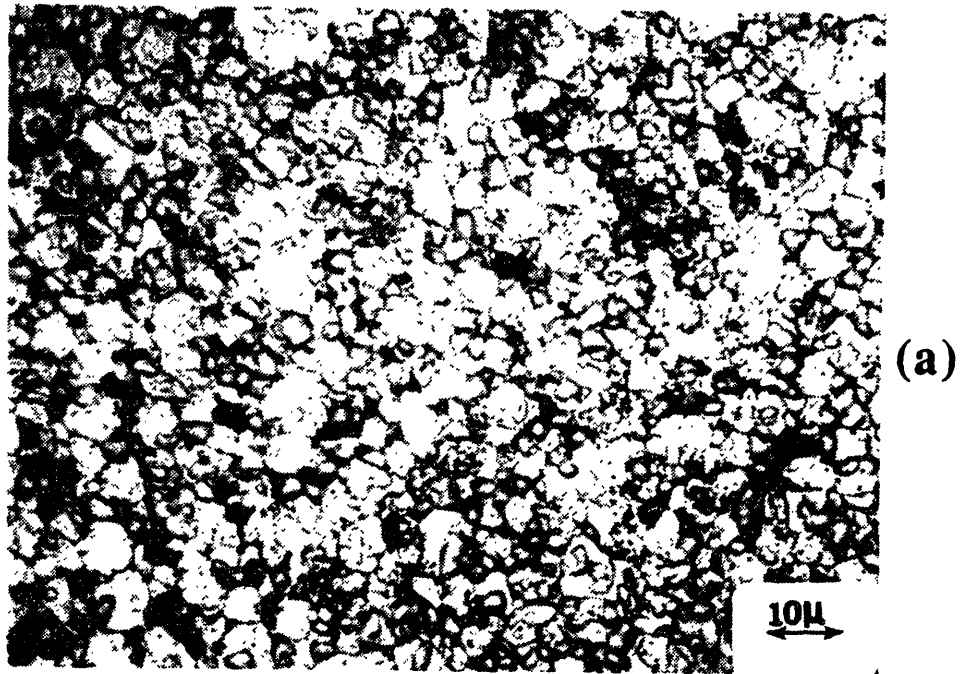


Figure 3.3 Typical microstructure of powder metallurgy Gatorized<sup>®</sup> IN100 with an average grain size of 3-5  $\mu\text{m}$ . (a) Optical micrograph, (b) SEM micrograph exhibiting a duplex  $\gamma$  structure.

## 3.2 Test Specimen

### Specimen Geometry

The specimen geometry used in this investigation of the fatigue crack growth behavior of small cracks in turbine disk alloys at elevated temperature is shown in Figure 3.4. The specimen is essentially an axisymmetric button-head low-cycle fatigue specimen with a 6.35 mm diameter gage section. It was chosen to be suitable for both elastic and elastic-plastic loading conditions. A modified low-cycle fatigue specimen with flats on opposite faces of the gage section, Figure 3.5, was adopted when it was found that the curvature of the cylindrical specimen surface may have contributed to a deflection of the crack when the surface crack length exceeded about 800  $\mu\text{m}$ . This problem will be discussed later.

### Specimen Preparation

All specimens used in this investigation were machined by low stress grinding or by electro-chemical machining. After low stress grinding, there exists a disturbed layer of about 50 to 100  $\mu\text{m}$  in depth which contains residual stresses [3.7]. This residual stress layer was removed to avoid interference with the fatigue propagation behavior of small cracks.

Removal of the residual stress layer was accomplished by the following procedures. Flat segments and round segments of specimen gage sections were hand ground with successively finer grades of SiC paper; 240, 320, 400 and 600 grit sizes. Gage section surfaces were ground in the longitudinal and transverse (circumferential) directions. Sharp corners were rounded to prevent crack initiation. In the final steps of hand grinding, 6  $\mu\text{m}$  diamond paste was used. Finally, the reduced section of each specimen was electropolished with a solution of 45% butyl-cellusolve, 45% acetic acid and 10% perchloric acid, at 40-50 volts for 30 seconds at a temperature of  $\sim 0$  to  $5^\circ\text{C}$ . Approximately 100  $\mu\text{m}$  of surface layer

was removed by the procedure described above. When artificially introduced surface defects were used as crack initiation sites, they were processed at this time.

Thermocouples were spot welded to precise locations below the gauge section to control the temperature using the set point technique in elevated temperature tests.

### Initiation of Small Cracks

Two important and practical considerations dictated the use of an artificial means to initiate small fatigue cracks: 1) Due to the statistical nature of intrinsic defects, the probability of having a characteristically maximum size defect intersecting the surface of the gage section of a laboratory test specimen is small. 2) The measurement of small crack lengths is experimentally difficult, however, this task can be greatly facilitated by knowing their exact location.

The desired defect geometry is that which is conducive to crack initiation at the smallest possible defect size. Such a pseudo-crack should have a sharp defect tip radius and be oriented normal to the principal applied stress. The process employed to produce defects must not induce significant residual stresses or large scale microstructural damage.

A pulsed laser was employed to introduce surface defects in fatigue test specimens to serve as initiation sites for small cracks. The principal advantage of this technique is that small sizes are obtainable ( $\sim 10 \mu\text{m}$ ). The laser used was a Quanta Ray, ND-YAG laser operating in the Q-switched mode with a wavelength of 532 nm. The incident beam diameter was  $\sim 3 \text{ mm}$  with an output energy of around  $10^{-3}$  joules/pulse and a pulse duration of 0.2  $\mu$  sec. The incident beam was focused by a series of two cylindrical lenses which generated an elliptical defect in the specimen surface as shown in Figure 3.6. From 100 to 500 pulses were used for each defect. The depth of each defect is determined by the number of pulses and the intensity of radiation in the incident beam. Similar defects were also made using a

spherical lens and translating the specimen with respect to the focal point to achieve the desired surface length. The disadvantage of the laser technique was the difficulty encountered in controlling the depth of the defect. This was due to the nonuniform spatial distribution of intensity in the incident beam and changes in the beam characteristics between each use of the laser.

### Precracking

In nearly all experiments where artificial defects were used, cracks were initiated by precracking at  $R = -1$  and a stress range of approximately  $\pm 520$  MPa. Precracking required from 20 K to 50 K cycles to achieve an initial crack depth of 100  $\mu\text{m}$ . Precracking was found to be necessary because:

- 1) Negative R-ratios promote crack initiation.
- 2) It was necessary to initiate and propagate cracks at least 10-20  $\mu\text{m}$  greater than the defect size to grow out of the local influence of the defect geometry.
- 3) It was necessary that cracks assume a stable crack front geometry before surface crack length measurements would correlate with crack depth. This was confirmed in subsequent experiments.

### **3.3 Crack Length Measurement by Plastic Replication**

The plastic replication technique was used to measure crack lengths. This technique has a resolution of about 1  $\mu\text{m}$  in crack length. In addition, it serves as a valuable record which can later be used to correlate crack growth rates with crack tip-microstructural interactions. Acetyl cellulose tape of 125  $\mu\text{m}$  thickness was used as the replicating material and acetone or methyl acetate as the solvent.

The replicating procedure was as follows:

- 1) Cyclic loading was stopped at zero load after a preset number of cycles.
- 2) Induction heating was automatically turned off in elevated temperature tests.
- 3) The specimen was loaded in tension to 50-80% of the peak cyclic load. This static load was decreased as the cracks became longer.
- 4) The softened side (with a few drops of solvent) of a piece of replicating film was applied to the specimen surface under a light pressure for about 15 seconds.
- 5) The film was allowed to dry for 10 minutes.
- 6) The film was peeled off and taped to a glass microscope slide with the replica facing up.
- 7) The replica was then viewed under a reflected light microscope at magnifications ranging from 50x to 500x.
- 8) Crack lengths were measured using a calibrated eyepiece micrometer.

### **3.4 Crack Length Measurement by A. C. Potential Drop**

Due to the considerable labor involved in monitoring crack length by replication, especially at elevated temperature, a program was undertaken to develop an A. C. Potential Drop system for the continuous and automated measurement of crack length [3.8]. A resolution of  $\sim 2 \mu\text{m}$  in crack length was achieved. Unfortunately, a significant problem was encountered in the long term stability of the system. Consequently, work proceeded using the plastic replication technique for measuring crack length.

### 3.5 Small Crack Growth Testing at Elevated Temperature

Test specimens were prepared in the manner described in previous sections. Three defects were introduced at orthogonal positions in the midplane of the round gage section specimens. Two defects were introduced on opposite faces of cylindrical-with-flats gage section specimens. Testing was performed on a closed-loop, servo-hydraulic testing machine. Water cooled grips were aligned on axis to within  $\pm 15 \mu\text{m}$  before every test. This tolerance is less than the lateral play in the actuator.

Specimens were heated by a 2.5 kilowatt - 400 kilohertz induction heating unit using an eight-turn, axisymmetric induction coil. The temperature in the plane of the crack was maintained at the desired test temperature within  $\pm 1\text{C}$ . The temperature gradient along the gauge length was less than  $\pm 5\text{C}$  as determined by a system calibration. Photographs of the high temperature testing system are shown in Figure 3.7.

#### Load Controlled Testing

Load controlled tests were performed at 20 cpm or 10 cpm using a sinusoidal waveform. The test frequency was chosen to match the available long crack data. Cycling was stopped at zero load and induction heating turned off automatically at preset cycle intervals. After the specimen cooled to room temperature, crack lengths were measured by replication. Tests were terminated when the largest surface crack length was in the 2-3 mm range. Specimens were separated along the crack plane by continuing to cycle at room temperature and a positive stress ratio.

The principal test variables were maximum stress and R-ratio (minimum stress/maximum stress). The stress was calculated as the engineering stress,  $P/A_0$ .

### Strain Controlled Testing

Strain (displacement) controlled tests were performed at 10 cpm using a sawtooth waveform. Longitudinal displacement was measured on specimen gauge sections to achieve total strain control. The effective gage length between extensometer probes was 14.4 mm. Extensometer probes contacted the specimen surface 90° from the small crack sites. Total strain,  $\epsilon_t$ , was measured and controlled to a precision of  $\pm 0.01\%$ .

At the end of each cycle interval; cycling was automatically stopped at zero strain, hydraulic pressure turned off returning to zero load along an elastic path and the induction heating turned off. After the specimen cooled to room temperature, the extensometer was removed and crack lengths were measured by replication. When elastic-plastic cycling occurred, care was taken to return the extensometer and the strain-load value to the appropriate position on the hysteresis loop. Tests were terminated in the same manner employed in load controlled tests.

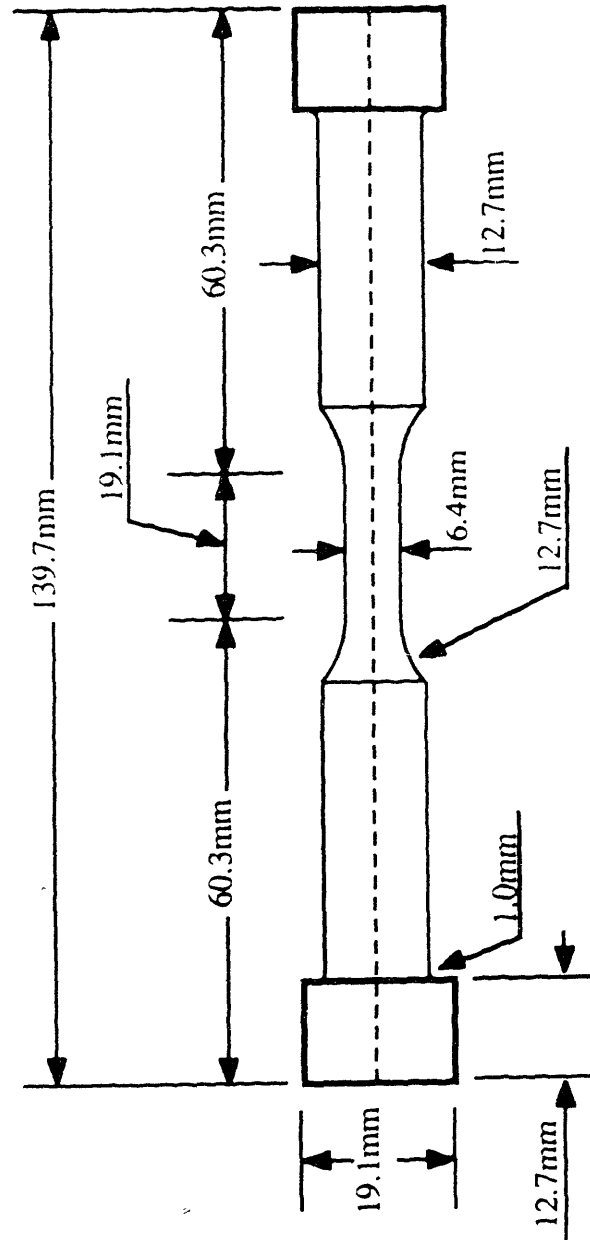


Figure 3.4 Specimen geometry used in this investigation; cylindrical gage section.

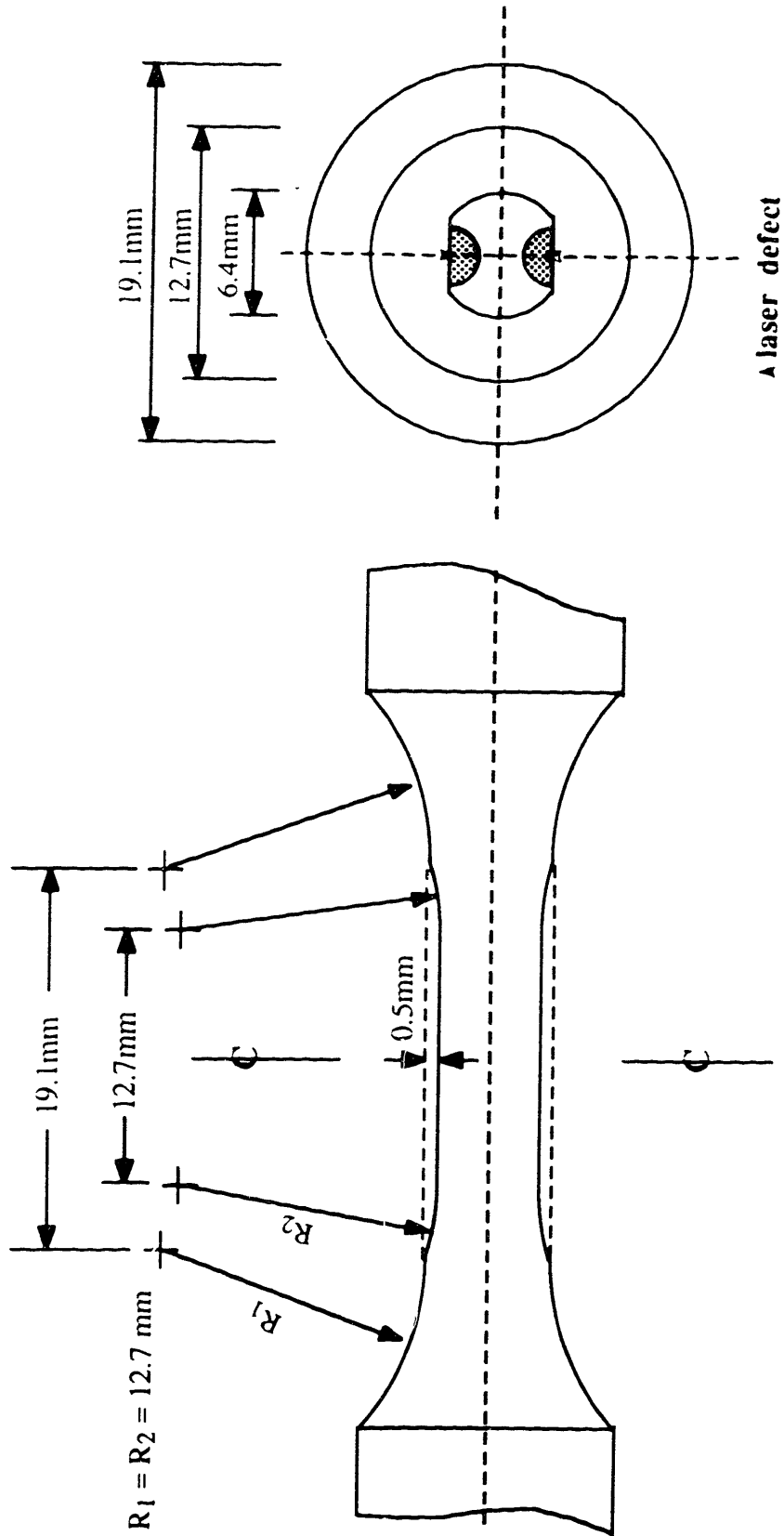


Figure 3.5 Modification to cylindrical gage section of specimen shown in Figure 3.4.

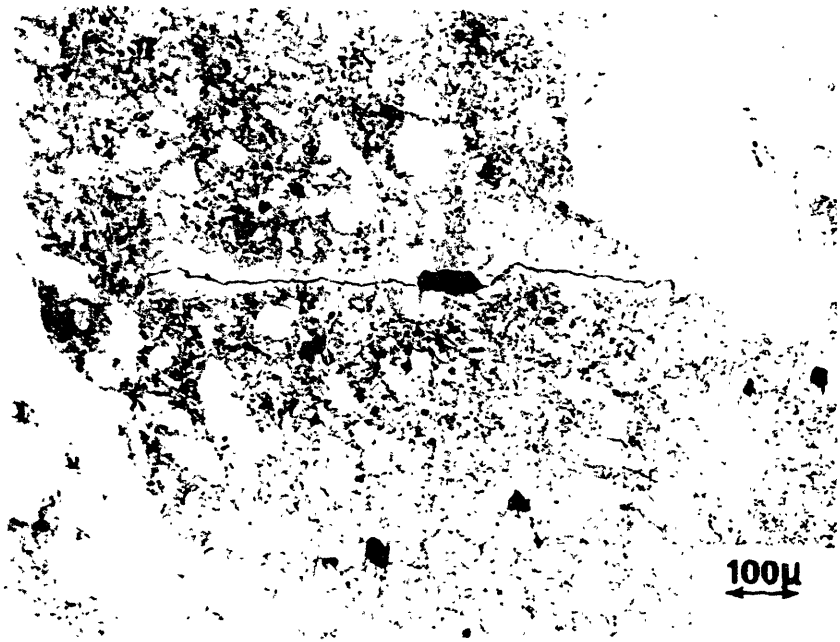


Figure 3.6 Typical laser defects.

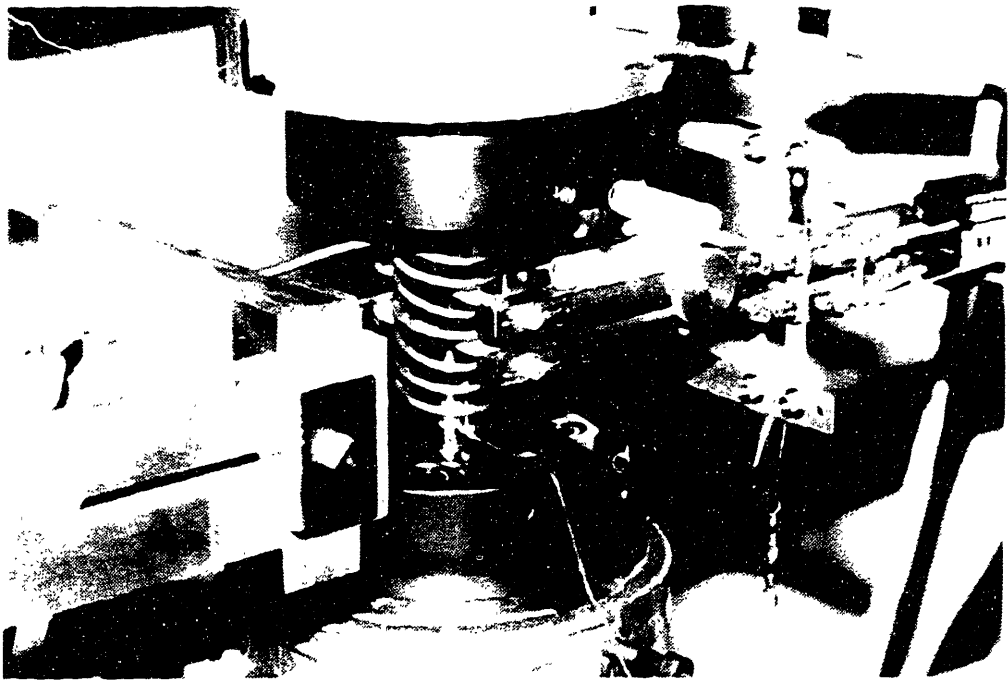
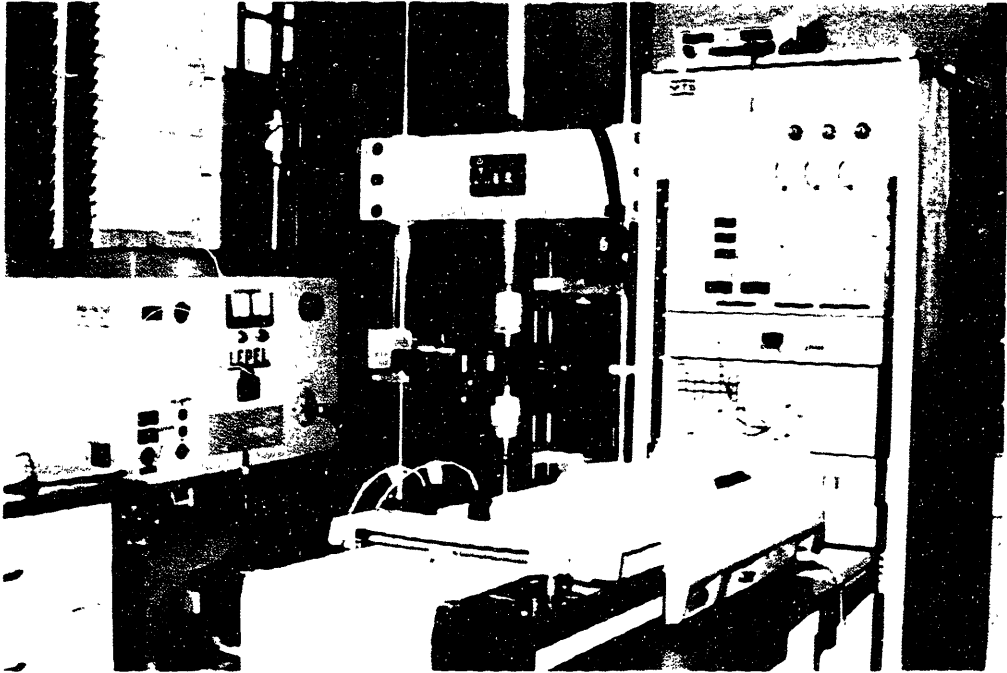


Figure 3.7 High temperature testing system.

### 3.6 Data Analysis

The raw data taken from each fatigue experiment was surface crack length,  $2c$ , versus cycle number,  $N$ . The desired presentation of the data is crack depth,  $a$ , versus  $N$  and crack growth rate,  $da/dN$ , versus an appropriate fracture mechanics parameter. This requires a determination of crack size and shape.

The shape of the cracks at the termination of high temperature testing was evident on fracture surfaces as a result of heat tinting. Figures 4.38, 4.40 and 4.43 show typical fracture surfaces with crack front profiles readily distinguished by the presence of oxidation. Cracks of different sizes were present in the same specimen due to the variability in the number of cycles required for initiation from the laser defects. In some cases, one or more cracks may have arrested. Careful measurements of surface crack length and crack depth were made. A  $c/a$  ratio of  $\sim 1$  was the predominant value over the full range of crack sizes considered and for the variety of testing conditions employed. Any variation from  $c/a = 1$  could not be related to testing conditions. Hence, all subsequent data reduction will be performed by first taking the crack depth,  $a$ , to be equal to half the surface length  $2c$ .

Each fatigue experiment yielded from 7 to  $\sim 30$  data points. These  $N_i, a_i$  pairs were tabulated and first plotted as  $a_i$  vs.  $N_i$ . The data was edited for potential measurement errors. If a data point appeared to fall erroneously out of place, the replica was measured again. Values of  $a$  were compared to artificial defect size and shape on the fracture surface. Data pairs were considered to be valid only after the crack assumed a semicircular shape encompassing the defect. For this reason some of the first  $N_i, a_i$  pairs may have been rejected.

### Computation of Crack Growth Rates

The determination of  $da/dN$  from a versus  $N$  was accomplished using two well established data processing techniques: the secant method and the incremental polynomial technique.

In some  $a$  versus  $N$  curves, it was obvious that considerable variability existed in crack growth rate. This was usually attributed to the interaction of short cracks with variable resistance in the microstructure. The secant or point-to-point technique was employed when depicting this variability. The secant method is simply a calculation of the slope of a straight line which connects two adjacent data points on the  $a$  versus  $N$  curve. The crack growth rate may be calculate as:

$$\frac{da}{dN} = \frac{a_{i+1} - a_i}{N_{i+1} - N_i} \quad (3.1)$$

The stress intensity factor range associated with this crack growth rate was calculated using the average crack length where  $a_m = (a_{i+1} + a_i)/2$ . The principal disadvantage of the secant method is that the variability calculated for  $da/dN$  often obscures trends in the data.

The bulk of the crack growth rate data was processed using the 7 point-incremental polynomial technique. This technique "smooths out" the crack growth rate curve and minimizes the influence of measurement error on  $da/dN$  by fitting the  $a$  versus  $N$  curve locally in increments. This technique involves fitting a parabola to successive 7-point subsets of the data using a "least squares" procedure. To determine  $da/dN$  at point  $i$ , the equation of a parabola was determined for data points  $N_{i-3}, a_{i-3}$  through  $N_{i+3}, a_{i+3}$ . The slope at point  $i$  is simply the first derivative of the equation of the parabola. In view of the limited number of data points for each experiment, the slope at the first and last three points was determined using the first and last fitted parabolas [3.9].

### Stress Intensity Factor Calculations

The essence of the "short crack" problem in fatigue is the inability of the stress intensity factor,  $K$ , based on linear elastic fracture mechanics, to consolidate crack growth rate data at very small crack sizes in some materials. The anomalous behavior of small cracks is generally characterized in terms of  $da/dN$  versus  $\Delta K$ . The breakdown of LEFM for short cracks is attributed to a lack of similitude between short and long cracks. In some cases, the apparent deviation from long crack behavior may be attributed to an inappropriate determination of the effective stress intensity factor range,  $\Delta K_{eff}$ . This may be due to an inaccurate characterization of crack geometry, failure to account for crack closure, or an incorrect assessment of the stress intensity factor.

The stress intensity factor solution employed in this investigation was that for a semi-elliptical surface crack. Irwin [3.10] developed an expression for the Mode I stress intensity factor around an elliptical crack embedded in an infinite elastic solid subjected to uniform tension. The most general formulation is given by:

$$K = \sigma \frac{\sqrt{\pi a}}{\Phi} \left( \sin^2 \theta + \frac{a^2}{c^2} \cos^2 \theta \right)^{1/4} \quad (3.2)$$

where  $\Phi$  is an elliptical integral of the second kind and is given by

$$\Phi = \int_0^{\pi/2} \left[ 1 - \frac{c^2 - a^2}{a^2} \sin^2 \theta \right]^{1/2} d\theta \quad (3.3)$$

The geometric variables  $a$ ,  $c$  and  $\theta$  are defined in Figure 3.8. As discussed in a previous section, the  $c/a$  ratio was found to be approximately one and constant over the full range of

crack sizes considered. By substituting  $c = a$ , the above expression for stress intensity simplifies to

$$K = \frac{2}{\pi} \sigma \sqrt{\pi a} = 0.637 \sigma \sqrt{\pi a} \quad (3.4)$$

This expression was first developed by Sneddon [3.11] and is valid for all values of  $\theta$  when  $c = a$ , that is for a circular internal crack of radius  $a$  (penny-shaped crack) embedded in an infinite solid.

The stress intensity factor for surface cracks in finite elastic bodies (laboratory specimens) may be expressed in terms of a boundary correction factor modification to the stress intensity factor for cracks in infinite bodies. The most general formulation is given by

$$K = \sigma \frac{\sqrt{\pi a}}{\Phi} \left( \sin^2 \theta + \frac{a^2}{c^2} \cos^2 \theta \right)^{1/4} F\left(\frac{a}{t}, \frac{a}{c}, \frac{c}{W}, \theta\right) \quad (3.5)$$

where  $F$  is the boundary correction factor. The geometric variables are defined in Figure 3.8.

Newman [3.12] has reviewed a significant number of boundary correction factors for surface cracks. For the case of the semicircular surface crack ( $a/c = 1$ ) and  $a/t < 0.2$ , the maximum value of  $F$  occurs at or near the intersection of the crack with the specimen surface ( $\theta = 0$ ) where  $F \approx 1.15$ . Hence, the maximum value of the Mode I stress intensity factor for small semicircular surface cracks may be approximated by

$$K = 1.15 \frac{2\sigma}{\pi} \sqrt{\pi a} = 0.73 \sigma \sqrt{\pi a} \quad (3.6)$$

The specimen geometry employed in the Waspaloy tests, shown in Figure 3.4, has a cylindrical gage section. Nisitani and Chen [3.13] have calculated stress intensity factors for semi-elliptical surface cracks in cylindrical rods by modifying the solution for elliptical

surface cracks in finite plates, Eq. 3.6. They have calculated this correction factor to be equal one when  $c/a = 1$  and  $(a / \text{specimen radius})$  is less than 0.2 which is approximately true for all crack lengths considered in this investigation.

Raju and Newman [3.14] calculated stress intensity factors for semi-elliptical flaws in cylindrical rods using a three dimensional finite element method. The results were presented in terms of  $K/(\sigma\sqrt{\pi a/Q})$  versus  $\theta$ . When  $c/a = 1$ ,  $Q = (\pi/2)^2$  and  $a/D \leq 0.2$ , therefore,  $K/(\sigma\sqrt{\pi a/Q}) = 1.15$  which is the boundary correction factor for small surface cracks in the cylindrical specimen. Note that this is the same value found for small semicircular surface cracks in rectangular cross sections, Eq. 3.6.

The stress intensity factor range was calculated using only the positive portion of the loading cycle. The tests were not instrumented for the measurement of crack opening-closure stresses, therefore, the stress range,  $\Delta\sigma$ , was taken as  $\sigma_{\max}$  when  $\sigma_{\min} \leq 0$  and as  $(\sigma_{\max} - \sigma_{\min})$  when  $\sigma_{\min} > 0$ . Cracks grew nominally perpendicular to the applied stress. Crack lengths were taken as their projected lengths on a plane perpendicular to the loading axis. Hence, for the specimen and crack geometries considered in this investigation, the nominal stress intensity factor range was calculated according to

$$\Delta K = 0.73 \Delta\sigma_{\text{pos}} \sqrt{\pi a} \quad (3.7)$$

Since identical specimen and crack geometries were considered for the elastic-plastic tests, the same flaw shape and boundary correction factor ( $Y = 0.73$ ) was used to calculate elastic-plastic fracture mechanics parameters.

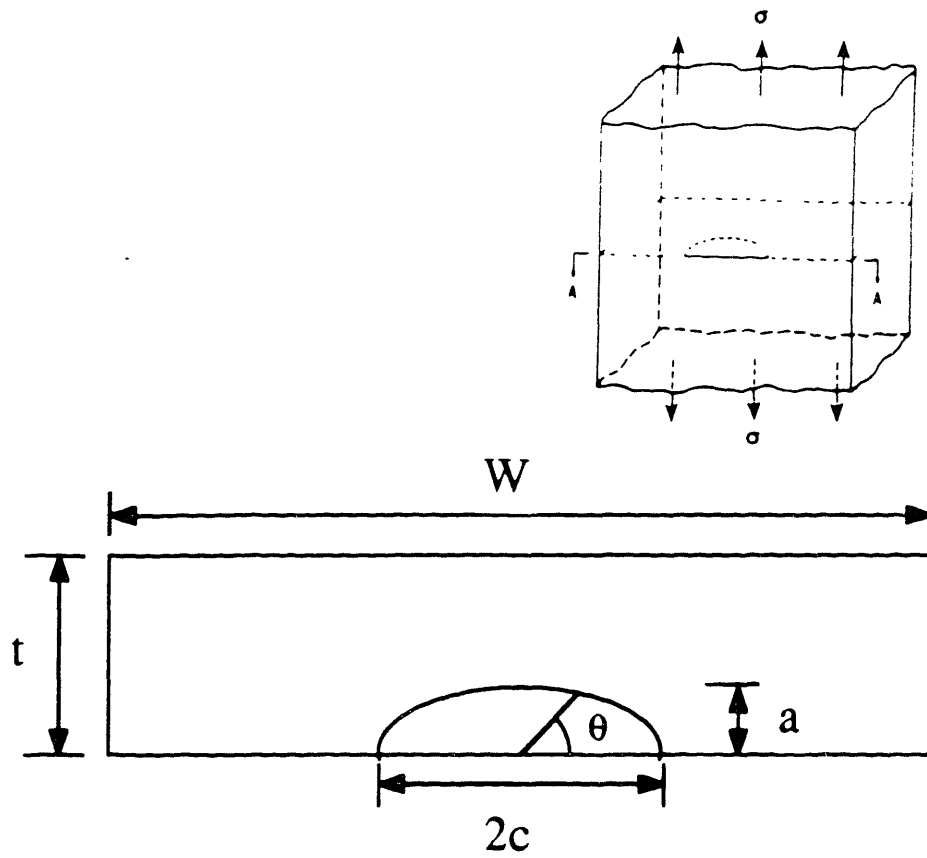


Figure 3.8 Semi-elliptical surface crack in a finite elastic body.

## 4. Results and Discussion

The fatigue behavior of small cracks was investigated in Waspaloy, Inconel 718 and powder metallurgy Gatorized® IN100 at elevated temperatures. Small cracks were initiated at laser defects and crack lengths measured by surface replication. Surface crack length,  $2c$ , was converted to crack depth,  $a$ , since crack front profiles were determined to be nearly semicircular ( $c/a = 1$ ) for all values of crack depth. Cracks propagated in a self-similar fashion after assuming a semicircular crack front around the initiation defect. Crack growth behavior was generally measured over the range  $100 \mu\text{m} < a < 1 \text{ mm}$ . Data is presented here as crack depth versus cycle number and crack growth rate versus a parameter expressing the crack driving force. Crack growth rates were determined using the seven point incremental polynomial method unless otherwise specified.

### 4.1 The Fatigue Behavior of Small Cracks in Waspaloy at 427C

The fatigue behavior of small cracks was investigated in Waspaloy at 427C (800F) under nominally elastic conditions. All tests were performed in load control on specimens with cylindrical gage sections (Figure 3.4). The principal test variables were maximum stress and R-ratio. Test conditions for Waspaloy are shown in Table 4.1. This alloy possessed a duplex grain size with mean grain sizes of  $200 \mu\text{m}$  and  $7 \mu\text{m}$ .

#### Effect of Maximum Stress

The effect of maximum stress on small crack growth behavior at  $R=-1$  is shown in Figures 4.1 and 4.2. Values of maximum stress employed were 504 MPa ( $0.60\sigma_{ys}$ ), 621 MPa ( $0.74\sigma_{ys}$ ) and 754 MPa ( $0.90\sigma_{ys}$ ). The values in parenthesis represent the fraction of the 0.2% offset yield strength (841 MPa) for Waspaloy at this temperature.

Crack depth versus cycle number shown in Figure 4.1 exhibits the expected behavior. The variation in crack growth rates noted at a maximum stress of 504 MPa may be attributed

to microstructural interactions. The influence of microstructure on crack growth rates was more prominent at lower stress ranges. Crack growth rates were calculated as the slope of the fitted curve at various crack depths as discussed in a previous section.

The stress intensity factor range was calculated as

$$\Delta K = 0.73 \Delta\sigma_{\text{pos}} \sqrt{\pi a} \quad (4.1)$$

where 0.73 is the flaw shape and boundary correction factor for a semicircular surface crack,  $\Delta\sigma_{\text{pos}}$  is the positive stress range and  $a$  is the crack depth.

Crack growth rates versus  $\Delta K$  for different stress ranges at  $R=-1$  are shown in Figure 4.2. The solid line represents crack growth behavior reported by Larsen et al. [4.1] on longer cracks ( $a > 1$  mm) at lower stress amplitudes in through thickness center crack specimens. These long crack data represent an upper bound to crack growth rates for small cracks ( $100 \mu\text{m} < a < 1$  mm) measured in this investigation. This result is likely due to the lack of metallurgical similitude between these small cracks tests and conventional long crack tests. In long crack tests, the resistance to crack extension offered by grain boundaries and variously oriented grains at the crack tip is averaged over a long crack front and many grains. An average crack growth rate results. For the small cracks considered in this investigation, the crack front encounters fewer grains and grain boundaries. The resistance to crack extension offered by unfavorably oriented grains will dominate and lead to lower crack growth rates. Also, since both fracture surfaces exhibit similar crystallographic features, out-of-plane deflections cause a more significant decrease in average Mode I conditions at the crack tip for small cracks and further reduce crack growth rates. The upper bound of crack growth rates may be expressed in terms of  $\Delta K$  by the Paris-Erdogan relationship:

$$\frac{da}{dN} = 3.50 \times 10^{-11} (\Delta K)^{2.73} \quad (4.2)$$

where  $da/dN$  is in m/cycle and  $\Delta K$  is in  $\text{MPa}\sqrt{\text{m}}$ .

The ability of  $\Delta K$  to consolidate crack growth rates within a factor of two for a range of net section stresses approaching 90% of the yield stress supports a contention that  $\Delta K$  expresses crack tip similitude under these conditions for  $R=-1$ . This is a particularly interesting outcome when one considers that the stress intensity factor best defines the near crack tip elastic stress field for small  $\sigma^\infty/\sigma_{ys}$  ratios. The tendency for small crack-high stress data to fall slightly below long crack data was also observed by Larsen et al. [4.1] for Waspaloy at 649C where net section stresses exceeded 80% of the monotonic yield stress.

#### Applicability of LEFM

Although  $\Delta K$  correlates the fatigue crack growth rates for small cracks and long cracks as shown in Figure 4.2, the validity of employing LEFM for such small cracks ( $100 \mu\text{m} < a < 1 \text{ mm}$ ) and high stresses ( $\sigma_{\text{max}} \sim 0.90\sigma_{ys}$ ) should be evaluated more explicitly. The basic assumptions of linear elastic fracture mechanics are: 1) the material behaves as a linear elastic isotropic continuum, 2) the crack tip plastic zone size is small with respect to all other dimensions (small scale yielding), and 3) the crack length is small compared to component or specimen dimensions.

The requirement for linear elastic behavior is met on a global scale since the macroscopic yield stress is not exceeded in any of these tests. On a microscopic scale, i.e. within a single grain, elastic-plastic behavior may be expected since micro-yielding can occur at  $\sim 1/3$  of the macroscopic yield stress.

Waspaloy used in this investigation may be considered an isotropic continuum when the size scale considered exceeds the grain size. When the size scale is on the order of the grain size, the continuum response is anisotropic. Since this Waspaloy has a duplex microstructure with a small average grain size of  $7 \mu\text{m}$  and a few grains as large as  $\sim 300$

$\mu\text{m}$ , the requirement for isotropic behavior may be violated locally as small cracks and their crack tip zones encounter large grains.

The second basic assumption for valid application of LEFM requires that the crack tip plastic zone size be small with respect to all other dimensions. Lankford et al. [4.2] have reviewed both theoretical calculations and experimental measurements of fatigue crack tip plastic zone sizes. The solution to this problem depends on the simplifying assumptions made in the calculation. The simplest estimate, proposed by Rice [4.3] and confirmed by Broek [4.4], is based on the elastic solution of the stresses at the tip of a sharp crack accounting for load redistribution caused by crack tip yielding. Accordingly, the monotonic plastic zone size,  $r_{pm}$ , under plane stress conditions may be estimated as

$$r_{pm} = \frac{1}{\pi} \left( \frac{K_I}{\sigma_{ys}} \right)^2 = 0.32 \left( \frac{K_I}{\sigma_{ys}} \right)^2 \quad (4.3)$$

substituting the stress intensity factor for a semicircular surface crack

$$r_{pm} = 0.53 \left( \frac{\sigma_{max}}{\sigma_{ys}} \right)^2 a \quad (4.4)$$

Since  $\sigma_{max}$  ranged from 60% to 90% of  $\sigma_{ys}$ ,  $r_{pm}$  ranged from 0.19a to 0.43a. In view of this estimate, can  $r_{pm} = 0.19a$  to  $0.43a$  be considered small with respect to crack length? According to Smith [4.5], the answer is no, because he argued that  $r_{pm}$  must be less than  $0.02a$  if the near crack tip elastic field is to dominate the crack tip plastic response.

Over the range of stress and crack length considered here,  $r_{pm}$  ranges from  $19 \mu\text{m}$  to  $430 \mu\text{m}$  which is reasonably small with respect to the minimum specimen dimensions of  $6.4 \text{ mm}$ .

Now we shall consider the above requirements for the validity of LEFM in terms of the reversed crack tip plastic zone size,  $r_{pc}$ . Rice [4.3] estimated  $r_{pc}$  by using a reverse flow

stress of  $2\sigma_{ys}$ . Therefore,  $r_{pc}$  is 1/4 of the monotonic plastic zone size under plane stress conditions. According to Eq. 4.3:

$$r_{pc} = \frac{1}{\pi} \left( \frac{\Delta K}{2\sigma_{ys}} \right)^2 = 0.08 \left( \frac{\Delta K}{\sigma_{ys}} \right)^2 \quad (4.5)$$

Lankford et al. [4.2] found that these theoretical estimates of monotonic and reversed plastic zone sizes significantly exceed the experimental values obtained by different measurement techniques. It was generally found that  $r_{pc} \approx r_{pm}/10$ . Therefore, in terms of  $r_{pc}$ , the requirement for small scale yielding places less stringent limitations on crack length. For the Waspaloy experiments considered here, small scale yielding may be approximately satisfied, since  $r_{pc} = 0.019a$  to  $0.043a$  using the experimental findings on  $r_{pc}$ .

It has been further reasoned that for a global application of fracture mechanics, the near crack tip elastic field dimension ( $a/10$ ) should be at least the size of the largest structural feature, that is, the grain size. Therefore, the crack length must be ten times the grain size if  $K$  is to accurately represent the elastic stresses in the crack tip field. In the case of these Waspaloy tests, crack length varied from 100  $\mu\text{m}$  to 1000  $\mu\text{m}$  and grain size varied from a few  $\mu\text{m}$ 's to  $\sim 200 \mu\text{m}$ . In most cases, crack depth,  $a$ , and crack front length,  $\pi a$ , were generally greater than  $10 \times$  grain size.

The validity of using  $K$  to define the intensification of stress in the near crack tip field when the remote stress approaches 90% of the yield stress in a material with a low hardening rate ( $n \approx 0.15$  for Waspaloy) is also a matter for concern. The expression:

$$\sigma_{ij} = \frac{K}{\sqrt{2\pi r}} f(\theta) \quad (4.6)$$

is only a first term approximation to a series solution for the near crack tip elastic stress field which ignores higher order terms. At  $\theta=0$  the stress perpendicular to the crack plane becomes:

$$\sigma_y = \frac{\sigma^\infty \sqrt{\pi a}}{\sqrt{2\pi r}} = \sigma^\infty \sqrt{\frac{a}{2r}} \quad (4.7)$$

The local stress falls to  $\sigma^\infty$  at  $r \geq a/2$ , i.e., at  $r \geq 5$  times the near crack tip elastic field dimension of  $a/10$ . This estimate ignores stress redistribution. Therefore,  $K$  does define a significant extent of stress intensification in the near-crack-tip region.

Perhaps one explanation for the good correlation of crack growth rates versus  $\Delta K$  for these high  $\sigma^\infty/\sigma_{ys}$  values lies in the constraint which may begin to develop for elements ahead of the crack front even for cracks as small as those investigated here ( $100 \mu\text{m} < a < 1 \text{ mm}$ ). Triaxial constraint can result in a significant hydrostatic stress directly ahead of the crack tip. For a nonhardening material satisfying the von Mises yield criterion, this can result in stresses which are three times the uniaxial yield stress ahead of the crack front [4.2]. A strain hardening material results in even higher stresses. Full plane strain conditions would not be expected in such small specimens, however, the constraint resulting from stress free material above and below the crack certainly results in a lower ratio of  $\sigma^\infty/\sigma_{ys(\text{effective})}$ .

### Similitude Requirements

If we compare the crack tip conditions between a long fatigue crack propagating at a low stress range and a small fatigue crack ( $100 \mu\text{m} < a < 1 \text{ mm}$ ) propagating at a high stress range in Waspaloy at 427C, there is a lack of mechanical similitude as discussed above in terms of having:

- 1) a small monotonic plastic zone size with respect to all length dimensions.
- 2) a small monotonic plastic zone size with respect to the distance over which the first term of the stress field solution is dominant.
- 3) an equivalent constraint; highly stressed specimens exhibit greater surface yielding since the yield criterion is exceeded to a greater depth and, therefore, encompassing a greater fraction of the crack front length for small cracks.

Mechanical similitude is satisfied in terms of equivalent  $K_{\max}$  and  $\Delta K$ . Experimental measurements of crack closure were not made. Metallurgical similitude is approximately satisfied in these tests since crack depth is generally greater than 10x grain size.

Although conditions of perfect similitude may not exist between long and small cracks for Waspaloy at 427C, the correlation of crack growth in terms of  $\Delta K$  as shown in Figure 4.2 suggests that similitude is sufficiently satisfied.

The good correlation of crack growth rates observed for small crack-high stress data at different stress ranges suggests a high degree of crack tip similitude between these tests.

#### Crack Growth Rate versus Plastic Zone Size

The crack extension which occurs in one cycle may be expressed by the Paris-Erdogan relationship

$$\Delta a = C \Delta K^m \quad (4.8)$$

Since fatigue crack extension is generally agreed to be related to the reversed crack tip plastic strain range, it is interesting to compare  $\Delta a$  to  $r_{pc}$ . Taking the conservative estimate of Rice and assuming plane stress, we have:

$$\frac{\Delta a}{r_{pc}} = 4\pi C (\sigma_{ys})^2 \Delta K^{m-2} \quad (4.9)$$

For the Waspaloy data generated in this investigation we can substitute values from Eq. 4.2 into Eq. 4.9 which becomes:

$$\frac{\Delta a}{r_{pc}} \approx 3 \times 10^{-4} \Delta K^{0.73} \quad (4.10)$$

Since  $\Delta K$  ranged from 10  $\text{MPa}\sqrt{\text{m}}$  to 40  $\text{MPa}\sqrt{\text{m}}$  in these tests,  $\Delta a/r_{pc}$  ranged from  $\sim 2 \times 10^{-3}$  to  $\sim 4 \times 10^{-3}$ . As can be seen, crack advance in a single cycle remained less than 1%

of the reversed plastic zone size, while  $da/dN$  varied over two orders of magnitude. Even using the smaller experimental determinations for  $r_{pc}$ ,  $\Delta a$  per cycle remains less than  $\sim 2.0\%$  of  $r_{pc}$  for all conditions.

At this juncture, it seems that crack growth rate may be more strongly dependent on the maximum crack tip strain range than the reversed plastic zone size, although  $\Delta\epsilon_p^{tip}$  and  $r_{pc}$  are most likely related. This issue will be addressed in a later section.

### Effect of R-ratio

The effect of R-ratio on small crack growth rates is shown in Figure 4.3 and 4.4. Values of stress ratio employed were:  $R=-1$ ,  $R=0$ ,  $R=0.3$  and  $R=0.5$ . The maximum stress was nominally 766 MPa in all tests except the  $R=0.5$  test where the maximum stress was necessarily increased to 903 MPa.

Crack growth rates versus  $\Delta K$  are shown in Figure 4.4 for these four tests with the expected results. The tendency for  $da/dN$  ( $R=0.3$ ) to decrease and then increase can be attributed to a slight perturbation in crack extension as seen in Figure 4.3 and is likely due to interactions with large grains and/or grain boundaries in the Waspaloy microstructure. The ordering of crack growth rates with respect to R-ratio is illustrated in Figure 4.5 where relative crack growth rates are compared at  $\Delta K_{app} = 20 \text{ MPa}\sqrt{\text{m}}$ . For positive R-ratios, the ordering of crack growth rates from high to low corresponds to R-values of 0.5, 0.3 and 0, respectively. This trend is also observed for long cracks. Crack growth rates at  $R=-1$  are nearly equivalent to that at  $R=0.5$ . Long crack data is generally not available at negative R-ratios since conventional compact tension specimens cannot be loaded in compression.

### Empirical Approaches to Consolidating R-ratio Data

Under nominally elastic conditions, the two mechanical variables in any fatigue loading situation are  $\sigma_{max}$  and  $\sigma_{min}$ . These are interrelated through  $R=\sigma_{min}/\sigma_{max}$  and,

correspondingly,  $R=K_{\min}/K_{\max}$ . The tendency for crack growth rates to increase with increasing R-ratio (for  $R>0$ ) has been addressed in a number of ways. The first are through empirical relationships which attempt to collapse  $da/dN$  versus  $\Delta K$  curves. Brock and Schijve [4.6], McMillan and Pelloux [4.7], and Erdogan [4.8] have concluded that the general equation relating stress and crack length to crack growth rate is of the form:

$$\frac{da}{dN} = f\left[\gamma(\sigma_{\max}\sqrt{a})^c(\Delta\sigma\sqrt{a})^b\right] \quad (4.11)$$

It is fair to state that the inclusion of  $\sigma_{\max}$  and  $\Delta\sigma$  in this crack growth expression was based on an assessment of crack growth mechanisms and therefore is not purely empirical.

Following the above approach, Walker [4.9] rewrote Equation (4.11) as

$$\frac{da}{dN} = f\left[\left(\gamma\sigma_{\max}^{1-\alpha}\Delta\sigma^\alpha\sqrt{a}\right)^\beta\right] \quad (4.12)$$

where  $1-\alpha = c/(c+b)$ ,  $\alpha = b/(c+b)$  and  $\beta = c+b$ . Since the product of the two stress terms has the dimensions of stress, an effective stress,  $\bar{\sigma}$  was defined as

$$\bar{\sigma} = \sigma_{\max}^{1-\alpha}\Delta\sigma^\alpha = \sigma_{\max}(1-R)^\alpha \quad (4.13)$$

Therefore, an effective stress intensity factor range can be defined as:

$$\overline{\Delta K} = Y\sigma_{\max}(1-R)^\alpha\sqrt{\pi a} \quad (4.14)$$

Walker consolidated crack growth rates for 2024-T3 and 7075-T6 aluminum alloys using  $\overline{\Delta K}$  for  $R=0.059$  to  $R=0.655$ . Values of  $\alpha$  used in computing  $\overline{\Delta K}$  were 0.5 for 2024-T3 aluminum and 0.425 for 7075-T6 aluminum. The possible use of  $\overline{\Delta K}$  to consolidate crack growth rates at  $R<0$  was not considered in Walker's original work. For the Waspaloy tests considered here, the Walker formulation for  $\overline{\Delta K}$  may be calculated according to

$$\overline{\Delta K} = 0.73\sigma_{\max}(1-R)^\alpha\sqrt{\pi a} = (1-R)^\alpha K_{\max} \quad (4.15)$$

When  $\alpha=0.5$ , crack growth rates versus  $\overline{\Delta K}$  can be nearly collapsed to a single line as shown in Figure 4.6. It is notable that  $R=-1$  data is also consolidated in this plot. Values of  $\alpha$  ranging from 0.4 to 0.6 were employed in Eq. 4.15 and resulted in significantly poorer consolidation of crack growth rates.

It is interesting to consider the inclusion of the two stress terms ( $\sigma_{\max}^{0.5}\Delta\sigma^{0.5}$ ) in  $\overline{\Delta K}$  to achieve the high level of correlation between crack growth rates depicted in Figure 4.6. If we employ the terms individually in calculating  $\Delta K$ , we have:  $\Delta K=K_{\max}$  when using only  $\sigma_{\max}^{1.0}$  and  $\Delta K=\Delta PK$  when using only  $\Delta\sigma^{1.0}$  ( $\Delta PK$  will be explored in a later section). Correlation of crack growth rates with  $K_{\max}$  or  $\Delta PK$  is poor for these Waspaloy tests ( $-1 < R < 0.5$ ).

Forman et al. [4.10] proposed a modification to the Paris-Erdogan equation which would account for unstable crack growth as  $K_{\max}$  approached  $K_{IC}$  by introducing the singularity  $((1-R)K_{IC} - \Delta K)$  into the denominator. The following are equivalent expressions of the Forman relationship:

$$\frac{da}{dN} = \frac{C\Delta K^m}{(1-R)K_{IC} - \Delta K} = \frac{C\Delta K^m}{(1-R)(K_{IC} - K_{\max})} = \frac{C\Delta K^{m-1}K_{\max}}{K_{IC} - K_{\max}} \quad (4.16)$$

Forman found a high level of correlation for crack growth rates in 7075-T6 and 2024-T3 aluminum alloys. In addition to predicting the theoretical asymptote at  $K_{IC}$ , the relationship correlated data at different R-ratios including  $R=-1$ .

The Forman equation was applied to Waspaloy tests at 427C.  $K_{IC}$  was estimated to be  $\sim 100 \text{ MPa}\sqrt{\text{m}}$ . Since crack growth rate cannot be correlated with a single parameter on the right hand side of the Forman equation, relative crack growth rates were calculated at  $\Delta K=20 \text{ MPa}\sqrt{\text{m}}$ . As seen in Figure 4.5, the Forman equation predicts crack growth rates for R-ratios

$\geq 0$ . At  $R=-1$ , the prediction is poor, perhaps due to the inability of equation 4.16 to account for the contribution of the negative stress excursion in effecting crack tip strain reversals.

#### Crack Closure Concepts Applied to Consolidating R-ratio Data

Elber [4.11] proposed that only a fraction of the positive loading cycle was effective in propagating cracks. He determined that a fatigue crack opens and closes at some positive value of stress ( $\sigma_{op} \approx \sigma_{cl}$ ) due to contact between crack surfaces behind the crack tip (plasticity induced closure). Elber made direct measurement of crack opening and closure in 2024-T3 aluminum alloy with stress intensity varying over the range  $13 < \Delta K < 40 \text{ MPa}\sqrt{\text{m}}$  and the stress ratio varying over the range  $-0.1 < R < 0.7$ . Crack length,  $2a$ , was greater than 30 mm in all cases.

The effective stress range was defined as:

$$\Delta\sigma_{\text{eff}} = \sigma_{\text{max}} - \sigma_{\text{op}} \quad (4.17)$$

where  $\sigma_{op}$  is the crack opening stress. The effective stress range was then defined as the fraction of the stress range for which the crack is open:

$$U = \frac{(\sigma_{\text{max}} - \sigma_{\text{op}})}{(\sigma_{\text{max}} - \sigma_{\text{min}})} \quad (4.18)$$

Consequently, the form of the crack growth rate expression becomes:

$$\frac{da}{dN} = C (\Delta K_{\text{eff}})^m = C (U \Delta K)^m \quad (4.19)$$

Elber performed constant amplitude tests to establish the relationship between  $U$  and the three variables:  $\Delta K$ ,  $a$  and  $R$ . He found only the  $R$ -ratio to be the significant variable affecting the crack opening stress. The relationship between  $U$  and  $R$  was found to be linear and expressed as:

$$U = 0.5 + 0.4R \quad (4.20)$$

for the 2024 aluminum alloy. Long crack growth rates were expressed as:

$$\frac{da}{dN} = C[(0.5 + 0.4R) \Delta K]^m \quad (4.21)$$

Other investigators have found different relationships for U such as:

$$U = 0.68 + 0.91R \quad \text{Ref. [4.12]}$$

and

$$U = 0.707 + 0.408R \quad \text{Ref. [4.13]}$$

It is apparent that there is not a single value of  $K_{Op}$  operative for all R-ratios and, therefore,  $K_{Op}=f_1(R)$  or  $U=f_2(R)$  must be determined experimentally.

For the Waspaloy tests considered here, the following question arises. Can the effect of R-ratio on crack growth rates be attributed to crack closure when  $\sigma_{Op}$  and  $\sigma_{cI}$  were not measured during testing? The possibility can be approached in a semi-empirical manner. The first approach was to attempt to find a single value of  $\sigma_{Op}$  which would consolidate the crack growth rate data of Figure 4.4 in terms of  $\Delta K_{eff}$ . When  $\sigma_{Op}$  was chosen to merge the extremes of crack growth rate curves, greater differences resulted at other R-ratios. Hence if crack closure is responsible for differences in  $da/dN(R)$  for Waspaloy at 427C, then  $\sigma_{Op}$  must be a function of R.

The second approach taken to consolidate the crack growth rate data of Figure 4.4 was to assume that the effective stress intensity was of the form proposed by Elber

$$\Delta K_{eff} = (A + BR) \Delta K \quad (4.22)$$

Using crack growth rate data for only positive R-ratios, a solution for A and B was attempted. A unique solution could not be found. The relationship was obviously nonlinear, perhaps due to the higher  $\sigma_{\max}$  in the R=0.5 tests.

### Effect of Temperature

The effect of temperature (427C versus 25C) on the crack growth rates of small cracks in Waspaloy can be seen in Figure 4.7 and 4.8 for R = -1 and R = 0, respectively. The room temperature tests were performed by Feng [4.14]. In both cases, crack growth rates were higher in the elevated temperature tests. This could be a result of a deleterious environmental interaction or a decrease in the crack closure stress experienced at 427C. The elevated temperature tests exhibited less crystallographic faceting on fracture surfaces as determined by stereographic observations. This could result in less roughness induced crack closure and, therefore, higher values of  $\Delta K_{\text{eff}}$ .

For R = -1 test results shown in Figure 4.7, crack growth rates at 427C serve as an upper bound to crack growth rates at 25C.

For R = 0 test results shown in Figure 4.8, crack growth at lower values of  $\Delta K$  (apparently subthreshold) in room temperature tests may be a result of a true "short crack" effect in these tests. Crack lengths were  $\ll 100 \mu\text{m}$  in many room temperature tests where Stage I - shear mode crack extension was often measured. There is a breakdown in mechanical and metallurgical similitude between these crystallographic cracks and the nominally Mode I cracks ( $a > 100 \mu\text{m}$ ) investigated at 427C.

**Table 4.1**  
**Test Conditions for Waspaloy**

Test#	Temp °C	R	$\sigma_{\min}$ MPa	$\sigma_{\max}$ MPa	Comments
GR1	427	-1	-504	504	2 cracks
GR4	427	-1	-621	621	3 cracks
GR2	427	-1	-754	754	3 cracks
GR3	427	0	0	766	1 crack
GR0	427	0.05	31	621	2 cracks
GR5	427	0.30	229	765	2 cracks
GR6	427	0.50	451	903	3 cracks
JF7*	25	-1	-483	483	10 cracks
JF10*	25	-1	-621	621	7 cracks
JF8*	25	-1	-758	758	10 cracks
JF9*	25	0	0	758	10 cracks

\* Room temperature tests were performed by Jun Feng.

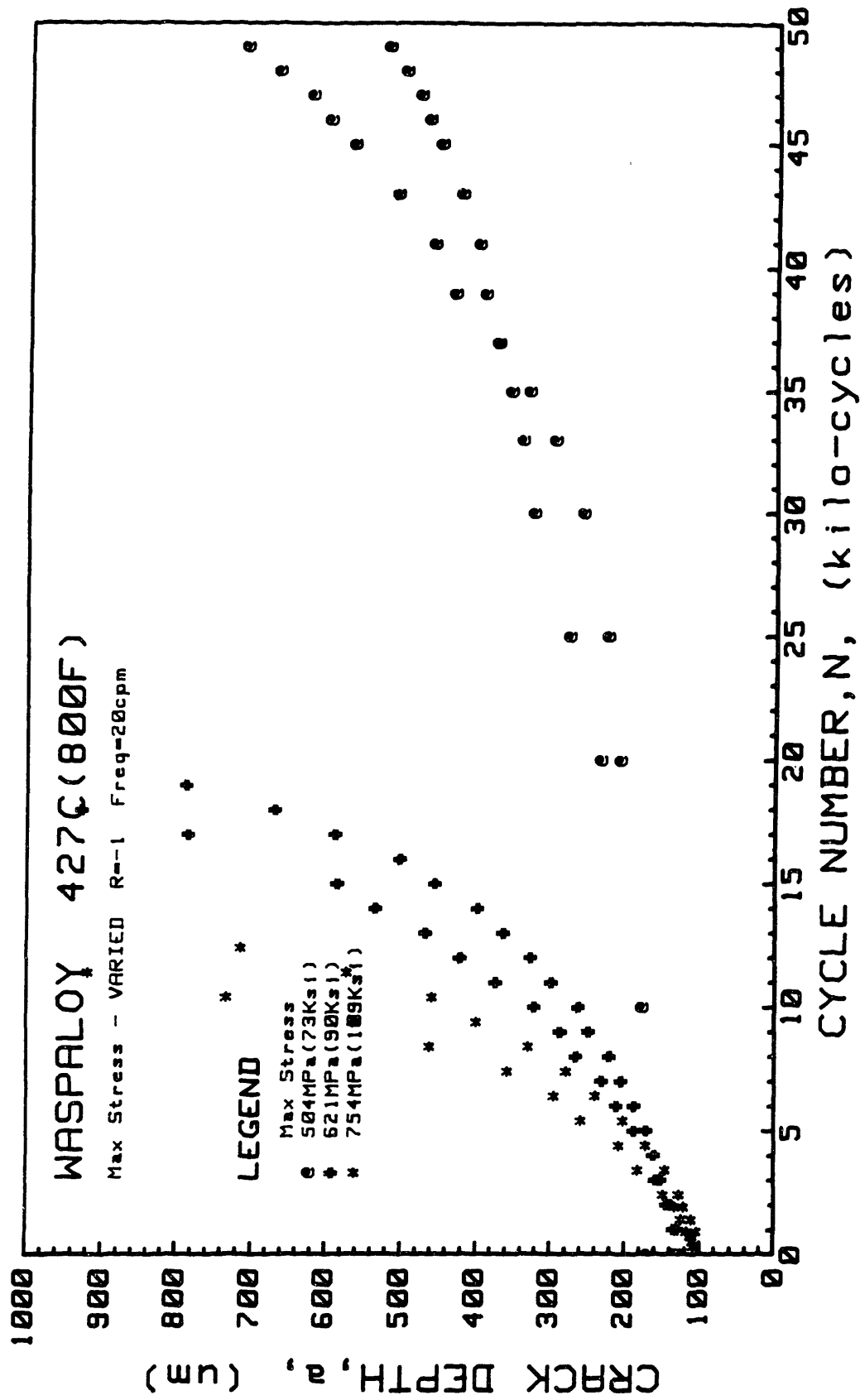


Figure 4.1 Crack depth versus cycle number for Waspaloy tested at 427C under nominally elastic fatigue conditions; stress range was varied at R=-1, Freq.=20 cpm.

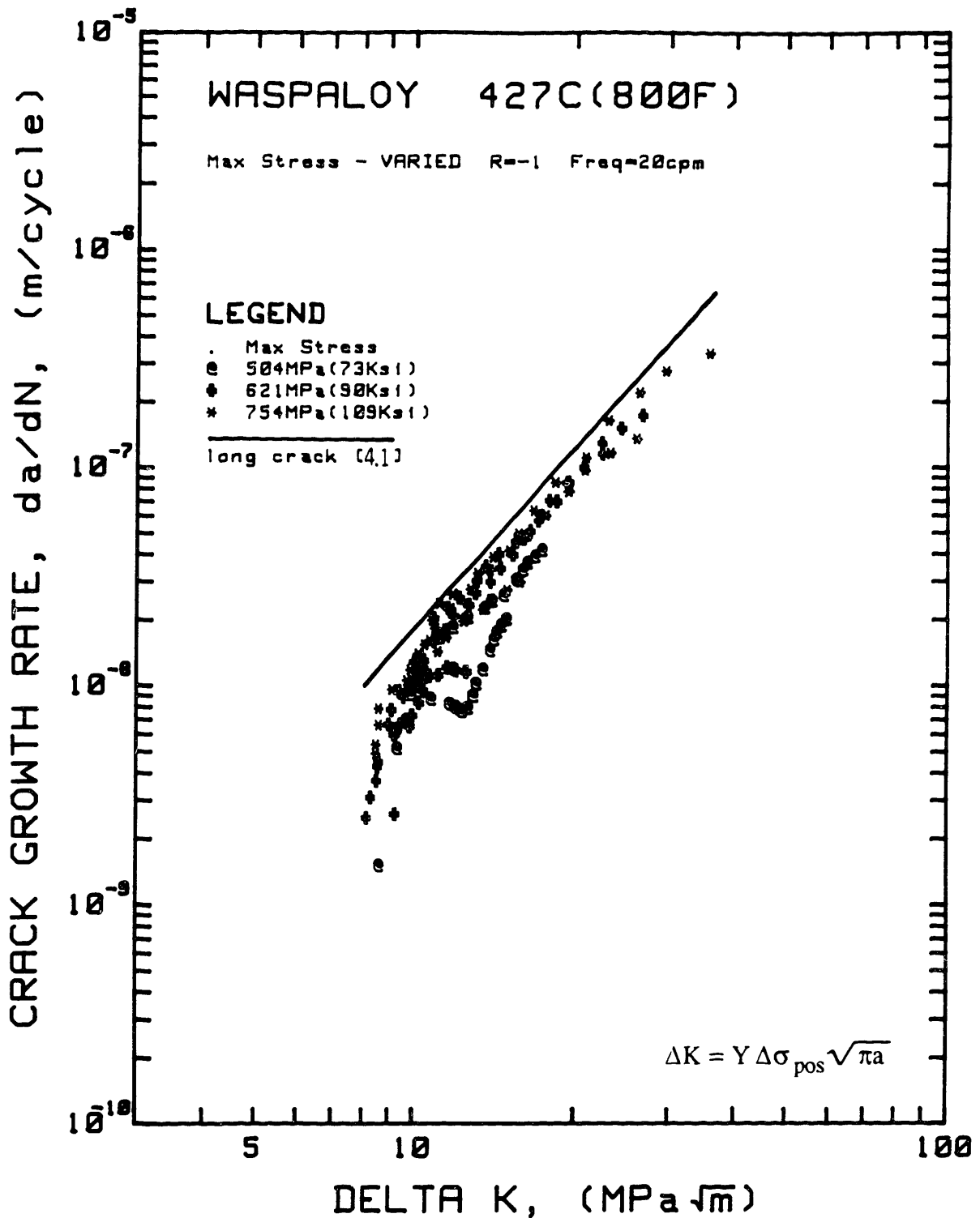


Figure 4.2 Summary of crack growth rates versus stress intensity factor range for Waspaloy tested at 427C under nominally elastic fatigue conditions; stress range was varied at R=-1, Freq.=20 cpm.

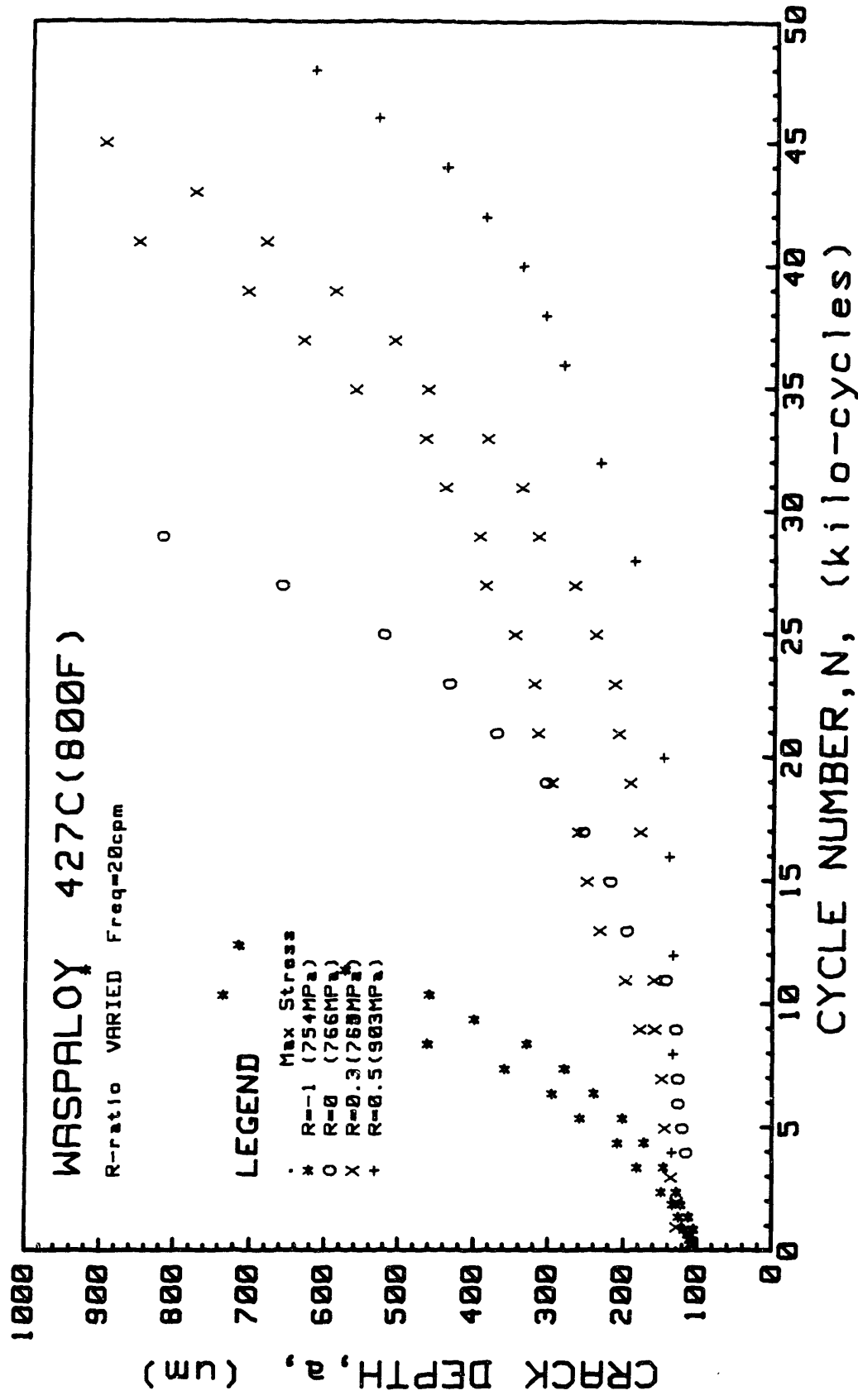


Figure 4.3 Crack depth versus cycle number for Waspalloy tested at 427C under nominally elastic fatigue conditions; R-ratio was varied, Freq.=20 cpm.

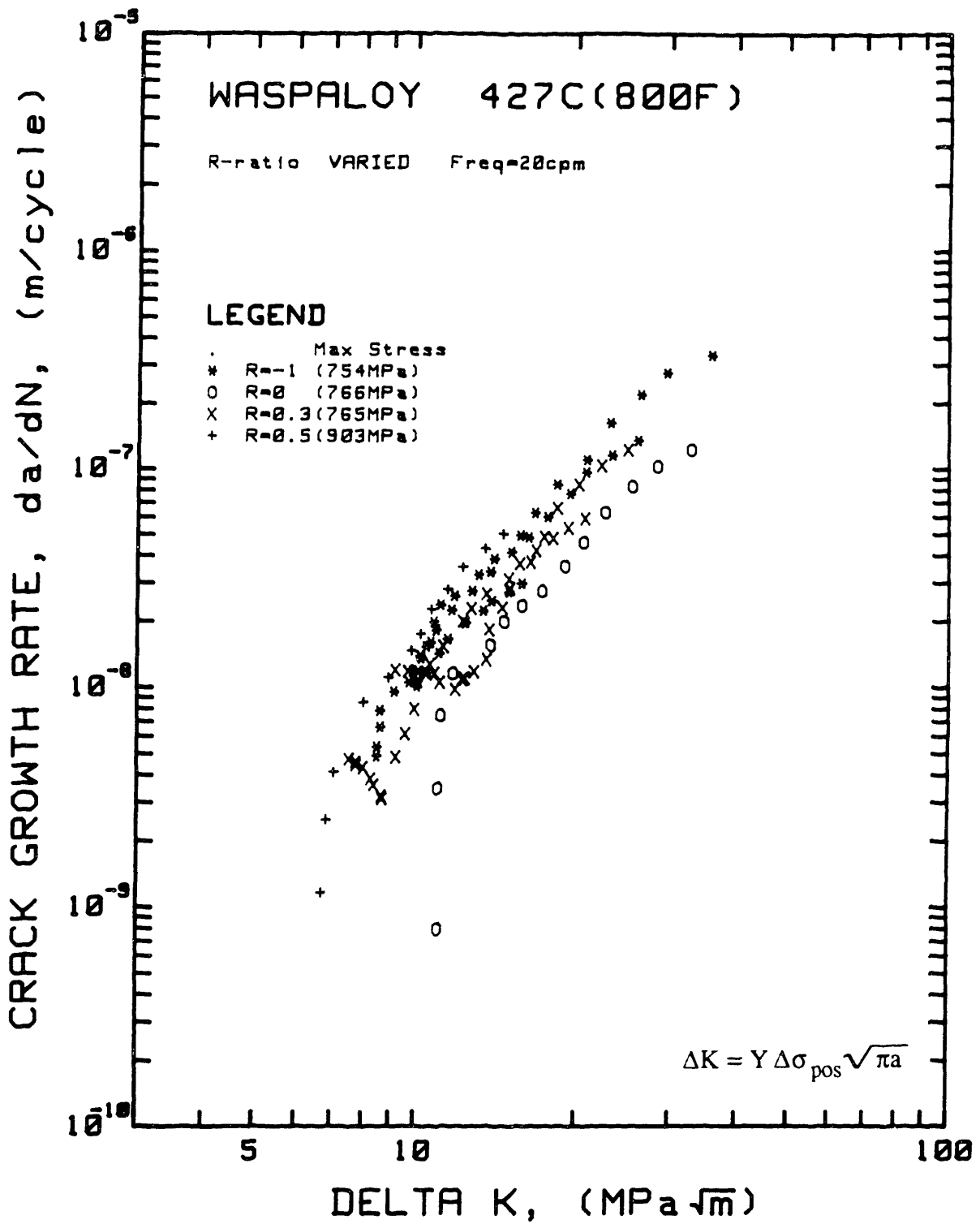


Figure 4.4 Summary of crack growth rates versus stress intensity factor range for Waspaloy tested at 427C under nominally elastic fatigue conditions; R-ratio was varied, Freq.=20 cpm.

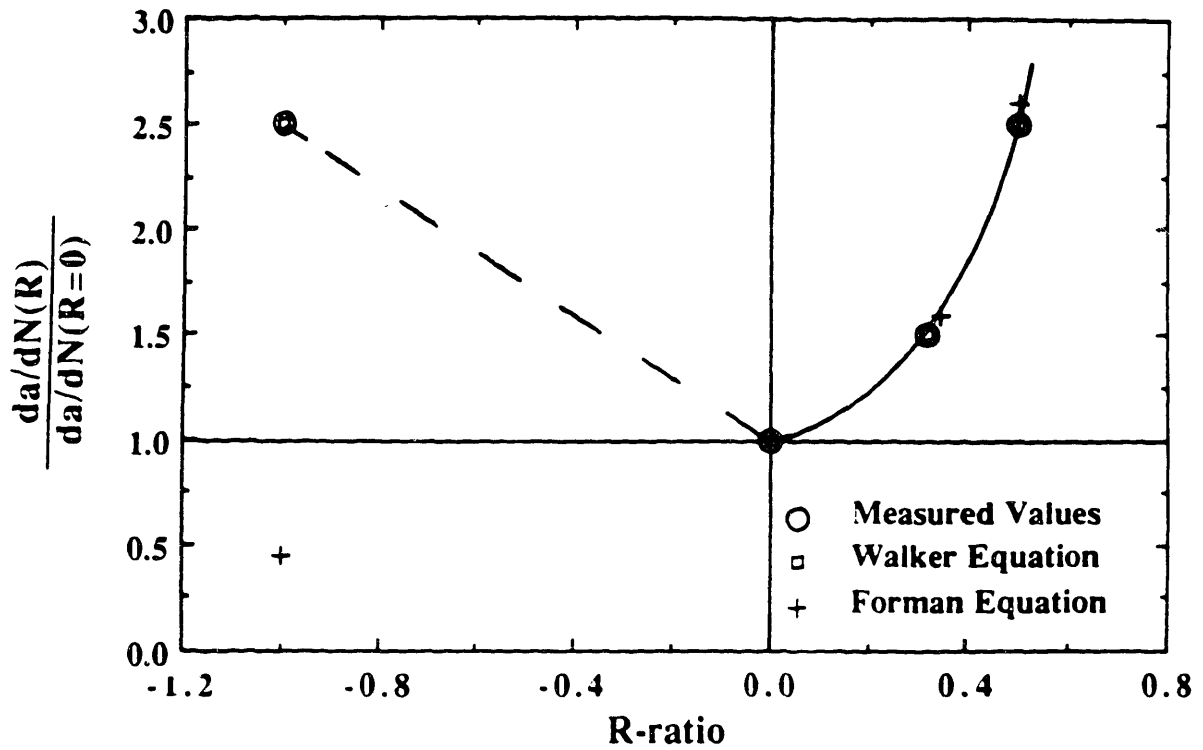


Figure 4.5 Effect of R-ratio on relative crack growth rates for Waspaloy tested at 427C under nominally elastic fatigue conditions. Crack growth rates are compared at  $\Delta K=20 \text{ MPa}\sqrt{\text{m}}$  and normalized with respect to  $da/dN(R=0)$ .

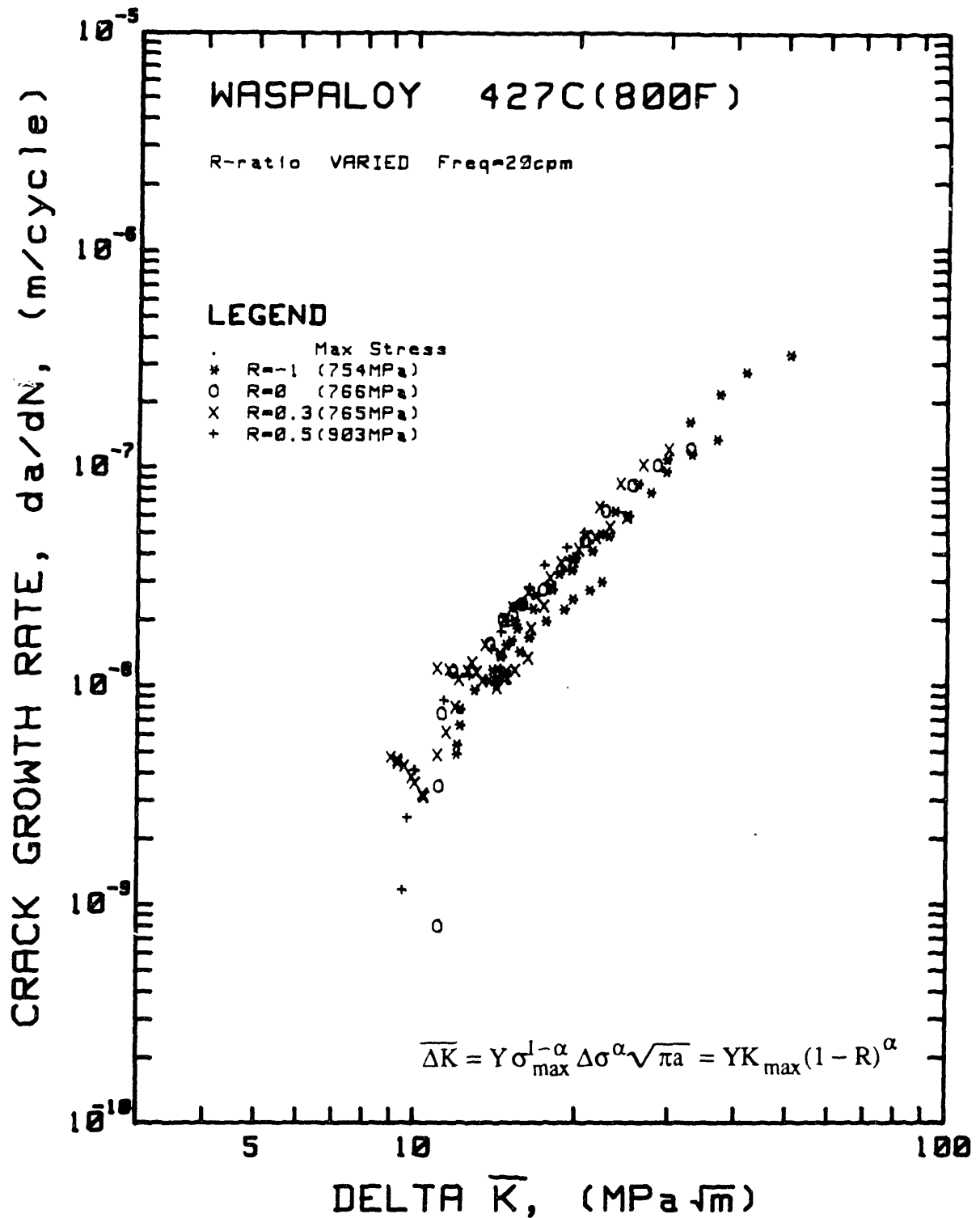


Figure 4.6 Summary of crack growth rates versus the Walker modified stress intensity factor range ( $\alpha=0.5$ ) for Waspalloy tested at 427C under nominally elastic fatigue conditions, R-ratio varied, Freq.=20 cpm.

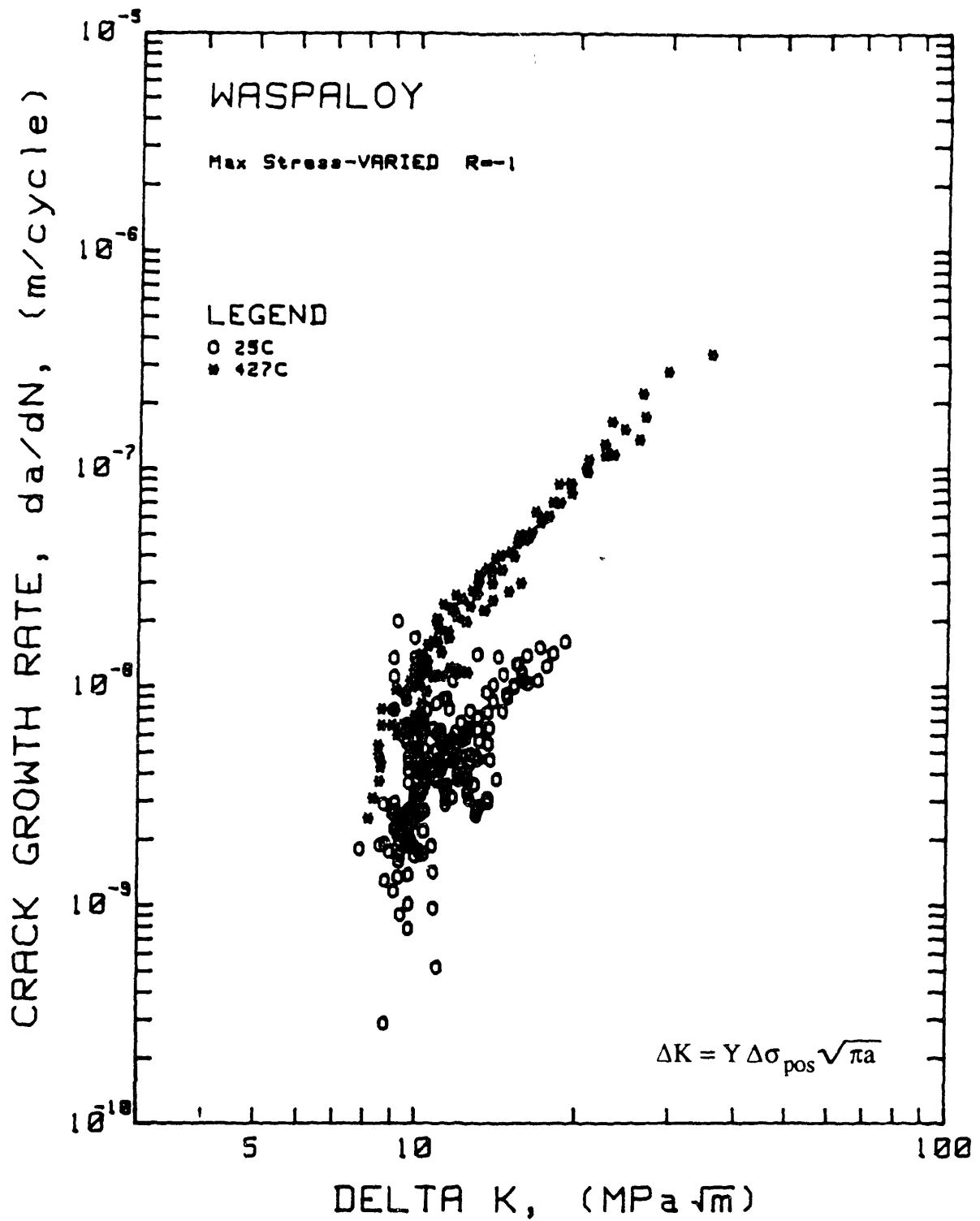


Figure 4.7 Comparison of crack growth rates versus stress intensity factor range for Waspaloy tested at 25C and 427C, R=-1.

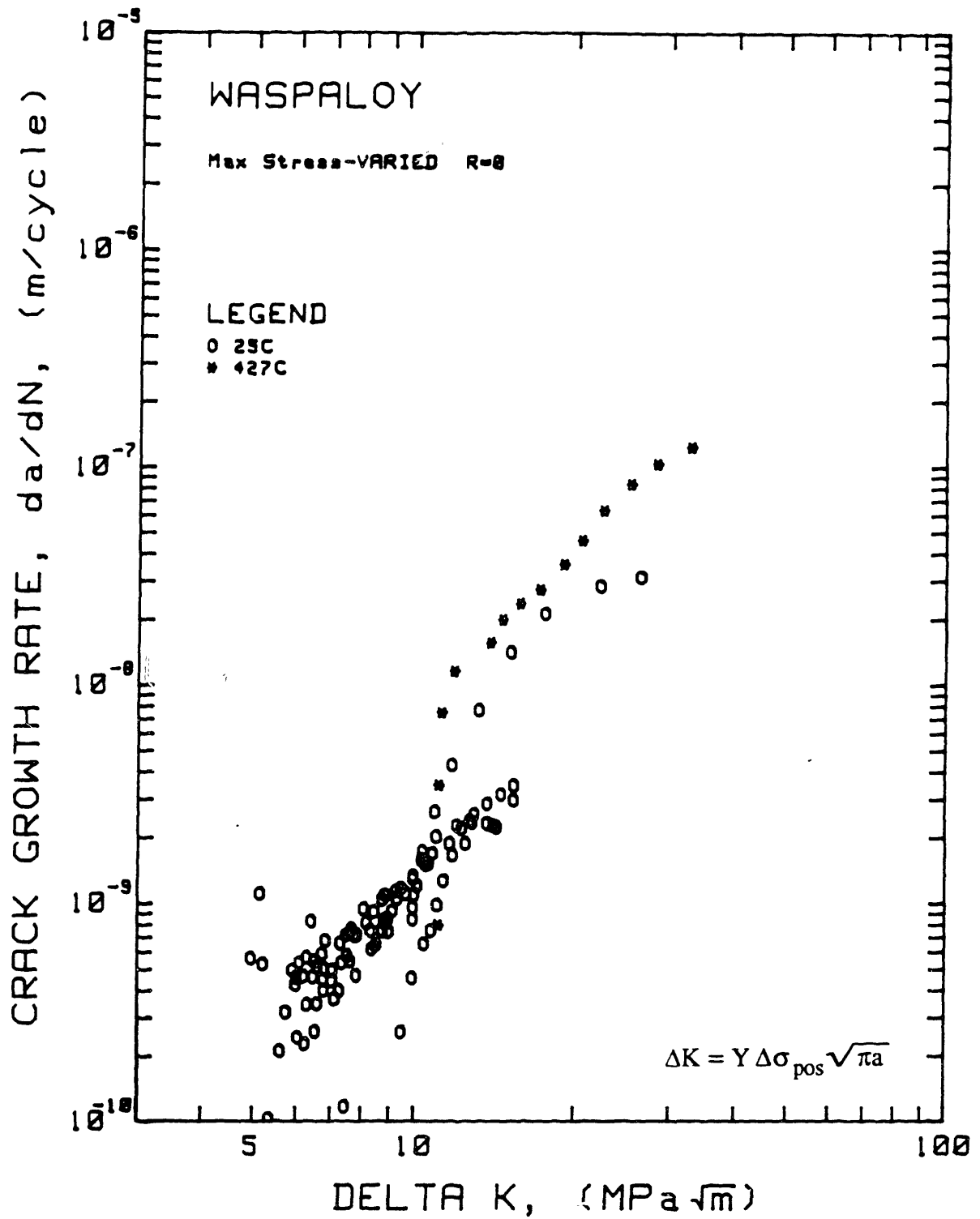


Figure 4.8 Comparison of crack growth rates versus stress intensity factor range for Waspalloy tested at 25C and 427C, R=0.

## 4.2 The Fatigue Behavior of Small Cracks in Inconel 718 at 427C

The fatigue behavior of small cracks in Inconel 718 was investigated at 427C (800F) under nominally elastic conditions. All tests were performed in load control on specimens with cylindrical gage sections plus two flats as shown in Figure 3.5. Unfortunately, this drawing was not strictly followed in the machining of six Inconel 718 specimens. The radii-to-flats were made smaller at 6.35 mm rather than the designated 12.7 mm. Consequently, three tests failed prematurely at this location. The principal test variables were maximum stress and R-ratio. Test conditions for Inconel 718 are shown in Table 4.2.

A composite plot of crack depth versus cycle number is shown in Figure 4.9.

### Small versus Long Crack Growth Behavior

The fatigue crack growth behavior of small cracks ( $100 \mu\text{m} < a < 1 \text{ mm}$ ) is compared to long cracks in Figure 4.10 at  $R=0.05$ . The stress intensity factor range was calculated according to Eq. 4.1. The long crack data was taken from the work of Krueger [4.15] where a single edge notch specimen was used ( $a > 1 \text{ mm}$ ). The general trend for small crack growth rates agrees with the long crack data and can be described by the Paris-Erdogan relationship:

$$\frac{da}{dN} = 7.92 \times 10^{-12} \Delta K^{2.94} \quad (4.23)$$

where  $da/dN$  is in m/cycle and  $\Delta K$  is in  $\text{MPa}\sqrt{\text{m}}$ .

The tendency for one crack to exhibit a regime of nearly constant crack growth rate ( $\sim 2 \times 10^{-8} \text{ m/cycle}$ ) can also be seen in Figure 4.9 where the  $a$  versus  $N$  curve is linear over the range  $100 \mu\text{m} < a < 300 \mu\text{m}$ . A regime of decreasing crack growth for one small crack at the  $R=0.05$  condition is also observed.

### Effect of Maximum Stress

The effect of maximum stress on small crack growth rates at  $R=-1$  can be seen in Figure 4.11. Values of maximum stress were 758 MPa ( $0.69\sigma_{ys}$ ) and 621 MPa ( $0.56\sigma_{ys}$ ). The values in parenthesis represent the fraction of the 0.2% offset yield strength (1100 MPa) for Inconel 718 at 427C. The stress intensity factor range consolidates crack growth rates for these two stress levels. There is a tendency for nearly constant crack growth rates at low values of  $\Delta K$ , i.e.,  $100 \mu\text{m} < a < 300 \mu\text{m}$ . This behavior is more clearly evident in the  $a$  versus  $N$  curves for these tests shown in Figure 4.9.

### Effect of R-ratio

The effect of R-ratio on small crack growth rates is shown in Figure 4.12 where the maximum stress was 758 MPa in both tests and the stress ratios were  $R=-1$  and  $R=0.05$ . Similar to the Waspaloy results, the general trend for higher crack growth rates at  $R=-1$  versus positive R-ratios is also observed in these Inconel 718 results. This again confirms the role of the compressive stress range in promoting faster crack growth rates at the same nominal value of  $\Delta K$ . Presumably, the compressive component of the stress range increases the magnitude and extent of the reversed crack tip plastic strain range.

### Applicability of LEFM

The arguments for and against applying LEFM to correlating crack growth rates of small cracks in Inconel 718 at 427C are similar to those given in the previous section for Waspaloy at 427C since yield strengths, stress ranges and crack length regimes are nearly equivalent in both cases. It will suffice here to give a brief summary of those arguments as they apply to small crack behavior in Inconel 718 used in this investigation.

The requirement for linear elastic behavior is met on a global scale since the macroscopic yield stress is not exceeded in any of these tests. On a microscopic scale, i.e. within a single grain, plastic behavior may be expected since micro-yielding can occur at  $\sim 1/3$  the macroscopic yield. The requirement for isotropic behavior may be violated locally as small cracks and their crack tip zones encounter large grains. Since  $\sigma_{\max}$  ranged from 56% to 69% of  $\sigma_{ys}$ ,  $r_{pm}$  ranged from  $0.17a$  to  $0.25a$  and, therefore, did not satisfy the small scale yielding requirement that  $r_{pm} \leq 0.02a$  if the near crack tip elastic field is to dominate the crack tip response. However, if we contend that  $r_{pc}$  defines the limitation on small scale yielding and use the experimental estimate that  $r_{pc} \approx r_{pm}/10$ , then  $r_{pc}$  ranged from  $0.017a$  to  $0.025a$  and therefore satisfied the small scale yielding requirement.

As stated previously, the crack length must be ten times the grain size if  $K$  is to accurately represent stresses in the crack tip elastic field. Since the crack length ranged from  $100 \mu\text{m}$  to  $1 \text{ mm}$  and the average grain size was  $32 \mu\text{m}$ , this requirement was met at most crack lengths.

Mechanical similitude between small cracks and long cracks in this heat of Inconel 718, although not strictly satisfied, is approximated sufficiently to give the correlation shown in Figure 4.10. Mechanical similitude between small cracks of equivalent size was also demonstrated in these tests.

**Table 4.2**  
**Test Conditions for Inconel 718 at 427C**

Test #	R	$\sigma_{\min}$ MPa	$\sigma_{\max}$ MPa	Comments
GR7	-1	-758	758	2 cracks
GR8	0.05	38	758	2 cracks
GR9	-1	-621	621	2 cracks

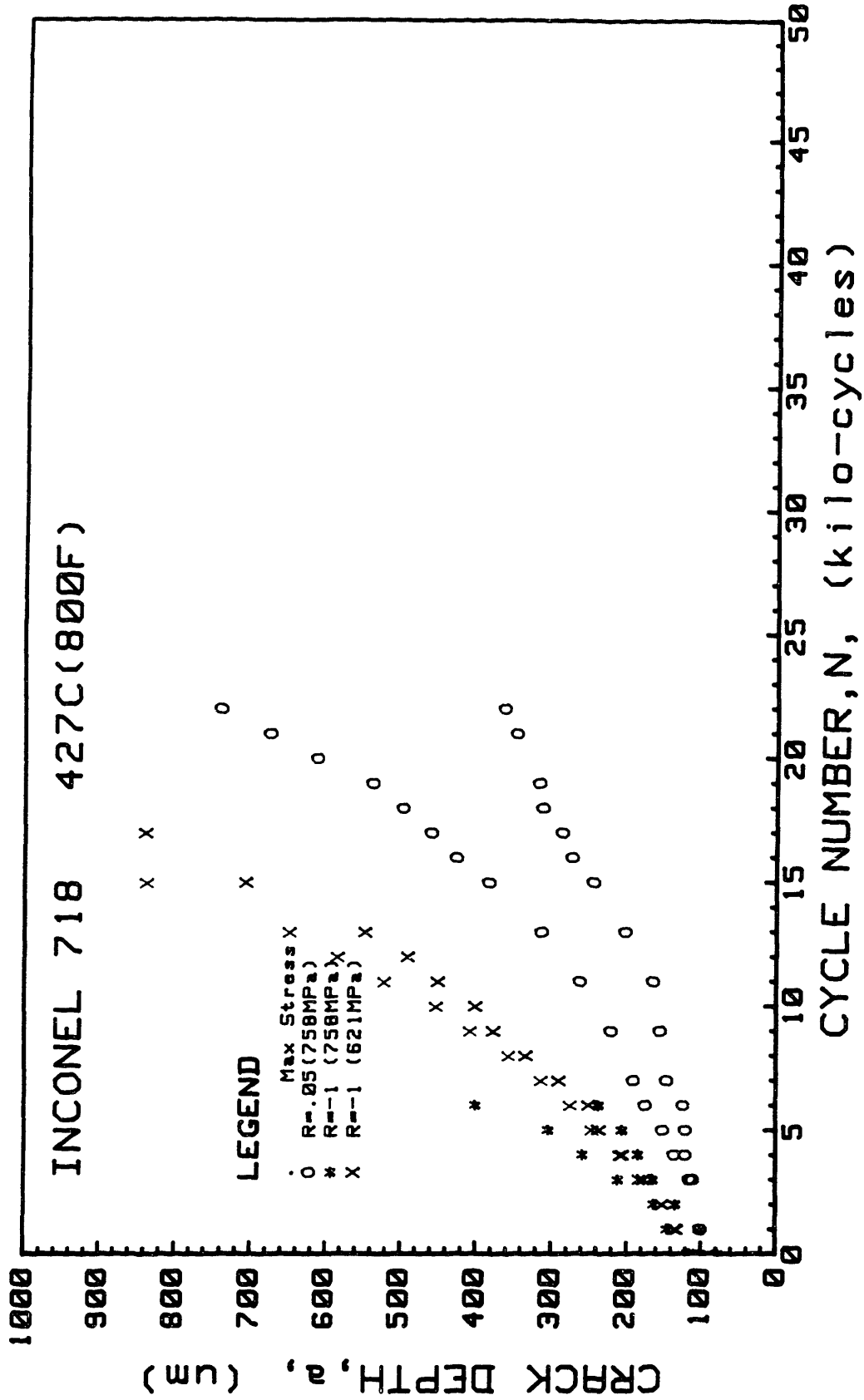


Figure 4.9 Crack depth versus cycle number for Inconel 718 tested at 427C under nominally elastic fatigue conditions; Freq = 20 cpm.

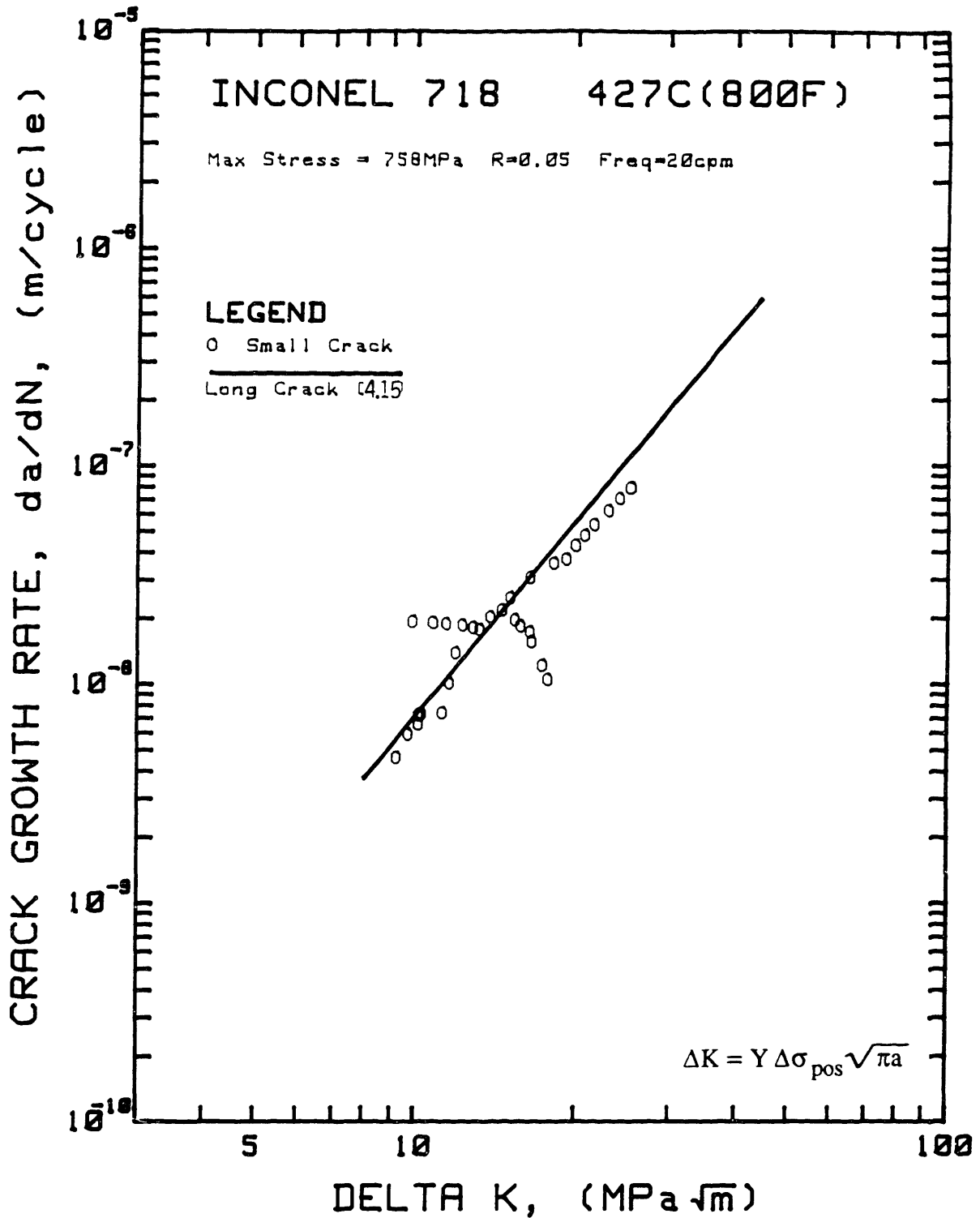


Figure 4.10 Crack growth rates versus stress intensity factor range for Inconel 718 tested at 427C under nominally elastic fatigue conditions; small crack versus long crack, R=0.05 and Freq = 20 cpm.

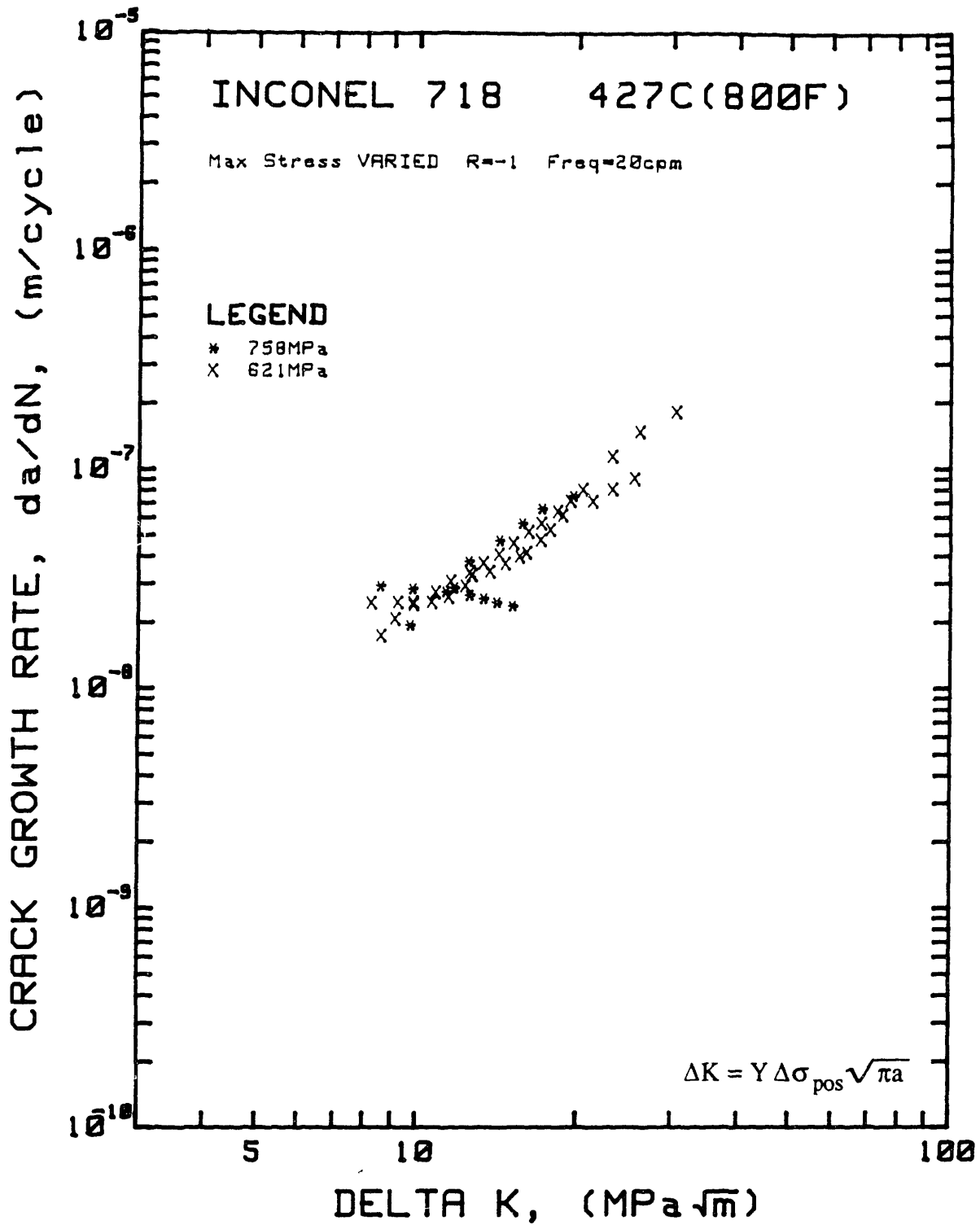


Figure 4.11 Summary of crack growth rates versus stress intensity factor range for Inconel 718 tested at 427C under nominally elastic fatigue conditions. Stress range was varied at R=-1, Freq. = 20 cpm.

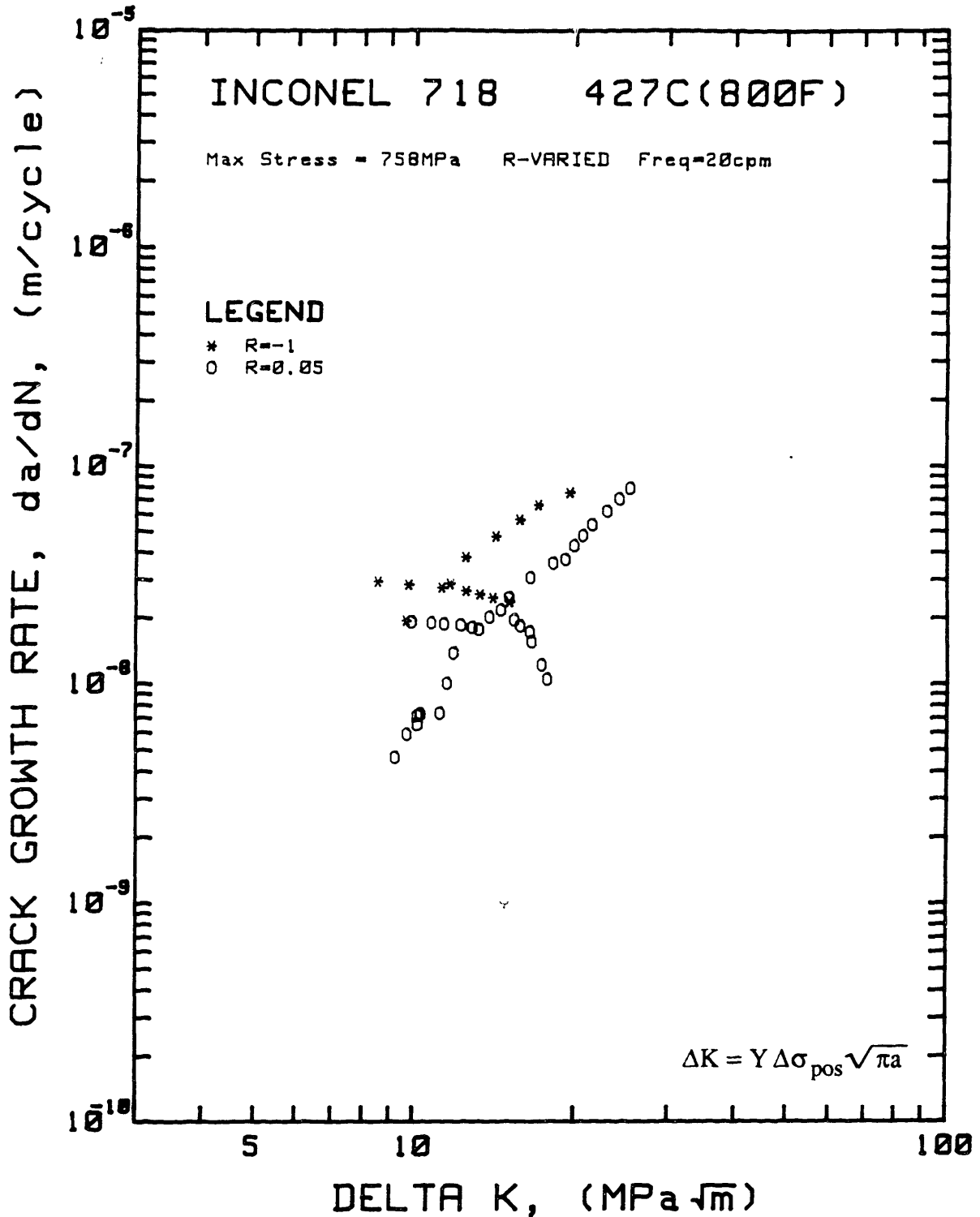


Figure 4.12 Summary of crack growth rates versus stress intensity factor range for Inconel 718 tested at 427C under nominally elastic fatigue conditions; R-ratio varied at Max. Stress = 758 MPa, Freq. = 20 cpm.

### 4.3 The Fatigue Behavior of Small Cracks in Powder Metallurgy Gatorized® IN100 at 649C ; Elastic Tests

The fatigue behavior of small cracks was investigated in powder metallurgy Gatorized IN100 at 649C (1200F) under nominally elastic conditions. All tests were performed in load control on specimens with cylindrical gage sections plus two flats as shown in Figure 3.5. Small cracks were initiated by laser defects and precracked to a depth of 100 μm. Crack growth behavior was measured over the range 100 μm < a < 1 mm. Test conditions are given in Table 4.3. The principal test variables were maximum stress and R-ratio.

#### Effect of Maximum Stress

The effect of maximum stress on small crack growth behavior at R=0.1 is shown in Figures 4.13 and 4.14. Values of maximum stress were 758 MPa (0.72σ<sub>0</sub>) and 965 MPa (0.92σ<sub>0</sub>). The values in parenthesis represent the fraction of the elastic limit stress (1050 MPa) for IN100 (PM) at 649C. Crack depths versus cycle number shown in Figure 4.13 exhibit the expected behavior. The stress intensity factor range was calculated as

$$\Delta K = 0.73 \Delta \sigma_{\text{pos}} \sqrt{\pi a} \quad (4.1)$$

where 0.73 is the flaw shape and boundary correction factor for a semicircular surface crack, Δσ<sub>pos</sub> is the positive stress range and a is the crack depth.

As seen in Figure 4.14, ΔK consolidates crack growth rates of small cracks for the two stress ranges at R=0.1. There is a break towards threshold behavior at ΔK=12MPa√m for both cracks. Two small cracks indicated by the arrows at B' and A' remained arrested at 9.4 MPa√m and 10.3 MPa√m, respectively, throughout testing (N<sub>p</sub> ≥ 3000 cycles). During precracking these cracks did not achieve sufficient length to exceed ΔK<sub>TH</sub> during subsequent testing. It is unlikely that these two small cracks of a = 70 μm (at 965 MPa) and a = 135 μm (at 758 MPa) could remain arrested for an infinite number of cycles under such high cyclic

stresses well above the high cycle endurance limit. However, this apparent threshold behavior at a significant number of cycles with respect to turbine disk life expectancy does indicate significant defect tolerance for this material under nominally elastic fatigue conditions at R=0.1.

The fatigue crack growth behavior of small cracks, shown in Figure 4.14 may be expressed in terms of  $\Delta K$  by the Paris-Erdogan relationship in the Stage II regime by:

$$\frac{da}{dN} = 3.10 \times 10^{-12} \Delta K^{3.96} \quad (4.24)$$

where  $da/dN$  is in m/cycle and  $\Delta K$  is in  $\text{MPa}\sqrt{\text{m}}$ .

The small crack data ( $100 \mu\text{m} < a < 1 \text{ mm}$ ) obtained in this investigation merges with long crack data ( $a > 20 \text{ mm}$ ) at high values of  $\Delta K$ . The long crack data was taken from the work of Larsen et al. [4.1] where compact tension specimens were used. There is, however, a divergence in slopes between these two data sets. The long crack data may be better represented by the following equation:

$$\frac{da}{dN} = 2.28 \times 10^{-10} \Delta K^{2.61} \quad (4.25)$$

where  $da/dN$  is in m/cycle and  $\Delta K$  is in  $\text{MPa}\sqrt{\text{m}}$ .

### Effect of R-ratio

The effect of R-ratio on small crack growth rates is shown in Figures 4.15 and 4.16. Values of stress ratio employed were: R=0.1, R=-0.5, R=-0.75 and R=-1. The maximum stress was constant at 965 MPa in all tests. R-ratios were chosen to match stress ratios observed in strain control tests, to be discussed in a later section (see Table 4.3). The objective of these tests was to assess the role of the compressive stress range in contributing to the mechanical driving force for crack growth.

Crack growth rates versus  $\Delta K$  are shown in Figure 4.16 for these four tests. Crack growth rates increase with decreasing R-ratio. This trend can also be seen in the  $a$  versus  $N$  curves of Figure 4.15. Crack growth rates differ by a factor of  $\sim 4$  in the Paris regime.

The potential for nonconservative errors in calculating an integrated crack propagation life at negative R-ratios when using  $R=0.1$  data is illustrated rather dramatically in the  $a$  versus  $N$  curves of Figure 4.13 and Figure 4.15. To be more critical of this visual estimate, we must realize that  $\Delta K$  ( $a=\text{constant}$ ) is 10% lower in the  $R=0.1$  tests and, furthermore, that  $R=0.1$  data exhibited considerable near threshold behavior which was absent from the negative R-ratio data.

A conservative calculation of crack propagation life may be based on the linear regime alone. The upper bound of crack growth rates for the  $R=-1$  test condition may be expressed by the Paris-Erdogan relationship:

$$\frac{da}{dN} = 6.55 \times 10^{-10} \Delta K^{2.48} \quad (4.26)$$

where  $da/dN$  is in m/cycle and  $\Delta K$  is in  $\text{MPa}\sqrt{\text{m}}$ . Integrating the above equation for  $R=-1$  data and Eq. 4.24 for  $R=0.1$  data between  $a=100 \mu\text{m}$  and  $a=1 \text{ mm}$ , the crack propagation lives are 512 cycles and 2033 cycles, respectively.

These tests demonstrate that the compressive stress range plays an important role in accelerating crack growth rates and must be accounted for in defect tolerant approaches to life extension.

#### Empirical Consolidation of R-ratio Data

Given the success of the Walker equation in consolidating crack growth rates for Waspaloy ( $-1 < R < 0.5$ ) in Section 4.1, it was applied to the IN100(PM) results ( $-1 < R < 0.1$ ). The Walker equation was used in the form given by Eq. 4.15 with  $\alpha=0.5$ . The results are

shown in Figure 4.17 where crack growth rates are nearly collapsed into a single line by the Walker-modified stress intensity factor range. The spread in the data at high  $\overline{\Delta K}$ 's can be attributed to experimental scatter; for example, the two cracks for the R=-0.5 test condition (points "E") are at the two extremes of the scatter band.

The inclusion of  $\Delta\sigma$  in the effective stress term of  $\overline{\Delta K}$ , i.e.,  $\overline{\sigma} = (\sigma_{\max})^{1-\alpha} \Delta\sigma^\alpha$ , demonstrates the importance of including the compressive stress range in the mechanical driving force for crack growth. Several physical arguments may be made to explain the increasing crack growth rates observed for decreasing R-ratios; in this case corresponding to a larger stress range since the maximum stress was constant at 965 MPa in all tests.

1) It may be argued that the crack opening-closure stress decreases with larger compressive stress excursions, causing fracture surface asperities to deform plastically. Therefore,  $\Delta K_{\text{eff}} = K_{\max} - K_{\text{op}}$  increases with decreasing R-ratio. This argument seems plausible, however, Elber and others found experimentally for aluminum alloys and long cracks that crack opening-closure occurs at positive stresses and that  $\Delta K_{\text{eff}} = (A + BR)\Delta K_{\text{applied}}$  increases with increasing R-ratios. There is an apparent inconsistency in using crack closure arguments to explain the full range of the R-ratio effect on crack growth rates.

2) A second argument is that the compressive stress excursion serves to resharpen the crack tip resulting in faster crack growth rates in R<0 tests. Although this explanation may be valid where fatigue cracks propagate by a ductile striation mechanism, it is unlikely to apply to powder metallurgy IN100 at 649C where crack extension occurred along an intergranular fracture path with the crack tip remaining sharp and nearly closed at high values of tensile stress. This fact was established by observations on plastic replicas of surface crack traces which were made at ~80% of the maximum cyclic tensile stress.

3) A physically plausible explanation for the effect of R-ratio on crack growth rates observed here is that crack extension in a given fatigue cycle is caused by the reversal of crack tip plastic strains. In positive R-ratio tests, the tensile plastic strain which develops ahead of the crack at  $K_{max}$  is reversed upon unloading. If crack closure occurs at some positive value of load, the extent of crack tip strain reversal is reduced. In terms of LEFM,  $\Delta K_{eff} = K_{max} - K_{closure}$  controls the crack tip strain range under nominally elastic conditions.

These small crack tests are unique in that the magnitude of the nominal stress range is a significant fraction of the yield stress (92% in the case presently being considered). Consequently, the crack tip strain reversal, which occurred by elastic unloading is further extended by the high magnitude of imposed bulk compressive stress. Crack closure may occur but will be less effective in shielding the crack tip from strain reversal. Therefore,  $\Delta K_{eff}$  has limits to its applicability in describing crack tip conditions, that is  $\Delta K_{eff} = K_{max} - 0$  since the Mode I stress intensity factor is not defined for negative stresses.

Hence, by using the empirical modification of  $\Delta K$  by the Walker equation which explicitly includes  $\Delta\sigma_{tot}$ , we can account for the contribution of the negative stress range in fatigue crack growth. This approach is in agreement with the basic concept of crack closure, but it further recognizes that high compressive stresses may override full crack tip shielding.

**Table 4.3**  
**Test Conditions for Powder Metallurgy GATORIZED® IN100 at 649C**

Control	Test #	†	R	$\sigma_{min}$ MPa	$\sigma_{max}$ MPa	$\sigma_{tot}$ MPa	$\epsilon_{min}$ %	$\epsilon_{max}$ %	$\Delta\epsilon_{tot}$ %	$\Delta\epsilon_e$ %	$\Delta\epsilon_p$ %	Comments
<u>laser defects</u>												
load	GR10		0.1	+69	689	620	0.033	0.329	0.296	0.296	0	premature X
load	GR15		0.1	+76	758	682	0.036	0.362	0.325	0.321	0	premature X
load	GR16	A	0.1	+76	758	682	0.036	0.362	0.325	0.325	0	1 crack
load	GR23	B	0.1	+97	965	868	0.046	0.460	0.414	0.414	0	1 crack
load	GR19	D	-1.0	-965	965	1930	-0.460	0.460	0.921	0.921	0	1 crack
load	GR30	D	-1.0	-965	965	1930	-0.460	0.460	0.921	0.921	0	2 cracks
load	GR31	C	-1.0	-758	758	1517	-0.362	0.362	0.723	0.723	0	1 crack
load	GR32	E	-0.5	-483	965	1448	-0.230	0.460	0.690	0.690	0	2 cracks
load	GR33	G	-0.75	-725	965	1690	-0.346	0.460	0.806	0.690	0	2 cracks
<u>laser defects</u>												
strain	GR20	O	-0.15	-167	1137	1304	0	0.631	0.631	0.621	0.010	2 cracks
strain	GR21	*	-0.44	-514	1180	1694	0	0.822	0.822	0.807	0.015	2 cracks
strain	GR17	*	-0.50	-556	1103	1659	0	0.805	0.805	0.790	0.015	2 cracks
strain	GR24	X	-0.72	-872	1203	2075	0	1.048	1.048	0.988	0.060	2 cracks
strain	GR34	Z	-0.88	-1087	1232	2319	0	1.23	1.23	1.104	0.130	2 cracks
strain	GR14	P	-1.12	-1152	1026	2178	-0.58	0.52	1.107	1.037	0.070	2 cracks
strain**	GR22	H	-0.51	-566	1100	1666	0	0.818	0.818	0.793	0.025	2 cracks
<u>smooth specimens</u>												
strain	GR26		-0.51	-592	1163	1755	0	0.80	0.80	0.580	0.020	Multiple cracks
strain	GR27		-0.52	-590	1140	1730	0	0.80	0.80	0.580	0.020	"
strain	GR28		-0.72	-874	1214	2088	0	1.00	1.00	0.945	0.055	"
strain	GR29		-0.78	-918	1170	2088	0	1.00	1.00	0.950	0.050	"

\*\* 60 sec hold † plotting symbol

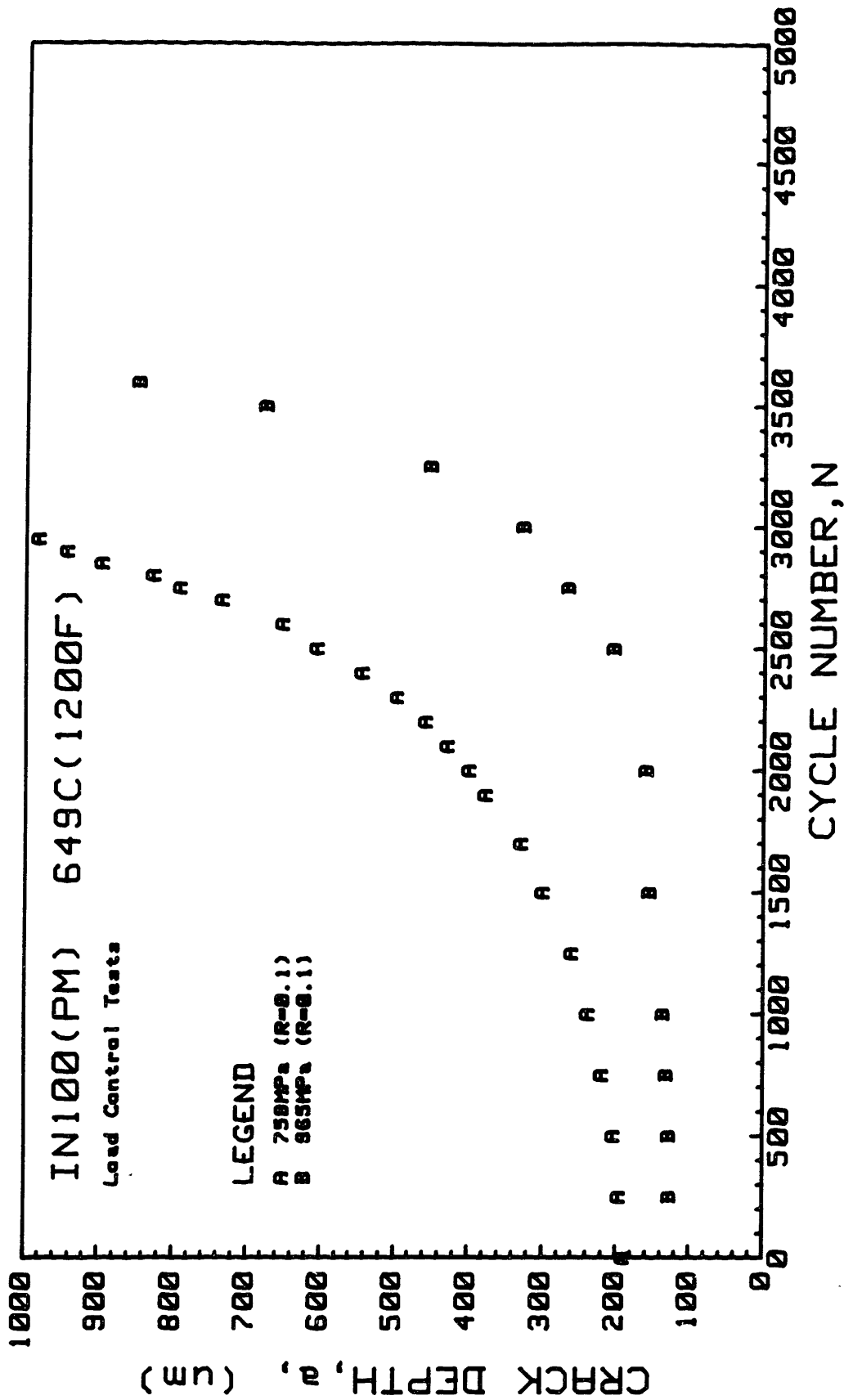


Figure 4.13 Crack depth versus cycle number for IN100(PM) tested at 649C under nominally elastic fatigue conditions; stress range was varied at R=0.1, Freq. = 10 cpm.

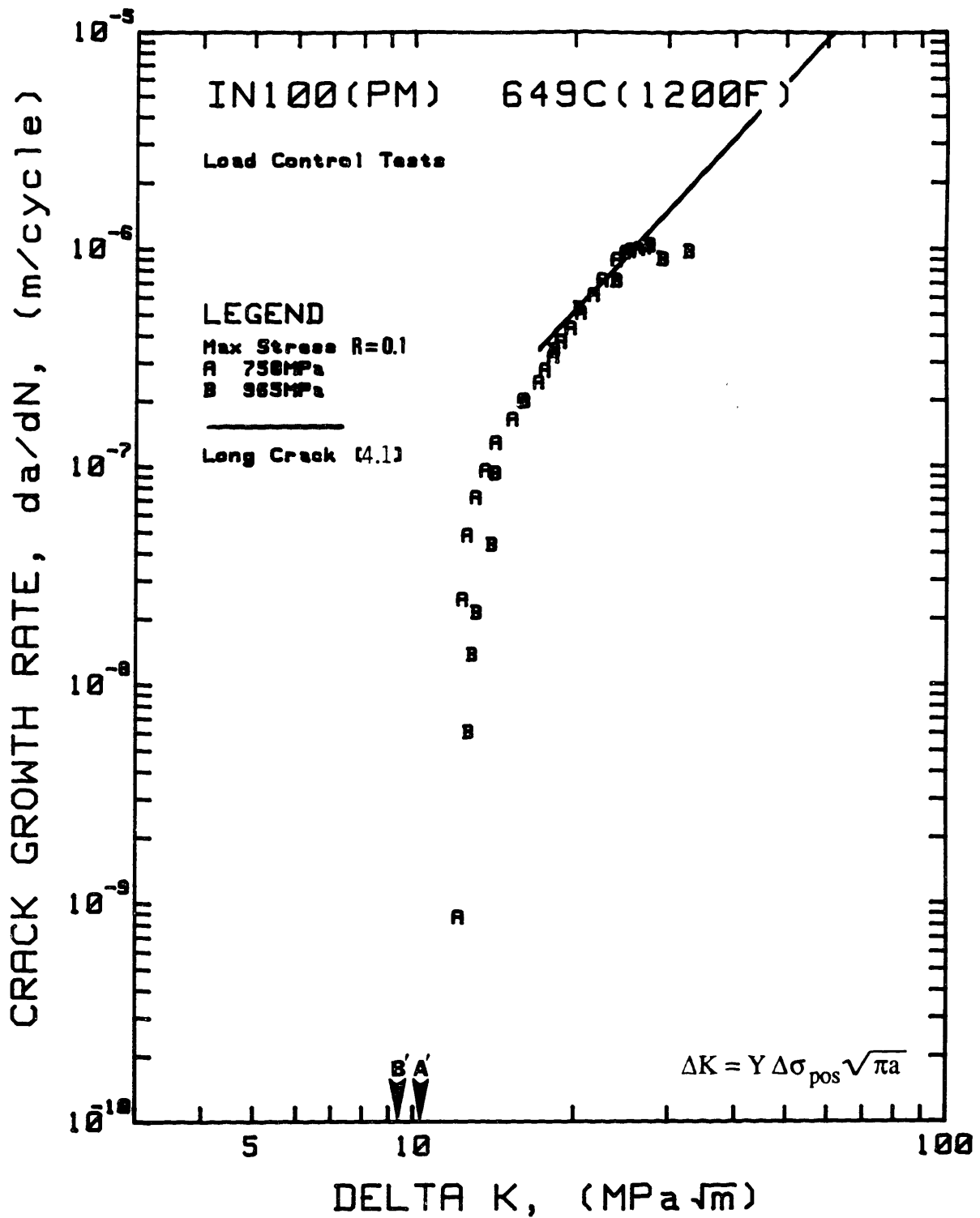


Figure 4.14 Summary of crack growth rates versus stress intensity factor range for IN100(PM) tested at 649C under nominally elastic fatigue conditions; stress range was varied at R=0.1, Freq.=10 cpm. Two cracks are shown arrested at A' and B'.

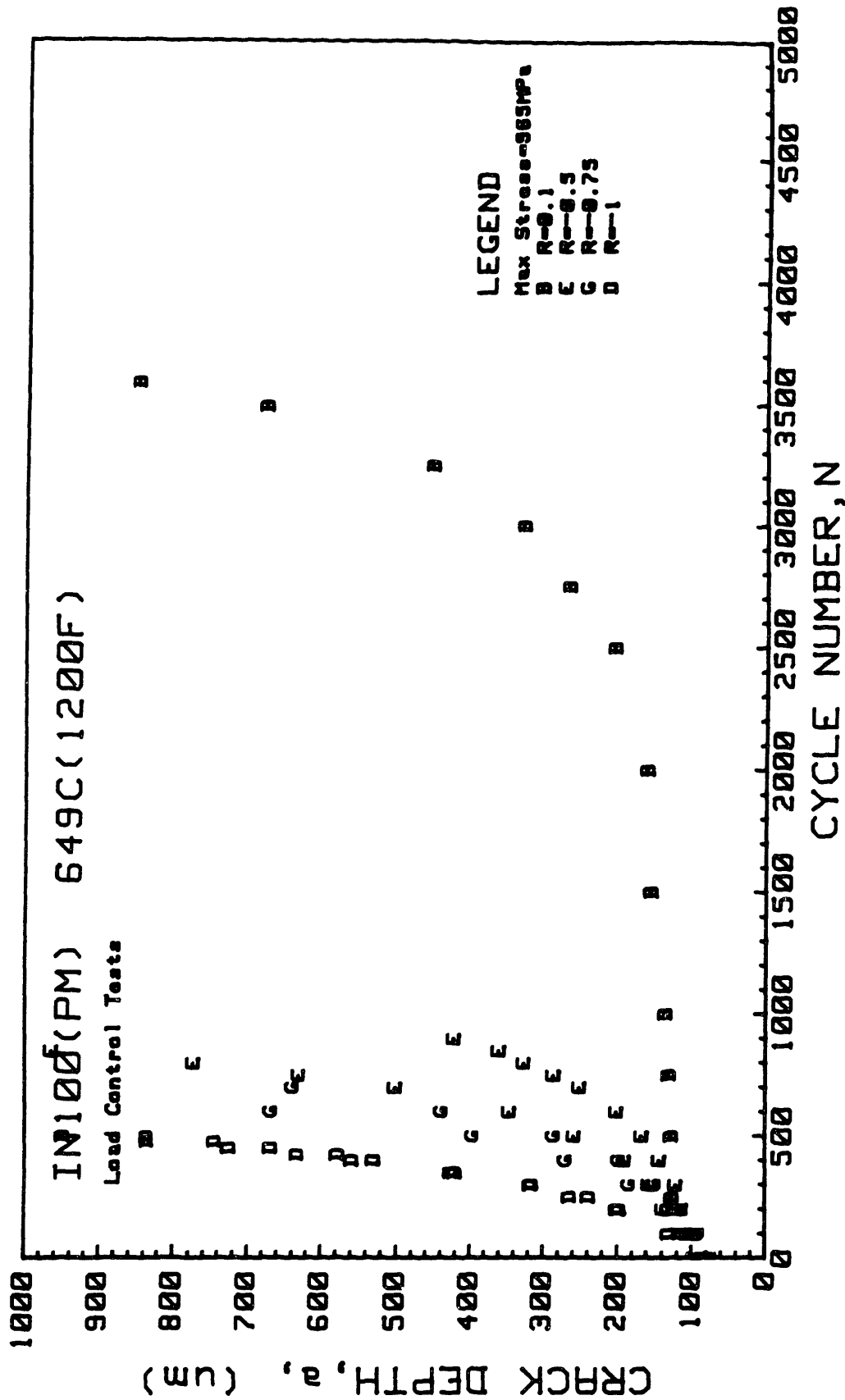


Figure 4.15 Crack depth versus cycle number for IN100(PM) tested at 649C under nominally elastic fatigue conditions; R-ratio was varied at a maximum stress of 965 MPa, Freq.=10 cpm.

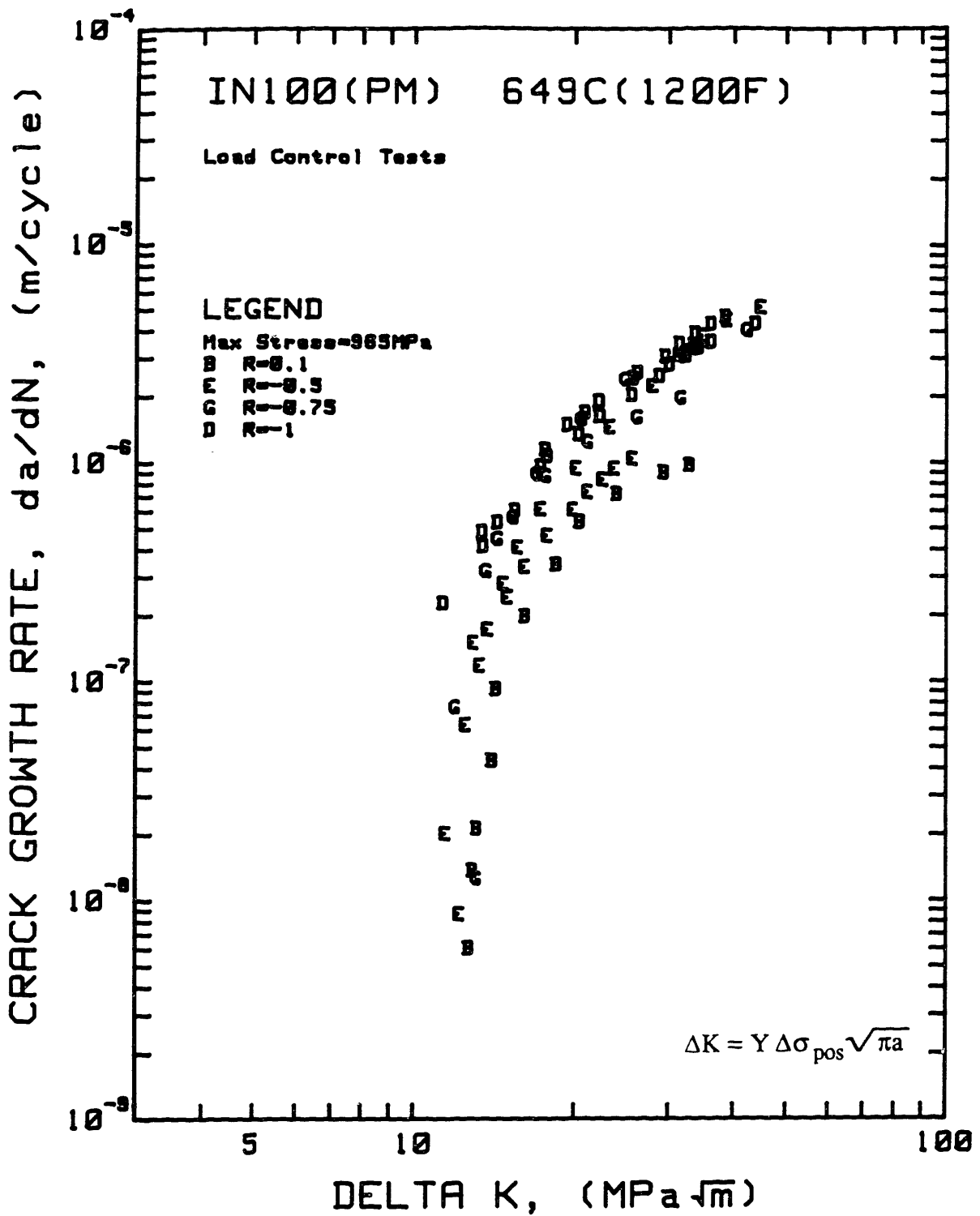


Figure 4.16 Summary of crack growth rates versus stress intensity factor range for IN100(PM) tested at 649C under nominally elastic fatigue conditions; R-ratio was varied at a maximum stress of 965 MPa, Freq.=10 cpm.

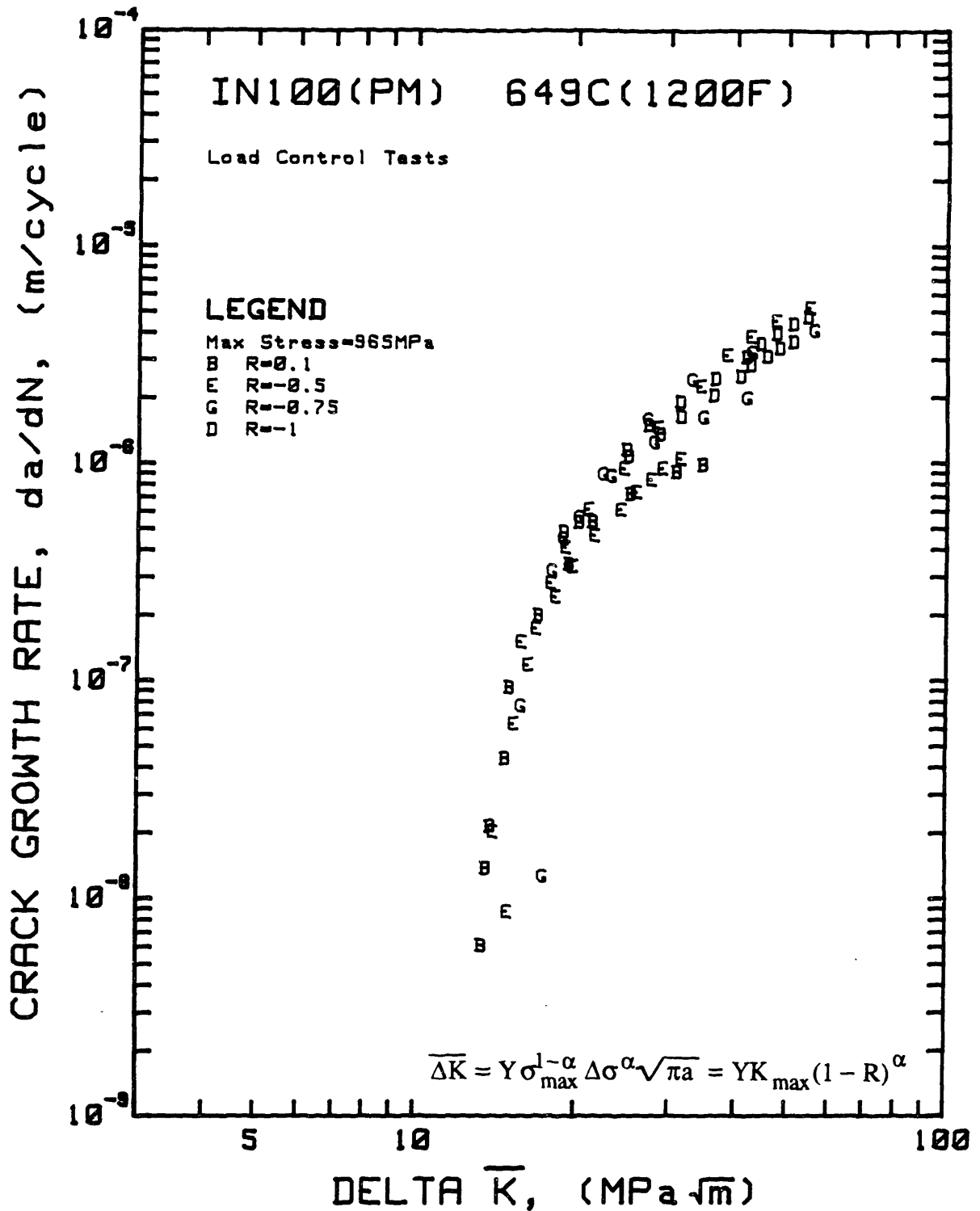


Figure 4.17 Summary of crack growth rates versus the Walker- modified stress intensity factor range ( $\alpha=0.5$ ) for IN100(PM) tested at 649C under nominally elastic fatigue conditions; R-ratio was varied at a maximum stress of 965 MPa, Freq.=10 cpm.

#### 4.4 Stress-Strain Response of Powder Metallurgy Gatorized® IN100 at 649C

The elastic-plastic test conditions used in this investigation are given in Table 4.3 along with the bulk stress-strain response. It is the objective of this section to define and discuss the stress-strain response of IN100(PM) at 649C subjected to fatigue cycling between total strain limits at  $R_\epsilon = 0$ . This analysis is essential to representing the mechanical driving force for fatigue crack growth under elastic-plastic conditions.

##### Monotonic Stress-Strain Response

The monotonic stress-strain response is shown in Figure 4.18. This test was performed in strain control using the same specimen geometry and servo-hydraulic test system employed for the fatigue tests. The strain rate was also similar to that used in the fatigue tests ( $\sim 0.3\%/sec$ ). The following measurements were made from the monotonic stress-strain curve:

- Elastic modulus,  $E=210$  GPa
- Elastic limit strain,  $\epsilon_0=0.5\%$  (for  $\epsilon_p \leq 0.01\%$ )
- Elastic limit stress,  $\sigma_0=1050$  MPa
- The 0.2% yield stress,  $\sigma_{ys}=1150$  MPa

After the onset of yielding, the stress may be related to the plastic strain by the empirical relationship generally attributed to Holloman [4.16], Ramberg [4.17] and Osgood [4.17, 4.18]:

$$\sigma = 1432 \epsilon_p^{0.036} \quad (4.27)$$

where  $\sigma$  is the true stress in MPa and  $\epsilon_p$  is the true plastic strain ( $R^2=0.996$ ). The monotonic strain hardening exponent is 0.036. Also shown in Figure 4.18 on the elastic loading curve are the maximum stress and strain ranges (indicated by arrows) imposed in the elastic fatigue tests discussed in the previous section. The maximum stress range in the elastic tests was  $\pm 0.92\sigma_0$ .

### Cyclic Stress-Strain Response

The cyclic stress-strain response of powder metallurgy IN100 at 649C is also shown in Figure 4.18 where typical stabilized hysteresis loops are superimposed on the monotonic response. These tests were performed in strain control with  $R_\epsilon=0$  to approximate the strain range ahead of a notch. A few salient features of the cyclic stress-strain response should be pointed out: i) A total strain range of 0 to  $\sim 0.6\%$  is required to produce a minimum measurable plastic strain range of 0.01%. This occurs after a monotonic plastic strain of 0.10%. It is often stated that the material near a notch may be treated as essentially elastic after yielding and strain hardening on the initial uploading half-cycle. It is then considered that similar bulk stress excursions should produce only elastic notch strains during subsequent cycling and, presumably, LEFM could be used to predict fatigue crack growth behavior. The results shown in Figure 4.18 illustrate that the validity of this approach is limited to a total tensile strain range somewhat less than 0 to 0.6% for IN100(PM) at 649C, ii) Also notable is the positive mean stress which occurs in the low total strain range hysteresis loops. This mean stress tends to zero in high strain range tests.

Quantitative representation of the cyclic stress-strain response is required for consideration of FCP under bulk elastic-plastic conditions. This can be achieved through analysis of hysteresis loops such as those shown in Figure 4.18. Since these tests were performed between limits of total strain, the simple continuous cycling loop can be broken down into elastic and plastic components of strain range.

$$\Delta\varepsilon_t = \Delta\varepsilon_e + \Delta\varepsilon_p = \frac{\Delta\sigma_t}{E} + \Delta\varepsilon_p \quad (4.28)$$

where  $\Delta\sigma_t$  represents the total stress range of the hysteresis loops. In cyclic stress-strain analysis it is customary to relate the total stress range to the plastic strain range. Total stress range versus plastic strain range is shown in Figure 4.19 for a multiple step test and the elastic-plastic FCP tests performed in this investigation. There is excellent agreement in the stress response for these tests. If we compare the total stress range imposed in elastic FCP tests to the total stress range response in elastic-plastic FCP tests, we find  $\Delta\sigma_t$  in the elastic tests (never yielded,  $\Delta\varepsilon_p=0$ ) is greater than the  $\Delta\sigma_t$  response in the low  $\Delta\varepsilon_t$  elastic-plastic tests where  $0 < \Delta\varepsilon_p < 0.03\%$ . This regime is particularly important to notch relevant strain-life behavior. The reduced flow stress, or Bauschinger effect [4.19, 4.20], is due to the back stress which develops during yielding; it assists deformation in the reverse direction. Consequently, the purely elastic strain range ( $\Delta\varepsilon_p=0$ ) available in the pre-yielded state is  $\sim 1\%$  (i.e.,  $\pm 0.5\%$ ), whereas in the post yielded state, the purely elastic strain range ( $\Delta\varepsilon_p=0$ ) available is somewhat less than  $0.6\%$  (see for example test #GR20). Figure 4.19 is also evidence that IN100(PM) at 649C obeys a combined isotropic plus kinematic hardening rule such that the yield surface expands in stress space with increasing  $\Delta\varepsilon_t$  and translates in the direction of yielding with a reversal of the direction of straining [4.21, 4.22].

In terms of the total strain range, the stress-strain behavior may be expressed in terms of the Ramberg-Osgood relation [4.17, 4.18]:

$$\Delta\varepsilon_t = \frac{\Delta\sigma_t}{E} + \left( \frac{\Delta\sigma_t}{A} \right)^{\frac{1}{n}} \quad (4.29)$$

where A and n are constants. Substituting for  $\Delta\varepsilon_t$  from Eq. 4.28 we have the more frequently used form of this relation:

$$\Delta\sigma_t = A \Delta\varepsilon_p^n \quad (4.30)$$

where A is the cyclic strength coefficient and n is the cyclic strain hardening exponent. This relation is the same as that used for the monotonic stress-strain behavior, Eq. 4.27. A logarithmic plot of  $\sigma$  ( $\Delta\sigma_t$ ) versus  $\varepsilon_p$  ( $\Delta\varepsilon_p$ ) yields a straight line as shown in Figure 4.20 for both the monotonic and cyclic stress-strain response of IN100(PM) at 649C. The cyclic stress-strain behavior may be represented by the following relation:

$$\Delta\sigma_t = 6357 \Delta\varepsilon_p^{0.149} \quad (4.31)$$

where  $\Delta\sigma_t$  is the true stress range in MPa,  $\Delta\varepsilon_p$  is the true plastic strain range and 0.149 is the cyclic strain hardening exponent ( $R^2=0.983$ ). The drop from the general trend line of Figure 4.20b at very low values of  $\Delta\varepsilon_p$  ( $\sim 0.01\%$ ) is generally observed for  $R_\varepsilon=0$  tests [4.23].

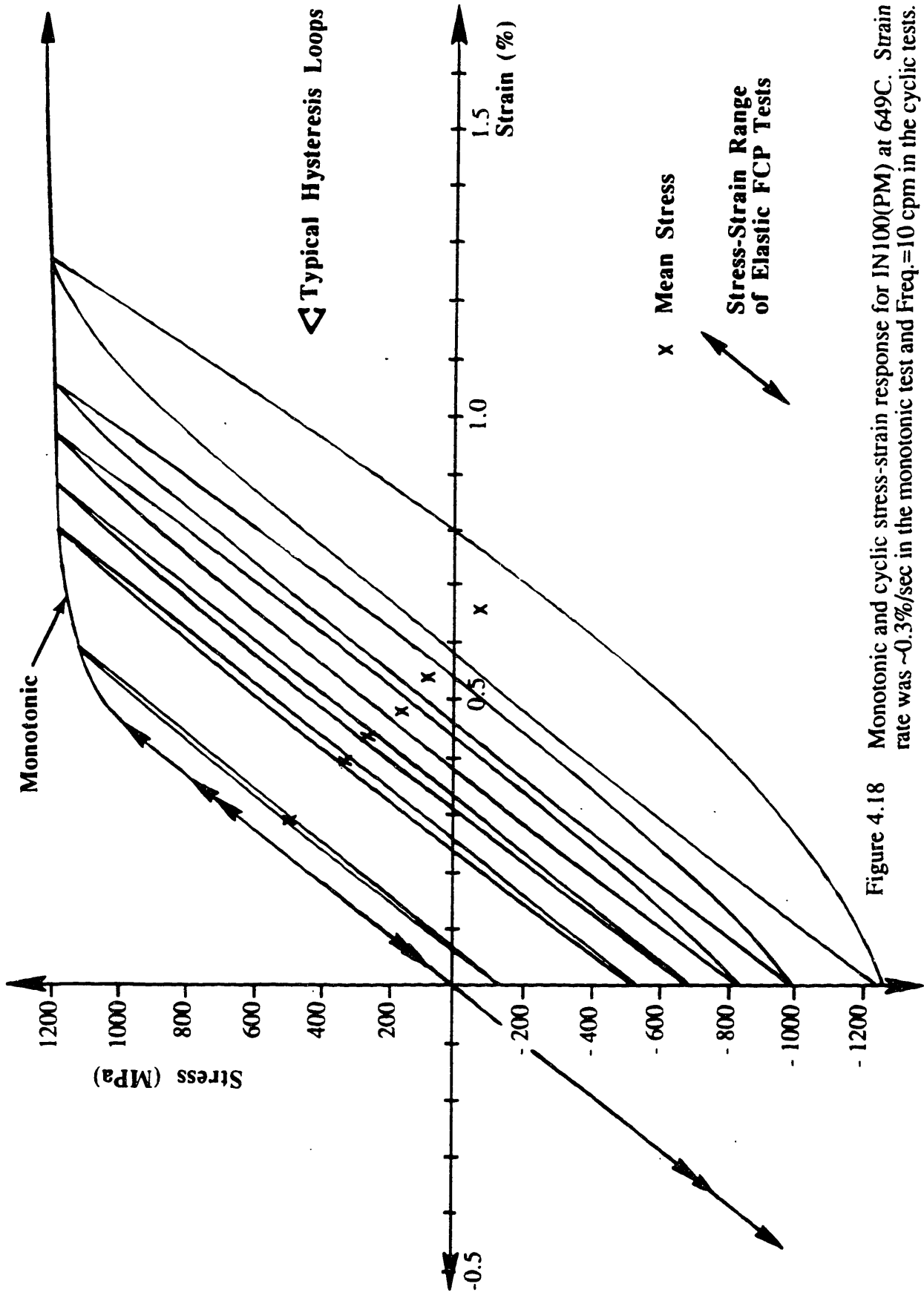


Figure 4.18 Monotonic and cyclic stress-strain response for IN100(PM) at 649C. Strain rate was ~0.3%/sec in the monotonic test and Freq.=10 cpm in the cyclic tests.

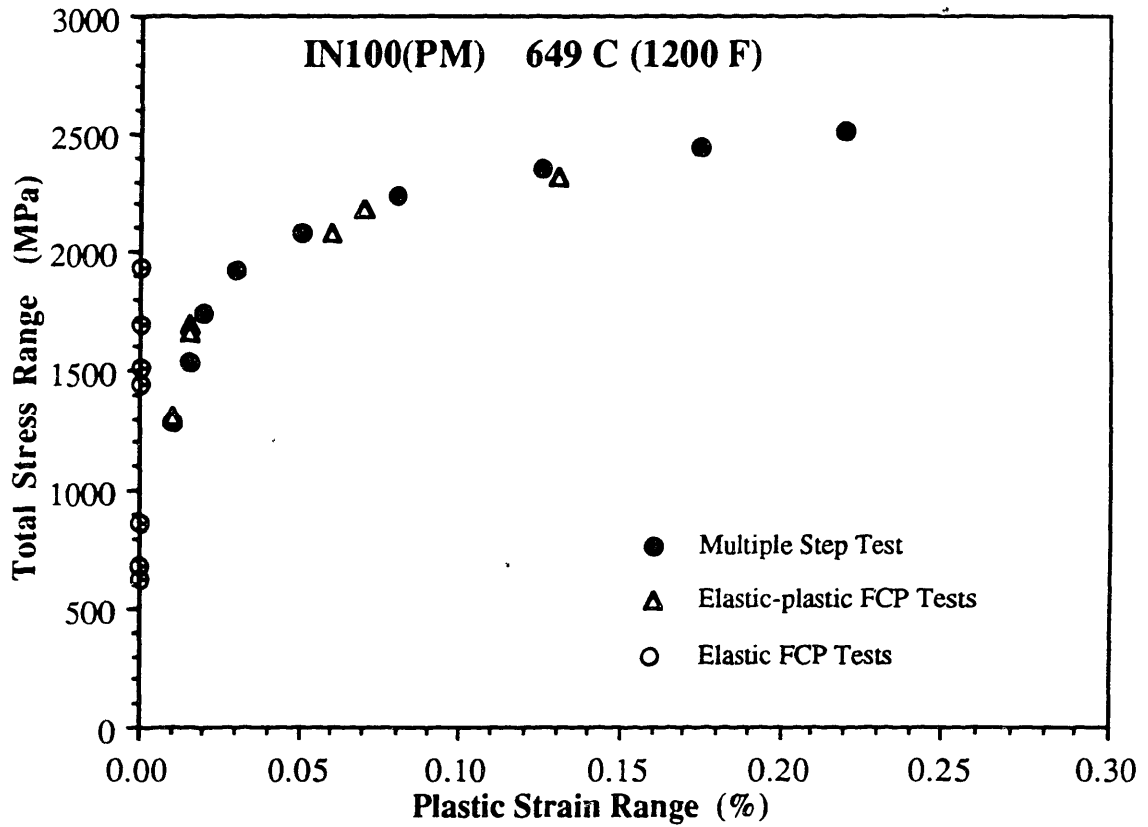


Figure 4.19 Total stress range versus plastic strain range for IN100(PM) at 649C. Test Freq.=10 cpm.

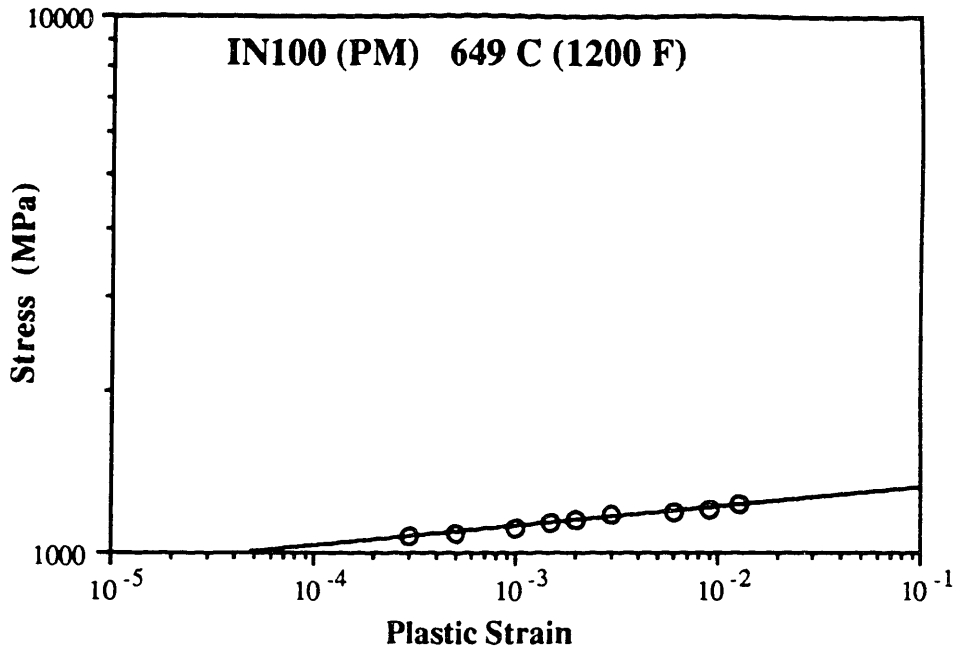


Figure 4.20a Monotonic stress versus plastic strain for IN100(PM) at 649C. Strain rate was ~0.3%/sec.

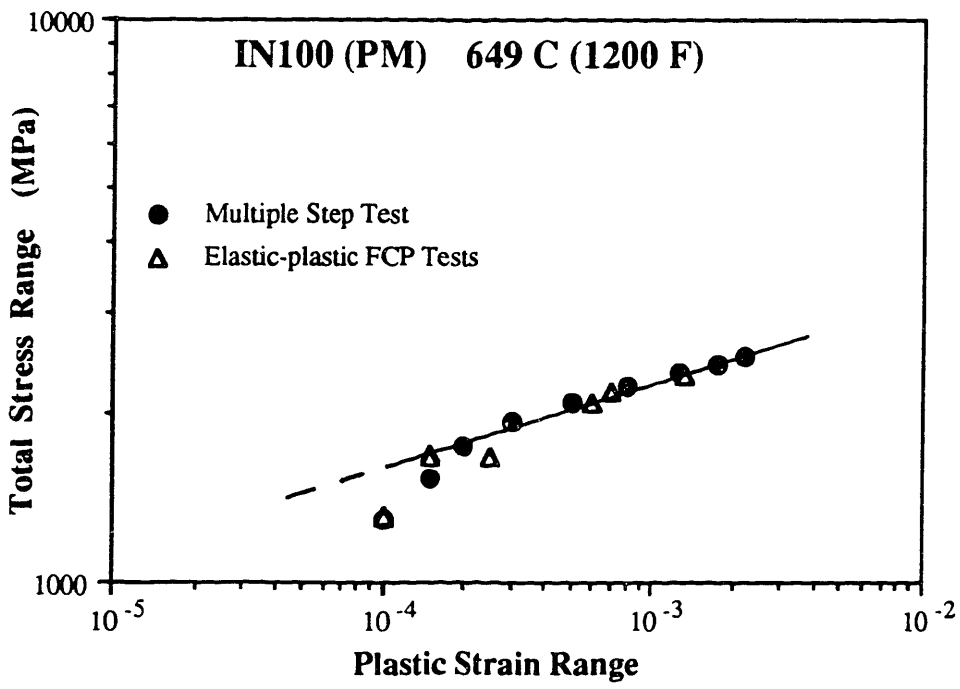


Figure 4.20b Cyclic total stress range versus plastic strain range for IN100(PM) at 649C. Freq. = 10 cpm.

#### 4.5 The Fatigue Behavior of Small Cracks in Powder Metallurgy Gatorized® IN100 at 649C; Elastic-Plastic Tests

As shown in the previous section, crack growth rates of small cracks ( $100 \mu\text{m} < a < 1 \text{ mm}$ ) correlated with long cracks using LEFM and exhibited threshold behavior when the maximum cyclic stresses were less than the elastic limit.  $\Delta K$  and the Walker-modified  $\overline{\Delta K}$  consolidated small crack growth rates for a variety of stress ranges and R-ratios. Anomalous behavior was not observed under elastic fatigue conditions.

At this juncture, the focus of this thesis turns to the fatigue crack growth behavior of small cracks in IN100(PM) under elastic-plastic conditions. Fatigue critical regions of turbine disks are often associated with notch configurations, such as bolt holes and blade attachments, where cracks initiate and propagate under elastic-plastic cyclic conditions. The defect tolerant approach to turbine disk life extension must consider crack growth under these conditions. The elastic-plastic test conditions used in this investigation are given in Table 4.3 along with the bulk stress-strain response. Since the notch configurations in fir-tree attachments may experience strain ranges on the order of 0.8%, the strain ranges employed in these tests were targeted around this value. In these tests  $\Delta\epsilon_t$  ranged from 0.6% to 1.2% and  $\Delta\epsilon_p$  ranged from 0.01% to 0.13%. All tests were performed with  $R_\epsilon = \epsilon_{\min}/\epsilon_{\max} = 0$  to approximate the conditions shown in Figure 1.4.

Before exploring crack growth rates under these conditions, we should first consider the strain-life behavior of smooth specimens of IN100(PM) tested in total strain control at 649C. Total strain range versus cycles to a 5% stress range drop is shown in Figure 4.21 for continuous cycling tests (20 cpm) and 900 sec. tensile strain dwell tests [4.23]. The continuous cycling tests resulted in a 10,000 cycle life at the target strain range of 0 to 0.8%, whereas a 900 sec. tensile strain dwell reduced life to 4,000 cycles. The tensile strain dwell tests are more relevant to turbine disk operating conditions (see Figure 1.4). Due to the

necessity of limiting the scope of this investigation, only one strain dwell test was performed. It should be recognized that cyclic life presented in Figure 4.21 represents both crack initiation and crack propagation.

It is the objective of this section to analyze crack propagation rates for small cracks in IN100(PM) at 649C under elastic-plastic continuous cycling conditions and to attempt correlation of crack propagation rates using EPFM parameters. Since EPFM may also be applied to the elastic tests, their crack growth rates will be compared to the elastic-plastic tests. First we will look at using LEFM to attempt a correlation of the elastic-plastic data.

### Stress Intensity Factor Range

The stress intensity factor range based on LEFM is obviously not valid for correlating fatigue crack growth rates when bulk plastic deformation occurs in each cycle. However, it serves as an interesting demonstration to view the results of crack growth rates versus the stress intensity factor range as shown in Figure 4.22, where  $\Delta K$  is calculated according to:

$$\Delta K = 0.73 \Delta\sigma_{\text{pos}} \sqrt{\pi a} = 0.73 \sigma_{\text{max}} \sqrt{\pi a} \quad (4.32)$$

Crack growth rates vary by a factor of ~25 at constant " $\Delta K$ ". It is not surprising that a parameter based on the maximum stress is not a sensitive representation of the mechanical driving force for crack extension under elastic-plastic conditions. Although the total strain range varied by a factor of two and the plastic strain range by a factor of 13, the maximum stress varied by only 8%. This can be explained by the low monotonic strain hardening rate as illustrated in Figure 4.18. Uploading to the maximum strain limit on the first fatigue cycle follows the monotonic stress-strain curve and the hysteresis loop which develops on subsequent strain reversals maintains nearly the same maximum stress throughout testing since IN100(PM) is cyclically stable at this temperature.

### Comparison of Elastic and Elastic-Plastic Tests in Terms of the Stress Intensity Factor Range

It was suggested that the tendency for crack growth rates to increase with increasing total strain range in  $R_\epsilon=0$  elastic-plastic tests may be attributed, in part, to the increasing component of compressive stress range experienced in these tests [4.24]. To explore this possibility, a number of elastic tests were performed in load control with  $\sigma_{\max}=0.92\sigma_o$  and  $R_\sigma$ -ratios approximately equivalent to the stress ratios observed in the strain control tests. As discussed in Section 4.3, these elastic tests exhibited increasing crack growth rates with decreasing R-ratios. The increase in crack growth rates were unambiguously attributed to the increasing compressive stress range in the elastic tests.

In Figure 4.23 through Figure 4.25, crack growth rates versus  $\Delta K$  for elastic-plastic tests performed in strain control are compared to elastic tests performed in load control where the stress ratios were approximately the same in each case. Surprisingly, there is excellent agreement in crack growth rates in spite of the fact that  $\Delta K$  is not theoretically applicable to elastic-plastic conditions where  $\Delta\epsilon_p$  is non-zero. We may speculate that the observed correlations may be attributed to the dominant role that the compressive stress-strain excursions play in promoting faster fatigue crack growth rates. Values of plastic strain range in the elastic-plastic tests shown in Figures 4.23, 4.24 and 4.25 are 0.015%, 0.06% and 0.07%, respectively. Although these are significant plastic strain ranges, the elastic strain ranges are dominant and represent greater than 94% of the total strain range in every case (see Table 4.3). It is not possible to give a definitive justification for the observations made in Figures 4.23 through 4.25 from the current experimental base.

The Walker-modified stress intensity factor range could not consolidate fatigue crack growth rates for IN100(PM) under elastic-plastic conditions.

### Pseudostress Intensity Factor Range

As discussed in Section 2.4, Solomon [2.52] successfully employed a pseudostress intensity factor range to correlate fatigue crack growth rates under elastic-plastic conditions. The pseudostress intensity factor range was defined as:

$$\Delta PK = Y E \Delta \epsilon_t \sqrt{\pi a} = Y E (\Delta \epsilon_e + \Delta \epsilon_p) \sqrt{\pi a} \quad (4.33)$$

where  $E\Delta\epsilon_t$  is the pseudostress (see Figure 2.15).  $\Delta PK$  is in fact a strain intensity parameter. Note that it includes the total strain range. Multiplication by the elastic modulus simply results in units of stress $\cdot\sqrt{a}$ . Calculation of  $\Delta PK$  for IN100(PM) at 649C was carried out using the following expression for elastic-plastic tests:

$$\Delta PK = 0.73 (210,000 \text{ MPa}) \Delta \epsilon_t \sqrt{\pi a} \quad (4.34)$$

where  $\Delta PK$  is in  $\text{MPa}\sqrt{\text{m}}$  and  $a$  is in meters.

A summary of crack growth rates versus  $\Delta PK$  is shown in Figure 4.26 for the elastic-plastic tests. The consolidation of the data in terms of  $\Delta PK$  is excellent, particularly for the data where  $\Delta\epsilon_t < 1.1\%$  ( $\Delta\epsilon_p < 0.07\%$ ). Crack growth rates for the  $\Delta\epsilon_t = 1.2\%$  ( $\Delta\epsilon_p = 0.13\%$ ) test condition are somewhat higher by a factor of  $\sim 2$ . The excellent correlation may be attributed to the inclusion of  $\Delta\epsilon_t$  in  $\Delta PK$ . As with the Walker -  $\overline{\Delta K}$  parameter, the inclusion of a total strain range factor accounts for the role of the compressive stress-strain excursion in each cycle.

As will be shown in a later section, fractographic evidence suggests that the mechanism of crack advance is similar under elastic and elastic-plastic fatigue conditions. Therefore, it is reasonable to postulate that the bulk compressive stress-strain excursion increased crack growth rates in manner similar to that observed for the elastic tests.

The test condition  $\Delta\epsilon_t=1.2\%$  ( $\Delta\epsilon_p=0.13\%$ ) may represent strain range conditions where the bulk plastic strain range is beginning to dominate the crack tip conditions. If we look back to the strain-life curve of Figure 4.21, we see that  $\Delta\epsilon_t=1.2\%$  represents a continuous cycling life of  $\sim 1000$  cycles and 900 sec. tensile strain dwell life of  $\sim 250$  cycles. This total strain range exceeds that which would be permissible in design of a disk notch configuration.

The pseudostress intensity factor range may also be applied to the elastic tests discussed in the previous section. Since  $\Delta\epsilon_t = \Delta\epsilon_e$ ,  $\Delta PK$  may be calculated as:

$$\Delta PK = 0.73 \Delta \sigma_t \sqrt{\pi a} \quad (4.35)$$

A summary of crack growth rates versus  $\Delta PK$  is shown in Figure 4.27 for the elastic tests. Crack growth rates for  $R_\sigma < 0$  tests agree within a factor of two. A higher crack growth rate is observed for  $R = 0.1$  tests at low values of  $\Delta PK$  ( $< 20 \text{ MPa}\sqrt{\text{m}}$ ). The explanation for this behavior is not obvious. Physically, crack tip plastic strain reversal occurs in  $R_\sigma > 0$  tests only by elastic unloading of the specimen. The extent of crack tip strain reversal is limited by crack closure. In  $R_\sigma < 0$  tests, crack closure is overridden by the bulk stress-strain excursion causing greater crack tip strain reversal.

A summary of crack growth rates versus  $\Delta PK$  is shown in Figure 4.28 for both elastic and elastic-plastic tests. There is excellent agreement between the elastic-plastic tests and negative  $R_\sigma$ -ratio elastic tests. The pseudostress intensity factor range is potentially an appropriate parameter for defining the mechanical driving force for crack growth from a notch. A small fatigue crack initiates and grows from the elastic-plastic field of the notch into a decaying strain range which is nominally elastic.  $\Delta PK$  can correlate crack growth rates under both conditions since the  $\Delta\epsilon_p$  component of  $\Delta\epsilon_t$  simply diminishes. There is no need

for using one parameter for elastic-plastic fatigue conditions and another for elastic fatigue conditions.

### Equivalent Stress Intensity Factor Range

Starkey and Skelton [2.54] proposed expressing the damaging strain range in an elastic-plastic fatigue cycle as  $\Delta\varepsilon_p + q_0\Delta\varepsilon_e$ , where  $q_0$  is the fraction of the stress range over which the crack was open (usually  $0.5 < q_0 < 1$ ). Multiplying this strain range by  $E$  yields an equivalent stress range,  $\Delta\sigma_{eq}$  (see Figure 2.16). The equivalent stress range can be used to calculate an equivalent stress intensity factor range as:

$$\Delta K_{eq} = YE (\Delta\varepsilon_p + q_0\Delta\varepsilon_e) \sqrt{\pi a} \quad (4.36)$$

where  $\Delta K_{eq}$  is in  $\text{MPa}\sqrt{\text{m}}$  and  $a$  is in meters.  $\Delta K_{eq}$  is, in fact, a strain intensity parameter. Multiplication by  $E$  simply converts the units to  $\text{MPa}\sqrt{\text{m}}$ . If we compare  $\Delta K_{eq}$  to  $\Delta PK$ , we find both parameters include  $\Delta\varepsilon_p$ , but  $\Delta K_{eq}$  includes only a fraction of the elastic strain range.

Calculation of  $\Delta K_{eq}$  for IN100(PM) tests at 649C was carried out using the following expression for both load and strain control tests.

$$\Delta K_{eq} = (0.73) \{ (210,000 \text{MPa}) \Delta\varepsilon_p + \Delta\sigma_{pos} \} \sqrt{\pi a} \quad (4.37)$$

where  $\Delta K_{eq}$  is in  $\text{MPa}\sqrt{\text{m}}$  and  $a$  is in m. In the above equation, the positive stress range,  $\Delta\sigma_{pos}$ , is substituted for  $E q_0 \Delta\varepsilon_e$  which follows from the assumption that crack opening occurs at zero load. Here  $\Delta\sigma_{pos}$  is used because  $\Delta\varepsilon_e$  was not symmetrical about zero load in these experiments.

A summary of crack growth rates versus  $\Delta K_{eq}$  is shown in Figure 4.29 for elastic-plastic tests performed in strain control. The consolidation of the data is poor with crack growth rates differing by a factor of 20 at constant values of  $\Delta K_{eq}$ . This is a good indication that ignoring the compressive component of  $\Delta\varepsilon_e$  in calculating the mechanical driving force

for fatigue crack growth in elastic-plastic tests is inappropriate. Hence,  $q_0$  in Eq. 4.36 is likely to be greater than 0.5. By taking  $q_0=1$ ,  $\Delta K_{eq}$  becomes  $\Delta PK$  and the correlation is identical to that shown in Figures 4.26 through 4.28. For elastic tests ( $\Delta\varepsilon_p=0$ )  $\Delta K_{eq} = \Delta K$  if  $\Delta K_{eq}$  is calculated according to Eq. 4.37.

### The Cyclic J-integral Range

Dowling [2.61] first used the cyclic J-integral range as a parameter to correlate the crack growth rates of small surface cracks in smooth axial specimens subjected to fully plastic cycling. In making the estimation of  $\Delta J_t$  for small semicircular surface cracks, Dowling developed expressions for the linear elastic and power law hardening cases separately and then combined the two for the more generalized elastic-plastic type of stress-strain behavior. A more explicit description of this approach can be found in Section 2.4. The resulting expression for the J-integral range under elastic-plastic cycling is:

$$\Delta J_t = \Delta J_e + \Delta J_p = 2\pi a Y^2 \{ \Delta W_e + f(n) \Delta W_p \} \quad (4.38)$$

or

$$\Delta J_t = Y^2 \frac{\Delta \sigma_t^2 \pi a}{E} + Y^2 (\Delta \sigma_t \Delta \varepsilon_p a) \left\{ 3.85 \frac{(1-n)}{\sqrt{n}} + \pi n \right\} \quad (4.39)$$

where  $n$  is the cyclic strain hardening exponent and  $Y$  is the same flaw shape and boundary correction factor used for the linear elastic case. Note that the total stress range is used in both the elastic and plastic work terms.  $\Delta J$  has received increasing use as a measure of the crack tip strain field under elastic-plastic fatigue conditions.

Calculations of  $\Delta J_t$  for IN100(PM) tests at 649C was carried out using the same expression for both elastic ( $\Delta\varepsilon_p=0$ ) and elastic-plastic tests. The cyclic strain hardening exponent,  $n$ , was determined to be 0.149 in accordance with Eq. 4.31:

$$\Delta J_t = 7.972 \times 10^{-3} \Delta \sigma_t^2 a + 47.72 (\Delta \sigma_t \Delta \epsilon_p a) \quad (4.40)$$

where the units are:  $\Delta \sigma_t$  in MPa,  $a$  in meters,  $\Delta \epsilon_p$  in % and the resulting  $\Delta J_t$  in  $\text{kPa} \cdot \text{m}$ .

Crack growth rates versus  $\Delta J_t$  are shown in Figure 4.30, 4.31 and 4.32. The consolidation of crack growth rates with  $\Delta J_t$  is excellent for both elastic and elastic-plastic fatigue conditions. Note that  $\Delta J_t$  includes the total stress range and thus accounts for the compressive stress-strain excursion as did  $\Delta PK$ . In fact, the consolidation of crack growth rates with  $\Delta J_t$  is nearly the same as that seen for  $\Delta PK$  in Figures 4.26, 4.27 and 4.28. Additionally, there is an equivalent correlation in terms of  $\Delta K_{eq}$  when  $q_0=1$ , that is when  $\Delta K_{eq}=\Delta PK$ .

Starkey and Skelton [2.54] have shown that  $\Delta J_t$  can be related to  $\Delta K_{eq}$  by

$$\Delta J_t \propto \frac{\Delta K_{eq}^2}{E} \quad (4.41)$$

and when  $q_0=1$

$$\Delta K_{eq} = \Delta PK = YE \Delta \epsilon_t \sqrt{\pi a} \quad (4.42)$$

Substituting Eq. 4.42 into Eq. 4.41 and rearranging

$$\frac{\Delta J_t / a}{\Delta \epsilon_t^2} = r \quad (4.43)$$

The ratio,  $r$ , was calculated and found to be nearly constant for all tests as shown in Table 4.4. For the elastic tests,  $r$  is constant and is equal to 35 from the definition of  $\Delta J_e$ . For the elastic-plastic tests,  $r$  ranged from 35.61 ( $\Delta \epsilon_t=0.63\%$ ) to 37.85 ( $\Delta \epsilon_t=1.23\%$ ) and is nearly equivalent to the  $r$ -value in the elastic tests. If we compare the columns  $\Delta \epsilon_p/\Delta \epsilon_t$  to  $\Delta J_p/\Delta J_t$  in Table 4.4, we find that the plastic component of  $\Delta PK$  ranges from 1.6% ( $\Delta \epsilon_t=0.63\%$ ) to

10.6% ( $\Delta\epsilon_t=1.23\%$ ) and that the plastic component of  $\Delta J_t$  ranges from 4.4% ( $\Delta\epsilon_t=0.63\%$ ) to 25.1% ( $\Delta\epsilon_t=1.23\%$ ). The fractional plastic component of  $\Delta J_t$  is ~2.5 times greater than that for  $\Delta PK$  in every case. The plastic component of the crack driving force is seen to increase in its contribution to the total as  $\Delta\epsilon_p$  becomes larger. In the disk relevant strain-life regime, where  $\Delta\epsilon_p$  must be very small, the success of  $\Delta J_t$  and  $\Delta PK$  in correlating crack growth may lie, not so much in the ability to account for the inelastic strain range, but in the ability to account for both the tensile and compressive components of the total strain range. This postulate has been discussed in previous sections with respect to  $\overline{\Delta K}$  - Walker and  $\Delta PK$ .

The importance of including the total stress-strain range in the calculation of  $\Delta J$  can also be demonstrated. Based on the assumption that only the positive portion of the hysteresis loop contributes to crack growth, Réger et al. [2.64, 2.65] substituted the positive stress range for the total stress range in calculating  $\Delta J^*$ . The resulting J-integral range may be expressed as:

$$\Delta J^* = Y^2 \frac{\Delta\sigma_{\text{pos}}^2 \pi a}{E} + Y^2 (\Delta\sigma_{\text{pos}} \Delta\epsilon_p a) \left\{ 3.85 \frac{(1-n)}{\sqrt{n}} \right\} \quad (4.44)$$

Crack growth rates versus  $\Delta J^*$  are shown in Figure 4.33 for the elastic-plastic tests. The consolidation of crack growth rates is poor compared to that obtained using the total stress range as shown in Figure 4.30. This further corroborates the theme that the total stress-strain range must be used to express the mechanical driving force for crack growth under elastic-plastic conditions.

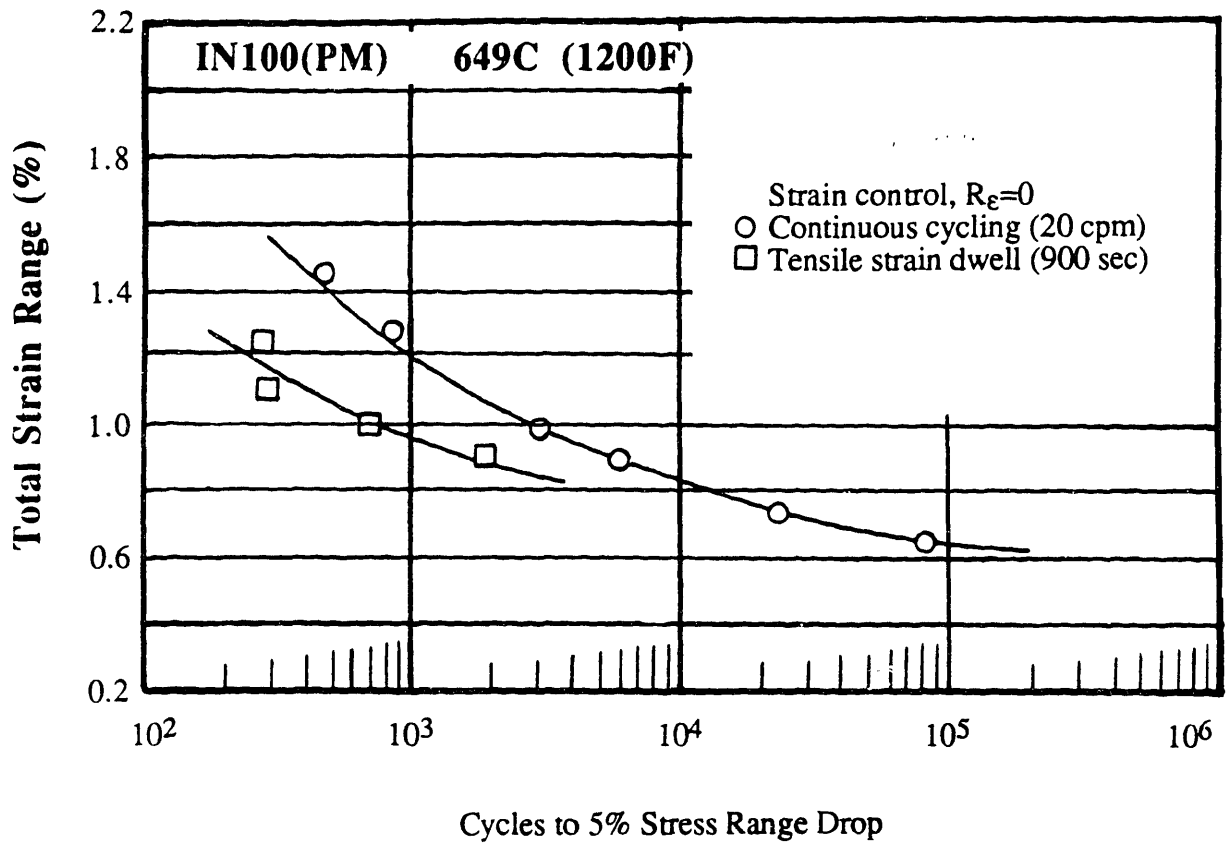


Figure 4.21 Total strain range versus cycles to a 5% stress range drop for IN100(PM) tested at 649C under continuous cycling and tensile strain dwell conditions, Ref [4.23].

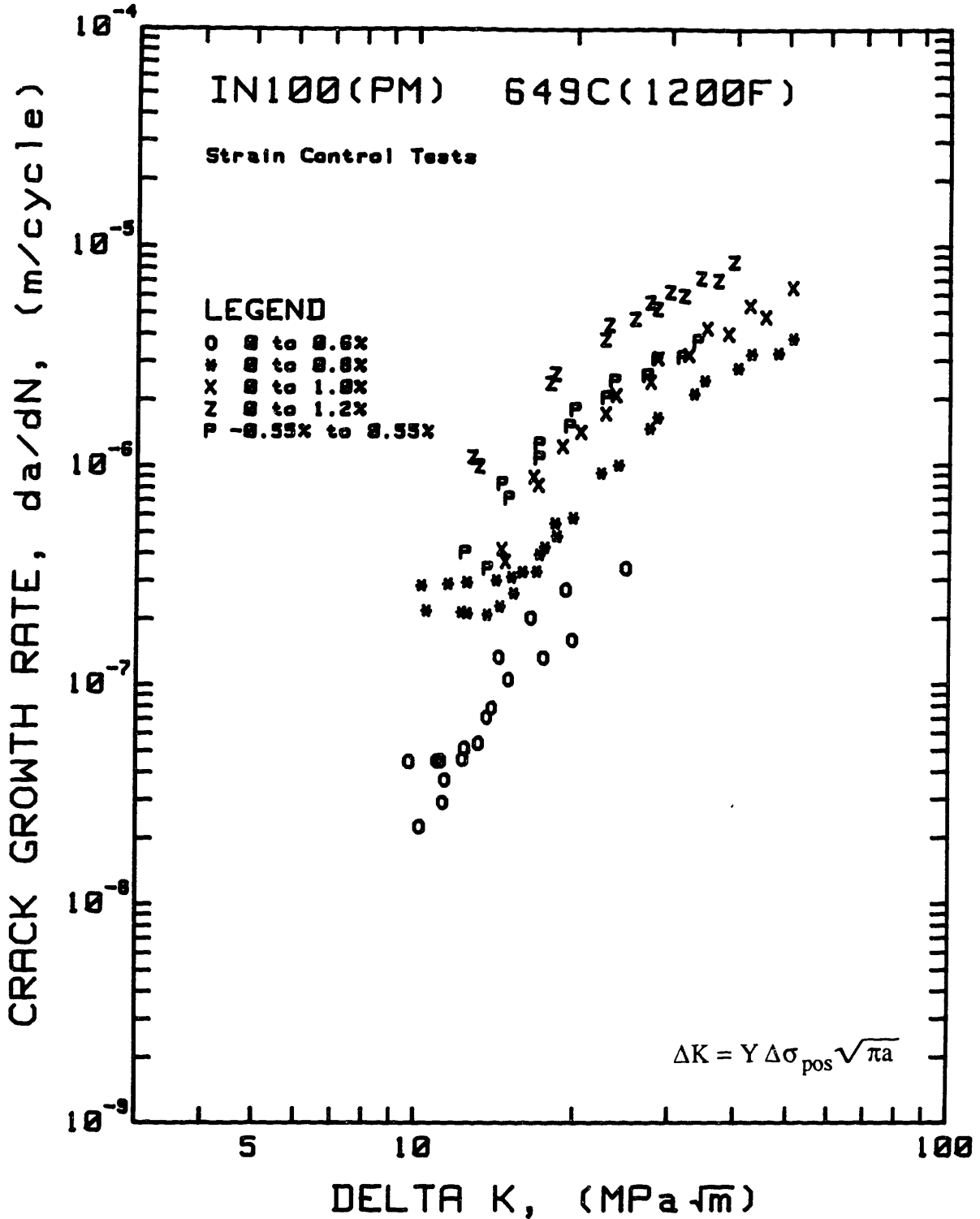


Figure 4.22 Crack growth rates versus stress intensity factor range for IN100(PM) tested at 649C under elastic-plastic fatigue conditions; total strain range was varied, Freq. = 10 cpm.

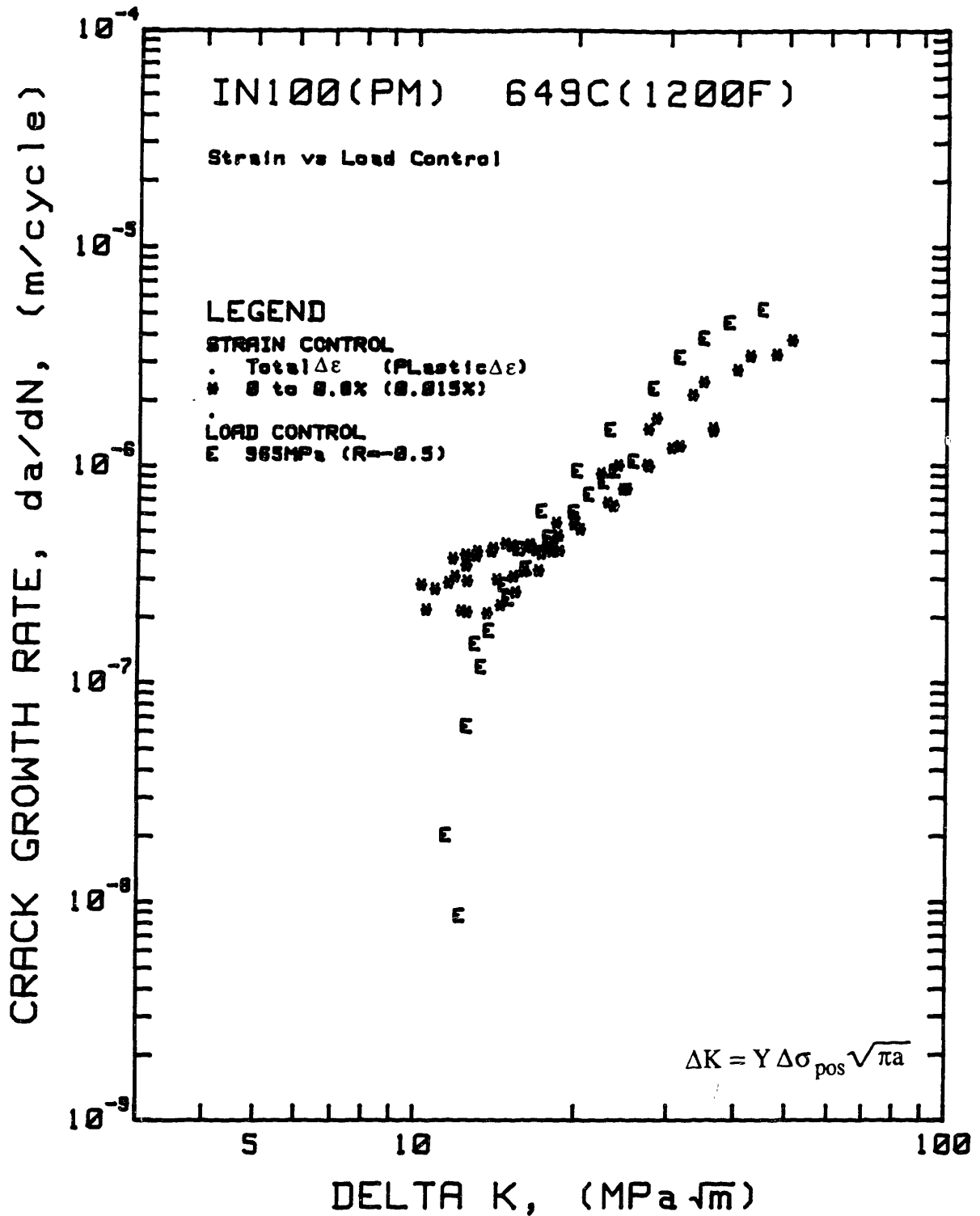


Figure 4.23 Crack growth rates versus stress intensity factor range for IN100(PM) tested at 649C under elastic and elastic-plastic fatigue conditions;  $R_{\sigma} \approx -0.5$  in both cases, Freq. = 10 cpm.

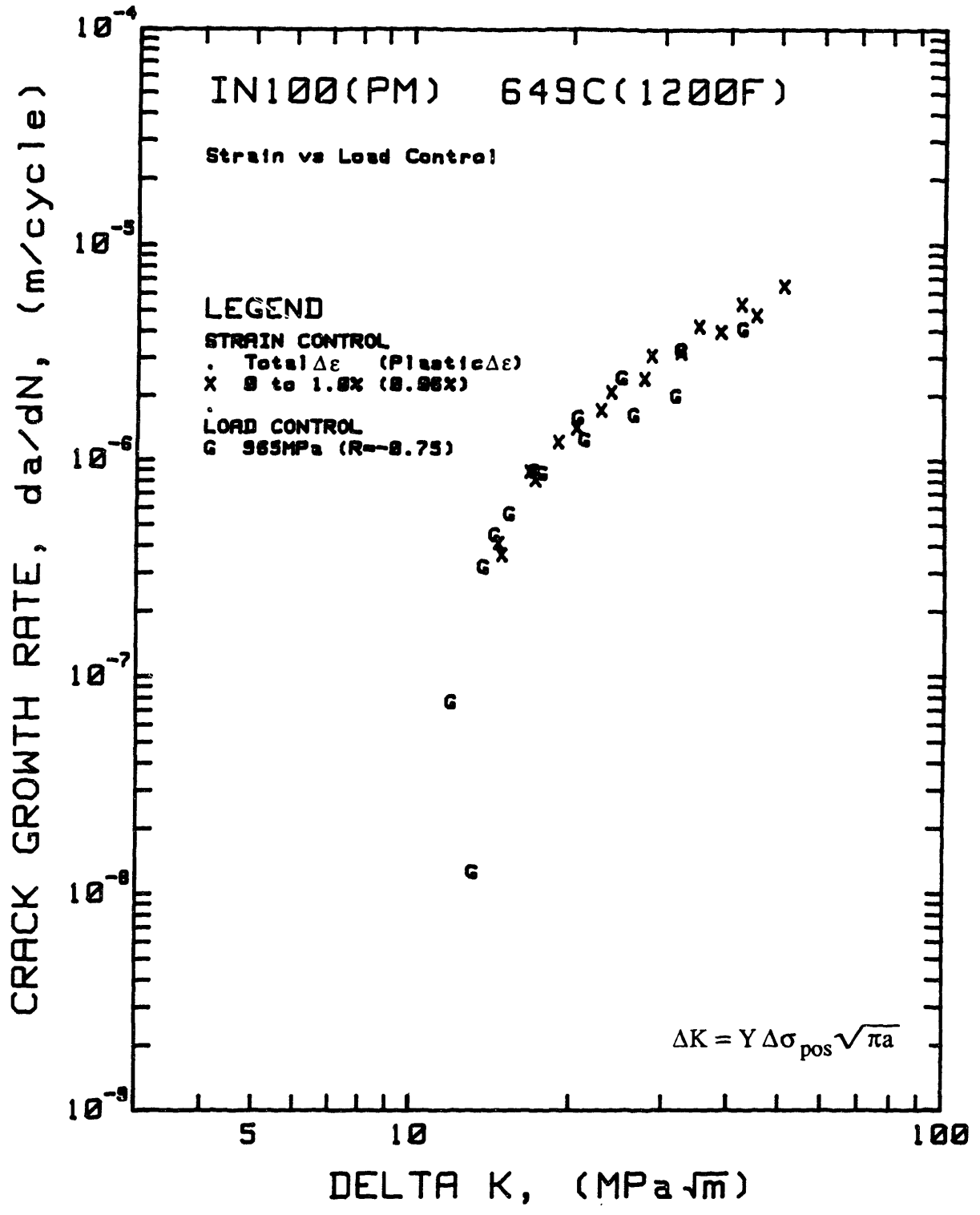


Figure 4.24 Crack growth rates versus stress intensity factor range for IN100(PM) tested at 649C under elastic and elastic-plastic fatigue conditions;  $R_{\sigma} \approx -0.75$  in both cases, Freq. = 10 cpm.

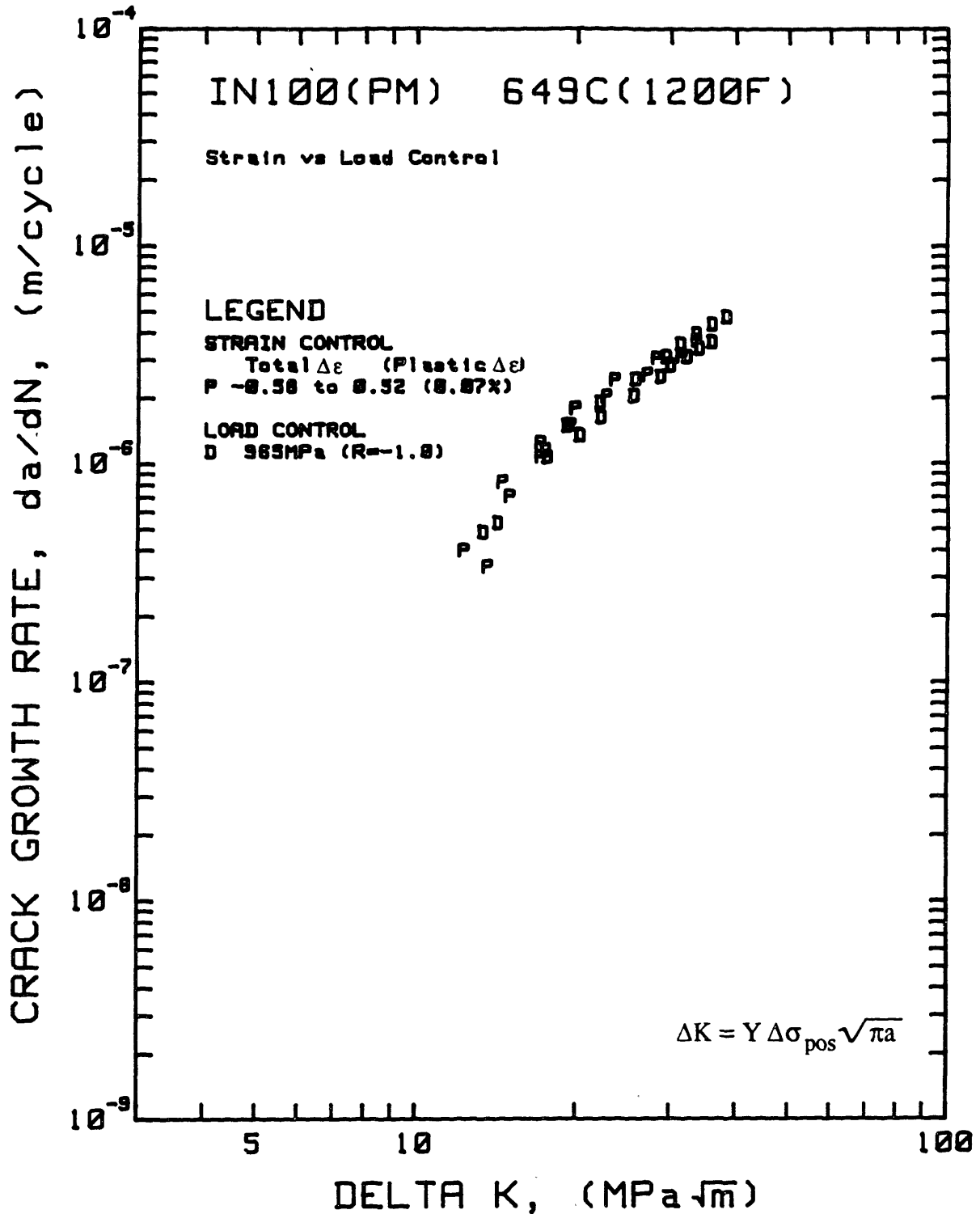


Figure 4.25 Crack growth rates versus stress intensity factor range for IN100(PM) tested at 649C under elastic and elastic-plastic fatigue conditions;  $R_{\sigma} \approx -1.0$  in both cases, Freq. = 10 cpm.

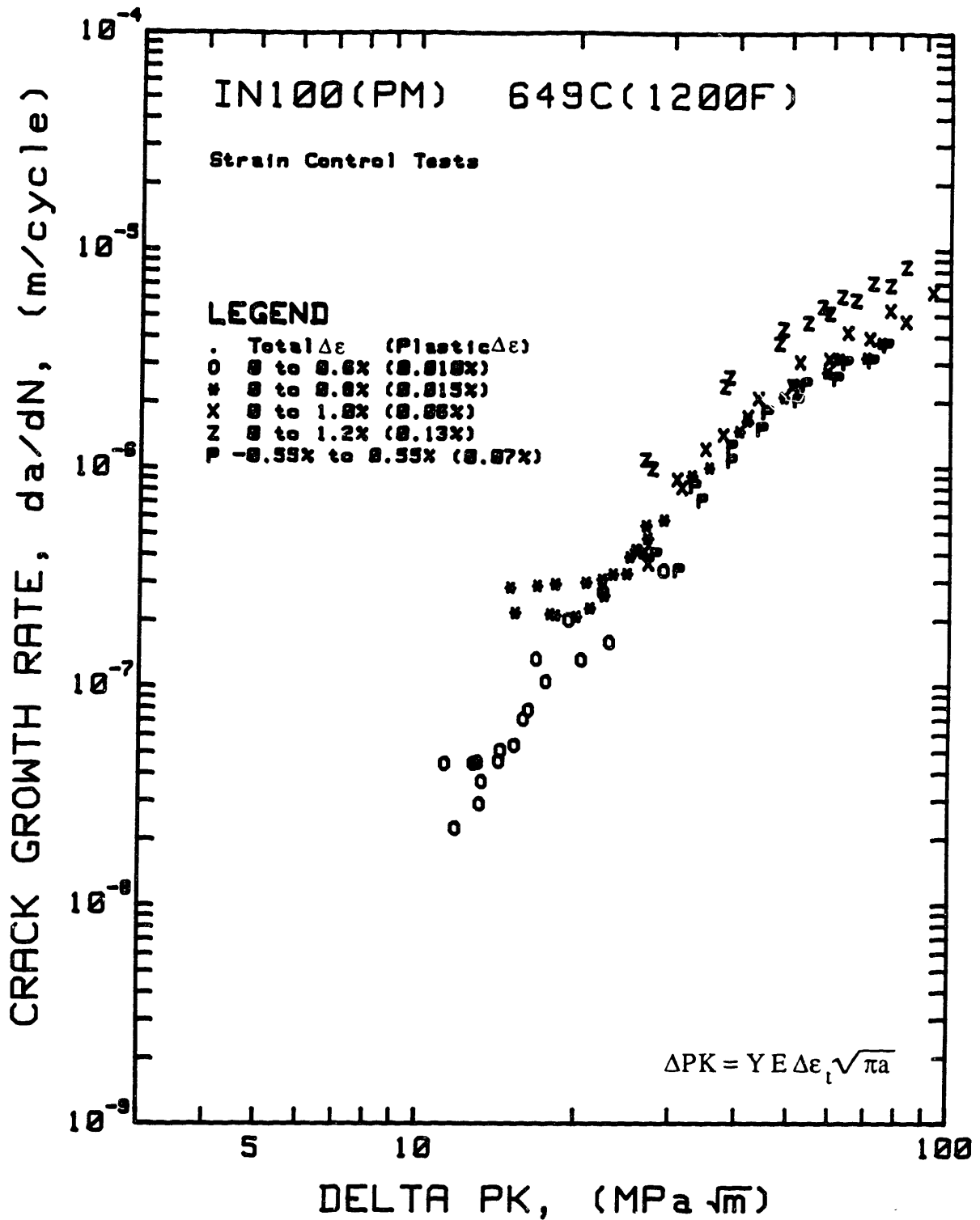


Figure 4.26 Crack growth rates versus the pseudostress intensity factor range for IN100(PM) tested at 649C under elastic-plastic fatigue conditions; total strain range was varied, Freq. = 10 cpm.

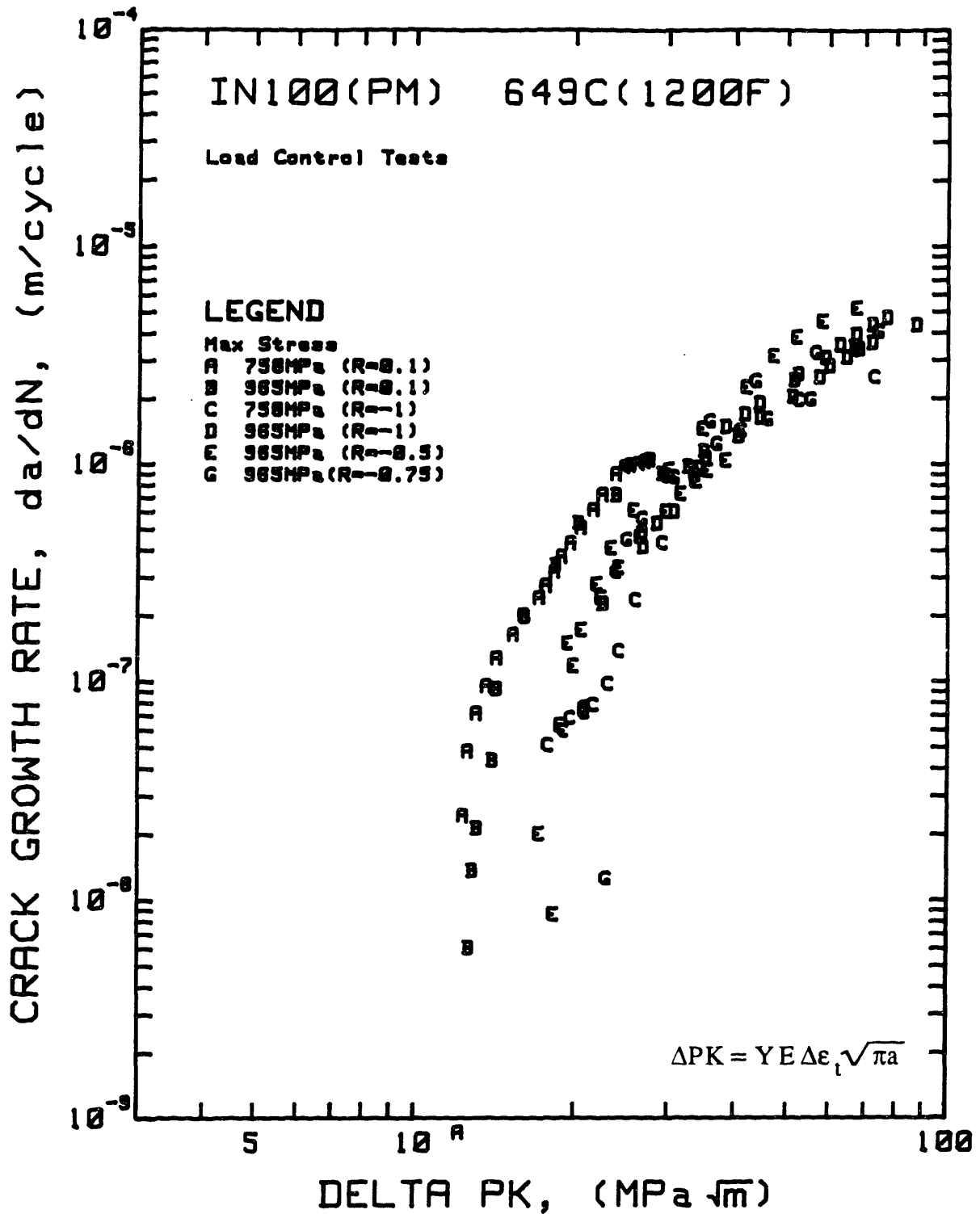


Figure 4.27 Crack growth rates versus the pseudostress intensity factor range for IN100(PM) tested at 649C under elastic fatigue conditions; total stress range was varied, Freq. = 10 cpm.

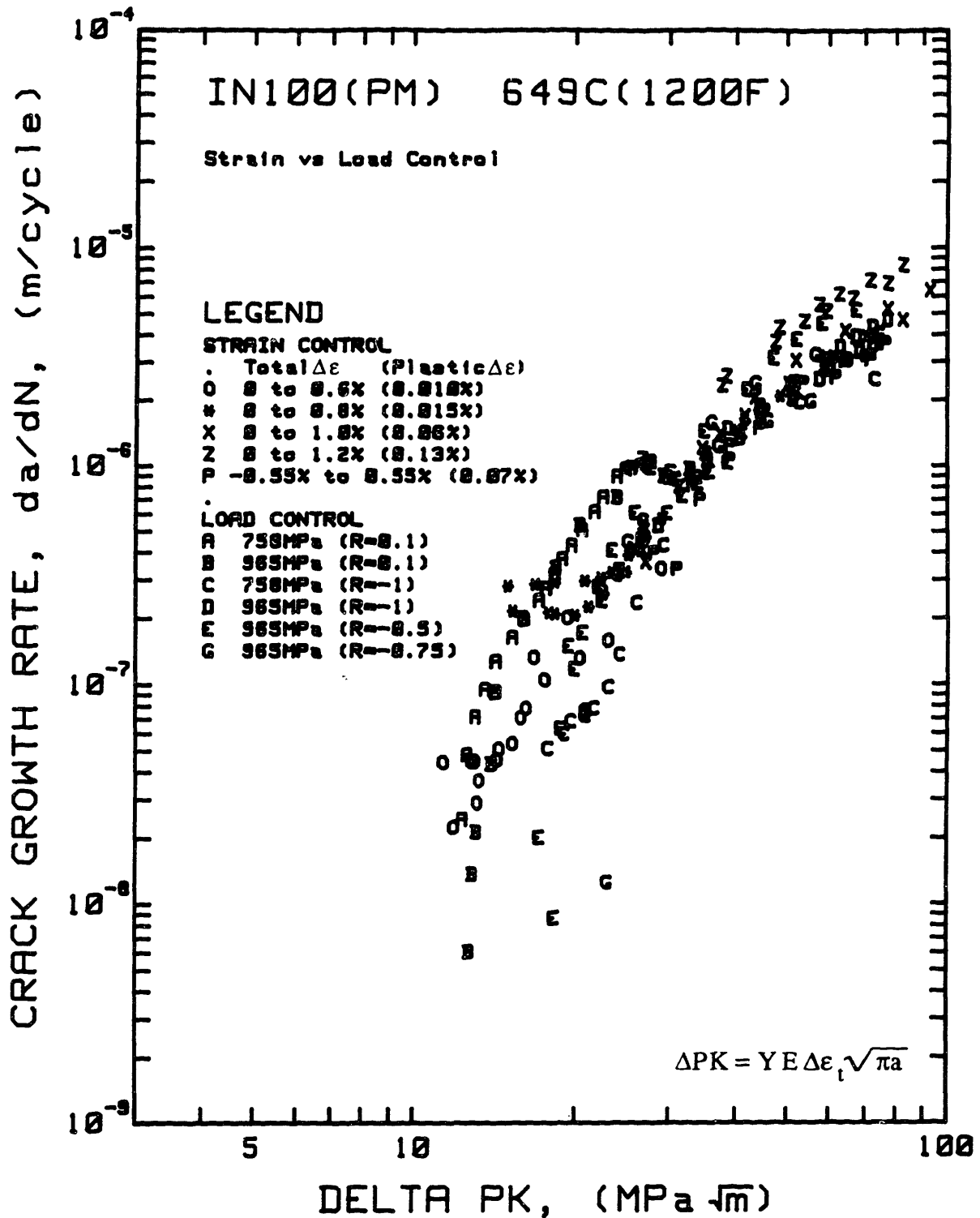


Figure 4.28 Summary of crack growth rates versus the pseudostress intensity factor range for IN100(PM) tested at 649C under elastic and elastic-plastic fatigue conditions; Freq. = 10 cpm.

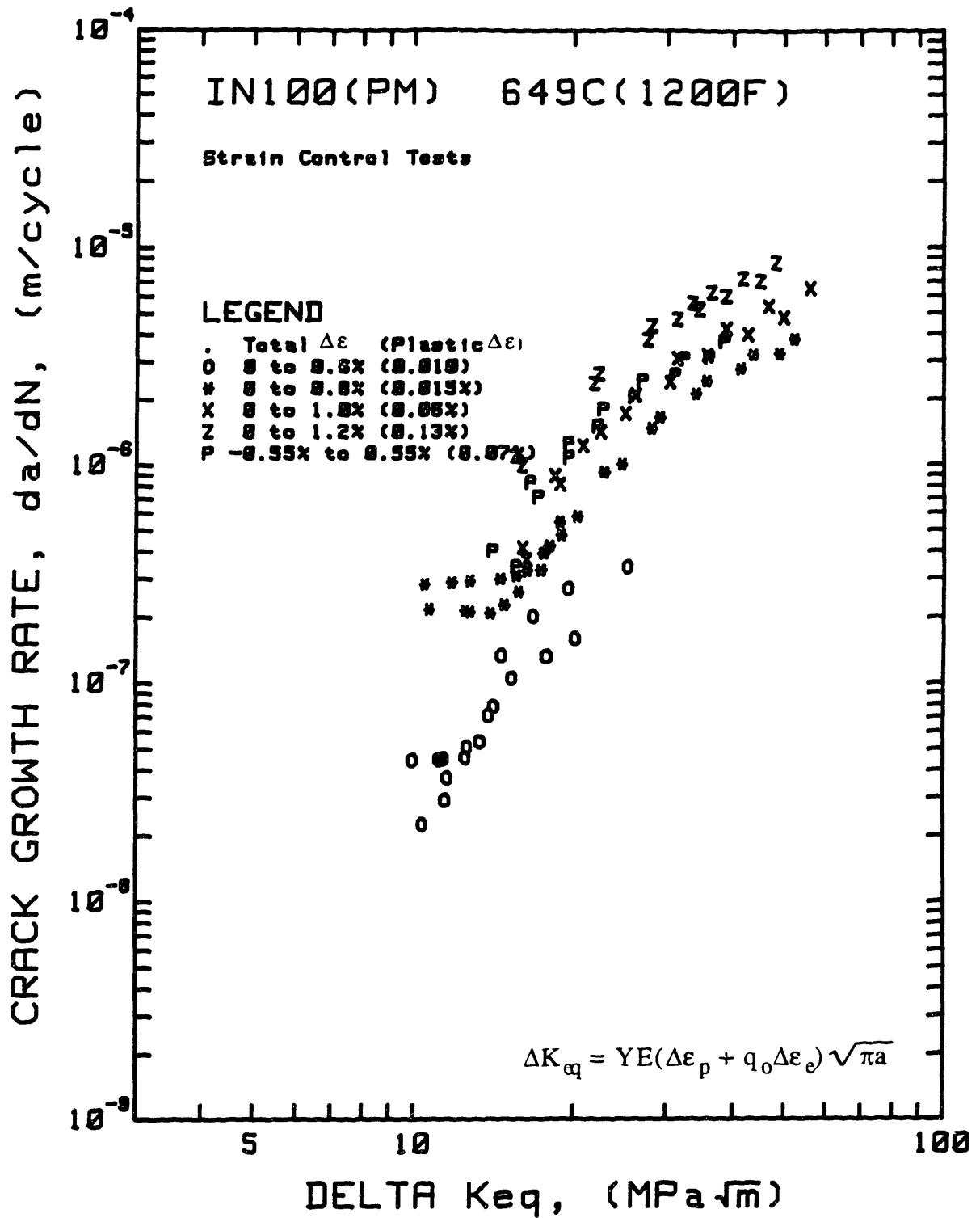


Figure 4.29 Crack growth rates versus the equivalent stress intensity factor range for IN100(PM) tested at 649C under elastic-plastic fatigue conditions; total strain range was varied, Freq. = 10 cpm.

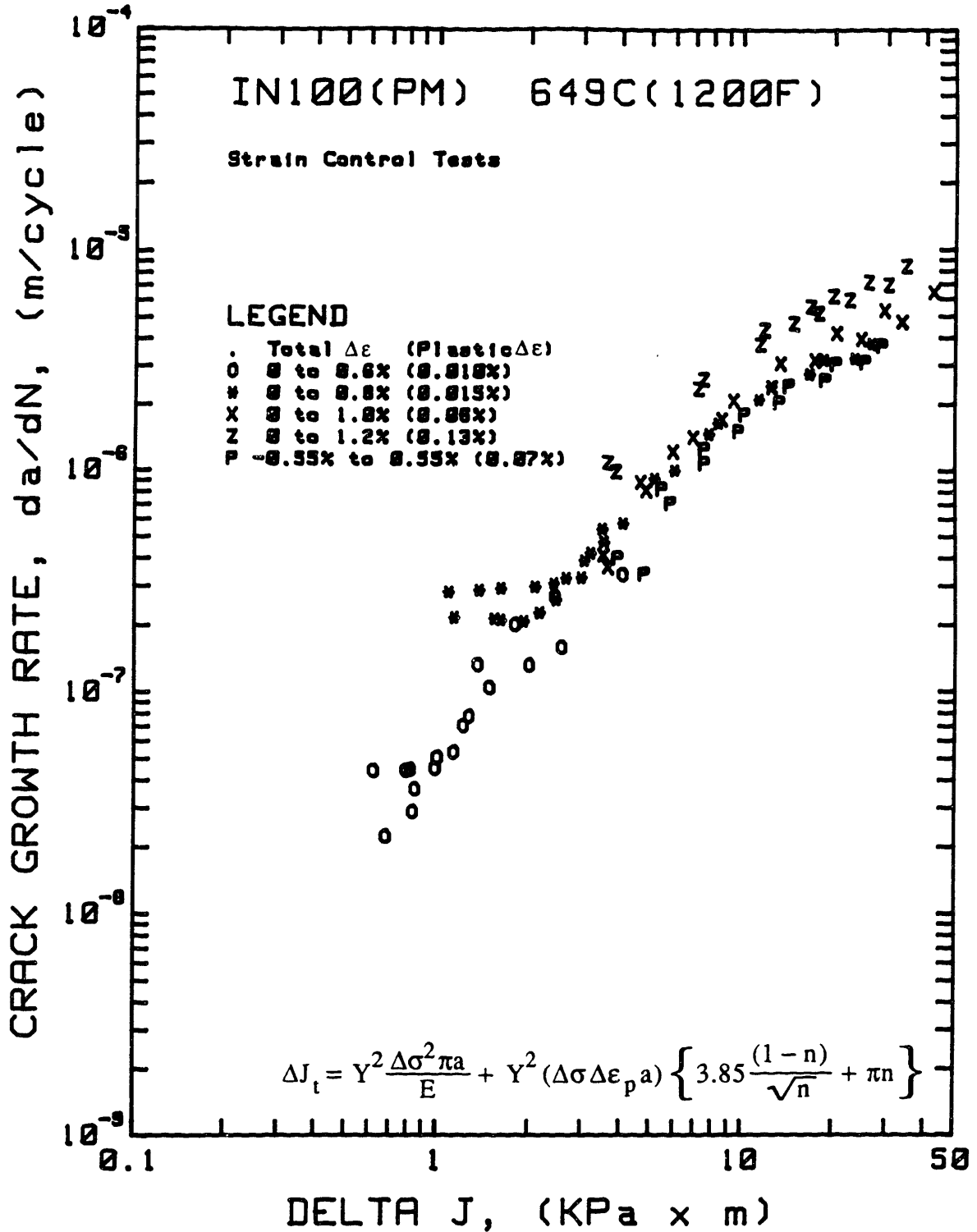


Figure 4.30 Crack growth rates versus the cyclic J-integral range for IN100(PM) tested at 649C under elastic-plastic fatigue conditions; total strain range was varied, Freq. = 10 cpm.

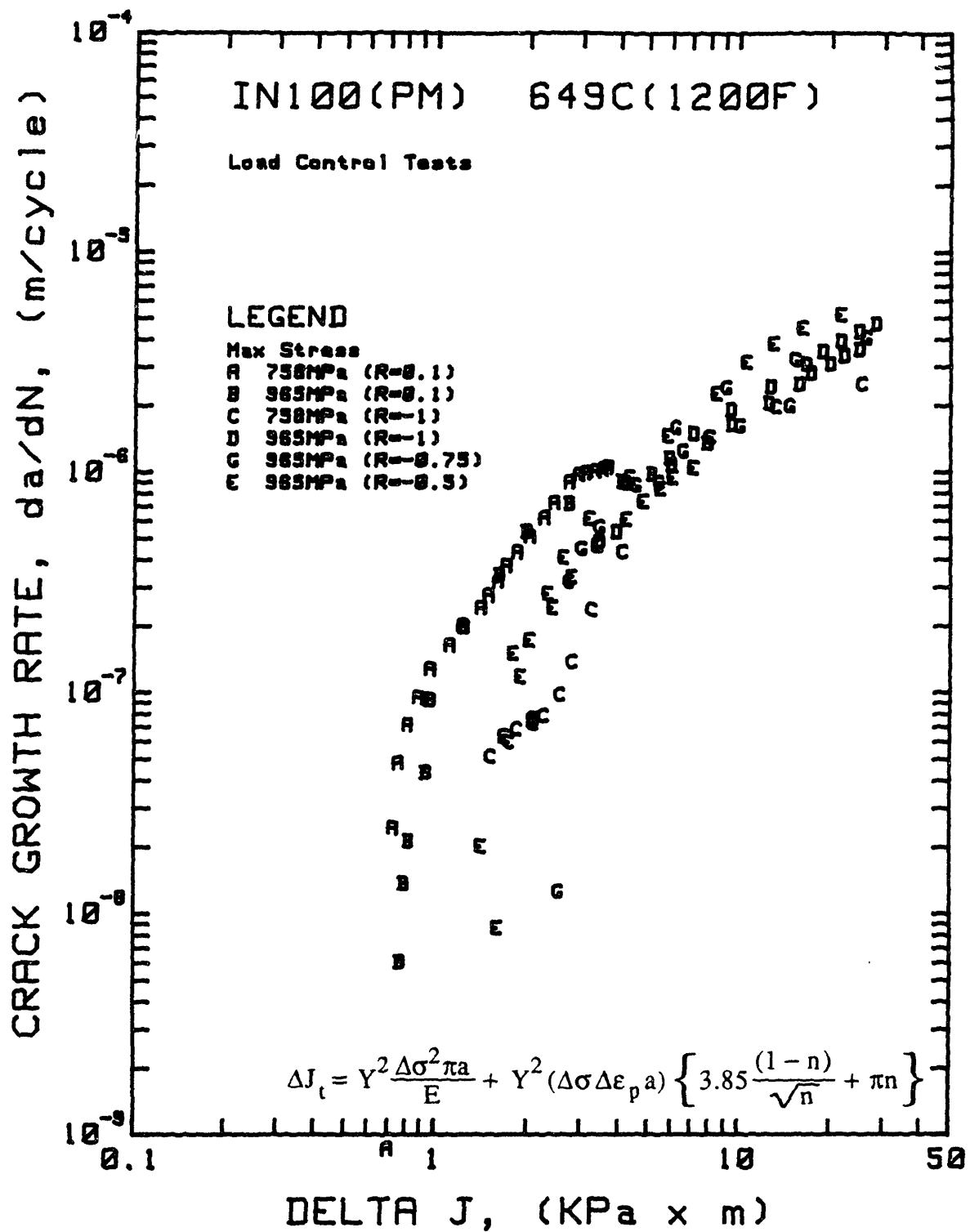


Figure 4.31 Crack growth rates versus the cyclic J-integral range for IN100(PM) tested at 649C under elastic fatigue conditions; total stress range was varied, Freq. = 10 cpm.

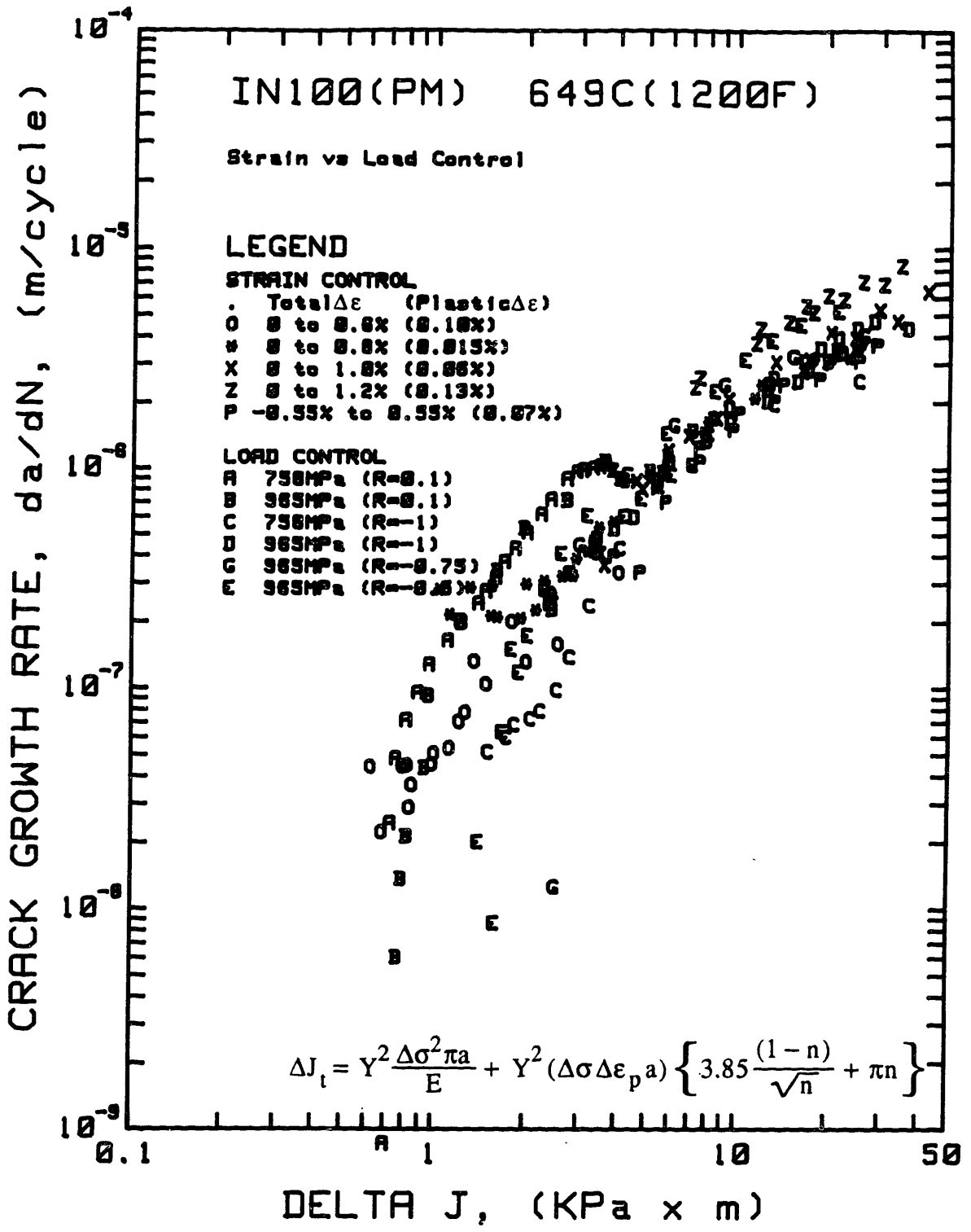


Figure 4.32 Summary of crack growth rates versus the cyclic J-integral range for IN100(PM) tested at 649C under elastic and elastic-plastic fatigue conditions; Freq. = 10 cpm.

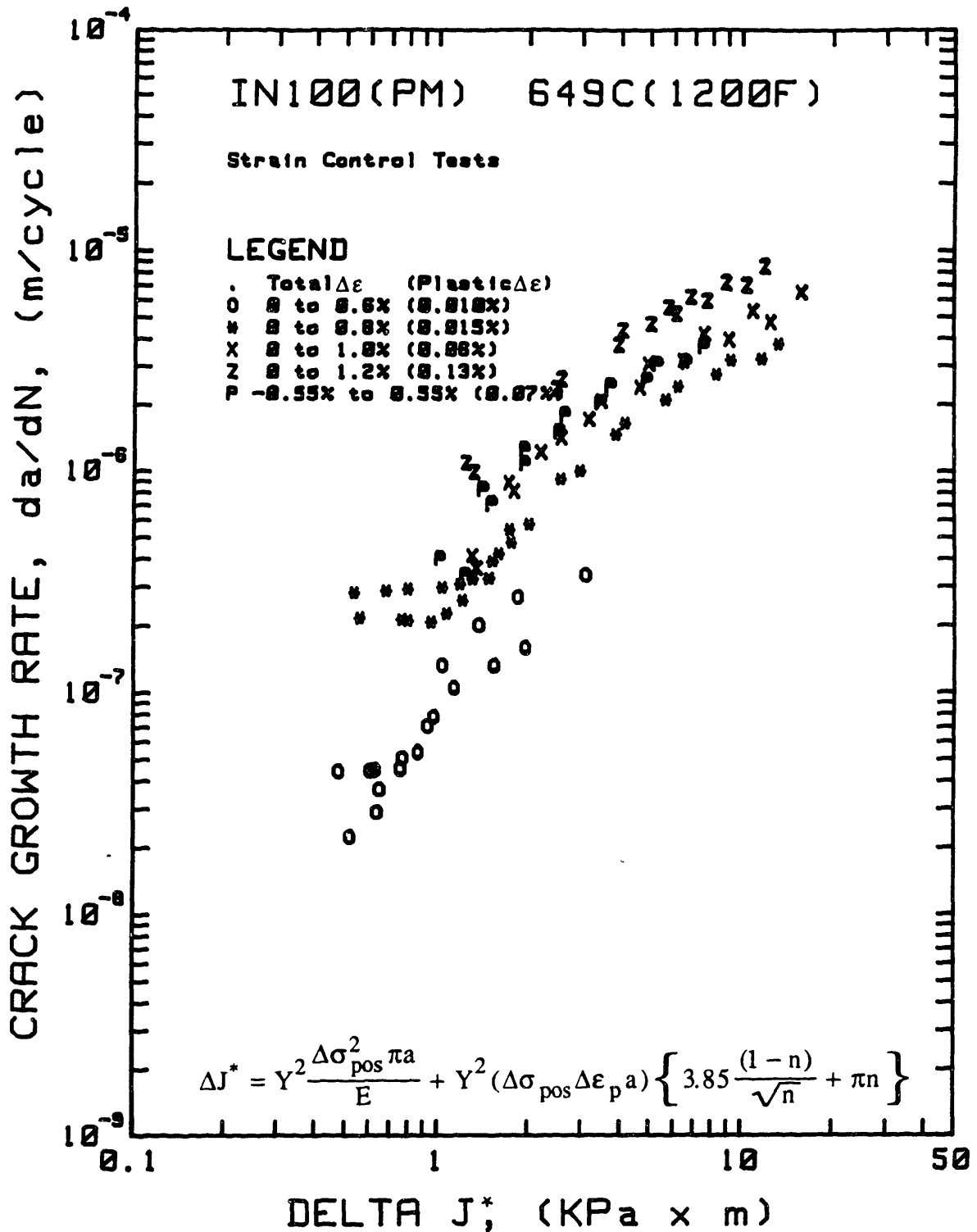


Figure 4.33 Crack growth rates versus the positive J-integral range for IN100(PM) tested at 649C under elastic-plastic fatigue conditions; only  $\Delta\sigma_{\text{pos}}$  was used to calculate  $\Delta J$ , Freq. = 10 cpm.

**Table 4.4**  
**Components of Strain Range and J-integral Range for IN100(PM) at 649C**

Test #	$\Delta\sigma_{tot}$ MPa	$\Delta\epsilon_{tot}$ %	$\Delta\epsilon_p$ %	$\Delta\epsilon_p/\Delta\epsilon_t$	$\Delta J_e/a$ MPa	$\Delta J_p/a$ MPa	$\Delta J/a$ MPa	$\Delta J_p/\Delta J_t$	$(\Delta J/a)/\Delta\epsilon_t^2$ I
<u>elastic tests</u>									
GR16	682	0.325	0	0	3.71	0	3.71	0	35.11
GR23	868	0.414	0	0	6.01	0	6.01	0	35.04
GR19	1930	0.921	0	0	29.69	0	29.69	0	35.01
GR30	1930	0.921	0	0	29.69	0	29.69	0	35.01
GR31	1517	0.723	0	0	18.35	0	18.35	0	35.10
GR32	1448	0.690	0	0	16.71	0	16.71	0	35.11
GR33	1690	0.806	0	0	22.77	0	22.77	0	35.05
<u>elastic-plastic tests</u>									
GR20	1304	0.631	0.010	0.0158	13.56	0.62	14.18	0.044	35.61
GR21	1694	0.822	0.015	0.0182	22.88	1.21	24.09	0.050	35.65
GR17	1659	0.805	0.015	0.0186	21.94	1.19	23.13	0.051	35.69
GR24	2075	1.048	0.060	0.0573	34.32	5.94	40.27	0.148	36.66
GR34	2319	1.230	0.130	0.1057	42.87	14.39	57.26	0.251	37.85
GR14	2178	1.107	0.070	0.0632	37.82	7.28	45.09	0.161	36.80
GR22	1666	0.818	0.025	0.0306	22.13	1.99	24.11	0.082	36.04

## 4.6 Appendant Studies for IN100(PM) at 649C

### Continuous Cycling, $\Delta\epsilon_t = 0$ to 0.8%

An interesting feature of the  $\Delta\epsilon_t = 0$  to 0.8% ( $\Delta\epsilon_p = 0.015\%$ ) test condition can be seen throughout Section 4.5 where crack growth rates are plotted versus various elastic and elastic-plastic fracture mechanics parameters. Regardless of the parameter employed;  $\Delta K$ ,  $\Delta K_{eq}$ ,  $\Delta PK$  or  $\Delta J$ , there exists a region of constant crack growth rate ( $\sim 3 \times 10^{-7}$  m/cycle) over the crack length range from 60  $\mu\text{m}$  to 250  $\mu\text{m}$ . A corresponding linear regime also exists in the  $a$  versus  $N$  curves.

To substantiate that this observation was not due to experimental error, a duplicate test was performed. The same behavior resulted. To further prove that this anomaly was not due to the data processing scheme; crack growth rates were calculated by both the secant and incremental polynomial methods. The results are shown in Figure 4.34 where crack growth rates are plotted versus " $\Delta K$ " for two tests (4 cracks). This behavior is real, reproducible and may be a result of near surface elements in the test specimens experiencing a greater equivalent plastic strain range due to the reduced constraint there. The  $\Delta\epsilon_t = 0$  to 0.8% test condition represents the borderline strain range between the elastic and elastic-plastic fatigue conditions. It can certainly be stated that this strain range and the resulting high crack growth rates preclude any threshold behavior, i.e. nonpropagating cracks.

### Strain Hold Test; $\Delta\epsilon_t = 0$ to 0.8%

The effect of introducing a 60 second strain hold at maximum strain was considered for the 0 to 0.8% total strain range condition. The results are shown in Figure 4.35 where the hold time results are compared to continuous cycling (10 cpm) test results. Comparable crack growth rates are observed in an initial crack length regime, whereafter, crack growth rates accelerated in the strain hold test. These higher crack growth rates may be attributed to a

greater environmental degradation occurring in the longer cycle period (66 seconds versus 6 seconds).

Alternatively, the higher crack growth rates may have resulted from the higher value of plastic strain range (0.025% versus 0.015%) due to stress relaxation in the strain hold test. Higher values of crack growth rates were observed for higher values of  $\Delta\varepsilon_p$  when results were evaluated in terms of  $\Delta K$  as shown in Figure 4.22. Even greater environmental degradation and stress relaxation would be expected in actual turbine disk service.

#### Crack Growth from Intrinsic Microporosity

Crack initiation was observed at intrinsic pores, particularly when the elastic limit ( $\varepsilon_0 = 0.5\%$ ,  $\sigma_0 = 1050$  MPa) was exceeded. A typical pore initiation site is shown in Figure 5.2. Crack growth rates were measured from surface and near surface pores in a number of smooth test specimens.

Typical results are shown in Figure 4.36 where crack growth rates for  $\Delta\varepsilon_t = 0$  to 0.8% test condition are plotted versus  $\Delta K$  for both crack initiation at pores ( $a_0 \approx 10$   $\mu\text{m}$ ) and laser defects ( $a_0 \approx 60$   $\mu\text{m}$ ). The maximum strain exceeded  $\varepsilon_0$  by 60% and the peak tensile stress exceeded  $\sigma_0$  by 9%. Here again, there is an absence of threshold behavior in the presence of very small values of cyclic plastic strain. This is in contrast to the apparent threshold behavior depicted in Figure 4.14 for cyclic stress ranges as high as 92% of  $\sigma_0$ . Crack growth rates from pores merge with results from laser defects as cracks become larger.

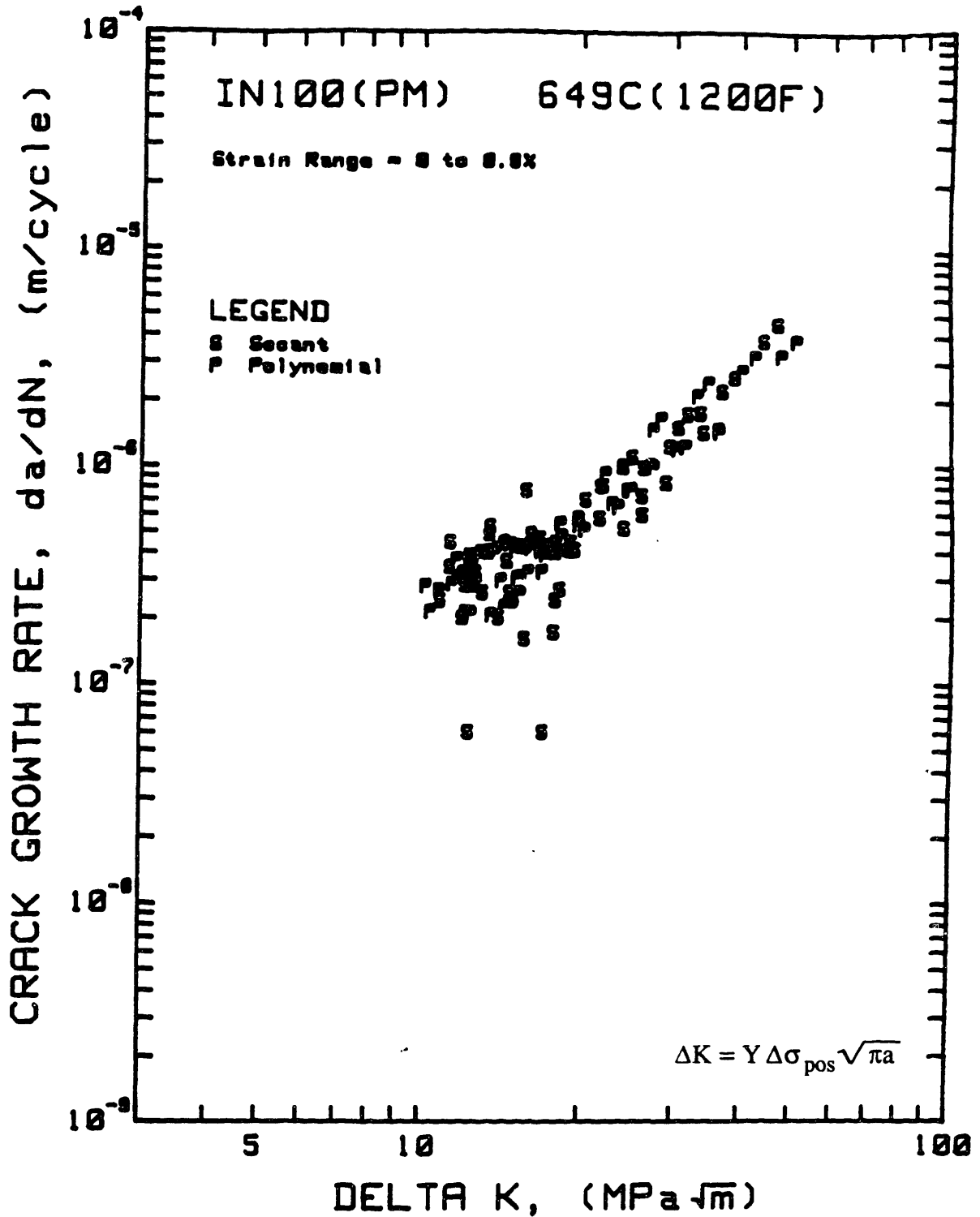


Figure 4.34 Crack growth rates versus  $\Delta K$  for two elastic-plastic tests at  $\Delta \epsilon_t = 0$  to 0.8%. Crack growth rates were determined by both the secant and 7-point polynomial technique.

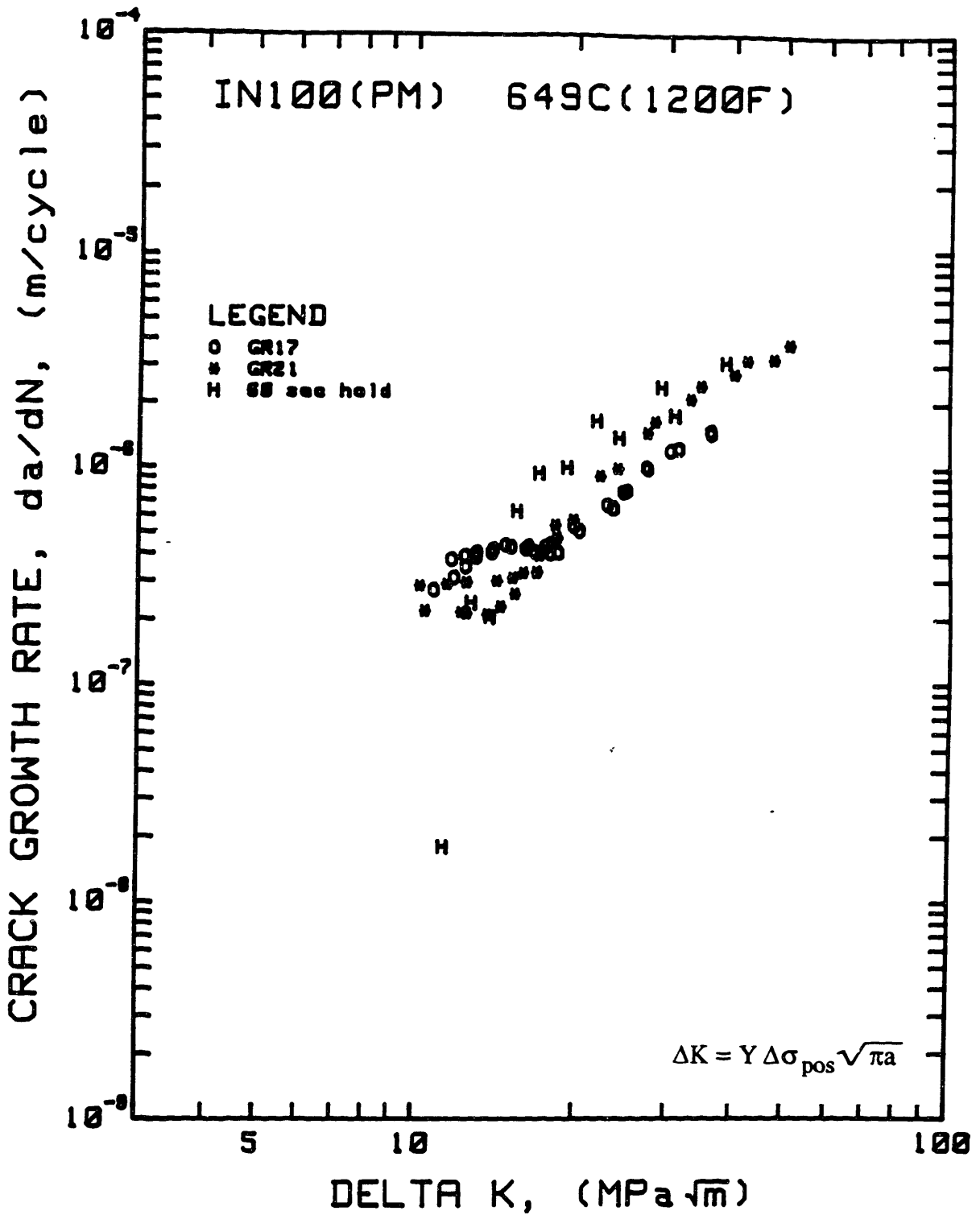


Figure 4.35 Crack growth rates versus  $\Delta K$  for elastic-plastic tests at  $\Delta \epsilon_t = 0$  to 0.8%. Comparison of continuous cycling data (10 cpm) with 60 sec hold at maximum strain data.

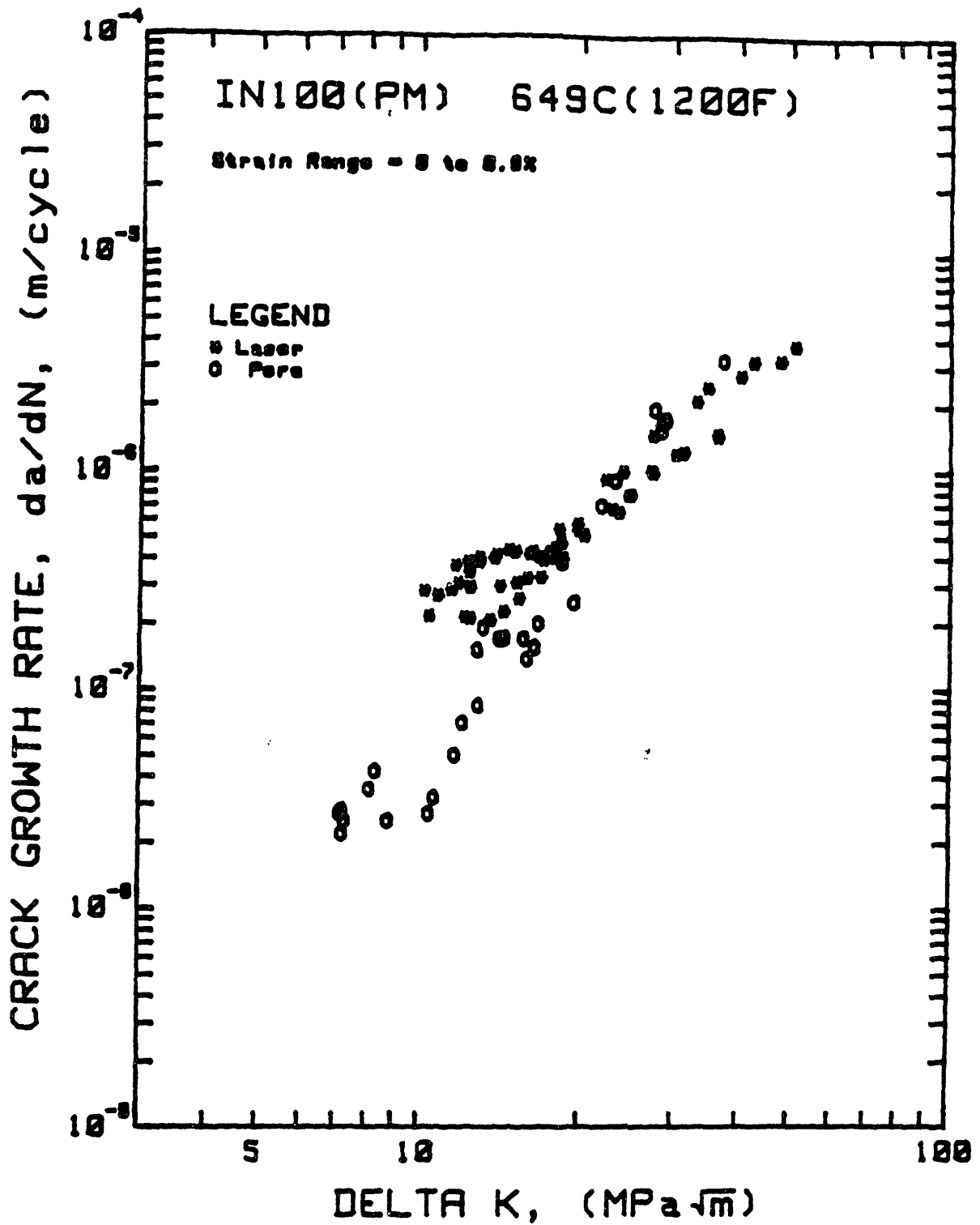


Figure 4.36 Crack growth rates versus  $\Delta K$  for elastic-plastic tests at  $\Delta\epsilon_t = 0$  to 0.8%. Comparison of crack growth behavior from pores to that from laser defects.

## 4.7 Fractography

### Waspaloy at 427C: Elastic Fatigue Conditions

Small crack fatigue tests were performed on Waspaloy at 427C under elastic conditions using the specimen geometry shown in Figure 3.4 (cylindrical gage section). Macroscopic fracture surface features are shown in Figure 4.37. The shape of cracks at the termination of high temperature testing was evident on fracture surfaces as a result of heat tinting. Cracks of different sizes were present in the same specimen due to the variability in the number of cycles required for initiation from the laser defects. In some cases, one or more cracks may have arrested. Careful measurements of surface crack length and depth indicate that the crack shape was approximately semicircular ( $c/a \approx 1$ ) and independent of crack depth. The fracture path is nominally perpendicular to the specimen axis with the exception of near-surface regions beyond a surface crack length of  $\sim 800 \mu\text{m}$  where the crack deflects out of plane. This was suspected to be related to the curvature of the specimen surface. Consequently, the specimen geometry was modified (Figure 3.5) to include two flats from which cracks were initiated. This solved the crack deflection problem. The crack deflection is believed to have caused slight deviation from  $c/a = 1$ . Although accounting for this slight change in crack geometry is tractable, it did not manifest itself in the crack growth behavior. Therefore, data reduction was carried out in the manner described in Chapter 3.

Typical fracture surface features can be seen in Figure 4.38. In Figure 4.38a the laser defect is shown surrounded by the precrack region which has assumed a semicircular crack front prior to high temperature testing. Figure 4.38b shows typical fracture surface features which were observed to be independent of crack length, stress range and R-ratio for the test conditions considered. The fracture path is transgranular and similar to that observed for room temperature tests. However, fatigue fracture paths in room temperature tests exhibited

greater deviation from the nominal fracture plane than was observed in 427C tests, particularly at low values of  $\Delta K$ . This was established by stereographic observations.

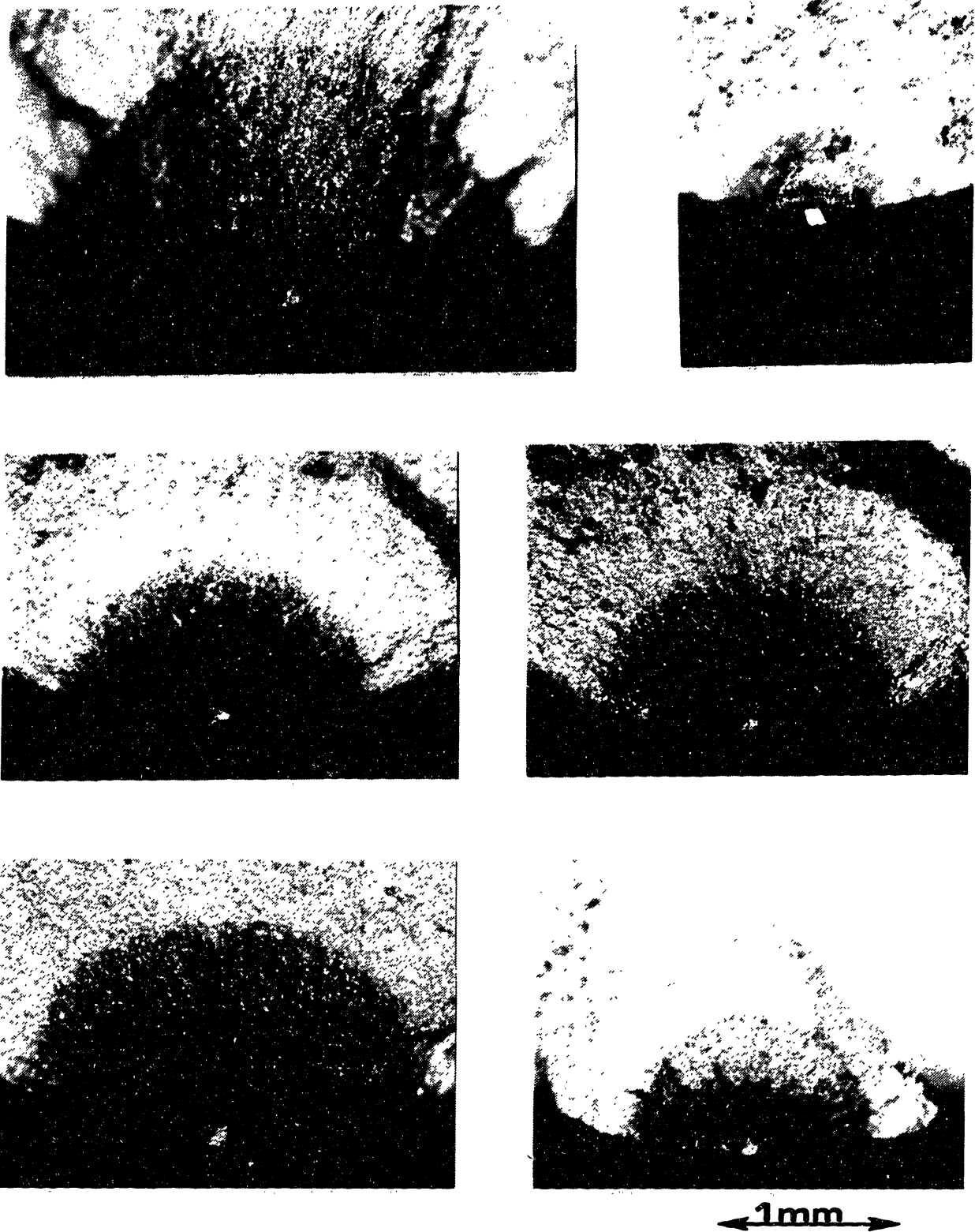


Figure 4.37 Crack front profiles as evidenced by the presence of oxidation on the fracture surfaces of Waspaloy specimens tested at 427C under elastic fatigue conditions.

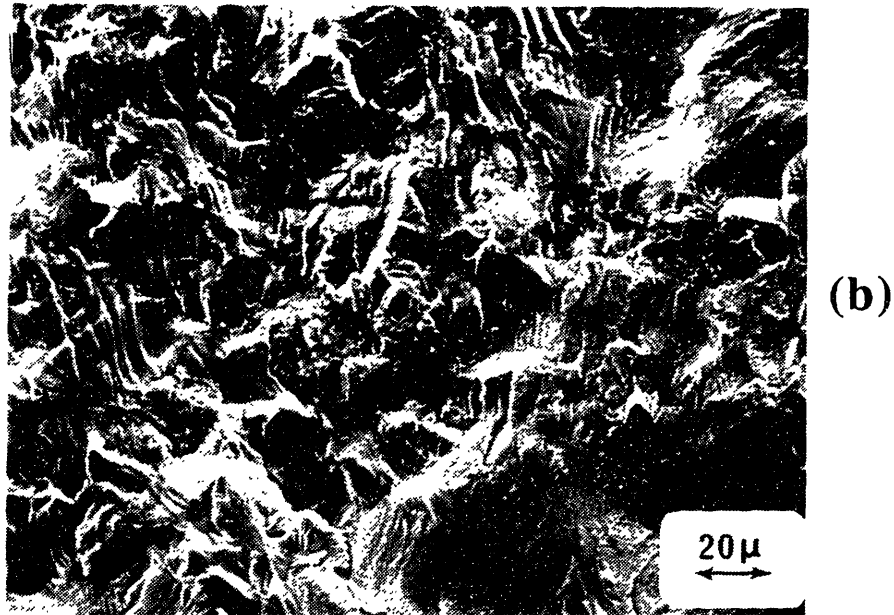
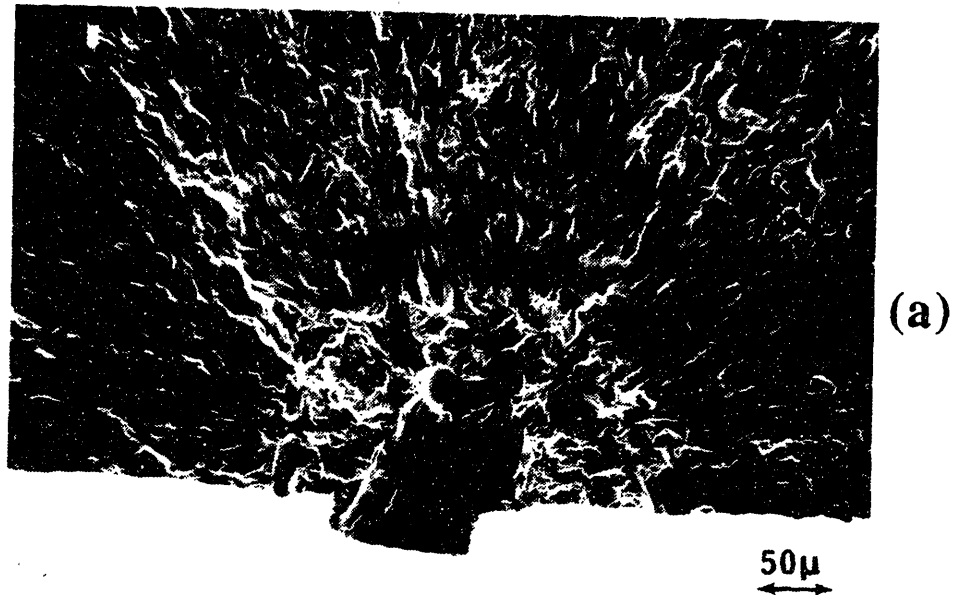


Figure 4.38 Fractographs of Waspaloy tested at 427C under nominally elastic fatigue conditions; (a) laser defect surrounded by the precrack region, (b) typical transgranular fracture surface features.

### Inconel 718 at 427C: Elastic Fatigue Conditions

Small crack fatigue tests were performed on Inconel 718 at 427C under elastic conditions using the specimen geometry shown in Figure 3.5 (cylindrical gage section plus two flats). Macroscopic fracture surface features are shown in Figure 4.39 for two cracks. The crack front aspect ratio ranged from  $c/a = 1.0$  to 1.1. Since the variation in  $c/a$  could not be related to crack length or test conditions for the few tests performed here,  $c/a$  was taken to be one for purposes of calculating the stress intensity factor.

Optical micrographs of a typical surface crack trace shown in Figure 4.40 reveals the fracture path to be crystallographic and transgranular. On a local scale the crack deviates significantly from the nominally Mode I fracture plane. Crack extension generally occurred parallel to or perpendicular to persistent slip bands forming ahead of the crack tip.

Typical fracture surface features are shown in Figure 4.41. The fracture surfaces are crystallographic and exhibit a high degree of roughness.

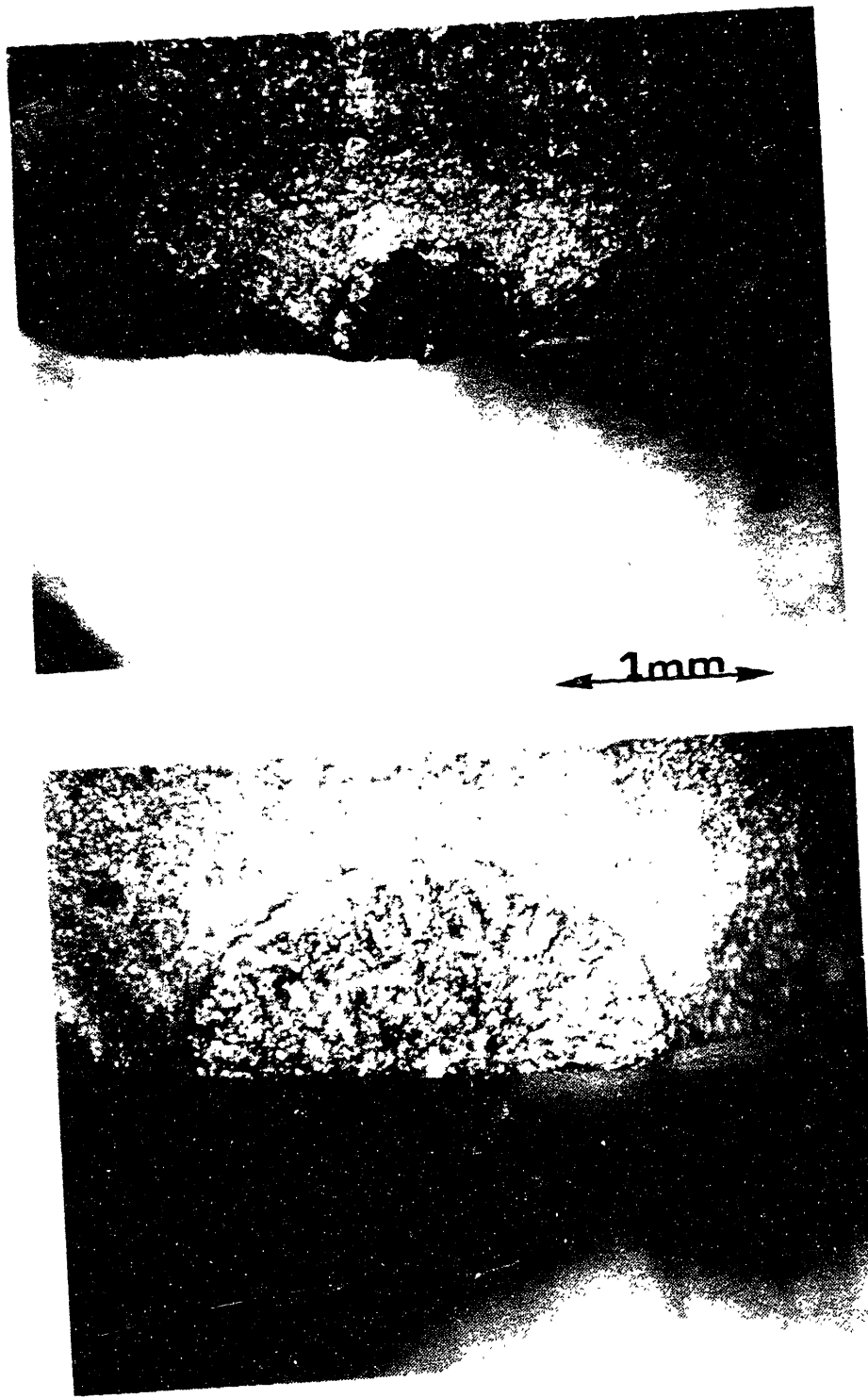


Figure 4.39 Typical crack front profiles as evidenced by the presence of oxidation on the fracture surfaces of Inconel 718 specimens tested at 427C under elastic fatigue conditions.

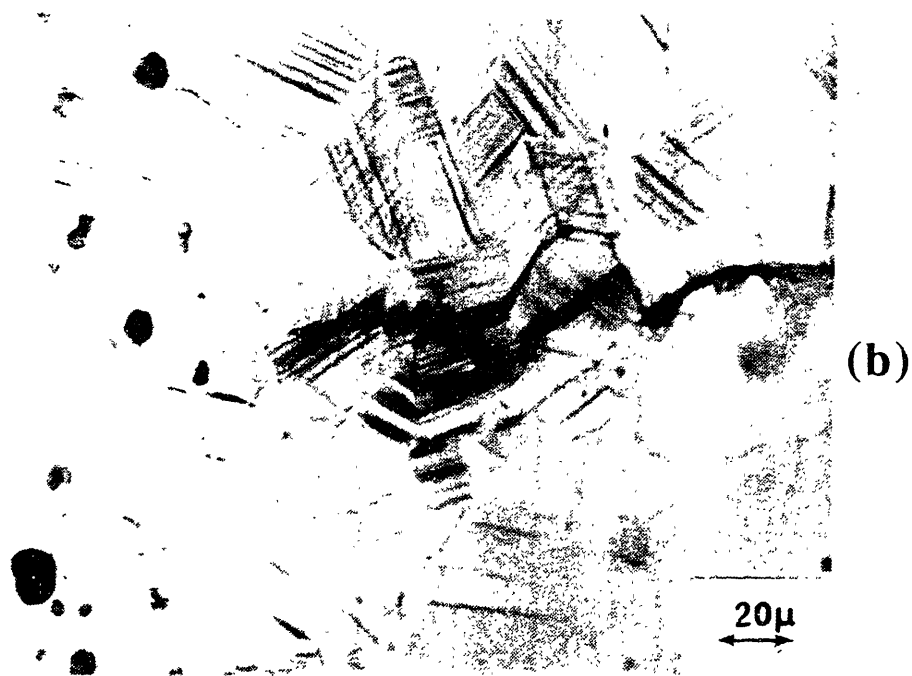
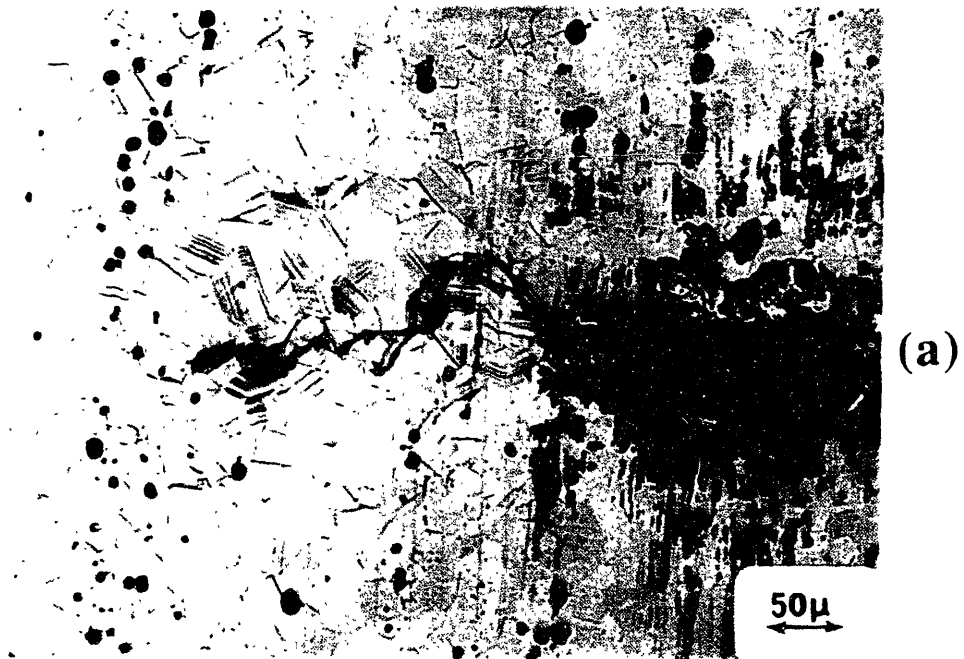


Figure 4.40 Optical micrographs of a typical surface crack trace in Inconel 718 tested at 427C under elastic fatigue conditions; (a) small crack propagating from laser defect, (b) crack tip extending parallel and perpendicular to persistent slip bands.

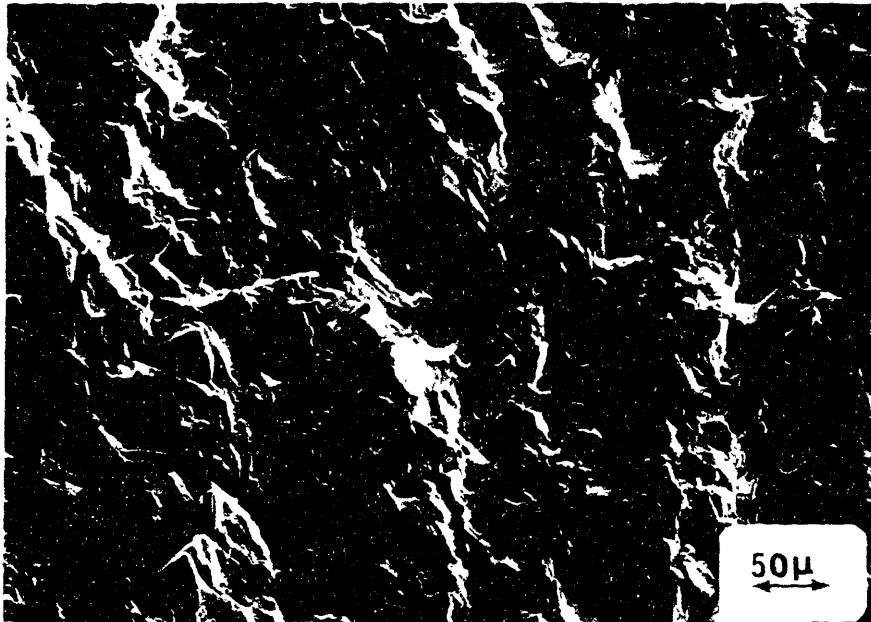


Figure 4.41 Typical transgranular fracture surface features for Inconel 718 tested at 427C under elastic fatigue conditions.

### IN100(PM) at 649C: Elastic Fatigue Conditions

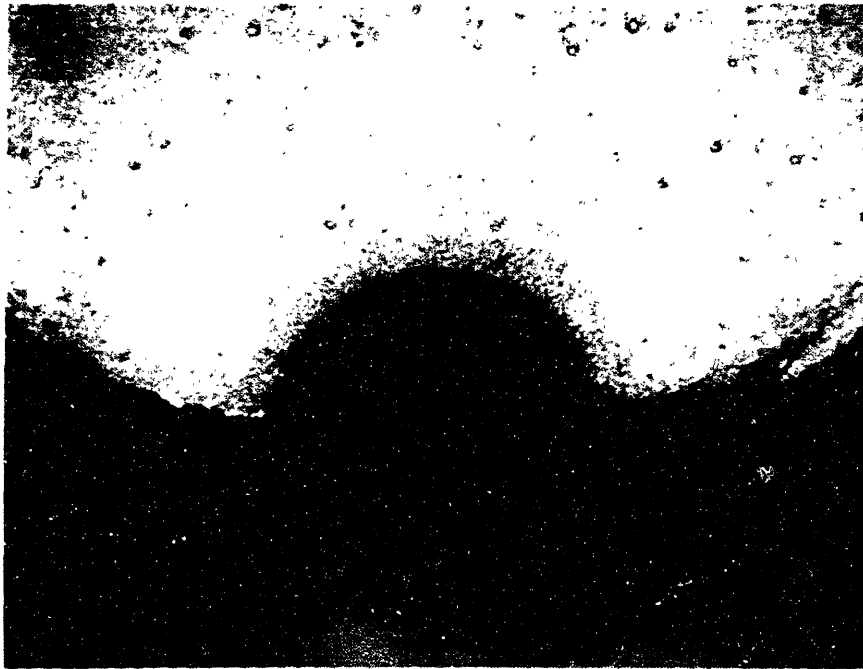
Small crack fatigue tests were performed on IN100(PM) at 649C under elastic conditions using the specimen geometry shown in Figure 3.5 (cylindrical gage section plus two flats). Macroscopic fracture surface features are shown in Figure 4.42 for two small cracks initiated from laser defects. The crack front aspect ratio ranged from  $c/a = 0.95$  to 1.05. Since this small variation in  $c/a$  could not be related to crack length or test conditions,  $c/a$  was taken to be equal to one for calculating the stress intensity factor.

Typical fracture surface features are shown in Figure 4.43. Figure 4.43a was taken in the precracked region and exhibits a transgranular fracture path. Recall that precracking was performed at room temperature. The same transgranular fracture surface appearance was also observed beyond the high temperature crack front since specimens were separated by fatigue cycling at room temperature.

Figure 4.43b was taken in the high temperature fatigue crack region and exhibits an intergranular fracture path with some secondary cracking perpendicular to the nominal fracture plane. This fracture surface appearance was the same for all crack lengths and elastic fatigue conditions considered in this investigation. The propensity for intergranular fracture in IN100(PM) at 649C may be attributed to the environmental degradation of grain boundary cohesive strength ahead of the crack tip. Intergranular fracture has been observed for many nickel-based superalloys at elevated temperatures.

Figure 4.44 shows a metallographic section through a fatigue crack in the specimen from test GR23 ( $\sigma_{\max} = 965$  MPa and  $R = 0.1$ ). The fatigue fracture path is predominantly intergranular for the primary crack as well as the secondary cracks. Much of the fracture path follows the interface between the large blocky  $\gamma$  phase and the surrounding matrix. The large  $\gamma$  reside primarily at grain boundaries.

A second type of defect, intrinsic microporosity, was also observed to be an effective initiation site in high stress elastic fatigue tests. Figure 4.45 shows fatigue cracks which initiated at two different pores in test GR23 ( $\sigma_{\max} = 965$  MPa and  $R = 0.1$ ). The initial fatigue crack extension from the pores (light areas) resulted from precracking at  $\pm 780$  MPa. The darker region beyond the precrack resulted from fatigue crack growth at 649C. The crack shown in Figure 4.45a was the dominant crack in this test with an initial precrack length of  $2c = 280$   $\mu\text{m}$  compared to  $2c = 252$   $\mu\text{m}$  for the dominant laser defect. Consequently, specimen separation occurred along the plane containing the two pores. The fatigue crack shown in Figure 4.45b represents crack growth from  $a_0 = 90$   $\mu\text{m}$  to  $a_f = 450$   $\mu\text{m}$  in 3600 cycles. This is twice the number of cycles that would be predicted by integrating Eq. 4.24, therefore indicating either some degree of near threshold behavior or a period of crack arrest.



← 1mm →

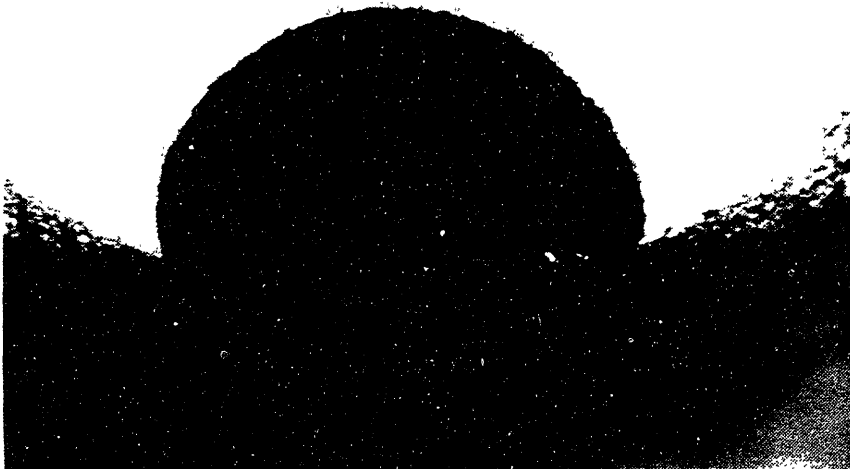


Figure 4.42 Typical crack front profiles as evidenced by the presence of oxidation on the fracture surfaces of IN100(PM) specimens tested at 649C under elastic fatigue conditions.

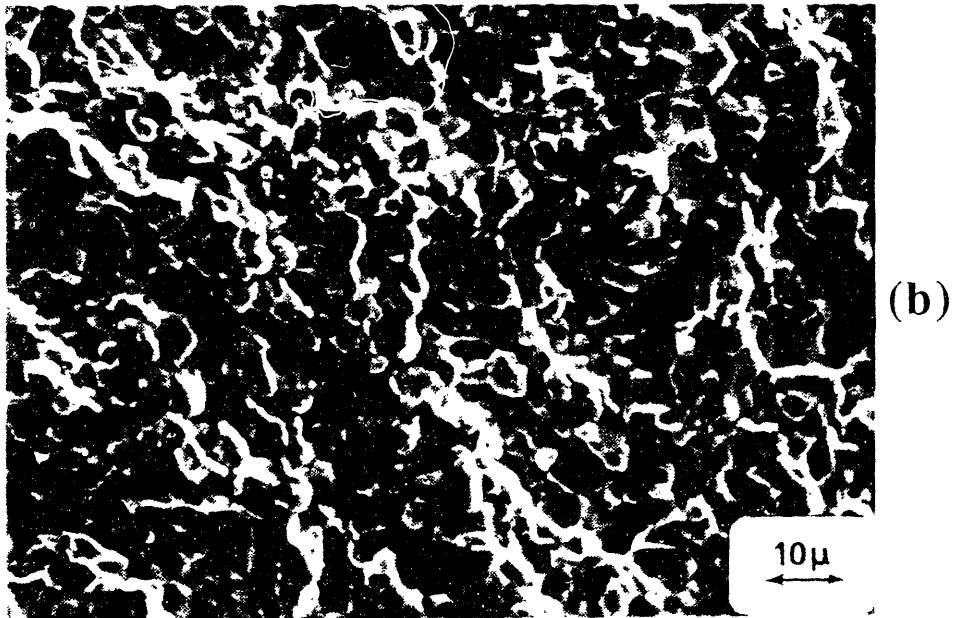
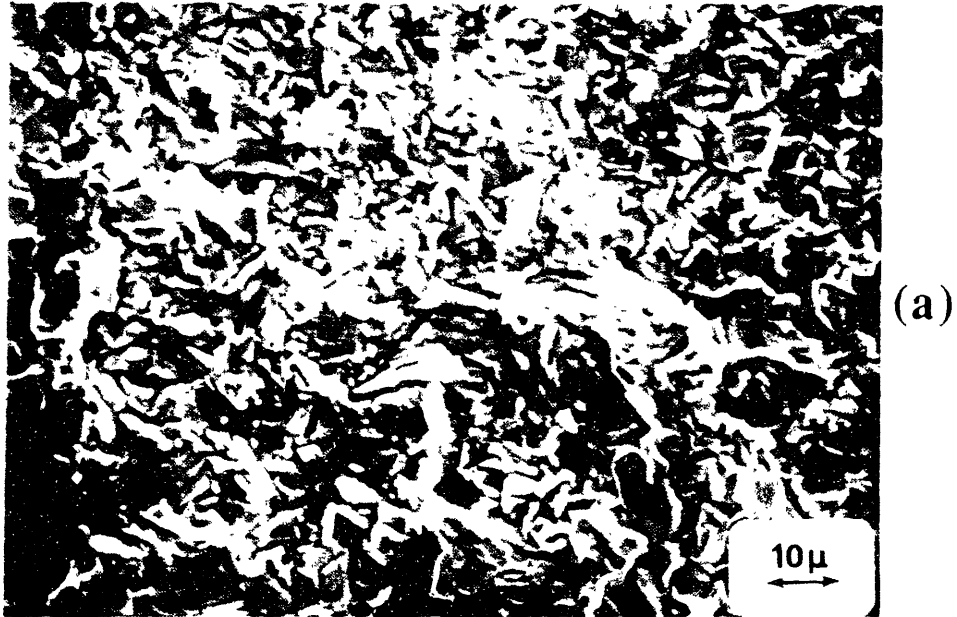


Figure 4.43 Typical fracture surface features for IN100(PM) tested at 649C under elastic fatigue conditions; (a) room temperature precracked region exhibiting a transgranular fracture path, (b) high temperature fatigue crack region exhibiting an intergranular fracture path.



Figure 4.44 Metallographic section through a fatigue crack in IN100(PM) tested at 649C under elastic fatigue conditions; Max stress = 965 MPa and R = 0.1. Fracture path is predominantly intergranular.

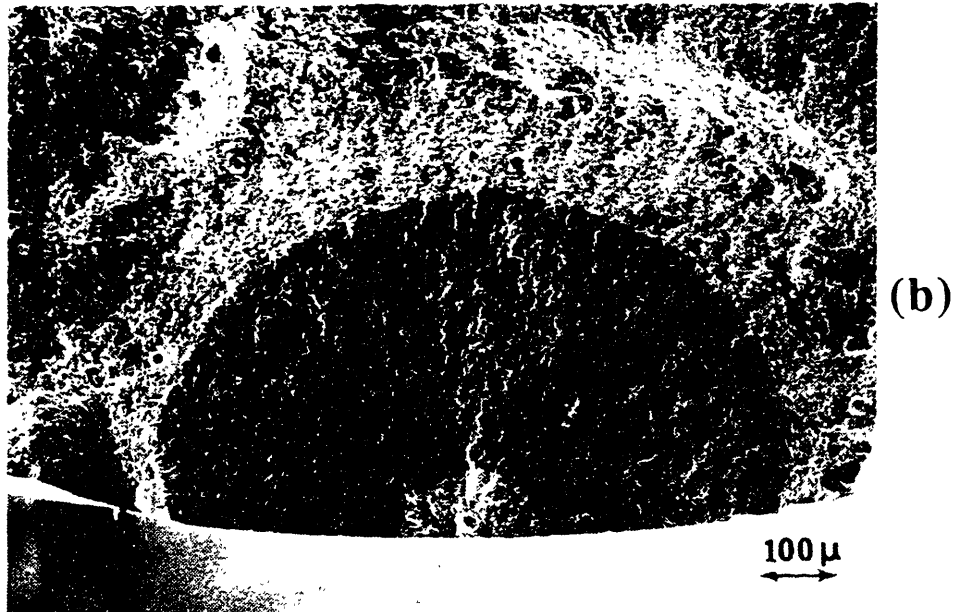
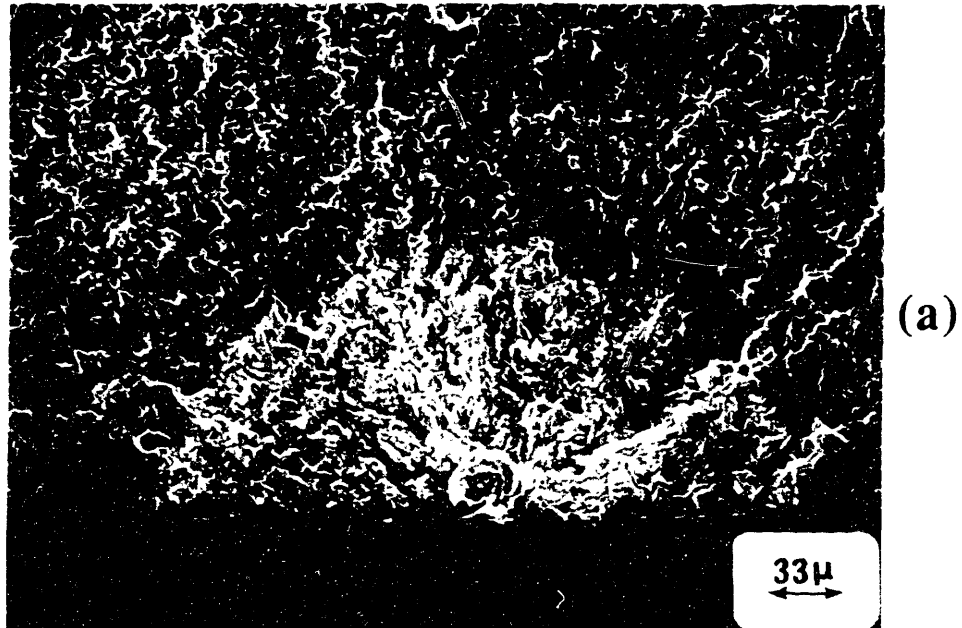


Figure 4.45 Crack initiation at slightly subsurface pores in IN100(PM) tested at 649C under elastic fatigue conditions; Max. stress = 965 MPa and R = 0.1; (a) dominant crack, (b) noncritical crack.

### IN100(PM) at 649C: Elastic-Plastic Fatigue Conditions

Small crack fatigue tests were performed on IN100(PM) at 649C under elastic-plastic fatigue conditions using the specimen geometry shown in Figure 3.5 (cylindrical gage section plus two flats). Macroscopic fracture surface features were identical to that observed for elastic fatigue conditions (see Figure 4.42). The crack front aspect ratio ranged from  $c/a = 0.95$  to  $1.05$  and was taken to be equal to one for calculating fracture mechanics parameters.

Typical fracture surface features are shown in Figure 4.46 for two elastic-plastic tests. Figure 4.46a was taken from test GR21 where  $\Delta\epsilon_t = 0$  to  $0.8\%$  ( $\Delta\epsilon_p = 0.015\%$ ) and exhibits an intergranular fracture path with secondary cracking perpendicular to the nominal fracture plane similar to that observed for elastic tests. Figure 4.46b was taken from test GR34 where  $\Delta\epsilon_t = 0$  to  $1.2\%$  ( $\Delta\epsilon_p = 0.13\%$ ) and exhibits an intergranular fracture path nearly identical to that observed for the elastic tests and lower strain range elastic-plastic tests.

Crack initiation from surface and slightly subsurface pores was prevalent in the elastic-plastic tests. Figure 4.47 gives typical examples of these two variations of pore initiation site. Figure 4.47a shows a surface-pore initiation site with a somewhat transgranular fracture path at very small crack lengths and a transition to an intergranular fracture path with increasing crack length. The dark phase is the large blocky  $\gamma$  present at grain boundaries. In Figure 4.48, the transition from a transgranular to an intergranular fracture path is evident on the fracture surface.

A review of the replica record for smooth specimens (no laser defects) tested under elastic-plastic conditions indicates that most small cracks initiate at pores intersected by the specimen surface. However, the dominant crack may suddenly emerge from a subsurface initiating site with a surface crack length exceeding all others. The rapid fatigue crack growth from slightly subsurface pores can be explained with the aid of Figure 4.49. For a surface

intersected pore, initiation may or may not occur depending on the orientation of the surrounding microstructure. If initiation occurs, it does so at the intersection of the pore with the specimen surface and the crack front quickly assumes a semicircular geometry with crack depth  $\approx 1/2$ (pore diameter). If the crack initiates at a slightly subsurface pore, the narrow ligament between the free surface and the pore soon fails due to the lack of constraint on both sides and the resulting high equivalent plastic strain range. Once a crack has formed, it rapidly propagates through the region having a "chevron notch" geometry and around the pore until it has assumed a semicircular crack front with crack depth  $\approx$  (pore diameter + t) where t is the thickness of the ligament between the pore and the specimen surface. Consequently, the slightly subsurface pore is a more potent crack initiation site. This was also shown in Figure 4.45.

Given an initial defect size, be it a pore or an inclusion, the lower limit of crack propagation life will be more likely associated with slightly subsurface defects than surface connected defects. The crack propagation life from deeply subsurface defects must be considered in the total life limit of a turbine disk, because a critical defect size could be reached before detection by nondestructive evaluation. Subsurface cracks will propagate in a vacuum. The appropriate database should be used to predict crack propagation lives under these conditions.

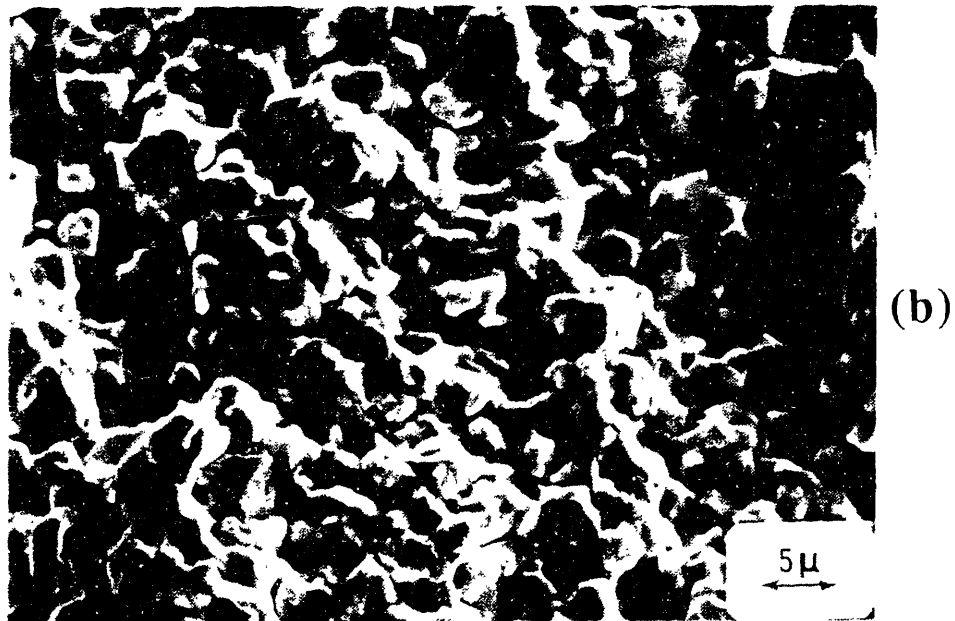
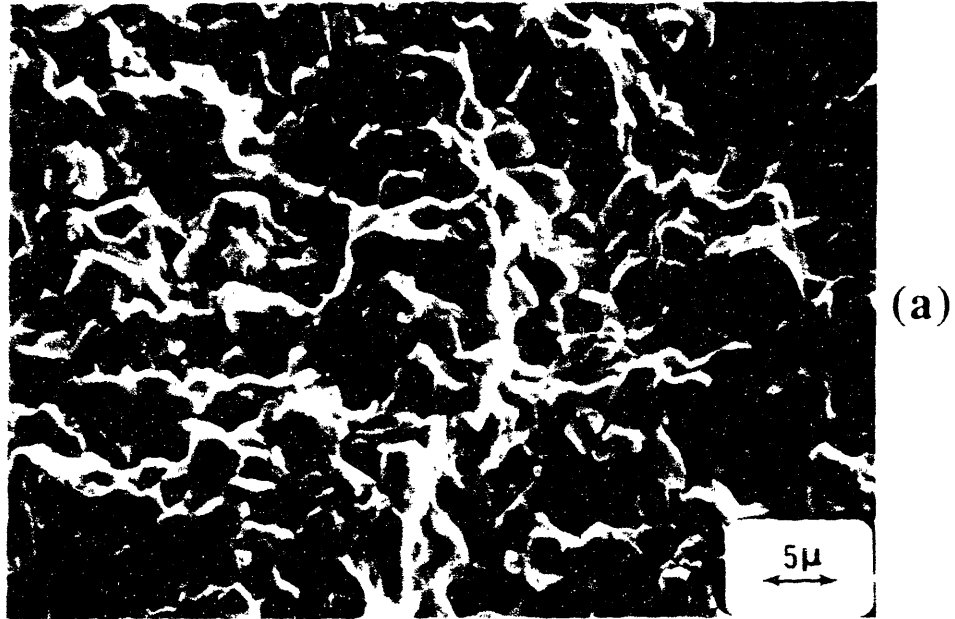


Figure 4.46 Typical fracture surface features for IN100(PM) tested at 649C under elastic-plastic fatigue conditions, (a) intergranular fracture path for  $\Delta\epsilon_t = 0$  to 0.82% ( $\Delta\epsilon_p = 0.015\%$ ), (b) intergranular fracture path for  $\Delta\epsilon_t = 0$  to 1.23% ( $\Delta\epsilon_p = 0.13\%$ ).

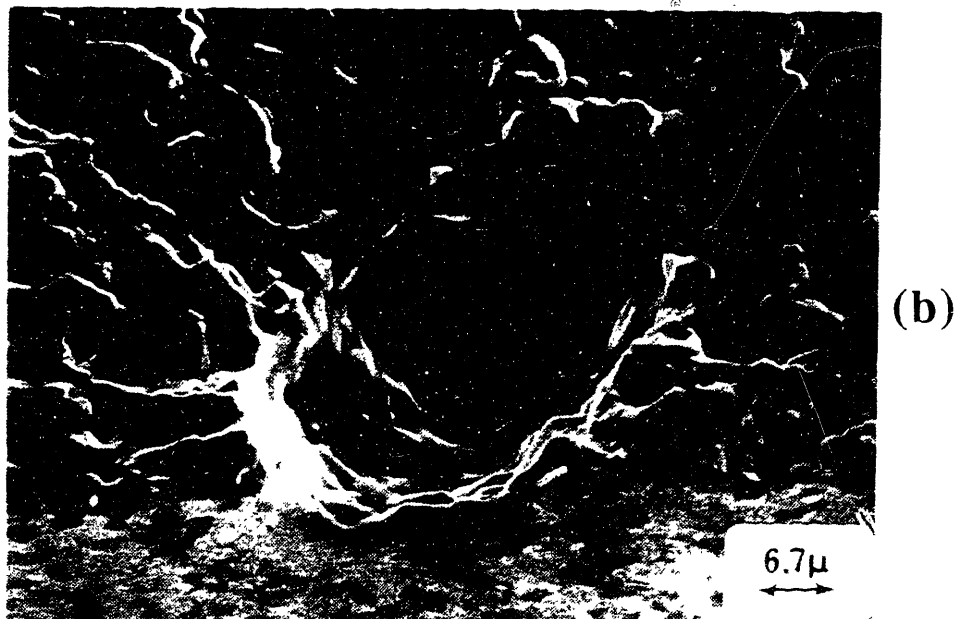
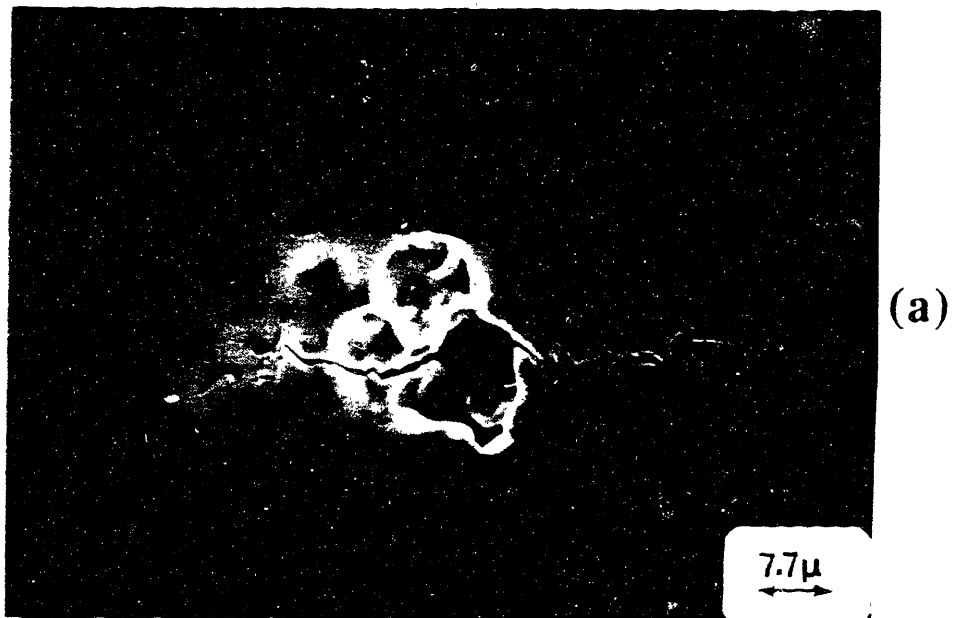


Figure 4.47 Crack initiation at pores in IN100(PM) tested at 649C under elastic-plastic fatigue conditions; (a) surface intersected pore and (b) slightly subsurface pore.

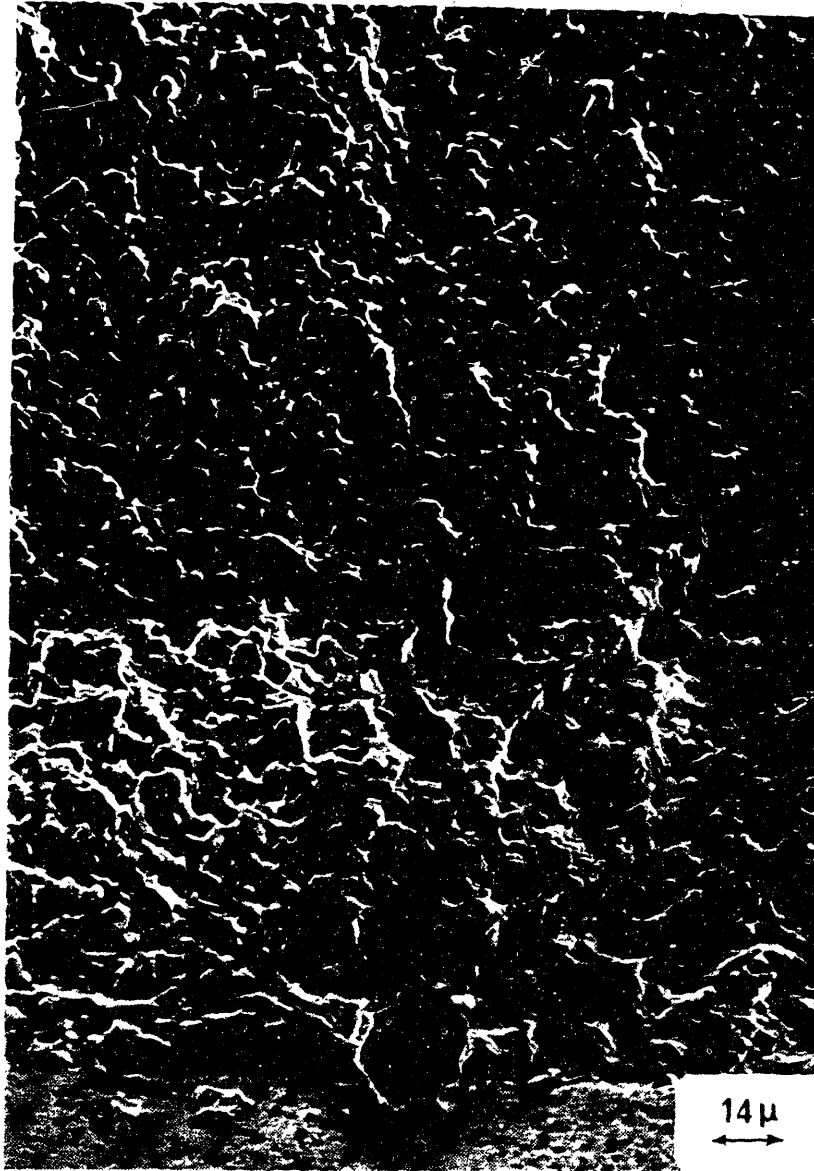
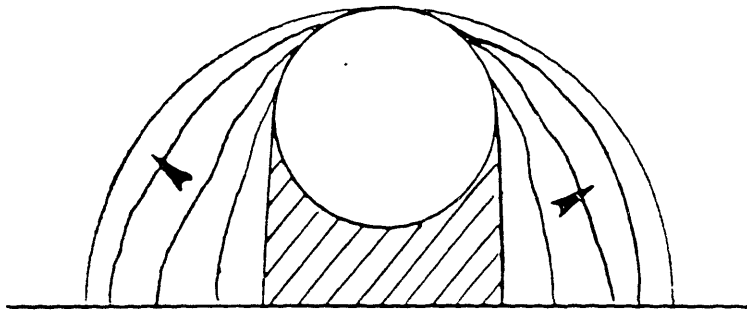
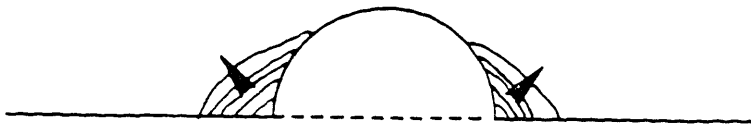


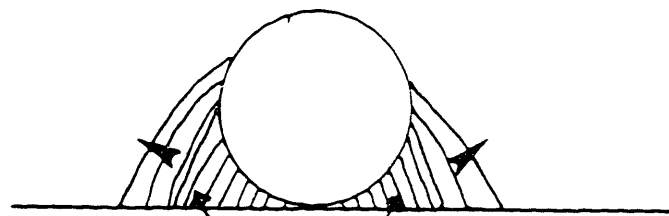
Figure 4.48 Transition from transgranular to intergranular fracture path with increasing crack length for IN100(PM) tested at 649C under elastic-plastic fatigue conditions.



pore at subsurface location



pore at free surface



"chevron notch"

pore at near surface location

Figure 4.49 Schematic representing crack initiation at surface and subsurface pores.

## 5. General Discussion

As demonstrated in previous chapters, the study of the fatigue crack propagation behavior of small cracks in aircraft turbine disk alloys entails not only small crack sizes but also very high stresses and strains, often exceeding the elastic limit. One of the principal objectives at the outset of this investigation was to define the lower limit of crack size and upper limit of stress for which LEFM is applicable under elastic fatigue conditions. Although some of the requirements for valid application of LEFM were violated, particularly with respect to plastic zone size, the stress intensity factor range still served as a useful parameter to correlate small crack ( $100 \mu\text{m} < a < 1 \text{ mm}$ ) with long crack growth rates and consolidated crack growth rates at different stress levels. The R-ratio effect was accounted for by the Walker-modified  $\overline{\Delta K}$ . Values of maximum stress employed were as high as 92% of the elastic limit stress and yet Mode I cracks as small as  $100 \mu\text{m}$  in depth still exhibited threshold behavior. Reducing the initial crack size further under elastic fatigue conditions meant monitoring the progress of arrested cracks; not a fruitful endeavor. With  $\sigma_{\text{max}}$  at 92% of the elastic limit in many of these experiments, the utility of LEFM was also demonstrated over nearly the full elastic range. Anomalous fatigue crack growth behavior was not observed under elastic fatigue conditions in the turbine disk alloys studied here for crack lengths greater than  $100 \mu\text{m}$ .

The study of the fatigue behavior of very small cracks is unique in that subcritical fatigue crack growth rates can be measured at very high stress ranges and under elastic-plastic conditions which is relevant to turbine disk operating conditions. Such high stress and strain ranges are not possible in the study of the fatigue behavior of long cracks since the material's fracture toughness would be exceeded. Miller [5.1] has stated that fatigue crack propagation of long cracks under low net section stresses represents an anomalous engineering condition. This is particularly true for aircraft turbine disks.

It was found that EPFM parameters such as  $\Delta PK$  and  $\Delta J_I$  consolidated crack growth rates under elastic-plastic fatigue conditions and correlated elastic with elastic-plastic fatigue crack growth behavior.

Perhaps the single most interesting conclusion to emerge from these small crack fatigue tests is that the compressive component of stress and strain served to increase crack growth rates. Furthermore, empirical correlation of crack growth rates with LEFM or EPFM parameters required explicitly accounting for the total stress-strain range in the mechanical driving force. This finding appears to run counter to the conventional wisdom which holds that crack advance (or damage) occurs only when the crack tip is experiencing tensile stress and strain. In fact the Mode I stress intensity factor,  $\Delta K_I$ , is defined only for positive stresses. The effect of stress ratio is generally studied for positive stress ranges and the reduction in  $\Delta K$  to  $\Delta K_{eff}$  is attributed to crack closure at positive values of stress.

The objective of this chapter is to explore the role of the compressive stress-strain excursion under elastic and elastic-plastic fatigue conditions. The approach will be basically an interrogation of the literature to seek an explanation for this behavior. The following path will be followed:

- 1) A review of published data to find other examples of the effect of negative stress-strain excursion ( $R_\sigma < 0$ ) on crack growth rates.
- 2) Since the effective range of the mechanical driving force is generally attributed to crack opening-closure, examples of direct physical measurement of crack opening and closure under  $R_\sigma < 0$  conditions will be reviewed.
- 3) Analytical and numerical models of crack closure will be reviewed for insight into the role of the compressive stress-strain excursion.

- 4) Finally an attempt will be made to reconcile measurements, mechanisms and models with global fracture mechanics parameters which consolidate fatigue crack growth rates.

## 5.1 The Effect of Negative R-ratio on Fatigue Crack Growth Rates

The number of investigations in which the effect of R-ratio on fatigue crack growth rates was studied is too numerous to mention. However, the majority of these studies involved only positive R-ratios and elastic fatigue conditions. The specimen geometries employed usually prohibited compressive loading. In general, crack growth rates were observed to increase with increasing positive R-ratios. This behavior was usually attributed to the crack closure phenomenon and an increase in the effective range of  $\Delta K$  with increasing R-ratio.

Only a few investigations have explored the effect of negative R-ratios on fatigue crack growth rates. For valid comparisons, it is important that  $\Delta K$  be calculated using only the positive stress range since  $K_I$  is not defined for compressive loading. Unfortunately many studies reported in the literature appear to use  $\Delta\sigma_{tot}$  when  $R < 0$  without stating this explicitly. In some cases, it is not clear how  $\Delta K$  was calculated. In the examples given below, the effect of negative R-ratios on crack growth rate is considered using only the positive stress range in calculating  $\Delta K$ .

Maddox [5.2] reviewed the effect of R-ratio on fatigue crack growth rates in steels and aluminum alloys under nominally elastic conditions. For a variety of steels it was found that the number of cycles to crack initiation decreased and crack growth rates increased as R-ratios decreased in the  $R < 0$  regime [5.3-5.5]. It was concluded that at least part of the compressive stress range was damaging. The same conclusion was made for 2024-T3 and 7075-T6 aluminum alloys.

Maddox proposed that the compressive stress excursion was damaging only if it was part of a tension-compression fatigue cycle. He suggested that the damaging effect of the compressive portion of a  $R_\sigma < 0$  applied stress cycle could be explained in terms of a greater

effective tensile stress at the crack tip. He proposed two possible explanations, both of which may be true: 1) The compressive part of the cycle may contribute to a reduction in the tensile residual stress field at the crack tip and therefore the residual compressive stress acting on the crack surfaces. This would reduce the crack closure stress and lead to an increase in crack growth rates. 2) Compressive applied stresses causing crack closure would then cause plastic deformation on the crack surface which would force the crack closure stress down, thus making a greater part of the stress range damaging.

Musuva and Radon [5.6] investigated the influence of R-ratio on fatigue crack growth rates in BS 4360-50C steel at room temperature. R-ratios varied from -0.7 to 0.7. The results were analyzed using linear elastic fracture mechanics and showed that an increase in both positive and negative R-ratios caused increased crack growth rates. It was concluded that the compressive portion of the load cycle at  $R < 0$  contributed to the driving force for crack growth.

Gamble and Paris [5.7] used LEFM analysis to predict allowable thermal fatigue crack growth rates in the blade attachment slot of Alloy A286 turbine disks. Start-stop operation imposed severe cyclic compressive and tensile stresses in this location. Laboratory fatigue crack growth rate data was obtained at 482C (900F) with  $R = 0$  and  $R = -1$ . Crack growth rates for the  $R = -1$  condition was approximately three times greater than the  $R = 0$  condition at any given  $\Delta K$ . Differences in crack growth rates at room temperature were less significant.

Larsen et al. [5.8] investigated the effect of maximum stress ( $0.6\sigma_{ys}$  and  $0.9\sigma_{ys}$ ) and R-ratio on crack growth rates and crack closure in titanium-aluminum alloys. Crack growth rates at  $0.9\sigma_{ys}$  were found to increase with increasing tension or compression cycling such that  $da/dN$  ( $R = 0.5$  and  $R = -1$ ) was greater than  $da/dN$  ( $R = 0.1$ ).

Njus and Stephens [5.9] investigated the influence of negative R-ratio on both constant amplitude fatigue crack growth rates and on delay following a single tensile overload

for three different yield strengths of AISI 4140 alloy steel (758 MPa, 1138 MPa and 1413 MPa). R-ratios of 0, -0.5 and -1 were employed. Crack growth rates at constant amplitude increased with decreasing R-ratio but were more dependent on yield strength. More dramatically, the delay following a single tensile overload was significantly reduced when subsequent fatigue cycles were carried out at  $R = -1$  compared to  $R = 0$ , particularly for the lower yield strength steel. The reduction in delay was attributed to cyclic relaxation of crack tip residual stresses and a reduction in the closure stress.

Stephens, McBurney and Oliphant [5.10] also reported similar behavior for 2024-T3 and 7075-T6 aluminum alloys where the R-ratios following tensile and/or compressive overloads were: 0, -0.5, -0.75, -1 or -2. As the R-ratio decreased, the beneficial effects of the tensile overload was reduced. The above two examples illustrate that the compressive stress excursions play a significant role in fatigue crack growth under spectrum loading conditions.

Dan and Wertman [5.11] studied the effects of crack closure on fatigue crack growth rate in a 7050 Al alloy and found that the compressive stress, either in cyclic loading or applied in a single spike can significantly increase crack growth rate. This behavior was attributed to a decrease in closure stress with decreasing R-ratio.

The above examples empirically corroborate the findings of this investigation on gas turbine disk alloys. It can be stated as generally true that compressive stress-strain excursions result in higher crack growth rates compared to tension only cycling under elastic fatigue conditions. The general variation of crack growth rate as a function of R-ratio is shown in Figure 5.1 for a variety of engineering alloys.

The role of stress ratio (mean stress) on fatigue crack growth rates under elastic-plastic conditions have not been systematically studied. The following sections will focus on physical explanations for the negative R-ratio effect.

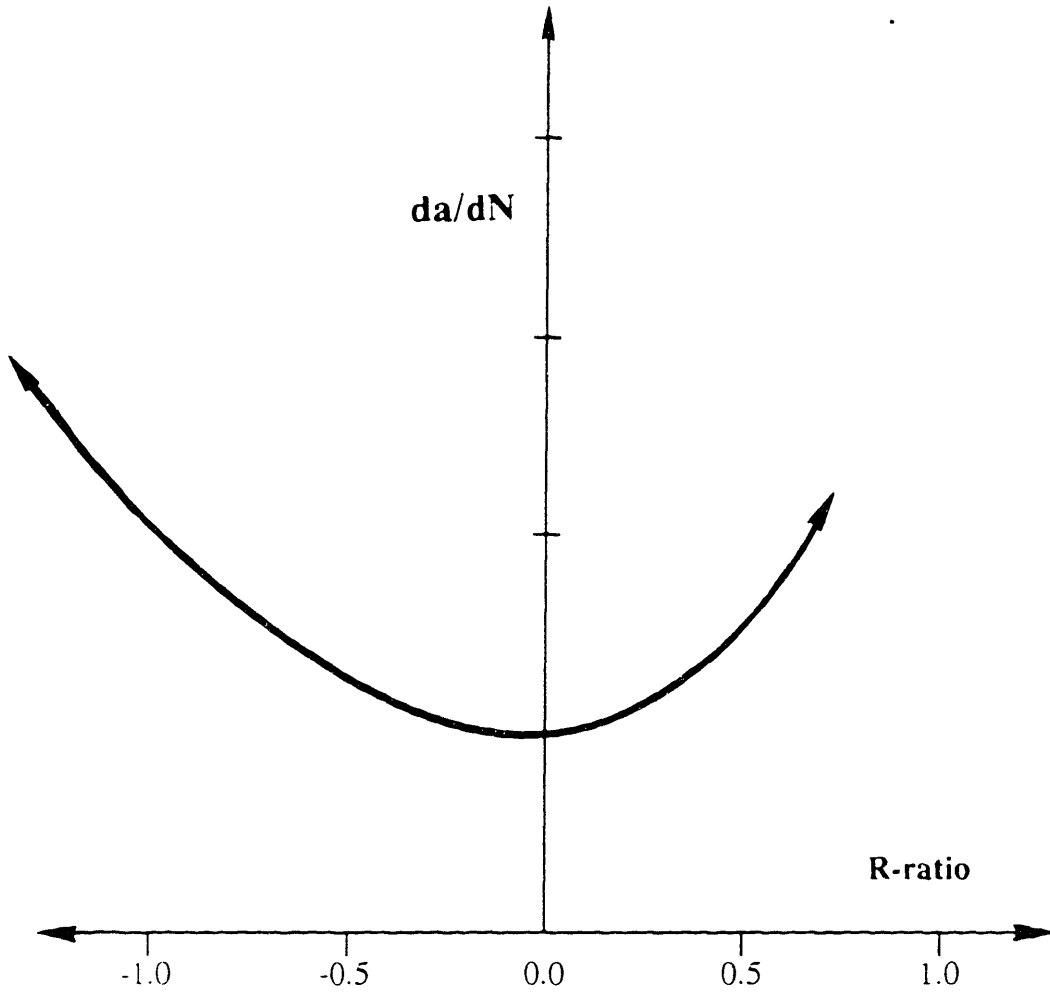


Figure 5.1 General variation in crack growth rate versus R-ratio for a variety of engineering alloys.

## 5.2 Crack Opening and Closure Measurements

The phenomenon of crack closure has been used by many investigators to explain R-ratio effects on crack growth rate and anomalous small crack behavior. The basic mechanisms responsible for crack closure: plasticity, fracture surface roughness and oxide wedging were introduced in the literature review. Under elastic fatigue conditions, crack closure above zero load serves to reduce the effective driving force such that

$$\Delta K_{\text{eff}} = K_{\text{max}} - K_{\text{op}} = Y(\sigma_{\text{max}} - \sigma_{\text{op}})\sqrt{\pi a} . \quad (5.1)$$

It is generally assumed that  $\sigma_c = \sigma_{\text{op}}$ . The basic premise behind using  $\Delta K_{\text{eff}}$  is that the crack will extend only when the crack tip is fully open. The objective of this section is to review the literature for examples of crack closure measurements under conditions of negative R-ratio.

### Crack Opening-Closure under Elastic Fatigue Conditions

Crack closure under elastic fatigue conditions has been measured by a variety of techniques, all of which define closure as the load at which there is a distinct change in specimen compliance on unloading. This is generally accomplished by measuring the crack opening displacement as a function of the applied load. Measurement techniques employed for large cracks determine bulk closure conditions and are not suitable for small crack studies. In most of the examples given below, the determination of crack opening compliance and closure of small cracks was accomplished using a unique laser interferometric displacement gage (IDG) originally developed by Sharpe [5.12-5.14]. This system has a resolution capability of 0.01  $\mu\text{m}$ .

Jira et al. [5.15] measured crack closure during fatigue crack growth experiments on surface flaws ( $50 \mu\text{m} < a < 8 \text{ mm}$ ) in a high strength titanium alloy. Stress ratios of 0.5, 0.1

and -1.0 and net section stress levels from  $0.2\sigma_{ys}$  to  $0.9\sigma_{ys}$  were used. Crack lengths and closure loads were determined from load displacement data obtained with the laser IDG. After the crack had propagated away from the starter notch, the crack closure load for the  $R = -1$  test condition remained essentially constant at a small positive value. The measured closure loads for the  $R = 0.1$  test condition were essentially identical to the  $R = -1$  condition. Consequently, crack growth rates could be consolidated using the applied  $\Delta K$ .

James and Sharpe [5.16] measured crack growth rates and CMOD using the laser IDG system for small cracks in A533B steel. A coarse and fine grained microstructure was investigated at R-ratios of 0.1 and -1. Values of  $P_{op}/P_{max}$  ranged from -0.25 to 0 for the  $R = -1$  condition over the crack length range  $50 \mu\text{m} < a < 250 \mu\text{m}$  for the coarse grained microstructure. Values of  $P_{op}/P_{max}$  were nearly constant and positive for both  $R = 0.1$  conditions and for the fine grained  $R = -1$  condition. Crack growth rates were generally higher in the fine grained condition compared with the coarse grained condition. Crack growth rates were also higher for the  $R = -1$  test condition.

Lee and Sharpe [5.17] measured crack closure for small cracks ( $35 \mu\text{m} < a < 500 \mu\text{m}$ ) in notched specimens of 2024-T3 aluminum under elastic fatigue conditions at R-ratios of 0.5, 0, -1.0, and -2.0. The laser IDG system was used to measure crack closure. Crack closure occurred at positive loads for all R-ratios except the  $R = -2.0$  condition where  $P_{op}/P_{max}$  was as low as -0.38 but generally on the order of -0.10. The scatter in the data was greater at negative R-ratios.

Sehitoglu [5.18] investigated crack opening and closure levels in a 1070 steel using a two stage replication technique. Double edge notched specimens were tested at R-ratios of 0.33, 0, -0.33, -1 or -3 and circular notched specimens were tested at R-ratios of 0 and -1. Crack lengths varied from  $40 \mu\text{m}$  to 5 mm. Results indicated that crack opening and closure level may be different from one another depending on R-ratio and crack length. The stress

level at crack closure and crack opening was in the tensile region for long cracks in double edge notch specimens even for  $R = -3$ . The crack opening level was negative ( $P_{op}/P_{max} = -0.1$ ) for small cracks ( $\sim 100 \mu\text{m}$ ) growing from a circular notch under  $R = -1$  loading conditions.

Some investigators [5.19, 5.20] have demonstrated that the crack closure level depends on the location of measurement. Ashbaugh [5.19] studied crack closure in René 95 using three specimen geometries and three displacement measurement techniques (clip gage, back face strain gage and the laser IDG). With the very sensitive IDG technique, the closure level determined  $80 \mu\text{m}$  behind the crack tip could not be determined  $2.5 \text{ mm}$  behind the tip. He concluded that the contact along the fracture surface near the tip was confined to a region at the surface of the specimen and deformation of the bulk of the specimen masked the closure occurring in the near crack tip region. It should be pointed out that the IDG technique measures crack mouth opening displacement (CMOD). However close the crack tip this may be in the case of small surface cracks, it is not a direct measurement of crack tip opening displacement (CTOD). The bulk closure load is defined at the change in bulk compliance. Crack tip closure may have occurred at a higher load.

A common misinterpretation of closure is often made by viewing the surface crack trace on an unloaded specimen such as that shown in Figure 5.2 for IN100(PM). By noting that the crack is open at the surface at zero load, some investigators conclude that the closure load must be compressive. However, according to the definition of plasticity or roughness induced closure, the crack is mechanically closed without fracture path mating at the specimen surface.

In summary, the above examples indicate that, for elastic fatigue conditions and negative R-ratios, crack opening occurs at either low positive values of  $P_{op}/P_{max}$  or slightly negative values of  $P_{op}/P_{max}$ . Crack closure was found to be dependent on specimen

geometry, crack length, loading history, yield stress, microstructure, crack closure mechanism as well as the unique 3-dimensional geometry of individual small cracks. Consequently, it may be stated that small fatigue crack tips are mechanically closed for most of the compressive stress-strain excursion. The compressive stress-strain excursion may serve to decrease the crack opening stress, although some examples indicate little effect of R-ratio on crack opening stress level.

### Crack Opening-Closure under Elastic-Plastic Fatigue Conditions

Iyyer and Dowling [5.21] measured crack mouth opening and closure in 4340 steel cycled under elastic to high strain elastic-plastic conditions ( $\Delta\epsilon_t = 0.48\%$  to  $2.5\%$ ;  $R_\epsilon = -1$ ) CMOD was measured from the plastic replica record made on small surface cracks at different stress-strain locations around the hysteresis loop. The applied stress needed to open a small crack was found to be less for the nominally elastic condition. For increasing values of  $\Delta\epsilon_t$ , the relative crack opening level,  $\sigma_{op}/\sigma_{max}$ , was observed to decrease and approached the value of  $R_\sigma = -1$ . Full crack mouth closure occurred only at the minimum stress, but crack mouth opening occurred at a higher stress level, although  $\sigma_{op}$  was significantly negative. In this study one must realize that full crack mouth closure at the specimen surface may not correspond to crack closure as defined by fracture surface contact and the resulting change in specimen compliance observed in elastic tests. Therefore, crack mouth opening-closure may not coincide with crack tip opening-closure. The bulk strain range on the uncracked specimen ligament appears to dominate crack mouth opening and closure in this case.

McClung and Sehitoglu [5.22] measured crack tip opening and closure of small cracks ( $100 \mu\text{m} < a < 1.5 \text{ mm}$ ) in SAE1026 steel cycled under elastic and elastic-plastic conditions using the two stage replication technique on edge notched specimens. Test conditions were  $R_\epsilon = -1$  and  $\Delta\epsilon_t = 0.2\%$  to  $1.4\%$  ( $\Delta\epsilon_p = 0.001\%$  to  $0.52\%$ ). The results are shown in Figure 5.3. The circles represent the averaged measured value of  $\sigma_{op}$  for each

strain amplitude. At low strain ranges, the crack tip remained closed at significant tensile stresses. At high strain ranges, the crack opened under a low compressive stress,  $\sigma_{op}/\sigma_{max} \approx 0.1$ . Crack closure levels also decreased with increasing strain amplitude, and closure levels were significantly lower than opening levels at high strains. Correlations of constant amplitude crack growth rates based on  $\Delta J$  or  $\Delta CTOD$  were more successful when the effective stress range ( $\sigma_{max} - \sigma_{op}$ ) was used.

The obvious disagreement between small crack opening levels under high strain elastic-plastic conditions for the two examples given above is most likely attributable to the experimental approach rather than other factors. Iyyer and Dowling measured CMOD at the specimen surface for semicircular surface cracks, whereas McClung and Sehitoglu measured CTOD on the side surface of SEN specimens. It appears that the results of McClung better represents the crack tip condition.

With regard to this investigation of small crack growth rates in aircraft turbine disk alloys, it seems reasonable to assume that crack tip opening occurred at lower tensile stress levels or perhaps slightly compressive levels ( $\sigma_{op}/\sigma_{max} \approx -0.1$ ) when the bulk  $R_{\sigma}$ -ratio was negative and particularly when the crack length was small.



Figure 5.2 Surface crack trace open at zero load in an IN100(PM) specimen after testing at 649C in strain control ( $\Delta\epsilon_t = 0$  to 0.8%).

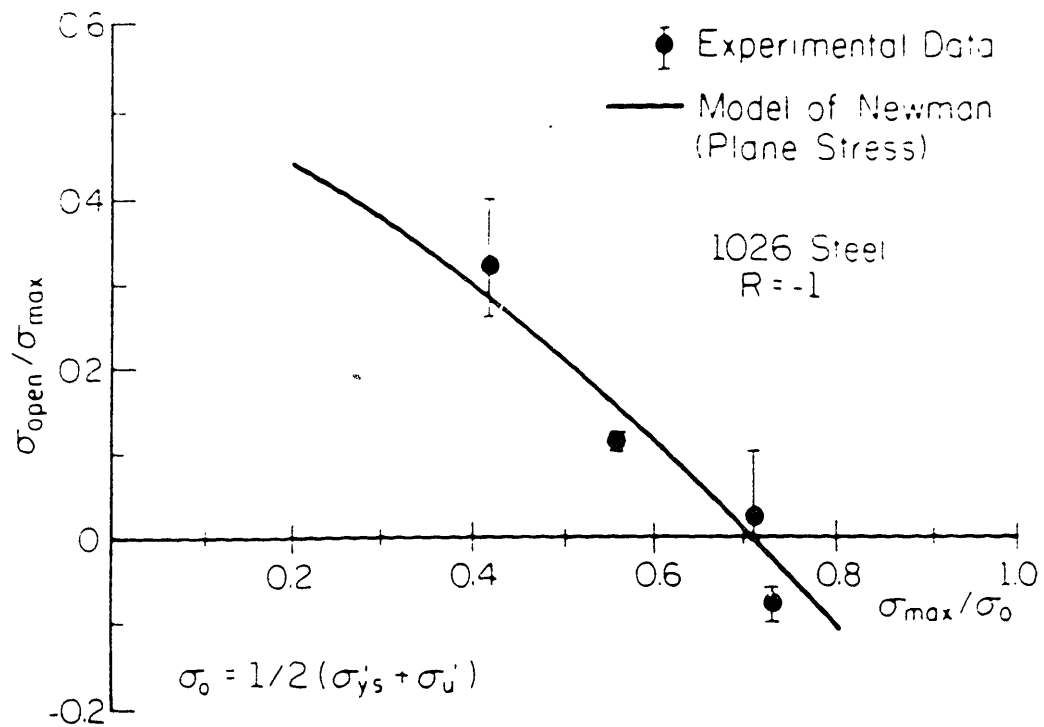


Figure 5.3 Comparison of experimental results with Newman's analysis for normalized crack opening stress versus maximum stress for a 1026 steel,  $R = -1$ . From Ref. [5.22].

### 5.3 Models for Predicting Crack Opening and Closure

Since crack opening and closure were not measured in this investigation, we now turn to existing crack closure models to explain the role of the compressive stress-strain excursion on the mechanical driving force for fatigue crack growth. Most of these models attempt to describe the effects of crack closure by the plasticity mechanism. Attempts to model crack closure generally fall into two categories: finite element simulations and simple analytical models.

Newman [5.23] developed a two-dimensional elastic-plastic finite element program to analyze plasticity induced closure and crack growth for long cracks in center-cracked panel specimens under cyclic loading. Spring elements were introduced along the crack plane to account for closure. Crack opening stresses were found to be significantly lower than crack closure stresses in all cases. Simulations were run for  $R = 0$  and  $R = -1$ . During the compressive loading ( $R = -1$ ), all nodes along the crack surfaces closed. The applied compressive stress caused the crack surface near the crack tip to yield in compression, thereby lowering the subsequent crack opening stress. The crack opening stress for  $R = -1$  was lower than the opening stress obtained for the  $R = 0$  case. Based on the effective stress concept, fatigue crack growth rates for  $R = -1$  were predicted to be two times faster than for  $R = 0$ . This prediction was corroborated by results obtained by Hudson [5.24] who found approximately the same difference in crack growth rates for a 2024-T3 aluminum alloy at  $R = 0$  and  $R = -1$ .

Other investigators [5.25-5.28] have used the finite element method to model fatigue crack closure and crack propagation. Their results, as with the case cited above, serve to support the findings of the current investigation. However, lacking the resources to simulate the material and test conditions of this investigation, finite element results cannot be used in a quantitative manner to analyze the role of compressive stress-strain excursions in this study.

A number of physically based analytical models have been developed [5.29 - 5.31] to predict the crack opening stress. The model most adaptable to this investigation is that developed by Newman [5.31] which is based on the Dugdale strip-yield model [5.32], modified to leave plastically deformed material in the wake of the advancing crack tip. The model was developed for center cracked tension specimens at various applied stress levels and R-ratios.

Figure 5.4 shows a schematic of the Newman model [5.31] at maximum and minimum applied stress. The model consists of a linear elastic body containing a fictitious crack of half length  $c+\rho$ , a crack tip plastic region of length  $\rho$ , and a residual plastic deformation region along the crack surfaces. The physical crack is of half length  $c$ . The fictitious crack is composed of rigid-perfectly plastic bar elements with a flow stress  $\sigma^*$  which is taken as the average between the yield strength and the ultimate tensile strength. At any applied stress level, the bar elements are either intact (in the crack tip plastic zone) or broken (residual plastic deformation in the crack wake). The broken elements can only carry compressive loads, and only when they are in contact. Yielding of the elements in compression occurs when the contact stress reaches  $-\sigma^*$ . Those elements that are not in contact do not affect the calculation of crack surface displacements. An effective flow stress,  $\alpha\sigma^*$ , was used to evaluate yielding of the intact elements in the plastic zone, with  $\alpha = 1$  and  $3$  under simulated plane stress and plane strain conditions, respectively.

The results of Newman's analysis indicate that  $\sigma_{op}$  is a function of R-ratio and stress level,  $\sigma_{max}/\sigma^*$ . Some salient features of his analysis are as follows:

- At constant  $\sigma_{max}$ ,  $\sigma_{op}/\sigma_{max}$  increases with increasing R-ratio. At  $R \leq 0$ ,  $\sigma_{op}/\sigma_{max}$  is a linear function of R-ratio. At  $R \geq 0$   $\sigma_{op}/\sigma_{max}$  rapidly approaches the value of R.
- At any given R-ratio and  $\sigma_{max}$ ,  $\sigma_{op}/\sigma_{max}$  is higher for lower values of  $\alpha$ .

- For plane strain ( $\alpha = 3$ ),  $\sigma_{op}/\sigma_{max}$  is nearly independent of  $\sigma_{max}/\sigma^*$ .
- For plane stress ( $\alpha = 1$ ),  $\sigma_{op}/\sigma_{max}$  decreases with increasing  $\sigma_{max}/\sigma^*$ . This effect is rather dramatic for  $R < 0$ .

This model was used to correlate crack growth rates under constant amplitude loading and to predict crack growth under spectrum loading on 2219-T851 aluminum alloy plate material.

In his initial analysis, Newman presented results in graphical form [5.31]. He later developed simple expressions for the crack opening stress in terms of R-ratio and stress level [5.33]. The relations are as follows:

$$\sigma_{op}/\sigma_{max} = A_0 + A_1R + A_2R^2 + A_3R^3 \quad \text{for } R \geq 0 \quad (5.2)$$

and

$$\sigma_{op}/\sigma_{max} = A_0 + A_1R \quad \text{for } -1 \leq R \leq 0 \quad (5.3)$$

when  $\sigma_{op} \geq \sigma_{min}$ . The coefficients are:

$$A_0 = (0.825 - 0.34\alpha + 0.05\alpha^2)[\cos(\pi\sigma_{max}/2\sigma^*)]^{1/\alpha} \quad (5.4)$$

$$A_1 = (0.415 - 0.071\alpha)\sigma_{max}/\sigma_{op} \quad (5.5)$$

$$A_2 = 1 - A_0 - A_1 - A_3 \quad (5.6)$$

$$A_3 = 2A_0 + A_1 - 1 \quad (5.7)$$

These equations will be used to calculate  $\sigma_{op}$  for the IN100(PM) tested in this investigation.

Nakamura and Kobayashi [5.34, 5.35] have also demonstrated the validity of the Newman model to define the crack opening stress levels when fatigue crack closure is caused by fracture surface asperities (roughness).

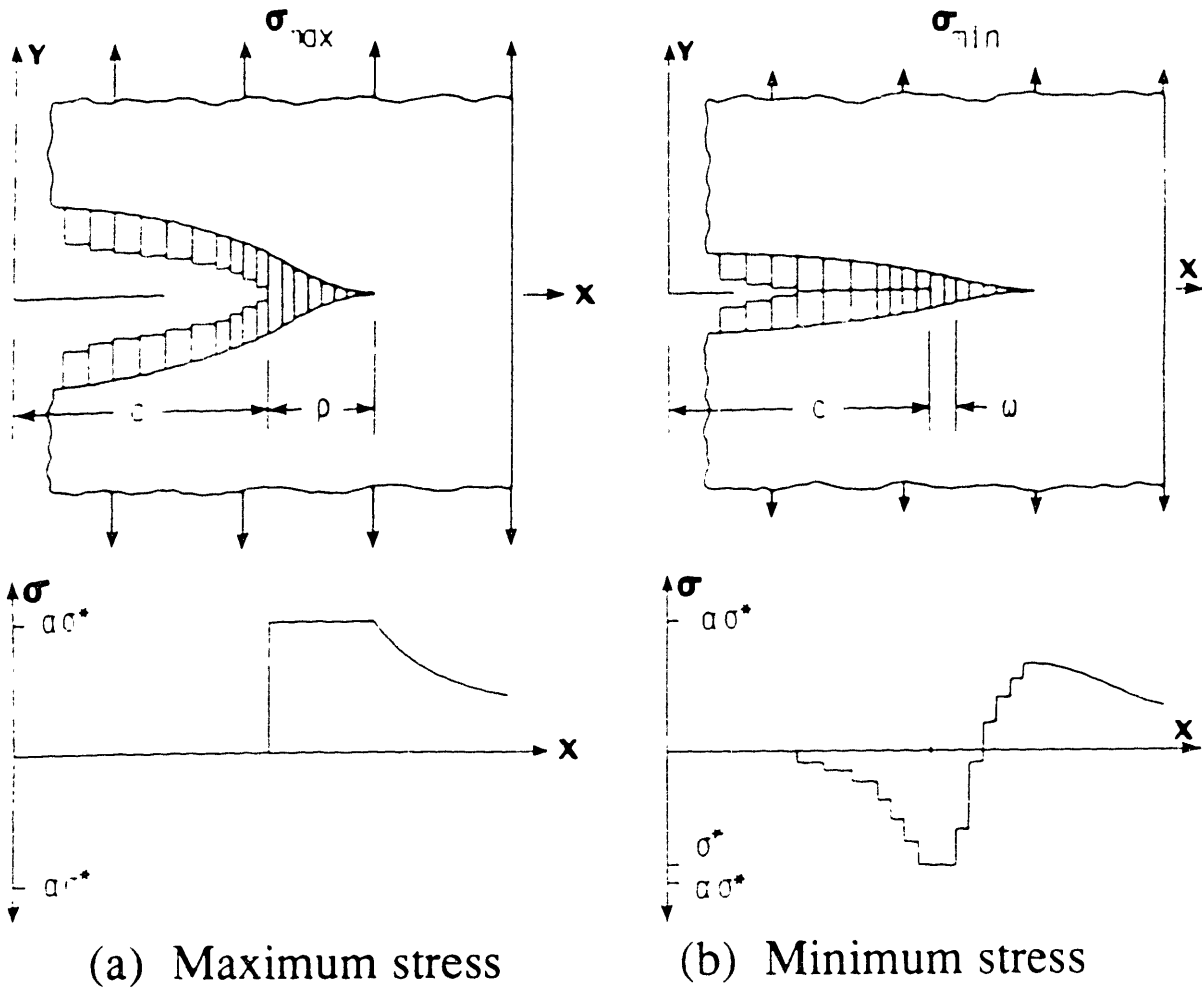


Figure 5.4 Crack surface displacement and stress distribution along the crack line for Newman's modification to the Dugdale strip yield model. From Ref. [5.31].

#### 5.4 Newman's Model Applied to IN100(PM) at 649C

Using the above equations representing Newman's crack opening model, the effective stress range ( $\Delta\sigma_{\text{eff}} = \sigma_{\text{max}} - \sigma_{\text{op}}$ ) can be calculated for the fatigue crack propagation results of this investigation. Since  $\sigma_{\text{op}}$  was not measured directly in these tests, this is the only option.

##### Elastic Tests

First consider the series of IN100(PM) tests conducted under elastic fatigue conditions. The maximum stress was constant at 965 MPa and R-ratios included: -1, -.75, -.5 and 0.1. The value of  $\sigma^*$  is estimated as:  $(1380 + 1050)/2 = 1215$  MPa. Assuming plane stress conditions ( $\alpha=1$ ) due to the high maximum stress and small crack size, the expressions for normalized crack opening stress become:

$$\frac{\sigma_{\text{op}}}{\sigma_{\text{max}}} = 0.170 + 0.273R + 0.944R^2 - 0.387R^3 \quad \text{for } R_{\sigma} \geq 0 \quad (5.8)$$

and

$$\frac{\sigma_{\text{op}}}{\sigma_{\text{max}}} = 0.170 + 0.273R \quad \text{for } -1 \leq R_{\sigma} \leq 0 \quad (5.9)$$

These two expressions are shown graphically in Figure 5.5. The general trend for  $\sigma_{\text{op}}/\sigma_{\text{max}}$  to decrease with decreasing R-ratio was observed in other experimental investigations cited in a previous section. Furthermore, measured values of  $\sigma_{\text{op}}/\sigma_{\text{max}}$  were approximately -0.1 when  $R = -1$  in many cases involving high strength materials. Using calculated values of  $\sigma_{\text{op}}$ , the effective stress intensity factor range may be expressed as:

$$\Delta K_{\text{eff}} = 0.73(965 - \sigma_{\text{op}})\sqrt{\pi a} \quad (5.10)$$

where  $\Delta K_{\text{eff}}$  is in  $\text{MPa}\sqrt{\text{m}}$  and  $a$  is in meters. Crack growth rates versus  $\Delta K_{\text{eff}}$  are plotted in Figure 5.6 for the IN100(PM) tests performed under elastic fatigue conditions. The

consolidation of crack growth rates is excellent and within experimental scatter; see for example points "E" which represent two cracks tested under identical conditions. The consolidation of crack growth rates achieved with  $\Delta K_{eff}$  is identical to that achieved with the Walker modified  $\overline{\Delta K}$  shown in Figure 4.17.

### Elastic-Plastic Tests

Newman's model for normalized crack opening stress level was originally developed for elastic fatigue conditions, however, McClung and Sehitoglu [5.22] extended its application to elastic-plastic fatigue conditions. They measured crack tip opening stress levels for small cracks (100  $\mu\text{m}$  to 1.5 mm) in SAE1026 steel subjected to high strain fatigue conditions;  $\Delta\epsilon_t = 0.2\%$  to  $1.4\%$  ( $\Delta\epsilon_p = 0.001\%$  to  $0.52\%$ ) and  $R_\epsilon = -1$ . Measured values of the normalized crack opening stress level  $\sigma_{op}/\sigma_{max}$  agreed with that predicted by Newman's model for  $\sigma_{max}/\sigma^*$  ranging from 0.4 to 0.75. The stress ratio was not a variable in these tests since  $R_\epsilon = -1$  and the resulting  $R_\sigma \approx -1$ , assuming nearly balanced hysteresis loops. Better correlations of crack growth rates were achieved using estimates of  $\Delta J$  and  $\Delta CTOD$  based on the effective stress range.

Given the success of the Newman crack opening model in the case cited above, it was employed to calculate crack opening levels for IN100(PM) tested under elastic-plastic fatigue conditions for this investigation. Since  $R_\sigma < 0$  in all these elastic-plastic tests, Eqs. 5.3 - 5.5 were used to calculate  $\sigma_{op}/\sigma_{max}$ . In this case  $\sigma_{max}$  and  $R_\sigma$  vary from test to test and the normalized crack opening stress is strongly dependent on both. The value of  $A_0$  varies considerably (see Eq. 5.4) with small changes in  $\sigma_{max}$ . The correlation which will be demonstrated does not follow from the apparent simplicity of Eq. 5.3. It is not linear when  $\sigma_{max}$  is not constant.

Values of  $\sigma_{op}$  calculated using Newman's model were used to estimate  $\Delta\sigma_{eff}$ . This effective stress range was used to calculate  $\Delta J_{eff}$  for elastic-plastic and elastic tests. Crack growth rates versus  $\Delta J_{eff}$  are shown in Figure 5.7 for elastic-plastic tests and in Figure 5.8 for both elastic and elastic-plastic tests. Consolidation of crack growth rates is comparable to that achieved using  $\Delta\sigma_{tot}$  to calculate  $\Delta J_{tot}$  and is again far superior to consolidation of crack growth rates achieved using  $\Delta\sigma_{pos}$  to calculate  $\Delta J^*$  (see Figure 4.33).

#### Reconciliation: $\Delta\sigma_{tot}$ with $\Delta\sigma_{eff}$

In Chapter 4 we demonstrated that the compressive stress-strain excursion under elastic and elastic-plastic fatigue conditions contributed to the mechanical driving force for crack growth in aircraft turbine disk alloys. Higher crack growth rates resulted from decreasing  $R_\sigma$ . Consolidation of crack growth rates was achieved only when the total stress or total strain range was included in calculating the mechanical driving force.

In Chapter 5 we interrogated the literature to find:

- Other examples where crack growth rates were found to increase with decreasing  $R_\sigma$ . Thus the findings of this investigation appear to be generally true.
- Direct measurements have shown the crack opening stress to decrease with decreasing  $R_\sigma$ .
- A model developed by Newman was found to predict normalized crack opening stress levels under elastic and elastic-plastic fatigue conditions.

Newman's model was employed to calculate  $\Delta\sigma_{eff}$  for IN100(PM) at 649C subjected to elastic and elastic-plastic fatigue conditions. It was found that  $\Delta\sigma_{eff}$  could be used to correlate crack growth rates as well as  $\Delta\sigma_{tot}$  under both conditions. The question arises; how is  $\Delta\sigma_{eff}$  related to  $\Delta\sigma_{tot}$ ? Since  $\Delta\sigma_{eff}$  was calculated as  $(\sigma_{max} - \sigma_{op})$  using Eq. 5.3 and  $\Delta\sigma_{tot}$  was measured in each test,  $\Delta\sigma_{eff}$  is plotted versus  $\Delta\sigma_{tot}$  in Figure 5.9. As can be seen the relationship is linear. Therefore, an increase or decrease in  $\Delta\sigma_{tot}$  results in a proportional increase or decrease in  $\Delta\sigma_{eff}$ . For the elastic tests:

$$\Delta\sigma_{\text{eff}} = 523 + 0.28 \Delta\sigma_{\text{tot}} \quad ; R^2 = 1.00 \quad (5.11)$$

and for the elastic-plastic tests ( $R_{\epsilon} = 0$ ):

$$\Delta\sigma_{\text{eff}} = 531 + 0.47 \Delta\sigma_{\text{tot}} \quad ; R^2 = 1.00 \quad (5.12)$$

For a given  $\Delta\sigma_{\text{tot}}$  and  $R_{\sigma}$ -ratio, the elastic-plastic tests exhibit a higher  $\Delta\sigma_{\text{eff}}$  due to higher values of  $\sigma_{\text{max}}/\sigma^*$ . It is interesting to note that the single elastic plastic test where  $R_{\epsilon} = -1$  does not correlate with the other elastic-plastic tests.

The above demonstrates that the use of  $\Delta\sigma_{\text{eff}}$  or  $\Delta\sigma_{\text{tot}}$  in calculating the mechanical driving force will result in an equivalent empirical consolidation of crack growth rates for the conditions studied here. The generality of these findings cannot be established with the limited data available in the literature on fatigue crack growth rates of small cracks under elastic and elastic-plastic conditions.

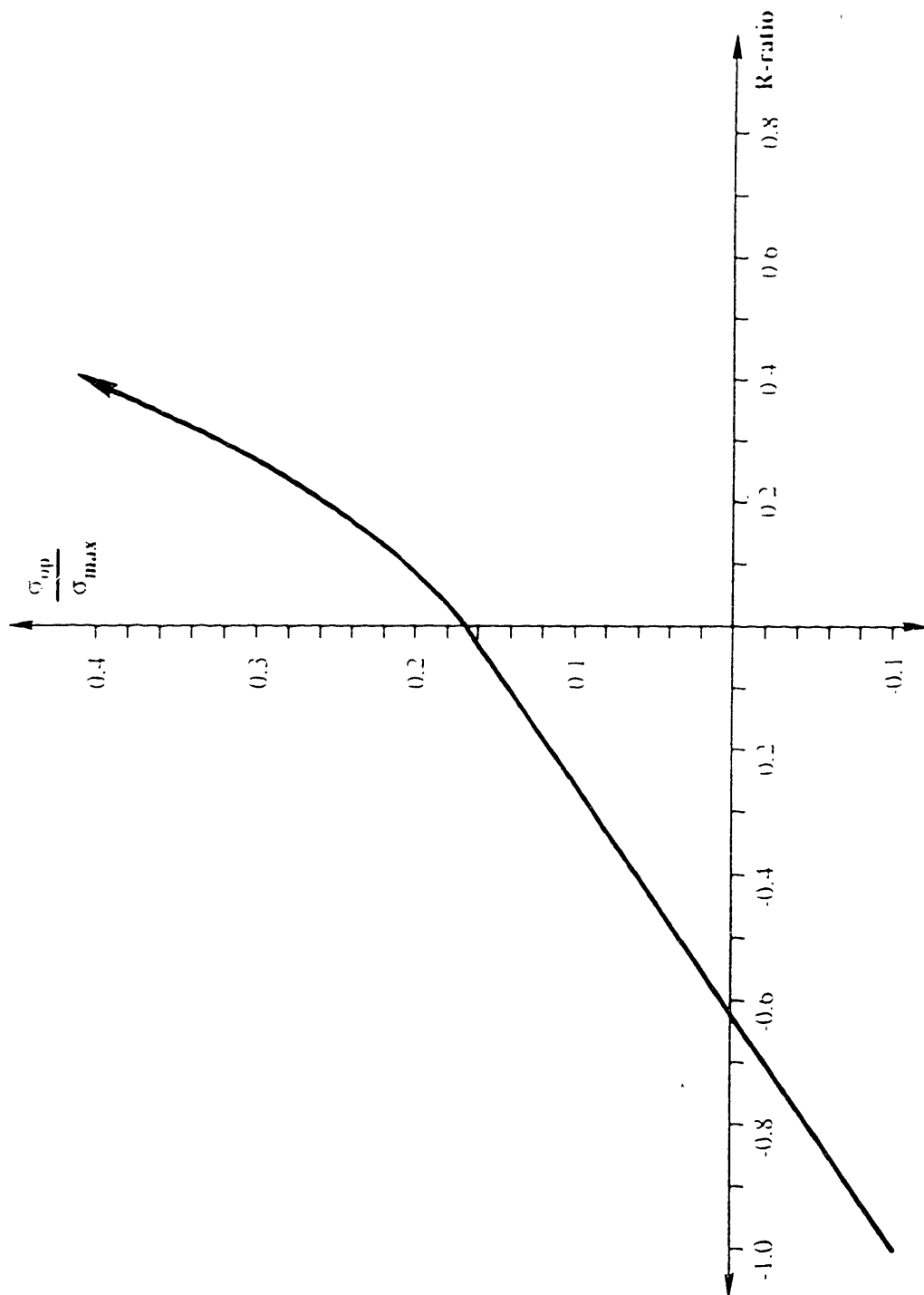


Figure 5.5 Normalized crack opening stress level (calculated from Newman's model) versus R-ratio for IN100(PM) tested at 649C under elastic fatigue conditions; max. stress = 965 MPa.

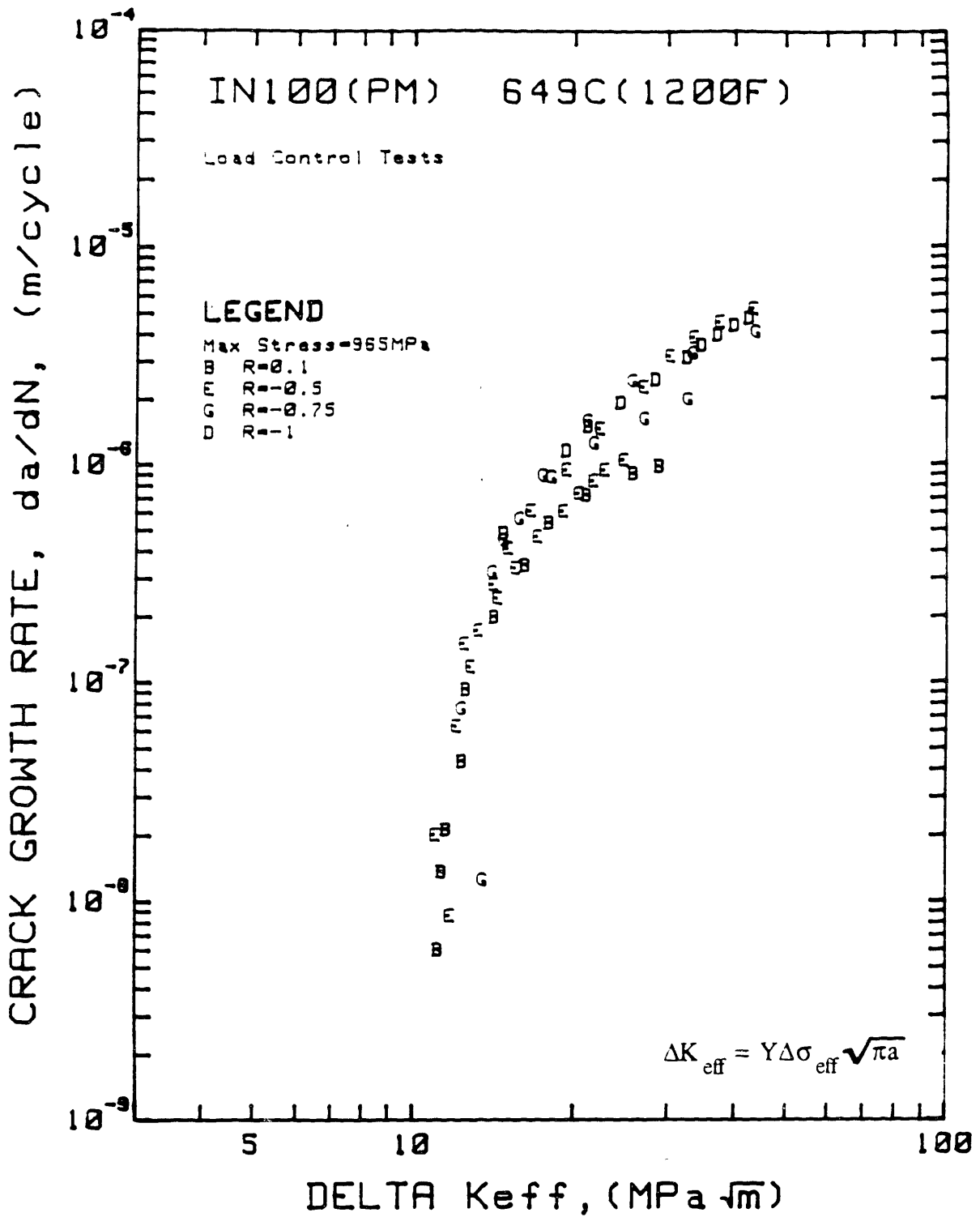


Figure 5.6 Crack growth rates versus the effective stress intensity factor range (calculated using  $\Delta\sigma_{eff}$  from Newman's model) for IN100(PM) tested at 649C under elastic fatigue conditions; R-ratio was varied at max. stress = 965 MPa, Freq. = 10 cpm.

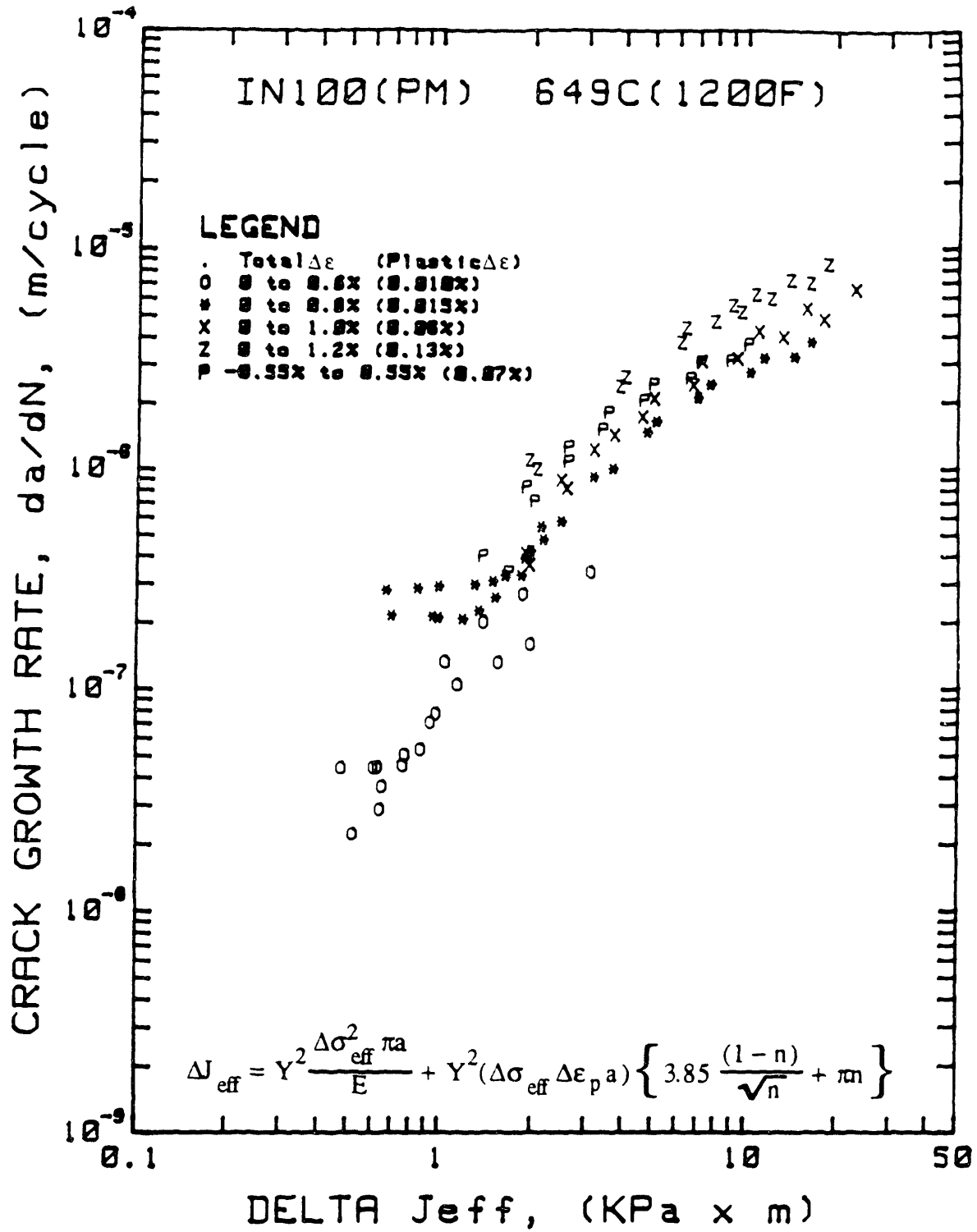


Figure 5.7 Crack growth rates versus the effective J-integral range, (calculated using  $\Delta\sigma_{eff}$  from Newman's model) for IN100(PM) tested at 649C and under elastic-plastic fatigue conditions; total strain range was varied, Freq. = 10 cpm.

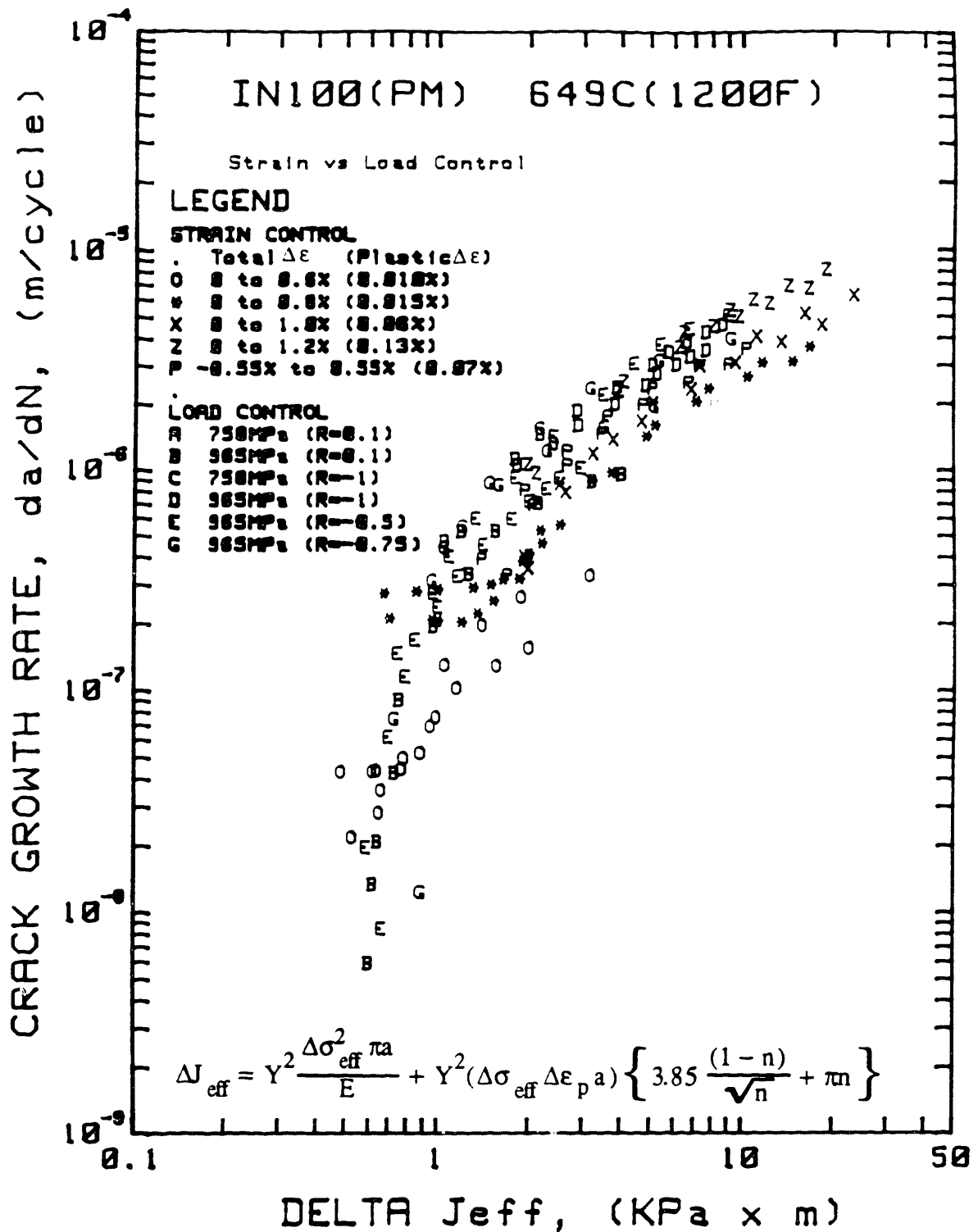


Figure 5.8 Summary of crack growth rates versus the effective J-integral range, (calculated using  $\Delta\sigma_{\text{eff}}$  from Newman's model) for IN100(PM) tested under elastic and elastic-plastic fatigue conditions; Freq = 10 cpm.

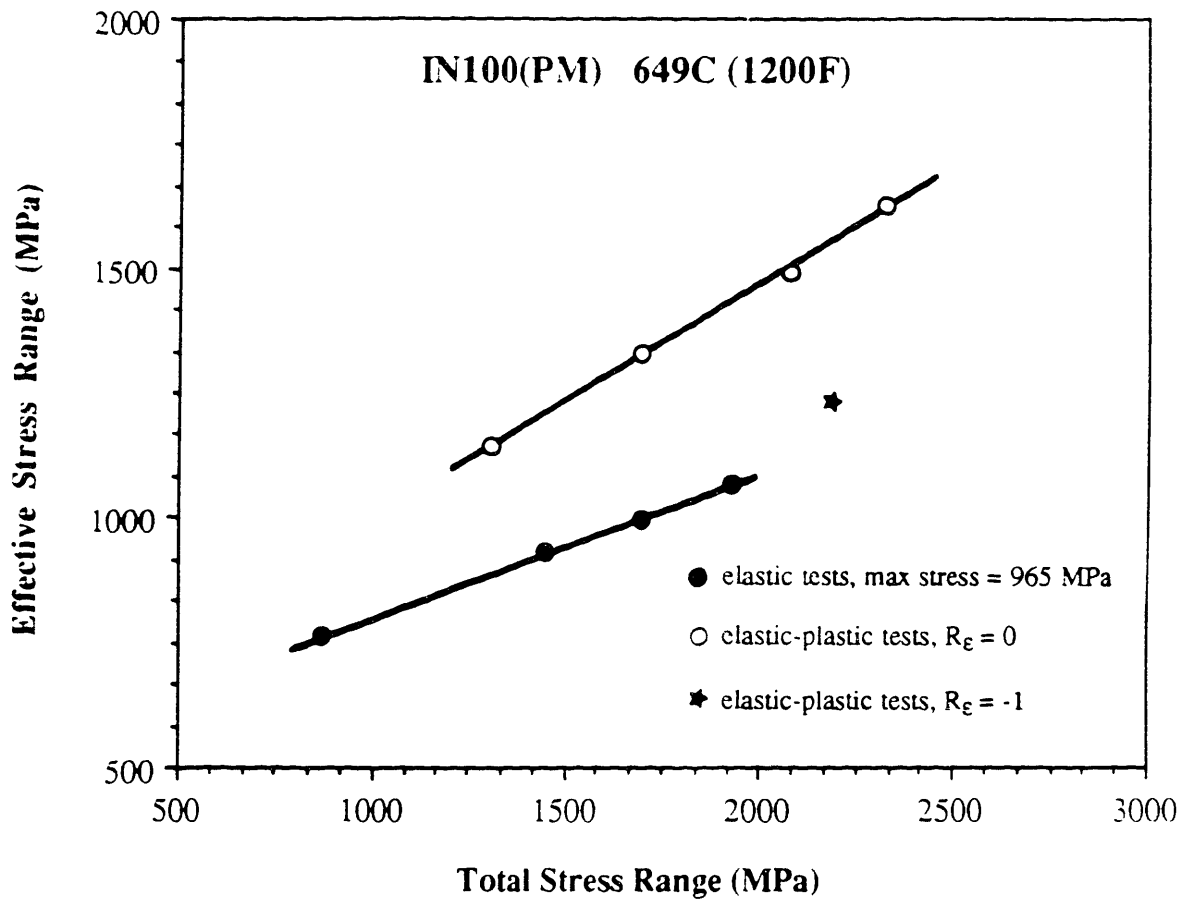


Figure 5.9 Effective stress range (calculated from Newman's model) versus total stress range for IN100(PM) tested under elastic and elastic-plastic fatigue conditions, Freq. = 10 cpm.

## 5.5 Fatigue Crack Growth and Crack Tip Strain Reversals

The problem of fatigue crack growth consists of both a mechanical driving force and a material response to that driving force. Under elastic fatigue conditions, the mechanical driving force is best defined in terms of linear elastic fracture mechanics. Under high strain fatigue conditions ( $\Delta\varepsilon_p > 0$ ), the mechanical driving force can be defined in terms of various elastic-plastic fracture mechanics parameters. The mechanical driving force defines the crack tip stress-strain field. It is generally agreed that the range of crack tip strain (or  $\Delta\text{CTOD}$ ) in the plastic zone is responsible for the increment of crack extension occurring in each cycle.

In the previous section it was demonstrated that the effective range of the mechanical driving force is often limited by the crack closure phenomenon. The effective stress-strain range is usually taken as the range over which the crack tip is open. A review of measurements and models indicate that the role of the compressive stress-strain excursion in  $R_\sigma < 0$  cycling is to lower the crack opening stress level, therefore increasing the effective range of the mechanical driving force. By demonstrating that  $\Delta\sigma_{\text{eff}}$  was linearly related to  $\Delta\sigma_{\text{tot}}$ , crack opening arguments appear to be a plausible explanation for the success of fracture mechanics parameters which include  $\Delta\varepsilon_{\text{tot}}$  or  $\Delta\sigma_{\text{tot}}$  in correlating crack growth rates. It can therefore be stated that the role of the compressive strain excursions is to override, to some extent, the mechanical crack closure which generally occurs at positive stresses on unloading from the maximum stress.

The forgoing explanation is physically sound. However, one may ask, if  $K$  defines the crack tip stress-strain condition and  $\Delta K$  defines the crack tip stress-strain range, then what role does the compressive-going stress-strain excursion play in creating damage in the crack tip plastic zone? The answer to this question, of course, depends on the mechanism of crack advance per cycle, (striation mechanism, ductility exhaustion, grain boundary decohesion, etc.) which in turn depends on: material, environment, frequency, stress-strain range, etc.

The compressive-going stress-strain excursion presumably reverses the tension going strain. It is reasonable to assume that the forward going crack tip strain would be of such a magnitude to accommodate the crack tip opening displacement. The maximum value would be limited by the fracture strain (accounting for state of stress) and further limited by the elastic-plastic envelope surrounding the crack tip which represents the material's intrinsic resistance to crack growth. Intrinsic resistance to crack growth incorporates macroscopic material properties (yield strength, ductility, strain hardening behavior, etc.) as well as microscopic properties (grain size, slip character, cohesive strength, etc.)

The reversal of crack tip strain is limited by the magnitude of the forward going strain and crack flank closure behind the crack tip. The unique feature of the small crack experiments in this investigation is that the bulk stress and strains are sufficiently high to override crack closure during the compressive excursion. Furthermore, the requirements for strain compatibility at the elastic-plastic boundary will cause crack tip strains to be reversed to nearly the same extent as the bulk strain range in elastic-plastic tests. Hence, it is reasonable to postulate that the compressive stress-strain excursion increases the magnitude and extent of the reversed crack tip strain range. This physical argument is not easily corroborated by direct physical measurements, particularly for fatigue crack growth in turbine disk alloys at elevated temperatures.

These arguments are supported by the results of Lalor and Sehitoglu [5.36] who modeled crack closure and crack tip plastic zones for small cracks propagating from circular notches using a two dimensional finite element method. The test variables considered were: stress range, stress state, hardening behavior, crack length, plastic wake with respect to total crack length, and R-ratio.

Here we will look at their results only with respect to comparing the two R-ratios ( $R = 0$  and  $R = -1$ ) and the two stress states (plane stress and plane strain). Crack tip conditions

are considered at a crack length =  $0.6 \cdot (\text{notch radius})$  which was considered a sufficient length to relieve the stress field of the notch over the open crack. The maximum stress was  $0.72\sigma_{ys}$ . The material properties were selected to fit a 1070 wheel steel.

Figures 5.10a and 5.10b show the stress fields at maximum and minimum load (plane stress and plane strain) for  $R = 0$  and  $R = -1$ , respectively. In the  $R = 0$  case, the compressive stress field surrounding the crack tip and crack flank at minimum load is only the residual stress caused by elastic unloading outside the plastic zone. The magnitude of this compressive stress is sufficient to cause only a limited extent of plastic strain reversal at the crack tip and no plastic strain reversal along the crack flank.

In the  $R = -1$  case, the compressive stress field surrounding the crack tip and crack flank at minimum load is caused by elastic unloading plus the applied compressive load. The magnitude of the compressive stress is sufficient to cause extensive plastic strain reversal at the crack tip and along the crack flank.

The size of the maximum (or monotonic) and reversed plastic zones are shown in Figure 5.11a and 5.11b for the four cases described above. The size of the monotonic plastic zones are similar because they depend primarily on  $K_{max}$  which was the same in all cases. The effect of the state of stress is somewhat less than expected. The size of the reversed plastic zone at minimum load is far more extensive in the  $R = -1$  case than the  $R = 0$  case.

The increasing plastic zone size which occurs with decreasing R-ratio may contribute to the increasing crack growth rates observed in this investigation. This argument is physically sound and supported by the above analysis. It is plausible that both a decreasing crack opening stress and increasing reversed plastic zone size contribute to the increase in crack growth rates which are generally observed as  $R_{\sigma}$  decreases.

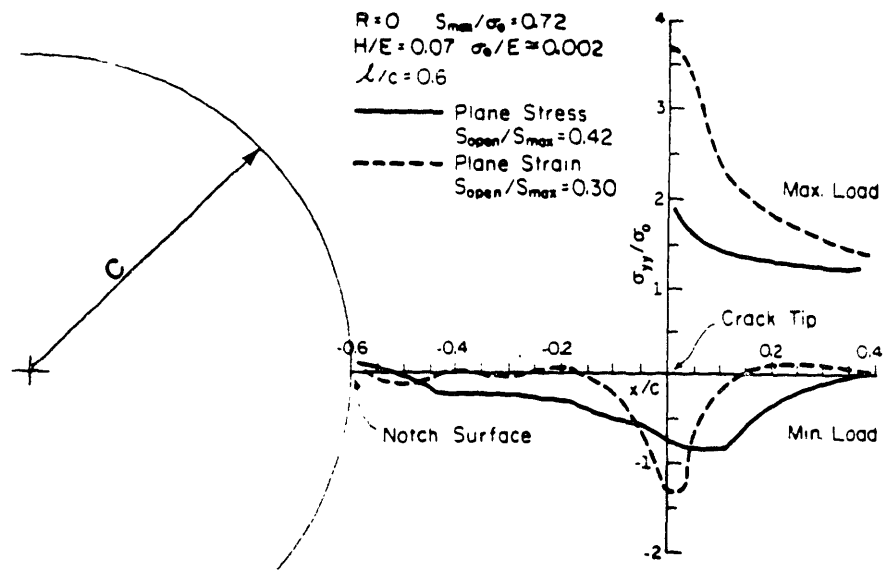


Figure 5.10a Crack tip stress fields and crack wake residual stresses for  $R = 0$  loading; max. stress =  $0.72\sigma_{ys}$ , crack length =  $0.6 \cdot$ (notch radius). From Ref. [5.36].

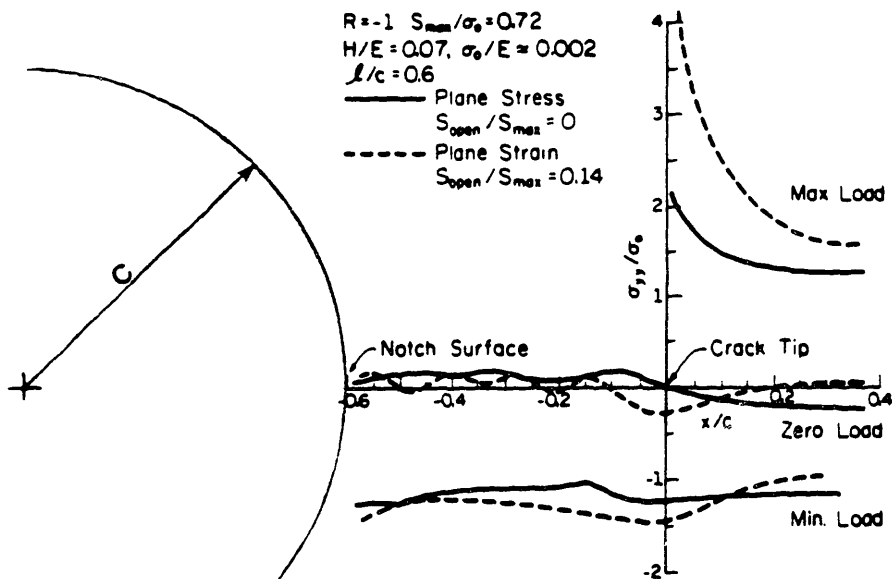


Figure 5.10b Crack tip stress fields and crack wake residual stresses for  $R = -1$  loading; max. stress =  $0.72\sigma_{ys}$ , crack length =  $0.6 \cdot$ (notch radius). From Ref. [5.36].

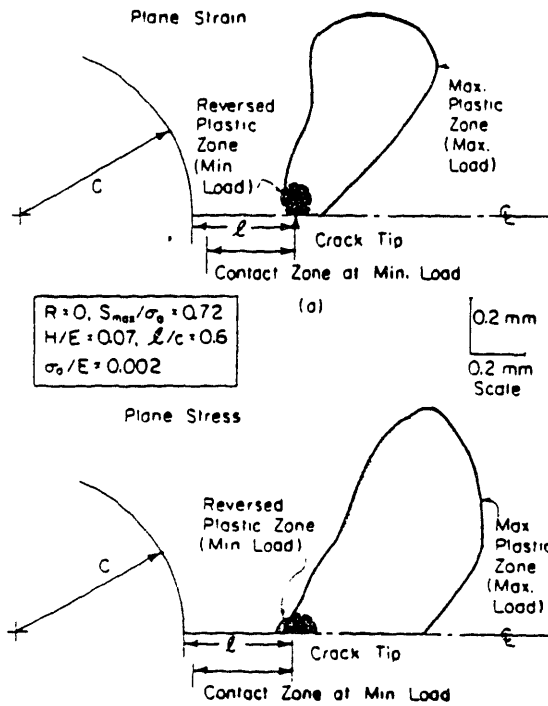


Figure 5.11a Crack tip monotonic and reversed plastic zones for  $R = 0$  loading; max. stress  $= 0.72\sigma_{ys}$ , crack length  $= 0.6 \cdot$ (notch radius). From Ref. [5.36].

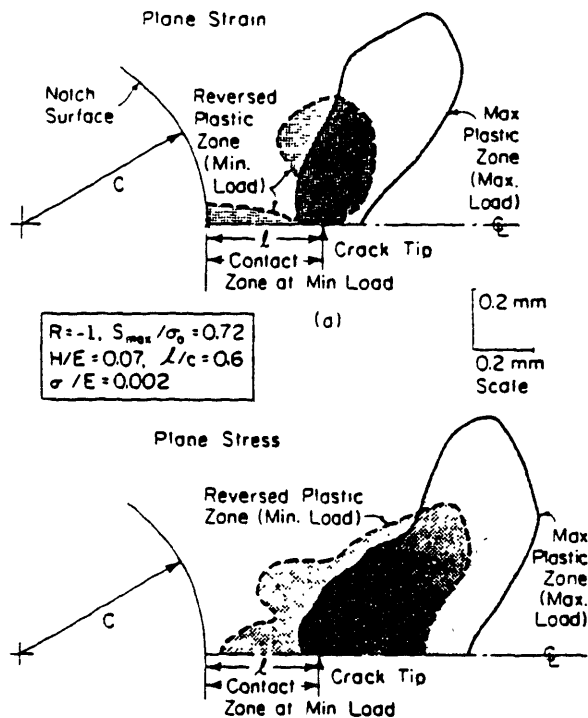


Figure 5.11b Crack tip monotonic and reversed plastic zones for  $R = -1$  loading; max. stress  $= 0.72\sigma_{ys}$ , crack length  $= 0.6 \cdot$ (notch radius). From Ref. [5.36].

## 6. Conclusions

The fatigue crack growth behavior of small cracks in three aircraft turbine disk alloys was investigated at elevated temperatures under elastic and elastic-plastic conditions over the crack length regime from 100  $\mu\text{m}$  to 1 mm. The following conclusions can be drawn from the crack growth rate data.

- 1) Anomalous crack growth behavior was not observed for small Mode I cracks under high stress elastic fatigue conditions. The LEFM stress intensity factor range correlated small crack with long crack growth rates and consolidated small crack growth rates at different stress levels for the same  $R_\sigma$ -ratio. Apparent threshold behavior for small cracks coincided with that for long cracks.
- 2) Under high stress elastic fatigue conditions, small crack growth rates at different  $R_\sigma$ -ratios were consolidated using the Walker-modified stress intensity factor range.
- 3) The pseudostress intensity factor range and the cyclic J-integral range, calculated using  $\Delta\varepsilon_t$  and  $\Delta\sigma_t$ , respectively, consolidated small crack growth rates under elastic and elastic-plastic fatigue conditions.
- 4) Values of  $\Delta\sigma_{\text{eff}}$  estimated from Newman's crack closure model were used to achieve excellent consolidation of small crack growth rates with  $\Delta K_{\text{eff}}$  and  $\Delta J_{\text{eff}}$  under elastic and elastic-plastic fatigue conditions, respectively. A linear relationship between  $\Delta\sigma_{\text{tot}}$  and  $\Delta\sigma_{\text{eff}}$  gives a physical justification for the consolidation of small crack growth rates with LEFM and EPFM parameters based on  $\Delta\sigma_t$  and  $\Delta\varepsilon_t$ .
- 5) Under all conditions, the compressive component of the fatigue cycle contributed to higher crack growth rates than tension-tension cycling. The compressive component

must be accounted for in expressing the mechanical driving force in terms of LEFM or EPFM parameters.

## 7. Recommendations for Future Research

- 1) A review of the open literature revealed that the majority of investigations of small crack behavior in aircraft turbine disk alloys were performed at room temperature. Such results are likely to be of little relevance for fine grained powder metallurgy alloy applications since room temperature fatigue fracture paths are usually transgranular, whereas, elevated temperature (~650C) fatigue fracture paths are intergranular. Consequently, in powder metallurgy alloys, future fatigue crack growth studies should be performed at disk relevant temperatures.
- 2) Additional small crack testing should be performed under notch relevant conditions, including strain hold tests. Small crack growth rates should also be measured in notch configurations.
- 3) An investigation of crack opening-closure should be conducted for small cracks in disk alloys at elevated temperatures to resolve the issue of crack opening stress levels under elastic-plastic fatigue conditions. The laser IDG technique appears to be suitable for this type of investigation.
- 4) Understanding the role of compressive stress-strain excursions in overriding crack closure should be considered as an objective of future work. Is closure more important with respect to the stress level at which crack flanks make contact or is strain reversal ahead of the crack tip more important? Is the size of the reversed plastic zone as important as the maximum strain therein? How are the two related to alloy mechanical properties and crack tip driving force?

## References

- [1.1] J.A. Harris, Jr., *Engine Component Retirement for Cause*, AFWAL-TR-87-4069, Vol. 1, Wright-Patterson AFB, OH, 1987.
- [1.2] J.M. Hyzak, W.H. Reimann and J.E. Allison, *The Development of Quantitative NDI for Retirement-for-Cause*, Air Force Materials Laboratory, Report AFML-TR-78-198, Wright-Patterson AFB, OH, 1979.
- [1.3] C.G. Annis Jr., J.S. Cargill, J.A. Harris Jr., and M.C. Van Wanderham, "Engine Component Retirement-for-Cause: A Nondestructive Evaluation (NDE) and Fracture Mechanics-Based Maintenance Concept", *Journal of Metals*, 1981, pp. 24-28.
- [1.4] W.D. Cowie, "Turbine Engine Structural Integrity Program (ENSIP)", *Journal of Aircraft*, Vol. 12, 1975, pp. 366-369.
- [1.5] United States Air Force, "Engine Structural Integrity Program", *Military Standard 1783, Aeronautical Systems Division*, Wright-Patterson Air Force Base, OH, 1984.
- [1.6] T.T. King, W.D. Cowie and W.H. Reimann, "Damage Tolerant Design Concepts for Military Engines", *AGARD Conference Proceedings*.
- [1.7] B.N. Leis, M.F. Kanninen, A.T. Hopper, J. Ahmad and D. Broek, *A critical Review of the Short Crack Problem in Fatigue*, AFWAL-TR-83-4019, 1983.
- [1.8] S. Suresh and R.O. Ritchie, "Propagation of Short Fatigue Cracks," *International Metals Reviews*, Vol. 29, No. 6, 1984.
- [1.9] M.J. Blackburn and R.A. Sprague, "Production of Components by Hot Isostatic Pressing of Nickel-Base Superalloy Powders," *Metals Technology*, August 1977, pp. 388-395.
- [1.10] S.A. Sattar and C.V. Sundt, "Gas Turbine Engine Disk Cyclic Life Prediction", *Journal of Aircraft*, Vol. 12, No. 4, 1975, pp. 360-365.
- [1.11] S. Majumdar, "Low-Cycle Fatigue and Creep Analysis of Gas Turbine Engine Components", *Journal of Aircraft*, Vol. 12, No. 4, 1975, pp. 376-382.
- [1.12] T.A. Cruse, "Residual Life Prediction of Surface Cracks in Complex Structural Details", *Journal of Aircraft*, Vol. 12, No. 4, 1975, pp. 369-375.
- [1.13] A. Coles, "Material Considerations for Gas Turbine Engines", *ICM3*, Vol. 1, 1979, pp. 3-11.
- [1.14] R.H. Van Stone, "Residual Life Prediction Methods for Gas Turbine Components" in *Mechanics and Physics of Crack Growth*, *Materials Science and Engineering*, Vol. A103, No. 1, 1988, pp. 49-61.

- [2.1] R. Wanhill, "Short Cracks in Aerospace Structures" in *Behavior of Short Fatigue Cracks*, K.J. Miller and E.R. del los Rios, ed., Mechanical Engineering Publications, London, 1986, pp. 27-36.
- [2.2] Military Standard, *Aircraft Structural Integrity Program, Airplane Requirements*, Mil-STD-1530 (USAF), Sept. 1972.
- [2.3] J. Harris Jr., *Engine Component Retirement for Cause*, AFWAL-TR-87-4069, Air Force Wright Aeronautical Laboratories, 1980.
- [2.4] P. Forsyth, *Proc. Roy. Soc. (London)*, Ser A, 1957, Vol. 242, p. 198.
- [2.5] P. Forsyth, "A Two Stage Process of Fatigue Crack Growth", *Proc. Crack Propagation Symp.*, Canfield, 1961, Vol. 1, p. 76.
- [2.6] R.G. de Lange, "Plastic Replica Methods Applied to the Study of Fatigue Crack Propagation in Steel 35 CD 4 and 26 St Aluminum Alloy", *Transactions of the Metallurgical Society of AIME*, Vol. 230, 1964, pp. 644-648.
- [2.7] N.E. Frost, "A Relation between the Critical Alternating Propagation Stress and Crack Length for Mild Steel", *Proc. Inst. Mechanical Engrs*, Vol. 173, 1959, pp. 811-827.
- [2.8] H. Kitagawa and S. Takahashi, "Applicability of Fracture Mechanics to Very Small Cracks or Cracks in the Early Stage", *Proc. of the Second International Conference on the Mechanical Behavior of Materials*, Boston, 1976, pp. 627-631.
- [2.8'] J. Lankford and D.L. Davidson, "The Role of Metallurgical Factors in Controlling the Growth of Small Fatigue Cracks", *Small Fatigue Cracks*, R.O. Ritchie and J. Lankford, eds., The Metallurgical Society of AIME, 1986, p. 53.
- [2.9] S. Pearson, "Initiation of Fatigue Cracks in Commercial Aluminum Alloys and the Subsequent Propagation of Very Short Cracks", *Engineering Fracture Mechanics*, Vol. 7, 1976, pp. 235-247.
- [2.10] M.H. El Haddad, K.N. Smith and T.H. Topper, "Fatigue Crack Propagation of Short Cracks", *ASME - CSME Joint Conference on Pressure Vessels and Piping, Nuclear Energy and Materials*, Montreal, 1978.
- [2.11] R.O. Ritchie and J. Lankford, "Overview of the Small Crack Problem", in *Small Fatigue Cracks*, R.O. Ritchie and J. Lankford, eds., The Metallurgical Society of AIME, 1986, pp. 1-5.
- [2.12] G.R. Irwin, *Journal of Applied Mechanics*, Trans. ASME, Vol. 24, 1957.
- [2.12'] D. Broek, *Elementary Engineering Fracture Mechanics*, 3<sup>rd</sup> Revised Edition, Martinus Nijhoff Publishers, 1982.
- [2.13] P.C. Paris and F. Erdogan, "A Critical Analysis of Crack Propagation Laws", *Journal of Basic Engineering*, Trans. ASME, Vol. 85, 1963, p. 528-534.

- [2.14] W. Elber, "The Significance of Fatigue Crack Closure", *Damage Tolerance in Aircraft Structures, ASTM STP 486*, 1971, pp. 230-242.
- [2.15] S. Suresh and R.O. Ritchie, "A Geometric Model for Fatigue Crack Closure Induced by Fracture Surface Morphology", *Metallurgical Transactions*, 13A, 1982, pp. 1627-1631.
- [2.16] N. Walker and C.J. Beevers, "A Fatigue Crack Closure Mechanism in Titanium", *Fatigue of Engineering Materials and Structures*, Vol. 1, 1979, pp. 135-148.
- [2.17] C.J. Beevers, R.L. Carlson, K. Bell and E.A. Starke, "A Model for Fatigue Crack Closure", *Engineering Fracture Mechanics*.
- [2.18] K. Minakawa and A.J. McEvily, "Our Crack Closure in Near-Threshold Region", *Scripta Metallurgica*, Vol. 15, 1981, pp. 633-636.
- [2.19] R.O. Ritchie and S. Suresh, "Some Consideration on Fatigue Crack Closure Induced by Fracture Surface Morphology", *Metallurgical Transactions*, Vol. 13A, 1982, pp. 937-940.
- [2.20] R.O. Ritchie, S. Suresh and C.M. Moss, "Near-Threshold Fatigue Crack Growth in 2 1/2 Cr-Mo Pressure Vessel Steel in Air and Hydrogen", *Journal of Engineering and Materials Technology*, Trans. ASME, Series H, Vol. 102, 1980, pp. 293-299.
- [2.21] S. Suresh, G.F. Zamiski and R.O. Ritchie, "Oxidation and Crack Closure, an Explanation for Near Threshold Corrosion Fatigue Crack Growth Behavior", *Metallurgical Transactions*, Vol. 12A, 1981, pp. 1435-1443.
- [2.22] S. Banerjee, *A Review of Crack Closure*, AFWAL-TR-84-4031, Air Force Wright Aeronautical Laboratories, Dayton, OH, 1984.
- [2.23] W.T. Evans and A.R. Luxmoore, *Journal of Strain Analysis*, Vol. 11, 1976, pp. 177-185.
- [2.24] W.K. Wilson, "Plane Strain Crack Toughness Testing of High Strength Metallic Materials", *ASTM STP 410*, American Society for Testing and Materials, Philadelphia, 1966, pp. 75-76.
- [2.25] R.A. Smith, "On the Short Crack Limitations of Fracture Mechanics", *International Journal of Fracture*, Vol. 13, 1977, pp. 717-720.
- [2.26] W.F. Brown and J.E. Srawley, "Plane Strain Crack Toughness Testing of High Strength Metallic Materials", *ASTM STP 410*, American Society for Testing and Materials, Philadelphia, 1966, pp. 1-65.
- [2.27] Plane Strain Fracture Toughness of Metallic Materials, *1982 Annual Book of ASTM Standards*, Part 10, Standard No. E399.
- [2.28] J. Lankford, "On the Small Crack Fracture Mechanics Problem", *International Journal of Fracture*, Vol. 16, 1980, pp. R7-R9.

- [2.29] D.L. Davidson and J. Lankford, *Fracture 1977*, University of Waterloo, Vol. 2, 1977, pp. 897-904.
- [2.30] M.A. Wilkins and G.C. Smith, *Acta Metallurgica*, Vol. 18, 1970, pp. 1035-1043.
- [2.31] M. Klesnil and P. Lukas, *Fracture*, Chapman and Hall, 1969, pp. 725-730.
- [2.32] B.N. Leis, M.F. Kanninen, A.T. Hopper, J. Ahmad and D. Broek, *A Critical Review of the Short Crack Problem in Fatigue*, AFWAL-TR-83-4019, Air Force Wright Aeronautical Laboratories, Dayton, OH, 1983.
- [2.33] R.P. Skelton in *Low-Cycle Fatigue and Life Prediction*, ASTM STP 770, American Society for Testing and Materials, Philadelphia, 1982, pp. 337-381.
- [2.34] A.T. Price and W.J. Elder, *Journal of the Iron and Steel Institute*, Vol. 204, 1966, pp. 594-598.
- [2.35] H.D. Solomon and L.F. Coffin in *Fatigue at Elevated Temperatures*, ASTM STP 520, American Society for Testing and Materials, Philadelphia, 1973, pp. 112-122.
- [2.36] P.S. Maiya, *Scripta Metallurgica*, Vol. 9, 1975, pp. 1277-1282.
- [2.37] H.D. Solomon, *Metallurgical Transactions A*, Vol. 4, 1973, pp. 341-347.
- [2.38] P.S. Maiya and D.E. Busch, *Metallurgical Transactions A*, Vol. 6A, 1975, pp. 1761-1766.
- [2.39] J. Wareing, *Metallurgical Transactions A*, Vol. 6A, 1975, pp. 1367-1377.
- [2.40] G. Baudry and A. Pineau, *Materials Science and Engineering*, Vol. 28, 1977, pp. 229-242.
- [2.41] R.P. Skelton, *Materials Science and Engineering*, Vol. 19, 1975, pp. 193-200.
- [2.42] R.P. Skelton, *Materials Science and Engineering*, Vol. 32, 1978, pp. 211-219.
- [2.43] R.P. Skelton, *Materials Science and Engineering*, Vol. 35, 1978, pp. 287-298.
- [2.44] J. Reuchet and L. Remy, *Fatigue of Engineering Materials and Structures*, Vol. 2, 1979, pp. 51-62.
- [2.45] R.P. Skelton, *Fatigue of Engineering Materials and Structures*, Vol. 2, 1979, pp. 305-318.
- [2.46] K. Yamaguchi and K. Kanazawa, *Metallurgical Transactions A*, Vol. 10A, 1979, pp. 1445-1451.
- [2.47] G. Chalant and L. Remy, *Acta Metallurgica*, Vol. 28, 1980, pp. 75-88.
- [2.48] J. Huang, R.M. Pelloux and J. Runkle, *Metallurgical Transactions A*, Vol. 11, 1980, pp. 899-904.

- [2.49] B. Tomkins, *Philosophical Magazine*, Vol. 18, 1968, pp. 1041-1066.
- [2.50] K. Yamaguchi, K. Kanazawa and S. Yoshida, *Materials Science and Engineering*, Vol. 33, 1978, pp. 175-181.
- [2.51] R.C. Boettner, C. Laird and A.J. McEvily Jr. "Crack Nucleation and Growth in High Strain-Low Cycle Fatigue", *Transactions of the Metallurgical Society of AIME*, Vol. 233, February 1965, pp. 379-387.
- [2.52] H.D. Solomon, "Low Cycle Fatigue Crack Propagation in 1018 Steel", *Journal of Materials*, JMLSA, Vol. 7, No. 3, 1972, pp. 299-306.
- [2.53] J.R. Haigh and R.P. Skelton, "A Strain Intensity Approach to High Temperature Fatigue Crack Growth and Failure", *Materials Science and Engineering*, Vol. 36, 1978, pp. 133-137.
- [2.54] M.S. Starkey and R.P. Skelton, "A Comparison of the Strain Intensity and Cyclic J Approaches to Crack Growth", *Fatigue of Engineering Materials and Structures*, Vol. 5, No. 4, 1982, pp. 329-341.
- [2.55] J.R. Rice, *Journal of Applied Mechanics*, *Trans. ASME*, Vol. 35, June 1968, pp. 379-386.
- [2.56] C.F. Shih and J.W. Hutchinson, "Fully Plastic Solutions and Large Scale Yielding Estimates for Plane Stress Crack Problems", *Journal of Engineering Materials and Technology*, Oct. 1976, pp. 289-295.
- [2.57] J.E. Srawley and W.F. Brown in *Fracture Toughness Testing Methods*, *ASTM STP 381*, 1965, pp. 133-196.
- [2.58] J.A. Begley and J.D. Landes in *Fracture Toughness, Proceedings of the 1971 National Symposium on Fracture Mechanics, Part II*, *ASTM STP 514*, American Society for Testing and Materials, 1972, pp. 1-20.
- [2.59] J.R. Rice, P.C. Paris and J.G. Merkle in *Progress in Flaw Growth and Fracture Toughness Testing*, *ASTM STP 536*, American Society for Testing and Materials, 1973, pp. 231-245.
- [2.60] N.E. Dowling and J.A. Begley, "Fatigue Crack Growth during Gross Plasticity and the J-integral", *Mechanics of Crack Growth*, *ASTM STP 590*, American Society for Testing and Materials, 1976, pp. 82-103.
- [2.61] N.E. Dowling, "Crack Growth during Low-Cycle Fatigue of Smooth Axial Specimens", *Cyclic Stress-Strain and Plastic Deformation Aspects of Fatigue Crack Growth*, *ASTM STP 637*, American Society for Testing and Materials, 1977, pp. 97-121.
- [2.62] M. Okazaki and T. Koizumi, "Crack Propagation of Steels during Low-Cycle Thermal-Mechanical and Isothermal Fatigue at Elevated Temperatures", *Metallurgical Transactions*, Vol. 14A, 1983, pp. 1641-1648.

- [2.63] M.S. Starkey and R.P. Skelton "A Comparison of the Strain Intensity and the Cyclic J Approaches to Crack Growth", *Fatigue of Engineering Materials and Structures*, Vol. 5, No. 4, 1982, pp. 329-341.
- [2.64] M. Réger and L. Remy in *Fracture and the Role of Microstructure, Proceedings of the 4th European Conference on Fracture*, Engineering Materials Advisory Services Ltd, Cradley Heath, U.K., Vol. 2, 1982, pp. 531-538.
- [2.65] M. Réger, F. Soniak and L. Remy in *International Conference on Fatigue and Fatigue Thresholds*, C.J. Beevers, eds., Engineering Materials Advisory Services Ltd, Cradley Heath, U.K., 1984, pp. 797-806.
- [2.66] M. Okazaki, I. Hattori, F. Shiraiwa and T. Koizumi, "Effect of Strain Wave Shape on Low Cycle Fatigue Crack Propagation of SUS 304 Stainless Steel at Elevated Temperatures", *Metallurgical Transactions*, Vol. 14A, 1983, pp. 1649-1659.
- [2.67] J.S. Huang and R.M. Pelloux, "Low Cycle Fatigue Crack Propagation in Hastelloy-X at 25C and 760C", *Metallurgical Transactions*, Vol. 11A, 1980, pp. 899-904.
- [2.68] M.H. El Haddad, K.N. Smith and T.H. Topper, "Fatigue Crack Propagation of Short Cracks", *ASME, CSME Joint Conference on Pressure Vessels and Piping*, Nuclear Energy and Materials, Montreal, June 25-29, 1978.
- [2.69] M.H. El Hadda, K.N. Smith and T.H. Topper, *Journal of Engineering Materials Technology*, Vol. 101, 1979, pp. 42-46.
- [2.70] H. Kitagawa, S. Takahasi, "Applicability of Fracture Mechanics to Very Small Cracks", *Second International Conference on Mechanical Behavior of Materials*, Boston, MA, Aug. 1976, pp. 627-631.
- [2.71] M.H. El Haddad, N.E. Dowling, T.H. Topper, and K.N. Smith, "J-Integral Applications for Short Fatigue Cracks at Notches", *International Journal of Fracture*, Vol. 16, No. 1, February 1980.
- [2.72] H. Ohuchida, S. Usami and A. Nishioka, "Elastic-Plastic Approach to Fatigue Crack Propagation and Fatigue Limit of Materials with Cracks", Preprint of the *3rd International Conference on Fracture*, Munchen, 1973, V-442/A.
- [2.73] H. Ohuchida, S. Usami and A. Nishioka, "Fatigue Limit of Steel with Cracks", *Japanese Society of Mechanical Engineers*, Vol. 18, No. 125, Nov. 1975, p. 1185.
- [2.74] S. Usami and S. Shida, "Elastic-Plastic Analysis of the Fatigue Limit for A Material with Small Flaws", *Fatigue of Engineering Materials and Structures*, Vol. 1, 1979, pp. 471-481.
- [2.75] M.M. Hammouda, R.A. Smith and K.J. Miller, "Elastic-Plastic Fracture Mechanics for Initiation and Propagation of Notch Fatigue Cracks", *Fatigue of Engineering Materials and Structures*, Vol. 2, 1979, pp. 139-154.

- [2.76] M.M. Hammounda and K.J. Miller, "Elastic-Plastic Fracture Mechanics Analyses of Notches", *Elastic-Plastic Fracture*, ASTM STP 668, J.D. Landes, J.A. Begley and G.A. Clarke, eds., American Society for Testing and Materials, Philadelphia, PA, 1979, pp. 703-719.
- [2.77] J. Lankford, "The Growth of Small Cracks in 7075-76 Aluminum", *Fatigue of Engineering Materials and Structures*, Vol. 5, 1982, pp. 233-248.
- [2.78] K. Tanaka, Y. Nakai and M. Yamashita, "Fatigue Growth Threshold of Small Cracks", *International Journal of Fracture*.
- [2.79] S. Taira, K. Tanaka and Y. Nakai, "A Model of Crack Tip Slip Band Blocked by Grain Boundary", *Mechanics Research Communication*, Vol. 5, No. 6, 1978, p. 375.
- [2.80] Y. Nakai and K. Tanaka, "Grain Size Effect on Growth Threshold for Small Surface Cracks and Long Through Cracks under Cyclic Loading", *Proceedings of 23rd Japan Congress on Materials Research*, 1980.
- [2.81] S. Taira, K. Tanaka and M. Hoshina, "Grain Size Effect on Crack Nucleation and Growth in Long-Life Fatigue of Low Carbon Steel", *Fatigue Mechanisms*, ASTM STP 675, 1979, p. 135.
- [2.82] W.L. Morris, M.R. James and O. Buck, "Growth Rate Models for Short Surface Cracks in Al 2219-T851", *Metallurgical Transactions*, Vol. 12A, January 1981, pp. 57-64.
- [2.83] W.L. Morris and M.R. James, "A Simple Model of Stress Intensity Range Threshold and Crack Closure Stress", *Engineering Fracture Mechanics*, Vol. 18, No. 4, 1983, pp. 871-877.
- [2.84] W.L. Morris, *Metallurgical Transactions*, Vol 8A, 1977, p. 589.
- [2.85] A.E. Green and I.N. Sneddon, *Proc. Cambridge Phil. Soc.*, Vol. 46, 1950, p. 159.
- [2.86] R.A. Smith, *International Journal of Fracture*, Vol. 13, 1977, p. 717.
- [2.87] C.Y. Yang and H.W. Liu, *Scripta Metallurgica*, Vol. 14, 1980, p. 785.
- [2.88] W.L. Morris, M.R. James and O. Buck, *Metallurgical Transactions*, Vol. 12A, 1981, p. 57.
- [2.89] W.L. Morris, *Metallurgical Transactions*, Vol. 11A, 1980, p. 1117.
- [2.90] V. Shahani and H.G. Popp, *Evaluation of Cyclic Behavior of Aircraft Turbine Disk Alloys*, General Electric Aircraft Engine Group, NASA-CR-159433, 1978.
- [2.91] B.A. Cowles, D.L. Sims and J.R. Warren, *Evaluation of the Cyclic Behavior of Aircraft Turbine Disk Alloys*, Pratt and Whitney Aircraft Group, NASA-CR-159409, 1978.

- [2.92] B.A. Cowles, D.L. Sims and J.R. Warren, *Evaluation of the Cyclic Behavior of Aircraft Turbine Disk Alloys, Part II*, Pratt and Whitney Aircraft Group, NASA-CR-165123, 1980.
- [2.93] B.A. Cowles, D.L. Sims, J.R. Warren and R.V. Miner, Jr., "Cyclic Behavior of Turbine Disk Alloys at 650C", *Journal of Engineering Materials and Technology*, Vol. 102, 1980, pp. 356-363.
- [2.94] J.E. King, "Fatigue Crack Propagation in Nickel-base Superalloys - Effects of Microstructure, Load Ratio and Temperature", *Materials Science and Technology*, Vol. 3, 1987, pp. 751-764.
- [2.95] M.A. Hicks and C.W. Brown, "A Comparison of Short Crack Growth Behavior in Engineering Alloys", *Fatigue '84*, C.J. Beevers, ed., Engineering Materials Advisory Services Ltd., Cradley Heath, UK, 1984, pp. 1337-1347.
- [2.96] C.W. Brown, J.E. King and M.A. Hicks, "Effects of Microstructure on Long and Short Crack Growth in Nickel Base Superalloys", *Metal Science*, Vol. 18, 1984, pp. 374-380.
- [2.97] C.W. Brown and J.E. King, "The Relevance of Microstructural Influences in the Sort Crack Regime to Overall Fatigue Resistance", *Small Fatigue Cracks*, R.O. Ritchie and J. Lankford, eds., The Metallurgical Society of AIME, 1986, pp. 73-95.
- [2.98] P.T. Newman and C.J. Beevers, "The Initiation and Growth of Microcracks in Nickel-Base Superalloys", *Fatigue '84*, C.J. Beevers, ed., EMAS, Birmingham, 1984, pp. 785-797.
- [2.99] P. Newman and C.J. Beevers, "Growth of Short Fatigue Cracks in High Strength Ni-Base Superalloys", in *Small Fatigue Cracks*, R.O. Ritchie and J. Lankford, eds., The Metallurgical Society of AIME, 1986, pp. 97-116.
- [2.100] J. Feng, Ph.D. Thesis, MIT, 1987.
- [2.101] F. Soniak and L. Remy, "Fatigue Growth of Long and Short Cracks in a Powder Metallurgy Nickel-Base Superalloy", *EGF Pub. 1*, K.J. Miller and E.R. de los Rios, eds., Mechanical Engineering Publications, London, 1986, pp. 133-142.
- [2.102] R.S. Vecchio and R.W. Hertzberg, "A Rationale for the 'Apparent Anomalous' Growth Behavior of Short Fatigue Cracks", *Engineering Fracture Mechanics*, Vol. 22, No. 6, 1985, 1049-1060.
- [2.103] J.F. McCarver and R.O. Ritchie, "Fatigue Crack Propagation Threshold for Long and Short Cracks in René 95 Nickel-base Superalloy", *Materials Science and Engineering*, Vol. 55, 1982, pp. 63-67.
- [2.104] J. Lankford, T.S. Cook and G.P. Sheldon, "Fatigue Microcrack Growth in a Nickel-Base Superalloy", *International Journal of Fracture*, Vol. 17, 1981, pp. 143-155.

- [2.105] G.P. Sheldon, T.S. Cook, J.W. Jones and J. Lankford, "Some Observations on Small Fatigue Cracks in a Superalloy", *Fatigue of Engineering Materials and Structures*, Vol. 3, 1981, pp. 219-228.
- [2.106] S.J. Hudak Jr., D.L. Davidson, K.S. Chan, A.C. Howland and M.J. Walsch, *Growth of Small Cracks in Aeroengine Disk Materials*, AFWAL-TR-88-4090, Air Force Wright Aeronautical Laboratories, 1988.
- [2.107] B.N. Leis, D.P. Goetz, J. Ahmad, A.T. Hopper and M.F. Kanninen, *Mechanics Aspects of Microcrack Growth in Inconel 718 - Implications for Engine Retirement for Cause Analysis*, AFWAL-TR-84-4041, Air Force Wright Aeronautical Laboratories, 1984.
- [2.108] T.S. Cook, J. Lankford and G.P. Sheldon, *Research on Growth of Microcracks in Nickel-Base Superalloys*, AFML-TR-78-133, Air Force Wright Aeronautical Laboratories, 1978.
- [2.109] R.H. Van Stone and M.F. Henry, *Processing Effects on Microstructure and Fatigue Properties of Nickel-Base Superalloys*, NADC-80124-60, Naval Air Development Center, 1982.
- [3.1] F. Schubert, "Temperature and Time Dependent Transformation: Application to Heat Treatment of High Temperature Alloys", *Phase Stability in High Temperature Alloys*, Applied Science Publishers, 1980, pp. 119-149.
- [3.2] C. Sims and W. Hagel, eds., *The Superalloys*, John Wiley and Sons, 1972.
- [3.3] R.F. Decker, "Strengthening Mechanisms in Nickel-Base Superalloys", *Steel Strengthening Mechanisms Symposium*, Zurich, Switzerland, May 1969.
- [3.4] M. Donachie, Jr., ed., *Superalloys Source Book*, American Society for Metals, 1984.
- [3.5] J.M. Oblak, D.F. Paulonis and D.S. Duval, "Coherency Strengthening in Ni-Base Alloys Hardened by DO<sub>22</sub>", *Journal of Metals*, October 1969, pp. 34-38.
- [3.6] *U.S. Patent 3519503*, July 7, 1970.
- [3.7] G. Bellows, *Low Stress Grinding*, Machinability Data Center, Pub. No. MDC, 78-103, 1978.
- [3.8] R. Pelloux, J. Feng and G. Romanoski, *A Study of the Fatigue Behavior of Small Cracks in Nickel-Base Superalloys*, Final Report, Grant #AFOSR-84-0075, 1988.
- [3.9] S.J. Hudak, Jr., A. Saxena, R.J. Bucci and R.C. Malcolm, *Development of Standard Methods of Testing and Analyzing Fatigue Crack Growth Rate Data*, Technical Report AFML-TR-78-40, 1978.
- [3.10] G.R. Irwin, *Journal of Applied Mechanics*, Trans. ASME, V. 29, No. 4, 1962, pp. 651-654.

- [3.11] I.N. Sneddon, "The Distribution of Stress in the Neighborhood of a Crack in an Elastic Solid", *Proc. Roy. Soc. London*, A187, 1946, pp. 229-260.
- [3.12] J.C. Newman, Jr., "A Review and Assessment of the Stress Intensity Factors for Surface Cracks", *Part-Through Crack Fatigue Life Prediction, ASTM STP 687*, J.B. Chang, ed., American Society for Testing and Materials, 1979, pp. 16-42.
- [3.13] H. Nisitani and D.H. Chen, "Stress Intensity Factor for a Semi-Elliptical Surface Crack in a Shaft under Tension", *Trans. Japan Soc. Mech. Engrs.*, Vol. 50, No. 453, 1984, pp. 1077-1082.
- [3.14] I.S. Raju and J.C. Newman, Jr., *Stress Intensity Factors for Circumferential Surface Cracks in Pipes and Rods under Tension and Bending Loads*, NASA Technical Memorandum 87594, 1985.
- [4.1] J.M. Larsen, B.J. Schwartz, C.G. Annis Jr., *Cumulative Damage Fracture Mechanics under Engine Spectra*, Pratt and Whitney Aircraft Group, AFML-TR-79-4159, 1980.
- [4.2] J. Lankford, D.L. Davidson and T.S. Cook, "Fatigue Crack Tip Plasticity", *Cyclic Stress-Strain and Plastic Deformation Aspects of Fatigue Crack Growth, ASTM STP 637*, 1977, pp. 36-55.
- [4.3] J.R. Rice, "Mechanics of Crack Tip Deformation and Extension by Fatigue", *Fatigue Crack Propagation, ASTM STP 415*, 1967, pp. 247-311.
- [4.4] D. Broek, *Elementary Engineering Fracture Mechanics*, Noordhoff International Publishing, The Netherlands, 1974.
- [4.5] R.A. Smith, "On the Short Crack Limitations of Fracture Mechanics", *International Journal of Fracture*, Vol. 13, 1977, pp. 717-720.
- [4.6] D. Brock and J. Schijve, *The Influence of the Mean Stress on the Propagation of Fatigue Cracks in Aluminum Alloy Sheet*, NLR-TR M.2111, National Lucht-en Ruimtevaart/Laboratorium, January 1963.
- [4.7] J.C. McMillan and R.M. Pelloux, "Fatigue Crack Propagation under Program and Random Loads", *Fatigue Crack Propagation, ASTM STP 415*, 1967, pp. 505-535.
- [4.8] F. Erdogan, *Crack Propagation Theories*, NASA CR901, National Aeronautics and Space Administration, October 1967.
- [4.9] K. Walker, "The Effect of Stress Ratio during Crack Propagation and Fatigue for 2024-T3 and 7075-T6 Aluminum", *Effects of Environment and Complex Load History on Fatigue Life, ASTM STP 462*, 1970, pp. 1-14.
- [4.10] R.G. Forman, V.E. Kearney and R.M. Engle, "Numerical Analysis of Crack Propagation in Cyclic-Loaded Structures", *Journal of Basic Engineering*, September 1967, pp. 459-464.
- [4.11] W. Elber, "The Significance of Fatigue Crack Closure", *Damage Tolerance in Aircraft Structures, ASTM STP 486*, 1971, pp. 230-242.

- [4.12] M. Jolles, "Constraint Effects on the Prediction of Fatigue Life of Surface Flaws", *Journal of Engineering Materials and Technology*, Vol. 105, 1983, pp. 215-218.
- [4.13] M. Katchner and M. Kaplan, "Effect of R-Factor and Crack Closure on Fatigue Crack Growth Rate for Aluminum and Titanium Alloys", *Fracture Toughness and Slow Stable Cracking*, ASTM STP 559, 1974, pp. 264-282.
- [4.14] J. Feng, *The Fatigue Behavior of Small Cracks in Nickel-Base Superalloys*, Ph.D. Thesis, Massachusetts Institute of Technology, 1987.
- [4.15] D. Kreuger, *Effects of Grain Size and Precipitate Size on the Fatigue Crack Growth Behavior of Alloy 718 at 427C*, M.S. Thesis, University of Cincinnati, 1985. Also: G.E. Aircraft Engine Group Report #R85AEB133.
- [4.16] J.H. Hollomon, *Trans. AIME*, 162, 1945, p. 268.
- [4.17] W. Ramberg and W.R. Osgood, *Description of Stress-Strain Curves by Three Parameters*, NACA Tech. Note No. 902, 1943.
- [4.18] W.R. Osgood, "Stress-Strain Formulas", *Proc. J. Aeronaut. Sci.*, Vol. 13, 1946, pp. 45-48.
- [4.19] J. Bauschinger, *Zivilingur*, Vol. 27, 1881, pp. 289-347.
- [4.20] R.E. Stolz and R.M. Pelloux, "The Bauschinger Effect, Monotonic and Cyclic Hardening in Precipitation-Strengthening Aluminum Alloys", *Work Hardening in Tension and Fatigue*, The Metallurgical Society of AIME, A.W. Thomson, ed., 1975, pp. 224-239.
- [4.21] B. Hunsaker Jr., D.K. Vaugham and J.A. Stricklin, "A Comparison of the Capability of Four Hardening Rules to Predict a Materials Plastic Behavior", *Journal of Pressure Vessel Technology*, *Trans. AIME*, Feb. 1976, pp. 66-74.
- [4.22] R.P. Skelton, "Cyclic Stress-Strain Properties during High Strain Fatigue", *High Temperature Fatigue*, Elsevier Applied Science, 1987, pp. 27-112.
- [4.23] *Evaluation of the Cyclic Behavior of Aircraft Turbine Disk Alloys*, Pratt and Whitney Aircraft Group, NASA-CR-165123, 1980.
- [4.24] J. Hill, private communication, Pratt and Whitney Aircraft Group.
- [5.1] K.J. Miller in *The Behavior of Short Fatigue Cracks*, K.J. Miller and E.R. de los Rios, eds., University Press, Cambridge, 1986.
- [5.2] S.J. Maddox, "The Effect of Mean Stress on Fatigue Crack Propagation, A Literature Review", *International Journal of Fracture*, Vol. 11, No. 3, 1975, pp. 389-408.
- [5.3] T.R. Gurney, "The Effect of Mean Stress and Material Yield Stress on Fatigue Crack Propagation in Steels", *Metal Constr.*, Vol. 1, No. 2, 1969, p. 91.

- [5.4] T.W. Crooker and E.A. Lange, *Fatigue Crack Propagation in a High Strength Steel under Constant Cyclic Load with Various Mean Loads*, NRL Report No. 6805, Nov. 1968.
- [5.5] T.W. Crooker, *Effect of Tension Compression Cycling on Fatigue Crack Growth in High Strength Alloys*, NRL Report No. 7220, January 1971.
- [5.6] J.K. Musuva and J.C. Radon, "The Effect of Stress Ratio and Frequency on Fatigue Crack Growth", *Fatigue of Engineering Materials and Structures*, Vol. 1, 1979, pp. 457-470.
- [5.7] R.M. Gamble and P.C. Paris, "Cyclic Crack Growth Analysis for Notched Structures at Elevated Temperatures", *Mechanics of Crack Growth, ASTM STP 590*, American Society for Testing and Materials, 1976, pp. 345-367.
- [5.8] J.M. Larsen, J.C. Williams and A.W. Thompson, "Crack Closure Effects on the Growth of Small Surface Cracks in Titanium-Aluminum Alloys", *Mechanics of Fatigue Crack Closure, ASTM STP 982*, J.C. Newman Jr. and W. Elber, eds., American Society for Testing and Materials, Philadelphia, 1988, pp. 149-167.
- [5.9] G.O. Njus and R.I. Stephens, "The Influence of Yield Strength and Negative Stress Ratio on Fatigue Crack Growth Delay in 4140 Steel", *International Journal of Fracture*, Vol. 13, No. 4, 1977, pp. 455-466.
- [5.10] R.I. Stephens, G.W. McBurney and L.J. Oliphant, "Fatigue Crack Growth with Negative R-ratio Following Tensile Overloads", *International Journal of Fracture*, Vol. 10, 1974, pp. 587-589.
- [5.11] D. Gan and J. Weertman, "Crack Closure and Crack Propagation Rates in 7050 Aluminum", *Engineering Fracture Mechanics*, Vol. 15, No. 1-2, 1981, pp. 87-106.
- [5.12] W.N. Sharpe Jr., "Interferometric Surface Strain Measurement", *International Journal of Nondestructive Testing*, Vol. 3, 1971, pp. 59-76.
- [5.13] W.N. Sharpe Jr. and D.R. Martin, *An Optical Gage for Strain/Displacement Measurements at High Temperature Near Fatigue Crack Tips*, Air Force Materials Laboratory Report AFML-TR-77-153, Wright Patterson Air Force Base, OH, 1977.
- [5.14] W.N. Sharpe Jr. and M. Ward, "Benchmark Cyclic Plastic Notch Strain Measurements", *Journal of Engineering Materials and Technology, Trans. ASME*, Vol. 105, 1983, pp. 235-241.
- [5.15] J.R. Jira, T. Weerasooria, T. Nicholas and J.M. Larsen, "Effects of Closure on the Fatigue Crack Growth of Small Surface Cracks in a High Strength Titanium Alloy", *Mechanics of Crack Closure, ASTM STP 982*, J.C. Newman Jr. and W. Elber, eds., American Society for Testing and Materials, Philadelphia, 1988, pp. 617-635.
- [5.16] M.N. James and W.N. Sharpe Jr., "Closure Development and Crack Opening Displacement in the Short Crack Regime for Fine and Coarse Grained A533B

Steel", *Fatigue and Fracture of Engineering Materials and Structures*, Vol. 12, No. 4, 1989, pp. 347-361.

- [5.17] J.J. Lee and W.N. Sharpe Jr., "Closure Measurements on Short Fatigue Cracks", *Mechanics of Fatigue Crack Closure, ASTM STP 982*, J.C. Newman Jr. and W. Elber, eds., American Society for Testing and Materials, Philadelphia, 1988, pp. 270-278.
- [5.18] H. Sehitoglu, "Crack Opening and Closure in Fatigue", *Engineering Fracture Mechanics*, Vol. 21, No. 2, 1985, pp. 329-339.
- [5.19] N.E. Ashbaugh, "Effects of Load History and Specimen Geometry on Fatigue Crack Closure Measurements", *Mechanics of Fatigue Crack Closure, ASTM STP 982*, J.C. Newman Jr. and W. Elber, eds., American Society for Testing and Materials., Philadelphia, 1988, pp. 186-196.
- [5.20] D.E. Macha, D.M. Corbly and J.W. Jones, "On the Variation of Fatigue Crack Opening Load with Measurement Location", *Experimental Mechanics*, Vol. 19, 1979, pp. 207-213.
- [5.21] N.S. Iyyer and N.E. Dowling, "Opening and Closing of Cracks at High Cyclic Strains", *Proceedings of the Second Engineering Foundations Conference / Workshop on Small Fatigue Cracks*, The Metallurgical Society, Inc., 1986, pp. 213-233.
- [5.22] R. McClung and H. Sehitoglu, "Closure Behavior of Small Cracks under High Strain Fatigue Histories", *Mechanics of Fatigue Crack Closure, ASTM STP 982*, J.C. Newman Jr. and W. Elber, eds., American Society for Testing and Materials, Philadelphia, 1988, pp. 279-299.
- [5.23] J.C. Newman Jr., "A Finite Element Analysis of Fatigue Crack Closure", *Mechanics of Crack Growth, ASTM STP 590*, American Society for Testing and Materials, 1976, pp. 281-301.
- [5.24] C.M. Hudson, *Effect of Stress Ratio on Fatigue Crack Growth in 7075-T6 and 2024-T3 Aluminum Alloy Specimens*, NASA TN D-5390, National Aeronautics and Space Administration, Washington, D.C., 1969.
- [5.25] J.C. Newman Jr. and H. Armen Jr., "Elastic-Plastic Analysis of a Propagating Crack under Cyclic Loading", *AIAA Journal*, Vol. 13, No. 8, 1975, pp. 1019-1023.
- [5.26] K. Ohji, K. Ogura and Y. Ohkubo, "Cyclic Analysis of a Propagating Crack and its Correlation with Fatigue Crack Growth", *Engineering Fracture Mechanics*, Vol. 7, No. 3, 1975, pp. 457-464.
- [5.27] M. Nakagaki and S.N. Atluri, "Elastic-Plastic Analysis of Fatigue Crack Closure in Modes I and II", *AIAA Journal*, Vol. 18, 1980, pp. 1110-1117.
- [5.28] T. Nicholas, A.N. Pulazotto and E. Bednarz, "An Analytical Investigation of Plasticity Induced Closure Involving Short Cracks", *Mechanics of Fatigue Crack Closure, ASTM STP 982*, J.C. Newman Jr. and W. Elber, eds., American Society for Testing and Materials, 1988, pp. 361-377.

- [5.29] B. Budiansky and J.W. Hutchinson, "Analysis of Closure in Fatigue Crack Growth", *Journal of Applied Mechanics*, Trans. ASME, Vol. 45, 1978, pp. 267-276.
- [5.30] M. Kanninen and Atkinson, "Application of an Inclined-Strip-Yield Crack-Tip Plasticity Model to Predict Constant Amplitude Fatigue Crack Growth", *International Journal of Fracture*, Vol. 16, 1980, pp. 53-69.
- [5.31] J.C. Newman Jr., "A Crack-Closure Model for Predicting Fatigue Crack Growth under Aircraft Spectrum Loading", *Methods and Models for Predicting Fatigue Crack Growth under Random Loading*, ASTM STP 748, J.B. Chang and C.M. Hudson, eds., American Society for Testing and Materials, 1981, pp. 53-64.
- [5.32] D.S. Dugdale, "Yielding of Steel Sheets Containing Slits", *Journal of Mechanics and Physics of Solids*, Vol. 8, 1960, pp. 100-104.
- [5.33] J.C. Newman Jr., "A Crack Opening Stress Equation for Fatigue Crack Growth", *International Journal of Fracture*, Vol. 24, pp. R131-R135, 1984.
- [5.34] H. Nakamura and H. Kobayashi, "Analysis of Fatigue Crack Closure Caused by Asperities Using the Modified Dugdale Model", *Mechanics of Fatigue Crack Closure*, ASTM STP 982, J.C. Newman Jr. and W. Elber, eds., American Society for Testing and Materials, Philadelphia, 1988, pp. 459-474.
- [5.35] H. Nakamura, H. Kobayashi, S. Yanase and H. Nakazawa, *Transactions of the Japan Society of Mechanical Engineers*, Vol. 51A, 1985, pp. 148-151 (in Japanese).
- [5.36] P.L. Lalor and H. Sehitoglu, "Fatigue Crack Closure Outside a Small Scale Yielding Regime" in *Mechanics of Fatigue Crack Closure*, ASTM STP982, J.C. Newman Jr. and W. Elber, eds., American Society for Testing and Materials, Philadelphia, 1987, pp. 342-360.